University of Cambridge

Cavendish Laboratory

Laboratory Astrophysics Group

The Far-Ultraviolet Spectroscopy of Molecules of Astrophysical Interest

by

Colin Michael Foale, BA.
Queens' College, Cambridge

Thesis submitted for degree of

Doctor of Philosophy

1981

ACKNOWLEDGEMENTS

The work presented in this dissertation was carried out between October 1978 and October 1981. Unless stated otherwise, the dissertation is original and is the result of my own work. It includes nothing which is the outcome of work done in collaboration. Furthermore, the results contained in this dissertation have not been submitted for a degree at any other University.

I would like to extend my thanks to Professor A.H.Cook for giving patient and helpful support during this project and to members of Imperial College, London and Dr. Joseph Hormes at the Physikalisches Institute, who taught me much about VUV spectroscopy while using the 2.5GeV synchrotron in Bonn.

This thesis and the work described within it would have been impossible without the generous help given to me by Mr.Ray Flaxman, Mr. Alex Page, and Mr. Roger Morley at the Cavendish Laboratory. I am extremely grateful to them for the time and trouble they spent on my behalf.

Finally, I should like to thank Professor A.Bradshaw at the Fritzhaber Inst., Berlin for arranging facilities in Bonn, and Joyce Hilling for her great patience whilst typing this thesis.

I acknowledge receipt of an S.E.R.C. research grant to enable this work to be carried out.

"Man must rise above the earth - to the top of the atmosphere and beyond - for only thus will he fully understand the world in which he lives".

Socrates 500B.C.

To Cathy and Chris

Abstract

The Far-Ultraviolet Spectroscopy of
Molecules of Astrophysical Interest

More than 40 different molecules have been observed in Interstellar space within the Galaxy. Many of these molecules are seen near hot OB-type stars whose far-ultraviolet emission is intense. Laboratory spectroscopy of such molecules will lead to a better understanding of their astrophysical behaviour, in particular Celestial Masers.

This thesis is preoccupied with the spectroscopy of H_2O, D_2O, OH, CO, and C_2H_2 in the region 1200Å-400Å and absolute absorption coefficients are derived for CO and C_2H_2 using the Thomas-Reiche-Kuhn Sum Rule. A possible Rydberg series of OH was observed, converging to a first ionisation potential of 13.36 eV and a likely inner shell two-electron resonance detected in the ionisation continuum of D_2O at 415A.

Both a synchrotron and a laser produced plasma continuum source were used for absorption measurements and the advantages of each source were compared. Experiments were undertaken to examine the radiation properties of laser produced plasmas with a view to their general use as far-ultraviolet continuum sources and a computer program was written to predict their net photon emission by Bremsstrahlung processes, with some success.

Optoacoustic spectroscopy was considered as a possible technique in the far-ultraviolet with a synchrotron source; its theory was extended to include ionisation and dissociation of molecules. However, optoacoustic experiments attempted were unsuccessful because of insufficient light intensity and excessive background noise near the synchrotron.

Colin Michael Foale,
Cavendish Laboratory,
Cambridge.

C O N T E N T S

CHAPTER 1

1.1 Introduction

An Astrophysical perspective for the study of interstellar Molecules.

Over the last twenty years more than forty different molecules have been detected in interstellar space, both in the spiral arms and towards the centre of our Galaxy. Nearly all the molecules were discovered using the fairly recent techniques developed in Radio Astronomy. The radio spectra are characterised predominantly by continuous radiation from synchrotron or thermal sources (Sciama, 1971), since transitions between atomic or molecular states are weak. One outstanding line in radio spectra is the 21cm wavelength radiation emitted by the weak magnetic dipole transition between the two hyperfine levels of the ground state in atomic hydrogen, a transition which has the very low probability of $10^{-21}s^{-1}$. However, there is so much atomic hydrogen in the Galaxy that appreciable signals are observed in all directions. Hyperfine transitions in all atoms are of comparable intensities and since all other atoms are far less numerous than hydrogen, the 21cm line is the only atomic radio-transition that can be detected.

Molecules show quite different behaviour. In addition to electronic energy, molecules have quantised energies of rotation and vibration, between which transitions lie in the near-infrared (vibrational transitions) and in the far-infrared and radio region (rotational transitions). Furthermore, there are internal molecular interactions which split the rotational states into still more closely spaced levels. Because transitions in all these groups are usually of the electric dipole type, they are much stronger than hyperfine transitions, and, therefore, much more likely to be seen with radio telescopes.

The first molecule to be discovered by Radio Astronomy was hydroxyl (OH) in absorption against a continuum source, by

1.1 Introduction

An Astrophysical perspective for the study of interstellar Molecules.

Over the last twenty years more than forty different molecules have been detected in interstellar space, both in the spiral arms and towards the centre of our Galaxy. Nearly all the molecules were discovered using the fairly recent techniques developed in Radio Astronomy. The radio spectra are characterised predominantly by continuous radiation from synchrotron or thermal sources (Sciama, 1971), since transitions between atomic or molecular states are weak. One outstanding line in radio spectra is the 21cm wavelength radiation emitted by the weak magnetic dipole transition between the two hyperfine levels of the ground state in atomic hydrogen, a transition which has the very low probability of $10^{-21} s^{-1}$. However, there is so much atomic hydrogen in the Galaxy that appreciable signals are observed in all directions. Hyperfine transitions in all atoms are of comparable intensities and since all other atoms are far less numerous than hydrogen, the 21cm line is the only atomic radio-transition that can be detected.

Molecules show quite different behaviour. In addition to electronic energy, molecules have quantised energies of rotation and vibration, between which transitions lie in the near-infrared (vibrational transitions) and in the far-infrared and radio region (rotational transitions). Furthermore, there are internal molecular interactions which split the rotational states into still more closely spaced levels. Because transitions in all these groups are usually of the electric dipole type, they are much stronger than hyperfine transitions, and, therefore, much more likely to be seen with radio telescopes.

The first molecule to be discovered by Radio Astronomy was hydroxyl (OH) in absorption against a continuum source, by

Weinreb et al (1963). The rotational transitions of OH lie in the far-infrared but these levels are split into lambda (Λ) doublets by an interaction between the nuclear rotation and the component of electronic angular momentum along the internuclear axis; furthermore, each doublet level is split by a hyperfine interaction between the proton spin and the electron in the $^2\Pi_{3/2}$ ground state. (For a description of molecular spectroscopic rotation see Herzberg, 1950). Thus there are four closely spaced levels in the electronic ground state with four allowed electric dipole transitions between them (Fig.1.1) at 1720, 1667, 1665, and 1612 MHz. It was these transitions Weinreb et al detected and with which the local temperature and relative velocity of the absorbing gas cloud were able to be calculated, based on the doppler broadening and doppler shifts of the transition lines. The detection of emission spectra by Weaver et al (1965) from these same four levels of hydroxyl followed two years later and in the period 1968-1970 emission from several excited rotational states was also observed. The emission spectra revealed many puzzling features entirely inconsistent with spontaneous emission of the excited states. First, the individual sources are found to be very small (10^{-2} — 10^{-4} arc sec) and the intensities are correspondingly great, equivalent to blackbody emission between 10^{12} and 10^{14} K but with doppler line widths appropriate to a temperature of some 100K. Second, the doppler shifts of each line seen in a particular direction do not correspond to a single set of mass velocities in the hydroxyl gas, with often one line blue-shifted and another red-shifted. Third, the radiation from each individual small spot is often circularly polarised, either left or right handedly. Spontaneous radiation, Zeeman split by a magnetic field, should give both right and left handed components of equal intensity (Cook$_a$, 1977). Nearly all the anomalous emission properties of OH can be explained if maser amplification of either the Cosmic background radiation or spontaneous emission is assumed (eg. Cook$_b$, 1977). The maser action requires an inversion mechanism by which a population trans-

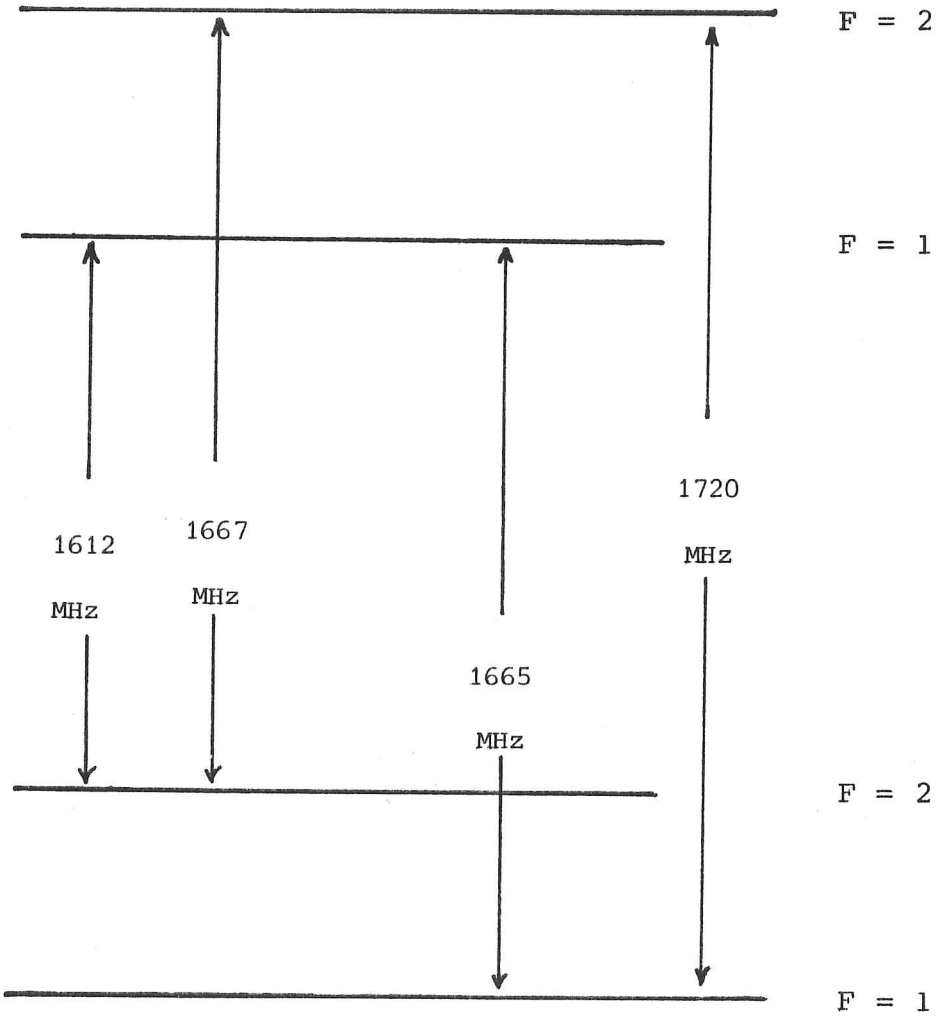

Fig. 1.1 Ground state quartet of hydroxyl

fer is induced from the two lower to the two upper doublet hyperfine states; such a pumping process must be balanced by the microwave emission rate and other relaxation processes.

Very strong maser emission with similar properties to OH sources has subsequently been found from a single transition in H_2O at 1.35cm, from rotation transitions of the excited vibration states of SiO, from CH_3OH, CH and maybe CH_4 (Fox et al,1978). As well as these masers a great many molecules have been detected by radio frequency spectroscopy, a list of which is presented in Table 1.1. Some molecules, in particular CO, (carbon monoxide), are widespread throughout the Galaxy, while others can only be detected towards the Galactic centre. However, one extremely important molecule, H_2, has been detected by neither radio nor infrared astronomy. Molecular hydrogen was seen by absorption of starlight near 1100Å in the far ultraviolet region of the spectrum, using instruments carried by the Copernicus satellite and others, above the atmosphere, which is opaque at such short wavelengths. Because molecular hydrogen is so light compared to all other molecules, its rotational levels are spaced too far apart for the transitions to be detected by Radio Astronomy, although it is the most abundant molecule in the Galaxy. Its abundance can sometimes be inferred from that of CO, as the two molecules often occur together.

In the Galaxy as a whole, molecules are usually unstable unless they are shielded by clouds of gas or dust from pervasive ultraviolet light emmanating from stars, which otherwise will cause them to dissociate quite rapidly. Even within an interstellar cloud with an optical absorption of some three magnitudes, molecular lifetimes of a thousand years will be increased to only a million years or more. Thus, molecules have a relatively short life, even in molecular clouds and the densities attained result from a dynamic balance between formation and destruction, highly

Table 1.1 Molecules Identified in Interstellar Space

Inorganic	Diatomic	Organic
H_2-hydrogen (UV)		CH-methyladyne radical
OH-hydroxyl radical		CH^+-methyladyne ion(optical)
SiO-silicon monoxide		CN-cyanogen radical
NS-nitrogen sulphide		CO-carbon monoxide
SO-sulphur monoxide		CS-carbon monosulphide
SiS-silicon sulphide		

Inorganic	Triatomic	Organic
H_2O-water		CCH-ethynyl radical
N_2H^+		HCN-hydrogen cyanide
H_2S-hydrogen sulphide		HNC-hydrogen isocyanide
SO_2-sulphur dioxide		HCO^+-formyl ion(X-ogen)
		HCO-formyl radical
		OCS-carbonyl sulphide

Inorganic	4-Atomic	Organic
NH_3-ammonia		H_2CO-formaldehyde
		HNCO-isocyanic acid
		H_2CS-thioformaldehyde
		H_2C_2
		C_3N^2

Inorganic	5-Atomic	Organic
		H_2CNH-methanimine
		H_2NCN-cyanamide
		HCOOH-formic acid
		HC_3N-cyanoacetylene
		CH_4
		HC_4

Inorganic	6-Atomic	Organic
		CH_3OH-methyl alcohol
		CH_3CN-methyl cyanide
		$HCONH_2$-formamide

Inorganic	7-Atomic	Organic
		CH_3NH_2-methylamine
		CH_3C_2H-methylacetylene
		$HCOCH_3$-acetaldehyde
		H_2CCHCN-vinyl cyanide
		HC_5N-cyanodiacetylene

Inorganic	8-Atomic	Organic
		$HCOOCH_3$-methyl formate
		CH_3C_2CN

Inorganic	9-Atomic	Organic
		$(CH_3)_2O$-dimethyl ether
		CH_3CH_2OH-ethyl alcohol
		HC_7N

Inorganic	10-Atomic	Organic
		HC_9N Cyanooctatetrayne

sensitive to the local astrophysical conditions. From their emission and absorption properties it is possible to infer something about the conditions in the sources - for example density, radiation temperature, mass velocity, spatial and temporal variations - which may give clues to both the processes of their own life cycles and also those of the energy sources which are driving the region. Molecules are detected in some of the most interesting parts of the Galaxy, near compact infrared sources such as in Orion (Wynn-Williams, 1981) where new stars seem to be forming, or in the circumstellar shells surrounding late type stars like Red Giants or Super Giants which are at a late stage in their evolution. (Elitzur, 1980). The responsiveness of molecules to their environments, together with their abundance throughout the Galaxy means that a powerful tool is available to Radio Astronomy to probe either Stellar Evolution or to answer more fundamental questions concerning the Cosmic background radiation or the abundance of dark matter, such as molecular hydrogen in dust clouds within the Galaxy (Cook, 1975).

The pumping systems of celestial masers are the most sensitive to the physical conditions of the source, such as molecular density, radiation intensity and kinetic temperature. Inevitably, quite different inversion mechanisms can be applied to the same maser source with similar degrees of success. A favourite model for OH masers, found near the shock-front of an expanding HII region, is based on the excitation of OH by ultraviolet radiation near 3070Å followed by preferential decays to the upper Λ doublet states of the $^2\Pi_{3/2}$ ground states (Litvak, 1966). This model applies quite well to HII regions where an expanding cloud of ionised gas near very hot, young O B-type stars contains a high radiation density in the ultraviolet region. Since OH will dissociate in an ionised HII region, the masers are proposed to lie near the expanding shock front, at the border between the hot HII gas and the surrounding

cold molecular hydrogen cloud from which the OB stars originally condensed. Cook (1968) proposed a different mechanism by which the molecule was excited in the far ultraviolet by the lyman - α hydrogen emission line, which he postulated might be coincident with one of the then unmeasured Rydberg absorption lines of OH. However, Douglas (1974) found appropriate Rydberg absorptions in OH at 1222Å away from the lyman - α line at 1215Å , implying that this particular inversion system had to be ruled out. (But this thesis contains results which tentatively suggest that the hydrogen lyman - γ , δ lines coincide with broad OH Rydberg absorption features at 972Å and 949Å so a far ultraviolet pumping scheme for hydroxyl should not be discounted arbitrarily). Appropriate to OH sources near infrared objects, photon pumps employing either microwave or infrared radiation have been proposed by Litvak (1969) and others (Cook, 1977).

A limitation of all photon pumping schemes is that in general at least one pumping photon is needed for each masing photon emitted: because the observed intensities of most maser sources are very great (eg.10^{48} photons s^{-1} near W49, Oka, 1971) the stellar source of energy must also provide a similar number of pumping photons, such as would be emitted in the ultraviolet by hot, young, OB-type stars. Oka (1971) has proposed a model for water masers which partially circumvents the usual requirement of a one-to-one correspondence between the exciting ultraviolet and the masing microwave photons. In water just a single maser line is involved; not a quartet, as with hydroxyl. The two levels are the 6_{16} and 5_{23} rotational levels of the ground electronic state (see Herzberg, 1950, for a description of the notation) and if collisions are less important than radiational transitions, the populations of the two states will be determined by the relative strengths of the infrared transitions between neighbouring levels, given some process that excites water molecules to states of high energy in the infrared, compared to the microwave maser transition.

Oka proposed that the initial excitation is by ultraviolet absorption, for example near an HII region, followed by dissociation of most rotational quantum states except those of the type J_{17}, which decay by radiation to less excited states such as the 6_{16} upper maser level. Because the lower 5_{23} state is depopulated by the absorption of dissociating ultraviolet radiation over a broad continuum of roughly 100Å width, an inverted population results between the two levels causing maser action to occur. It was with a similar mechanism in mind that both Viney (1979) and I were stimulated by Prof. A.H.Cook to investigate hydroxyl and other molecules in the far ultraviolet.

Other inversion mechanisms have been proposed involving excitation of the masers by collisions or by the course of chemical reactions. In particular, Gwinn et al (1973) proposes that if water is dissociated by ultraviolet radiation the hydroxyl produced will be in an excited state. Some of the collisional pumps have the advantage that they do not necessarily require a high photon density present near the maser source, as must be the case for most photon inversion mechanisms.

1.2 Relevance of Laboratory Studies on Molecules of Astrophysical interest.

There appears to have been no inversion model proposed so far which can account for all the features of maser radiation emitted from a variety of astrophysical molecules. There is also little doubt that a combination of some pumping models is pertinent in certain cases (Cook, 1977). Although many theoretical studies were performed more than ten years ago, few laboratory experiments concerned with pumping mechanisms have been reported yet. One obvious difficulty which applies to any relevant experiment is the vast difference between conditions which hold in interstellar space compared to those which can be achieved in the laboratory. Table 1.2 lists some relevant quantities assumed to hold in

the vicinity of an OH maser source, compared to the typical conditions of a laboratory experiment.

Table 1.2

Physical Quantity	Interstellar OH Source	Laboratory Experiment
kinetic temperature (K)	100	300-500
OH density n_{OH} (cm^{-3})	10^{-2}	10^{14}
total density (cm^{-3})	$10^{4} \times n_{OH}$	$10^{2} \times n_{OH}$
electron density (cm^{-3})	1	10^{8}
length OH region (m)	$10^{13}-10^{16}$	1
UV radiation density ($W\ m^{-2} H_z^{-1}$)	10^{-17}	10^{-6}

TABLE 1.2 A comparison of some relevant physical quantities as assumed to hold in the vicinity of the interstellar OH sources with the values obtainable in a laboratory experiment. The values given for the interstellar OH sources follow from the conditions required for an efficient operation of the population inversion mechanisms based on the excitation by UV radiation (Litvak et al 1966) or by electrons (Johnston, 1967).

Some attempts have been made to study the collisional excitation of OH using a hydroxyl Beam-maser in which a state-selected beam of hydroxyl molecules is probed with microwaves to determine the relative population levels of the hyperfine Λ -doublet quartet in the ground electronic state (Meulen, 1978). Viney (1979) undertook far infrared absorption studies of the first few rotational levels in the ground electronic state of OH between 40-230 cm^{-1} and attempted some preliminary spectroscopy of OH in the far-ultraviolet at wavelengths less then 1200 Å ; these wavelength regions have never been well observed in any molecules, although certain pumping models have been proposed which require a definite knowledge of OH in these spectral regions and which might also be extended to other astrophysical masers (Litvak, 1966; Cook, 1966).

At present, more information is needed concerning the spectra

of many molecules and about collisional or reaction processes undergone by molecules. At the most elementary level, the chance of discovering further molecules is now limited by a lack of laboratory measurements of radio transition frequencies in the face of the many spectral lines already seen by Radio Astronomy, which remain to be identified (Cook,1975). This thesis is preoccupied with the far-ultraviolet spectroscopy of a few molecules of astrophysical interest, including a re-examination of the proposed hydroxyl absorption features reported by Viney (1980) at wavelengths less than 1200Å.

Far-Ultraviolet spectroscopy in conjunction with a continuum source

We shall assume the far ultraviolet wavelength region to run from approximately 1200Å - 300Å . At longer wavelengths absorption tubes can be used with window materials which are able to transmit ultraviolet light, such as those made from LiF,but air, which is a strong absorber below 2000Å must always be excluded from ultraviolet experiments at shorter wavelengths. Below 1200Å there are no window materials and the far-ultraviolet radiation must be both generated and introduced to experiments while in a vacuum. The whole wavelength region between 2000Å - 300Å is commonly known to experimental physicists (who have to tackle these problems) as the Vacuum Ultraviolet (VUV) region. Photons with wavelengths shorter than 300Å behave progressively more like X-rays towards higher energies and the border region betwen 300Å -10Å is sometimes denoted as the Extreme Ultraviolet (XUV). Little attention is given to the region in this thesis.

Some general theoretical principles of VUV absorption spectroscopy are described in Chapter 2, with emphasis on a new approach to these wavelengths employing optoacoustic spectroscopy, as well as considering conventional absorption techniques (eg. Samson, 1967). Optoacoustic spectroscopy

is well known to infrared spectroscopists who use high power continuous-wave lasers to detect absorption by molecules which may be at a very low concentration in the absorption cell. Essentially, a mechanically chopped beam of monochromatic light at acoustic frequencies produces synchronous temperature/pressure variations in a gas cell if sufficient light is absorbed. The pressure variations constitute sound waves which can be detected by a microphone placed within the gas cell, picking up an acoustic tone at the same frequency as the light chopper. A requirement of both the optoacoustic and ordinary absorption techniques is the ability to produce continuum radiation throughout the VUV; with which either a monochromatic beam can be made, using a suitable Vacuum Monochromator, or a broad-band source can be used to form the background light for a Vacuum Spectrograph.

1.3 The need for a suitable VUV continuum source.

'Synchrotron Radiation' has been put to great use in recent years as a source of pure continuum light in the VUV and XUV spectral regions. It is the major loss mechanism in accelerators or storage rings by which radiation is emitted from electrons as they are accelerated to high energies, and the properties of the radiation are well understood. For a general review of Synchrotron Radiation and its advantages over other, alternative sources, Codling (1973) should be consulted. Until recently, synchrotron radiation was the best continuum source available below 600Å , where the helium discharge lamp ceases to provide an adequate alternative (Samson 1967). The work to be described in this thesis was proposed to be undertaken using the new 2.0GeV Synchrotron Radiation Source (SRS) recently constructed at Daresbury; it was with this intention that some optoacoustic experiments were designed. However, the SRS was not ready in time before completion of this thesis work and an alternative source had to be found. Eventually, Professor A. Braddshaw at the Fritz-Haber Institute, Berlin was contacted

who very kindly made arrangements for the use of the 2.5 GeV electron-synchrotron at Bonn (BonnI), in Germany. Unfortunately, the light intensity obtained using the BonnI synchrotron was a factor of 10^3 less then that expected from the SRS at Daresbury and thence compromised the optoacoustic aspects of the VUV absorption experiments undertaken in Germany. As an illustration of the typical light intensities calculated for the two synchrotron sources SRS and BonnI, Figs.1.2 and 1.3. show emissions which correspond to light emitted in a narrow cone along a tangent to the electron orbit. If the plane of the orbit (Synchrotron) is horizontal, then a larger, azimuthal angle of acceptance in a beam line will collect a proportionately greater section of tangential emission. The vertical extent of the light beam is of the order 1 mrad about the tangent line and the curves in Figs. 1.2 and 1.3 assume all such light is collected. The polar diagram of a low and high energy circular electron current is also shown schematically in Fig. 1.2. In practice, roughly 1% of the calculated radiation intensity is available to an experiment after it has passed through an XUV filtering mirror, a beamline and finally a normal incidence monochromator.

While waiting for a suitable synchrotron source, attention was directed to recent reports of Carroll et al (1980), which described intense VUV continuum emission from laser produced plasmas. Rare earth target metals had been heated and vapourised by focused Ruby laser radiation, condensed by a simple lens. During the brief duration of the laser pulse an extremely hot and dense fireball was produced which emitted continuum radiation down to XUV wavelengths. It occurred to us that such a source might be suitable for VUV spectrographic studies of simple molecules and the speculation stimulated me to undertake both an experimental and a theoretical study of the feasibility of such an experiment, against the event that a synchrotron source should no longer be available.

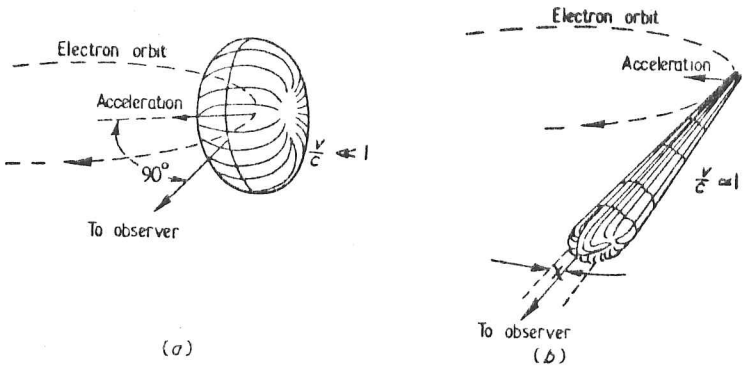

Qualitative radiation patterns for electrons in circular orbit (a) at speeds small compared with the speed of light, when the typical dipole radiation pattern is observed, and (b) at speeds approaching the speed of light, when the radiation pattern is distorted in the direction of the electron's motion so that the 'zeros' now occur at an angle $X = \{1-(v/c)^2\}^{\frac{1}{2}}$. From Tomboulian and Hartman (1956).

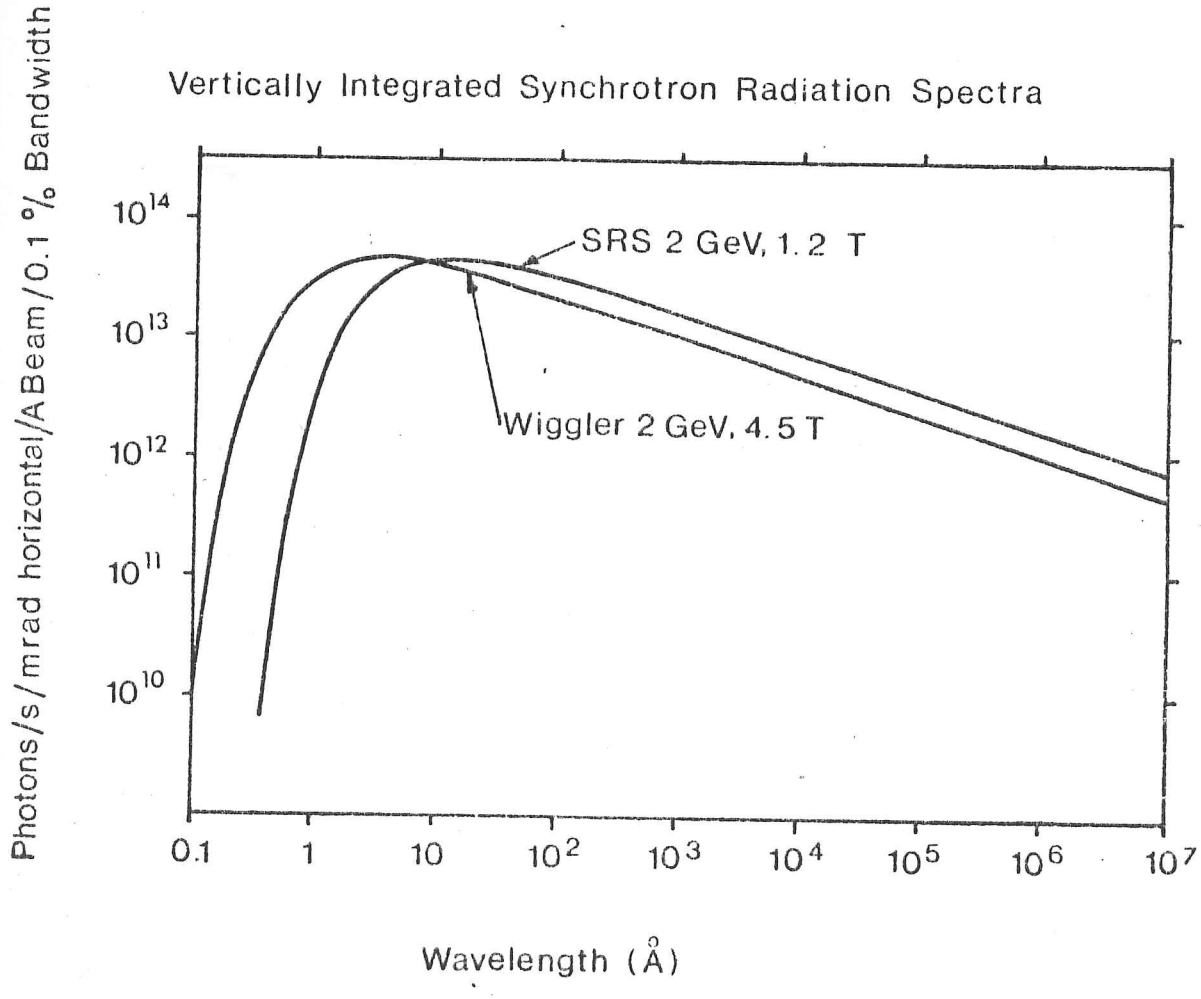

Fig. 1.2 (Daresbury SRS)

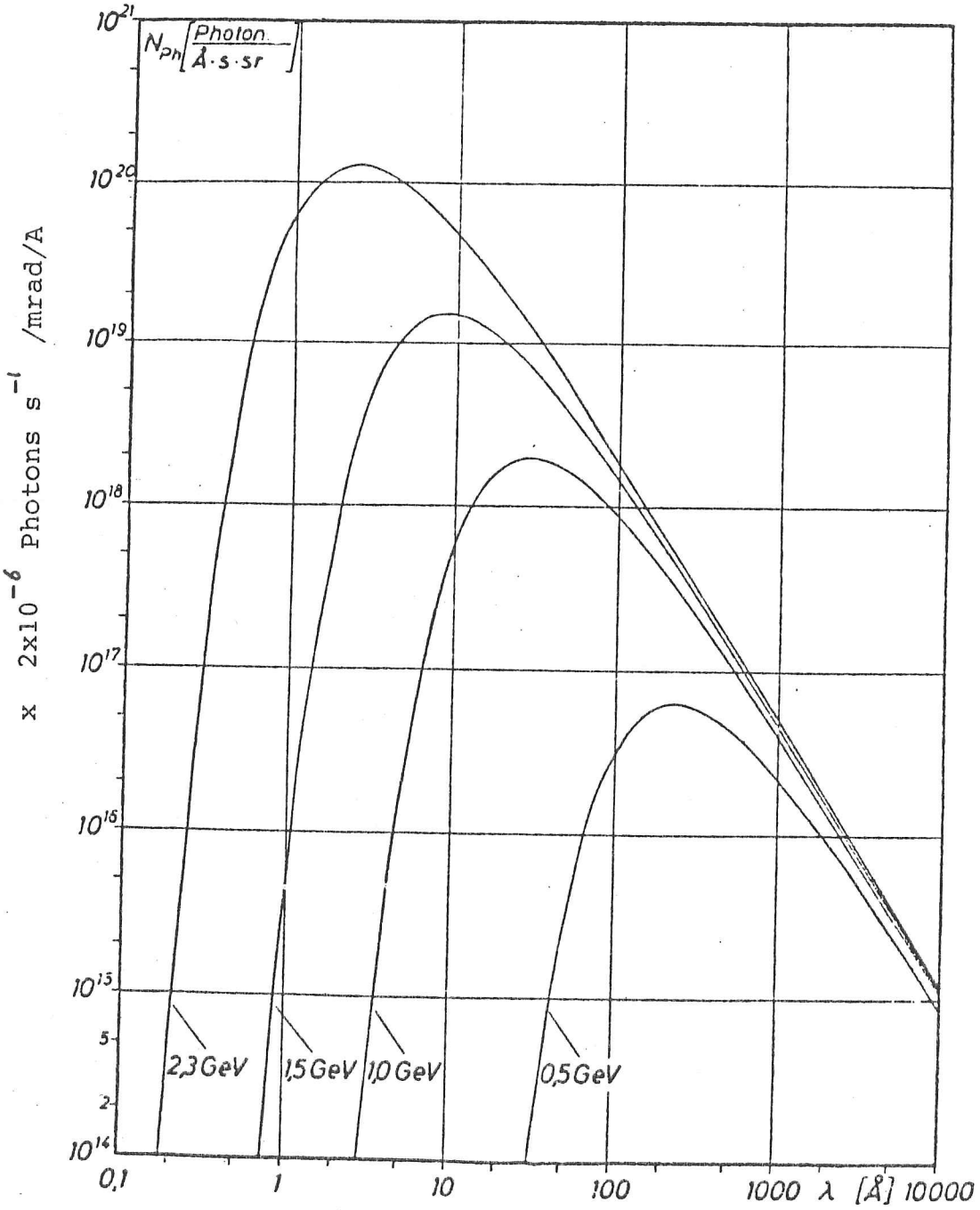

The Photon emission spectrum of the 2.5GeV synchrotron at BonnI for various electron energies, with a current of 30mA.

Fig.1.3

The uncertainty as to which VUV source might be employed played a major part in directing the work described in this thesis. The first half of the thesis is concerned primarily with optoacoustic and absorption VUV spectroscopy, using the BonnI synchrotron; the second part is preoccupied with the potential use and experimental properties of laser-produced plasmas in the VUV.

Within the first part, general theoretical principles of VUV optoacoustic spectroscopy are treated in Chapter 2. The theoretical extension of optoacoustic theory to the VUV is my own. Chapters 3 and 4 are concerned with the development and implementation of an experiment to measure absorption cross-sections of H_2O, D_2O, OH, CO and C_2H_2 between 1200Å - 400Åusing the BonnI synchrotron. Chapter 5 discusses the spectra obtained and proposes a little of their analysis.

In the second part of the thesis, Chapter 6 reviews the reports of laser-produced plasmas as background spectroscopic sources and an attempt is made to predict their continuum emission using a computer model designed and written by me. Chapter 7 describes experiments undertaken on laser-produced plasmas to determine more fully their emission characteristics and other properties, while Chapter 8 presents the results of a preliminary attempt to obtain the VUV spectra of CO and C_2H_2, employing a Vacuum Spectrograph and a laser-plasma as the continuum source.

In conclusion, Chapter 9 summarises the results of this thesis and suggests where its weaknesses and strengths might lie, together with more positive proposals for future study.

CHAPTER 2

2.1 General aspects of absorption and optoacoustic spectroscopy in the VUV.

It was mentioned in Chapter 1 that two possible Vacuum Ultraviolet photoabsorption techniques presented themselves to be both interesting and attractive methods by which the spectra of some simple Astrophysical molecules might be elucidated. The first method, Absorption Spectroscopy, is a conventional one and has been used on many occasions to determine absolute atomic or molecular absorption coefficients. It relies simply on a measurement of the variation of transmitted monochromatic light passing through a gas column as a function of wavelength. The second method, Optoacoustic Spectroscopy is less well known to ultraviolet spectroscopists but has been used in a variety of situations by researchers studying infrared absorption spectra, making use of high power continuous-wave lasers now available over a range of infrared wavelengths. The technique detects the light energy absorbed by a gas medium as a function of wavelength, rather than a variation of the transmitted light more fundamental to the first method. Since the two methods could be considered complementary to one another under certain conditions, an experiment was studied which would combine both techniques into one. This chapter discusses the theory behind the amalgamated experiment and includes a brief review of molecular absorption theory both above and below the first ionisation potential, with some emphasis on the usefulness of the Sum Rules in the VUV region.

The first method - convential absorption spectroscopy

This technique infers the amount of light intensity absorbed by a gas from the quantity transmitted through it. Consider a gas column of length ℓ with a molecular number density n. At one end of the column light which is nearly monochromatic enters and has an intensity Io, with units of Watts m^{-2} per ($rads^{-1}$). As the photons travel along the column some may be removed from the beam by gas molecules which happen to absorb at a frequency close to the average of the light, resulting in a steady attenuation of the beam

during its passage along the column. The situation is depicted in Fig 2.1 and is described well by Thorne (1979). The essential arguments and conclusions will be given below.

Fig.2.1

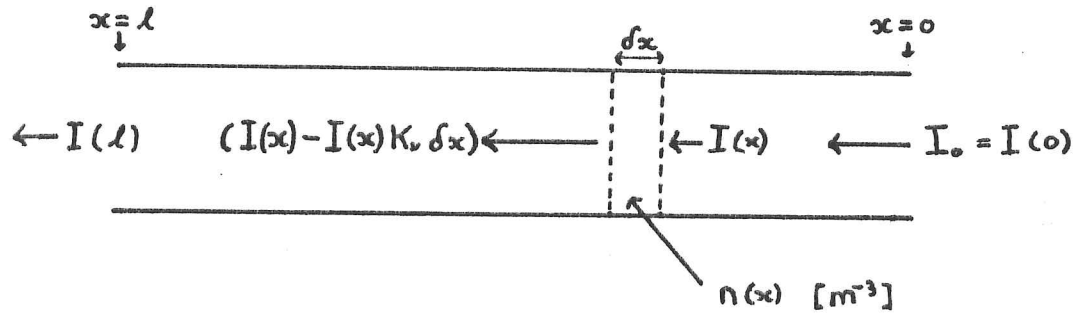

The energy absorbed in a distance δx is proportional to both δx and the incident intensity on a slab of unit cross-section, the proportionality constant being, in general, a function of frequency. In the diagram the absorbed intensity is shown to be $I K_\nu \delta x$ and the equation

$$-\delta I_\nu = K_\nu I_\nu(x)\,\delta x \qquad (2.1)$$

defines the absorption coefficient K_ν, usually expressed in units of reciprocal centimetres. The suffix ν denotes the average frequency of the nearly monochromatic light. For the length l of the absorbing molecular column the relation between the incident intensity $I_\nu(o)$ and the emergent intensity $I_\nu(l)$ is found by integrating equation (2.1) giving

$$I_\nu(l) = I_o e^{-\int_o^l K_\nu dx} \qquad (2.2)$$

if Io is equal to $I_\nu(o)$ at the origin. The integral

exponent is the optical depth of the gas column and is simply $K_\nu \ell$ if the medium is homogeneous, meaning that K_ν is a constant with respect to x. Thus

$$I_\nu(\ell) = I_0 e^{-K_\nu \ell} \qquad (2.3)$$

When an atom or molecule undergoes an electronic transition from a low energy level to a higher one by stimulated absorption of a photon of energy $h\nu_0$ the possible absorption will be spread over a finite frequency range by various broadening mechanisms. The plot of $I_\nu(\ell)$ against ν has the general form of Fig.2.2 and can be measured for a particular gas by performing an experiment in which the ratio of transmitted to incident intensity is measured as a function of the light frequency. The plot provides the experimental data from which K_ν is obtained as a function of frequency by the relation

$$K_\nu = \frac{1}{\ell} \ln \frac{I_0}{I_\nu(\ell)} \qquad (2.4)$$

for a homogeneous medium.

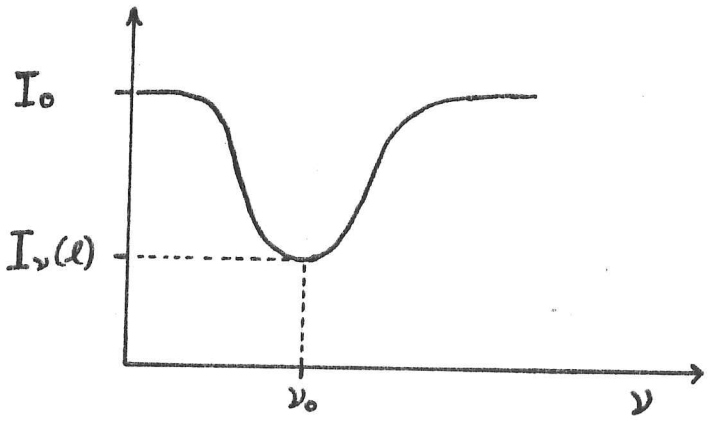

Fig. 2.2

A typical profile obtained for K_ν is shown in Fig. 2.3 as a function of ν .

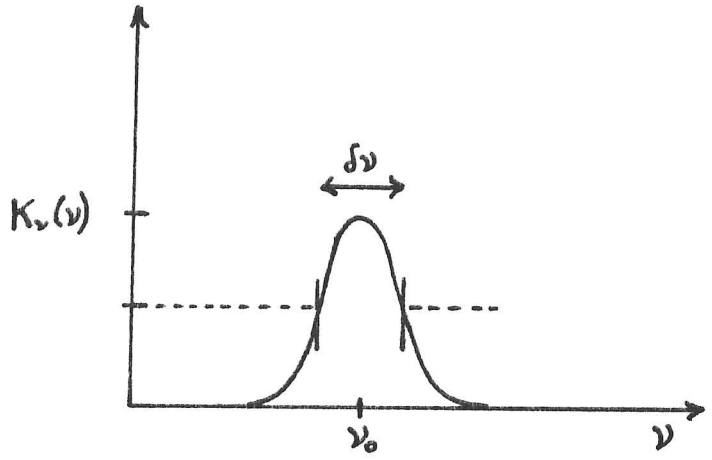

Fig. 2.3.

$\delta\nu$ is the half-power width of the absorption profile around ν_0 . Generally Fig. 2.2 only has the same shape as Fig. 2.3 when the optical depth is much less than one. Equation (2.3) then becomes

$$I_\nu(l) \approx I_0(1 - K_\nu l) \qquad K_\nu l \ll 1$$

Fig.2.2 which is observed directly, will become broader and more shallow as the optical depth is increased, while the absorption - coefficient profile in Fig. 2.3 will remain independent of optical depth.

The Molecular absorption-coefficient K_ν

Even though the shape of the K_ν curve depends on the broadening mechanisms involved, the total area represented by its integral must depend only on the total light intensity absorbed. From the quantum theory of radiation (eg.Loudon, 1973) the rate at which an electronic system, be it an atom

or molecule, undergoes transitions from one eigenstate ψ_o to another ψ_j under the influence of a light beam is given by the rate

$$(o \rightarrow j) \qquad \frac{dN}{dt} = B_{jo}\,\rho(\nu) \qquad [s^{-1}]$$

where

$$B_{oj} = \frac{\pi e^2}{3\varepsilon_o \hbar^2} |\langle \psi_j | \hat{r} | \psi_o \rangle|^2 \qquad [s^{-1}\,\text{per}\,(J\,m^{-3}\,\text{per rad}\,s^{-1})] \qquad (2.5)$$

and $\rho(\nu)$ is the energy density of the light causing the transitions. B_{jo} is an Einstein coefficient for stimulated emission and is related to the coefficient for spontaneous emission A_{oj} by the formula (Loudon, 1973)

$$A_{jo} = \frac{\hbar \omega_o^3 g_o}{\pi^2 c^3 g_j} B_{oj} \qquad (2.6)$$

where g_o & g_j are the degeneracies of the lower and upper states respectively and $\omega_o = 2\pi\nu_o$. Since K_ν depends on the rate of absorption of photons it must in turn depend on the transition rate, proportional to B_{jo}. The exact relationship may be found by considering the energy absorbed in a slab of gas of unit cross-section and thickness δx exposed to a radiation intensity I_ν as shown in Fig. 2.1. where I_ν has units of Watts m^{-2} per (rads^{-1}). The energy incident per second on the section δx of the column is simply $I_\nu \delta\nu$ for a frequency bandwidth $\delta\nu$ about ν_o. The energy absorbed per unit time is given by Equation (2.1) to be $(I_\nu \delta\nu\, K_\nu \delta x)$. When I does not vary appreciably with frequency near ν_o the total energy E absorbed per second is given by

$$-\frac{dE}{dt} = I_\nu\, \delta x \int_{\text{line}} K_\nu\, d\nu$$

or molecule, undergoes transitions from one eigenstate ψ_o to another ψ_j under the influence of a light beam is given by the rate

$$(o \rightarrow j) \qquad \frac{dN}{dt} = B_{jo}\,\rho(\nu) \qquad [s^{-1}]$$

where

$$B_{oj} = \frac{\pi e^2}{3\varepsilon_o \hbar^2} |\langle \psi_j | \hat{r} | \psi_o \rangle|^2 \qquad [s^{-1}\,\text{per}\,(J m^{-3}\,\text{per rad}\,s^{-1})] \qquad (2.5)$$

and $\rho(\nu)$ is the energy density of the light causing the transitions. B_{jo} is an Einstein coefficient for stimulated emission and is related to the coefficient for spontaneous emission A_{oj} by the formula (Loudon, 1973)

$$A_{jo} = \frac{\hbar \omega_o^3 g_o}{\pi^2 c^3 g_j} B_{oj} \qquad (2.6)$$

where g_o & g_j are the degeneracies of the lower and upper states respectively and $\omega_o = 2\pi\nu_o$. Since K_ν depends on the rate of absorption of photons it must in turn depend on the transition rate, proportional to B_{jo}. The exact relationship may be found by considering the energy absorbed in a slab of gas of unit cross-section and thickness δx exposed to a radiation intensity I_ν as shown in Fig. 2.1. where I_ν has units of Watts m^{-2} per ($rads^{-1}$). The energy incident per second on the section δx of the column is simply $I_\nu \delta\nu$ for a frequency bandwidth $\delta\nu$ about ν_o. The energy absorbed per unit time is given by Equation (2.1) to be $(I_\nu \delta\nu\, K_\nu \delta x)$. When I does not vary appreciably with frequency near ν_o the total energy E absorbed per second is given by

$$-\frac{dE}{dt} = I_\nu\, \delta x \int_{\text{line}} K_\nu\, d\nu$$

where the integration with respect to frequency is between the limits of the line-profile shown in Fig. 2.2. The expression can be related to the energy density $\rho(\nu)$ by the formula

$$-\frac{dE}{dt} = c\rho(\nu)\delta x \int_{line} K_\nu d\nu$$

which in turn is equal to the rate at which photons of energy $h\nu_0$ are removed from the beam by N_0 molecules per m^3 in the groundstate undergoing transitions from state ψ_0 to an excited state ψ_j. Therefore we obtain

$$(0 \to j) \qquad -\frac{dE}{dt} = \rho(\nu) B_{j0} h\nu_0 N_0 \delta x = c\rho(\nu)\delta x \int_{line} K_\nu d\nu$$

$$\Rightarrow \qquad \int_{line} K_\nu d\nu = \frac{h\nu_0 N_0 B_{j0}}{c} \qquad (2.7)$$

The result connects the absorption coefficient measured by an experiment to the fundamental electronic molecular structure of the gas under study and the coefficient B_{j0} can be determined if the light beam is sufficiently monochromatic to probe the line-shape K_ν as a function of frequency, permitting the integral in Equation (2.4) to be evaluated. The treatment here has not taken into account the stimulated emission of photons, which would put photons back into the absorbed light beam if sufficient molecules were present in the upper state j. However, in the VUV the upper state is likely to lie near or above the 1st ionisation potential with an excitation energy of the order 13eV. From Statistical Mechanics the Boltzmann factor $e^{-h\nu/kT}$ indicates roughly the fraction N_j/N_0 in the upper state if thermal equilibrium is obeyed and if the number of photon absorptions is much smaller than the total number of molecules, this fraction

will be less than 10^{-99} at room temperature, suggesting that for our purposes stimulated emission can be completely ignored.

It is worth noting that $K_\nu = \sigma_\nu N_o$ where σ_ν is the atomic or molecular absorption cross-section for the particular frequency ν. The units of absorption cross-section used in this thesis are 10^{-22} m^2, commonly expressed in units of the Nuclear Physicist as one Mega-Barn (Mb). Typical cross-sections of the astrophysical molecules studied in the VUV are tens of Megabarns (10^{-21} m^2). It is a matter of preference which description should be employed, but when cross-sections are used Equation (2.4) can be rewritten purely in terms of microscopic quantities by eliminating the Macroscopic number density N_o. Inserting the molecular absorption coefficient

$$K_\nu = N_o \sigma_\nu$$

gives

$$\int_{Line} \sigma_\nu \, d\nu = \frac{h\nu_o B_{io}}{c} = \frac{e^2}{4\epsilon_o mc} f_{io} \qquad (2.8)$$

where f_{io} can be introduced here as the Oscillator Strength, proportional to the B coefficient and is of the order 1 or less for a strong VUV transition.

Broadening Mechanisms

So far little has been said concerning the various mechanisms which broaden the function $K(\nu)$ about ν_o. Even if a stationary molecule or atom could be completely isolated from its neighbours, electronic transitions would occur from one energy level to another over a small but finite range of energies ΔE reflecting a Natural Width of the levels. This can be understood simply in terms of the Heisenberg Uncertainty Principle $\Delta E . \Delta t \approx \hbar$ where Δt is of the order of the lifetime of the excited

state. An electron in an eigenstate above the ground state will have a finite reciprocal lifetime equal to the Einstein A coefficient for spontaneous emission and the upperstate energy eigenvalue will have a finite spread ΔE given roughly by the Uncertainty Relation. For photoabsorption this corresponds to a finite range of photon frequencies distributed about a mean frequency ν_0 , which could be absorbed by the electron system. The orders of magnitudes are expressed in the following relations

$$\Delta E \approx \hbar/\Delta t \approx \hbar A_{i0}$$

$$\Rightarrow \quad \delta\nu \approx A_{i0}$$

Typically A_{i0} is of the order 10^8 sec^{-1} for strong atomic transitions in the visible so that $\delta\nu/\nu_0 \sim 10^{-7}$.

However, gas atoms or molecules at room temperature are generally in continuous thermal motion with typical speeds V of $600ms^{-1}$ for water vapour at room temperature 300K, spread ΔV, travelling in random directions to a fixed line of sight. For light at a frequency close to ν_0 for an electronic transition a random doppler shift $\Delta V\, \nu_0/c$ will be perceived by the molecules and a fraction of molecules will absorb incident light shifted a frequency difference $\delta\nu$ in the direction of the relative doppler shift $\Delta V\, \nu_0/c$, away from ν_0 . In this way the measured absorption profile $K(\nu)$ becomes broadened by an amount proportional to $\delta\nu$ and for most transitions at normal temperatures the Doppler width becomes greater than the Natural width. For example, a water transition in the visible wavelength region has a broadening factor $\delta\nu/\nu_0 \sim 3 \times 10^{-6}$. A more complete treatment of Doppler and other broadening mechanisms can be found in Thorne (1979) where the Lorentzian profile for Natural line widths and the Gaussian shape for Doppler widths are also derived, but for our purposes only the half-power width for a doppler broadened transition is

required, given by

$$\frac{\delta\nu_D}{\nu_0} = \frac{2}{c}\sqrt{\frac{2RT\ln 2}{M}} \qquad (2.9)$$

where ν_0 is the central frequency of the transition, R is the gas constant, T the temperature and M the molar mass. C is as usual the speed of light.

At low gas pressures of a few mmHg(Torr) or less, Doppler Broadening is normally the dominant broadening process and can be assumed throughout the experiments to be described in the next three chapters to pertain, as the gases studied were always at pressures less than 1 Torr. However, a third mechanism, Pressure Broadening, plays an important role in the description of laser-produced plasmas, constituting the last three chapters of this thesis. Although the details of the broadening mechanism are fairly complicated and have been treated elsewhere (Griem, 1964), its origin is simple to understand and will be explained.

In the case of Natural Broadening the frequency width $\delta\nu_N$ of $K\nu$ is equal to the reciprocal lifetime of the upperstate. If collisions with other molecules perturb the excited state during the Natural lifetime an effectively new, shorter, lifetime will be created, further broadening the upper energy levels by the Uncertainty Principle and consequently the photon transition frequency. The order of magnitude of the broadening due to collisions is easily related to the gas collision frequency ν_c , taken from Kinetic theory (eg. Tabor, 1969) to be

$$\nu_c \approx \pi \rho_0^2 \bar{v} N \approx \delta\nu_c$$

where ρ_o is the effective collision radius of a gas molecule, $\bar{v}$ is the mean molecular speed and N is the number density. At room temperature $\delta\nu_c/\nu_o \sim 10^{-8}$ for water at 1 Torr pressure in the visible spectrum but in the high density plasmas to be discussed in later chapters $\delta\nu_c/\nu_o$ rises to 10^{-2} in the same wavelength regions.

The Second Method - Optoacoustic Spectroscopy in the VUV

The essence of optoacoustic spectroscopy is quite simple. Light is passed into a gas column enclosed in an absorption cell containing a microphone. If the light frequency coincides with a molecular absorption line the light beam will be absorbed and excite the gas molecules; the excited molecules can either reradiate spontaneously, fragment by ionisation and dissociation or relax by thermal collisions down to the ground state. No matter what the relaxation process may be, if the gas is optically thick most of the light energy absorbed will be rapidly converted into heat, increasing the internal energy of the gas while raising its temperature and pressure. A mechanically chopped light beam periodically turned on and off will produce both temperature and pressure changes in synchrony with the chopper, with the result that an audio tone at the chopper frequency can be detected by the microphone insert, if the light energy converted to heat is sufficiently large. Dissociation and ionisation processes, which are common in VUV spectroscopy, could add to the small pressure oscillations produced, by concomitantly increasing and diminishing the molecular number density, proportional to the pressure. Simple formulae will be derived below relating the pressure changes produced in an optoacoustic cell to the incident light intensity traversing an absorbing gas, for the special case when the light chopper frequency has a period longer than the thermal decay time for heat loss from the gas to the walls of the cell. However, because the arguments used to derive general formulae for a range of optoacoustic parameters and chopping

frequencies also give some insight as to the variety of the complex processes that can occur, a fairly complete treatment will be given.

The Excitation of Sound-waves by temperature and particle density fluctuations caused by VUV photoabsorption processes

Derivation of a forced wave equation. The aim is to derive a forced wave equation (for sound) which describes both the absorption of photons converted directly into heat and the pressure changes caused by molecular fragmentation processes which might also occur. For the present we shall ignore thermal waves and assume the generation of sound waves is adiabatic. The criterion will be true if

$$D\omega/c^2 \ll 1$$

where D is the diffusivity of the gas, ω is the frequency of the sound and C is its speed in the gas. From Kinetic theory (Tabor, 1969)

$$D = \frac{1}{3}\lambda\bar{c}$$

if λ and $\bar{c}$ are the mean free path and mean molecular speed respectively. At a pressure of 1 mmHg (1Torr) and at 300K $D \sim 2\times10^{-2}\ m^2s^{-1}$ and $c \sim 330\ ms^{-1}$ for air so that even at high acoustic frequencies such as 10^5 $rads^{-1}$ the inequality holds well with $D\omega/c^2 \sim 2\times10^{-2}$.

Consider the gas volume V shown in Fig.2.4, bounded by a surface S. If V deforms to V', the point $\underline{r}$ relative to O moves to the point $(\underline{r}+\underline{\xi})$ where $\underline{\xi}$ is the displacement vector.

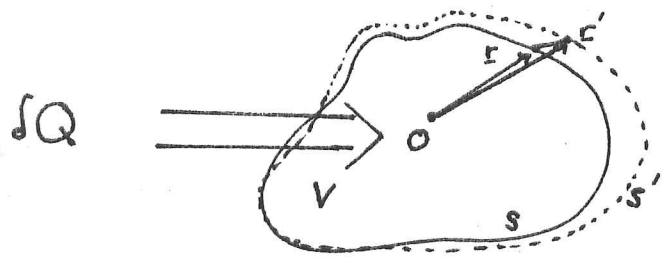

Fig.2.4

δQ is the heat input which has partly caused the deformation. The change in volume ΔV is given by

$$\Delta V = \int_S \underline{\xi} \cdot d\underline{s} = \int_V \operatorname{div} \underline{\xi} \, dV$$

using the Divergence theorem. In the limit $\Delta V \to 0$

$$\frac{dV}{V} = \operatorname{div} \underline{\xi}$$

If the ambient pressure is P_0 let the excess pressure $\Delta P_0 = p$ due to the deformation and heat increase of the gas region V. The force on the region must obey Newtons Laws so that the force is

$$\underline{F} = \int_S -p \, d\underline{s} = -\int_V \operatorname{grad} p \, dV = \int_V \rho \frac{\partial^2 \underline{\xi}}{\partial t^2} \, dV$$

again using the divergence theorem, where ρ is the gas density. Consequently:

$$-\operatorname{grad} p = \rho \frac{\partial^2 \underline{\xi}}{\partial t^2}$$

$$\Rightarrow \quad \nabla^2 p = -\rho \frac{\partial^2}{\partial t^2} [dV/V] \qquad (2.10)$$

and the next step is to find an expression for dV/V in terms of known quantities. There are three main processes by which a change in volume might occur within the gas due to the absorption of VUV radiation. They are:-

1) An increase in the number of particles due to fragmentation.

2) An increase in temperature due to the extra kinetic energy of the dissociated or ionised particles.

3) An increase in temperature due to absorption without fragmentation.

It will be supposed that all excited states, specifically those of the fragments in (1) and (2) and those of the complete molecules in (3) relax quickly by collision to their appropriate ground states compared to the period of the forcing radiation. Let there be n moles of gas in the volume V where there has been a molar change δn caused by molecular ionisation or dissociation. If N photons per volume are absorbed, each with energy $h\nu$, let $\alpha_\nu N$ dissociate or ionise where α_ν is the fragmentation branching ratio, never greater than unity. If b is the binding energy of the molecular fragments to form an original molecule conservation of energy implies

$$\alpha N h\nu = \alpha b N + t$$

where t is the additional translational kinetic energy acquired by the fragments if rapid collisional relaxation occurs. Similarly, for the molecules which do not ionise or fragment, all the remaining photon energy relaxes into heat, that is

$$(1-\alpha) N h\nu = q \qquad (2.11)$$

Therefore the total heat supplied per unit volume is

$$\frac{\delta Q}{V} = q + t = N(h\nu - \alpha b) \qquad (2.12)$$

From the 1st Law of Thermodynamics and the gas equation of state

$$dE = dQ - P\,dV \qquad P = \frac{nRT}{V} \qquad (2.13)$$

where P is the total pressure, not to be confused with the acoustic fluctuations p, R is the gas constant and T the temperature. E is the internal energy of the gas and is

related to the molar specific heat at constant volume, C_v of the original molecules and the molar specific heat C_n of the dissociated fragments by the relation

$$dE = C_v n dT + C_n T dn \tag{2.14}$$

assuming ideal gas behaviour. Therefore, using Equation (2.14) and (2.12) and dividing by T Equation (2.13) becomes

$$C_n dn + n C_v \frac{dT}{T} = (g+t)\frac{V}{T} - nR\frac{dV}{V} \tag{2.15}$$

Differentiating the equation of state and dividing by PV we obtain

$$\frac{dT}{T} = \frac{dV}{V} + \frac{dP}{P} - \frac{dn}{n} \tag{2.16}$$

which can be substituted into Equation (2.15) with some rearrangement to yield

$$n(C_v + R)\frac{dV}{V} = (g+t)\frac{V}{T} - nC_v\frac{dP}{P} + nC_v(1 - C_n/C_v)\frac{dn}{n} \tag{2.17}$$

Using Meyer's equation $C_p = C_v + R$ at constant pressure and denoting the ratio of the specific heats $C_p/C_v = \gamma$ Equation (2.17) can be rearranged to give an expression for dV/V close to that required.

$$\frac{dV}{V} = \frac{1}{\gamma P}\left[(g+t)(\gamma-1) - dP + P\left(1 - \frac{C_n}{C_v}\right)\frac{dn}{n}\right] \tag{2.18}$$

Now the finite differentials $dP = p$ and $dn = \alpha N V / N_A$ where N_A is Avogadro's number, can be substituted to give

$$\frac{dV}{V} = \frac{1}{\gamma P}\left[(h\nu - \alpha b)(\gamma - 1)N - p + \alpha\left(1 - \frac{c_n}{c_v}\right)NKT\right] \qquad (2.19)$$

remembering that $R = N_A K$ if K is Boltzmann's constant. On substituting Equation (2.19) into Equation (2.10) we finally obtain the forced wave equation

$$\nabla^2 p - \frac{1}{c^2}\frac{\partial^2 p}{\partial t^2} = -\frac{1}{c^2}\left[(h\nu - \alpha b)(\gamma - 1) + \alpha_\nu\left(1 - c_n/c_v\right)KT\right]\frac{\partial \dot{N}}{\partial t} \qquad (2.20)$$

where $$c = \sqrt{\frac{\gamma p}{\rho}} = \sqrt{\frac{\gamma RT}{M}}$$

$\dot{N}$ is the rate at which photons are absorbed per unit volume and C is the speed of sound in the gas. It is somewhat surprising that because α_ν is never greater than unity and because at ultraviolet wavelengths $h\nu \gg KT$ at normal temperatures, the pressure forcing term $\alpha_\nu(1 - c_n/c_v)KT/c^2\,\partial\dot{N}/\partial t$ due to fragmentation processes is insignificant compared to the thermal terms, which are dominated by the large photon energy. Only at infrared or microwave wavelengths will fragmentation processes possibly play an important part in generating the optoacoustic signal, but at these low photon energies even dissociation is unlikely to occur unless the gas molecules are particularly unstable.

Solutions of the forced wave equation. The equation can

be written more compactly as

$$\nabla^2 p - \frac{1}{c^2}\frac{\partial^2 p}{\partial t^2} = A\frac{\partial \dot{N}}{\partial t}$$

$$A = \frac{1}{c^2}\left[(h\nu - \alpha b)(\gamma - 1) + \alpha\left(1 - \frac{c_n}{c_v}\right)KT\right] \qquad (2.21)$$

The equation (2.21) is inhomogeneous and requires both complimentary functions and a Particular Integral to be found for its solution. Without becoming too involved with the details of the calculations, the outline of the work will be presented together with major assumptions important to the physics of optoacoustic spectroscopy. Most absorption cells are likely to be cylindrical with the light passing down the axis as shown in Fig.2.5 with cylindrical Polar coordinates also marked.

Fig. 2.5

If we assume axially symmetric wave solutions the azimuthal angle of ϕ can be ignored, as can the dependence of the solutions on z if the tube is short compared to the optical depth of the radiation. In a rigid absorption cell the gas displacement velocity must be zero at the cell walls and the boundary condition at $r=a$ will be

$$\left.\frac{\partial p}{\partial r}\right]_{r=a} = 0 \qquad (2.22)$$

where $p = p(r,t)$ and $\dot{N} = \dot{N}(r,t)$. If we define the time-fourier transforms

$$\hat{p}(r,\omega) = \frac{1}{\sqrt{2\pi}} \int_{-\infty}^{+\infty} e^{i\omega t} p(r,t)\, dt$$

$$\hat{N}(r,\omega) = \frac{1}{\sqrt{2\pi}} \int_{-\infty}^{+\infty} e^{i\omega t} \dot{N}(r,t)\, dt \qquad (2.23)$$

and use their derivative properties Equation (2.21) can be transformed to become

$$\left(\nabla^2 + \frac{\omega^2}{c^2}\right) \hat{p} = -i\omega A \hat{N} \qquad (2.24)$$

The Equation can be solved by first finding the Normal mode of its homogeneous equation

$$\left(\nabla^2 + \frac{\omega^2}{c^2}\right) \hat{p} = 0 \qquad (2.25)$$

and then finding a series expansion of the general solution in terms of the normal modes using Sturm-Liouville theory (Riley 1974). The homogeneous equation (2.25) can be written in cylindrical polars to become a special case of Bessel's equation (Riley 1974)

$$\frac{1}{r} \frac{\partial}{\partial r}\left(r \frac{\partial \hat{p}}{\partial r}\right) + \frac{\omega^2}{c^2} \hat{p} = 0$$

$$r\hat{p}'' + \hat{p}' + k^2 r \hat{p} = 0 \qquad (2.26)$$

where primes denote a derivative with respect to r, and

k is the wave number. Equation (2.26) has two independent solutions, one of which is divergent at $r=0$. The other is given by Riley (1974) to be a Bessel function of zero order

$$\hat{p}(r) = a_k J_0(kr) \qquad (a_k \text{ constant})$$

and must satisfy the boundary condition Equation (2.22). Therefore, if μ_n are the roots of the equation $J_0'(x) = 0$ and noting that $J_1(x) = -J_0'(x)$

$$J_1(ka) = 0$$

$$\Rightarrow \quad ka = \mu_n \quad \text{if} \quad J_1(\mu_n) = 0 \qquad (n = 0, 1, 2 \cdots)$$

and the eigenvalues kn^2 are given by

$$k_n^2 = \left(\frac{\mu_n}{a}\right)^2$$

The first few roots are $\mu_0 = 0$, $\mu_1 = 3.85$, $\mu_2 = 7.00$, $\mu_3 = 10.15$. The general solution of the homogeneous equation is then

$$\hat{p}(r) = \sum_n a_n J_0\left(\frac{\mu_n r}{a}\right) \delta\left(\omega - c\frac{\mu_n}{a}\right) \qquad (2.27)$$

where a_n are arbitrary constants which can only be determined if the boundary conditions are fully specified. $\delta(x)$ is the Dirac delta function and will henceforth only be implied.

The normalised eigenfunctions

$$\hat{p}_n = c_n J_0(\mu_n r/a)$$

form a complete set and span the space, where the normalisation constants c_n satisfy the orthonormality relation

$$\int_0^a r \hat{p}_n \hat{p}_m \, dr = \delta_{nm} \qquad (2.28)$$

If the forcing radiation is chopped at a frequency ω with a wavevector $\underline{K}$, the Inhomogeneous equation can be written in self-adjoint form as

$$r\hat{p}'' + \hat{p}' + K^2 r\hat{p} = i\omega A \hat{N}_v \tag{2.29}$$

From Equation (2.26) $(r\hat{p}_n')' = -k_n^2 r\hat{p}_n$

where p_n are the eigenfunctions of the homogeneous equation which satisfy the boundary conditions at the cylinder walls. Expanding the particular integral in terms of these functions

$$\hat{p} = \sum_n a_n \hat{p}_n \tag{2.30}$$

which can be substituted into Equation (2.29) to give

$$\sum_n a_n [-k_n^2 r\hat{p}_n + K^2 \hat{p}_n r] = -i\omega A \hat{N}_v$$

Multiplying by $\hat{p}_m$ and integrating over r

$$a_m = \frac{-i\omega A}{K^2 - k_m^2} \int_0^{r=a} r \hat{p}_m \hat{N} \, dr$$

remembering the eigenfunctions $\hat{p}_n$ are orthonormal (Equation 2.28). Substituting the a_m into Equation (2.30) gives the particular integral of the forced wave equation, expressed as a fourier series

$$\hat{p}(r,\omega) = Ac^2 \sum_n \frac{i\omega \hat{p}_n}{\left(\omega_n^2 - \omega^2 + i\frac{\omega\omega_n}{Q_n}\right)} \int_0^a r \hat{p}_n \hat{N} \, dr \tag{2.31}$$

where the damping term $i\omega/Q_n\omega_n$ has been introduced to prevent divergent solutions whenever the chopper frequency of the absorbed light hits one of the normal frequencies

ω_n . In reality the normal 'Ringing' modes of the cylinder will inevitably loose energy through viscous and thermal mechanisms and each mode will have its own Q-factor. Generally the optoacoustic pressure signal $\hat{p}$ is greatest at low frequencies near to zero-order acoustic mode $\omega_0 = 0$ unless the Q-factor for a higher mode happens to be very large, in which case resonant operation at that particular frequency might produce a larger acoustic response. The integral in Equation (2.31) effectively picks out the Bessel functions $J_0(\mu_n r/a)$ constituting the incident radiation's radial intensity distribution. For example, if $\hat{N}(r,\omega)$ has an intensity distribution about the cylinder axis which falls off as $J_0(\mu_1 r/a)$ towards the cylinder walls with none of the other $J_0(\mu_n r/a)$ eigen-components, then only one term will be non-zero in the series Equation (2.31). First-order resonant operation is likely to be the strongest for such an intensity profile and the solution, Equation (2.31) simplifies to become

$$\hat{p}(r,\omega) = \frac{i\omega A c^2}{\left(\omega_1^2 - \omega^2 + i\frac{\omega\omega_1}{Q_1}\right)} C_1 J_0(\mu_1 r/a)\hat{N}(0,\omega) \qquad (2.32)$$

However, zero-order non-resonant operation represents the simplest form of acoustic response. The eigenvalue ω_0 is zero since μ_0 is zero and this model produces a uniform response throughout the whole cylinder because the mode profile $J_0(0 \times r/a)$ is unity for all values of r . This mode could easily be derived without recourse to the wave equation as it corresponds to a uniform heating and cooling of the gas with a concomitant pressure variation. Again, if the intensity profile has the same form as the zero-order mode, that is a uniform one, only this mode can possibly be excited. Because ω_0 is zero the damping term (ω_0/Q_0) should be more appropriately written as $1/\tau_T$ where τ_T is a thermal damping time of the mode, which degrades the forced temperature increases. With a uniform light intensity across the cylinder in Fig.2.5 Equation

(2.31) simplifies to

$$\hat{p}(r,\omega) = \frac{-iAc^2}{(\omega - i/\tau_T)} \hat{N}(\omega)$$

and produces the greatest signal when the chopper period becomes greater than the thermal time τ_T. Substituting for Ac^2 from Equation (2.21), with $h\nu >> KT$ we obtain finally

$$\hat{p}(\omega) = \tau_T (h\nu - \alpha b)(\gamma - 1) \hat{N}(\omega)$$

$$h\nu \gg KT \quad \omega\tau_T \leq 1 \qquad (2.33)$$

Equation (2.33) has a simple form and indicates the best optoacoustic signal which could be obtained using a light beam with a nearly constant radial intensity distribution. Typically τ_T will be of the order a^2/b and is about 10^{-3} seconds for air at 1Torr in a cylinder of radius 1cm, implying that chopper frequencies less then than 500Hz are needed for optimum zero-order acoustic performance.

Forced Temperature Oscillations in an optoacoustic cell caused by absorption of light in the VUV.

It was shown above that the maximum optoacoustic signal will be limited by the thermal diffusion time of the gas in the absorption cell when operation is restricted to the zero-order mode. A solution of the forced thermal diffusion equation should yield eventually a result similar to Equation (2.33) and include a suitable expression for τ_T.

Consider again the volume element V in the gas, which is approximately fixed. It is bounded by a surface S with heat $\dot{Q}_o$ absorbed inside it per second per unit volume,

due to photoabsorption of VUV radiation. If k is the thermal conductivity of the gas and C_{vol} is the volume specific heat, conservation of energy into and out of the region V through the surface S is given by

$$\int_V \dot{Q}_o \, dV = \int_V C_{vol} \frac{dT}{dt} dV - \int_S k \, \mathrm{grad} T \cdot \underline{ds}$$

$$\nabla^2 T - \frac{1}{D} \frac{\partial T}{\partial t} = -\frac{\dot{Q}_o}{k} \qquad (2.34)$$

if $D = k/C_{vol}$. D is the thermal diffusivity of the gas, defined earlier and Equation (2.34) is the forced thermal diffusion equation. Its exact solutions can be found using cylindrical polars and Laplace transform methods in conjunction with Sturm-Liouville theory, but because here we are concerned only with a quasi-static forcing function $\dot{Q}_o(t)$ whose period is slower than the thermal decay time in the zero-order mode of operation, Equation (2.34) can first be solved when $\dot{Q}_o$ has been on for a time longer than τ_T when $\partial T/\partial t \sim 0$ and, second, when $\dot{Q}_o$ has just been turned off and the subsequent temperature decay is given by the homogeneous equation

$$\nabla^2 T - \frac{1}{D} \frac{\partial T}{\partial t} = 0 \qquad (2.35).$$

We shall assume axially symmetric solutions throughout the calculations and the same geometry depicted in Fig.2.5. While light uniformly illuminates the tube, $\dot{Q}_o$ (Watts m^{-3}) are absorbed and we find

$$\nabla^2 T(r) \approx -\frac{\dot{Q}_o(\omega)}{k} \qquad (\omega \tau_T \ll 1)$$

$$\Rightarrow \quad T(r) = E + B \ln r - \frac{\dot{Q}_o r^2}{4k}$$

where E and B are arbitrary constants of integration and are fixed by the boundary conditions. These require T to be finite at r=0 (therefore B=0) and to be equal to room temperature (T_R) at the cylinder walls. Therefore

$$T(r) = T_R + \frac{\dot{Q}_0 a^2}{4k}(1 - r^2/a^2) \qquad (2.36)$$

If, now, the light is turned off (by the chopper) Equation (2.35) will next describe T (r) and a separable solution can be found which satisfies the initial boundary condition at $t = 0$ expressed by Equation (2.36). Looking for a separable solution $T = R(r)\tau(t)$

$$\frac{\nabla^2 R}{R} - \frac{1}{D}\frac{1}{\tau}\frac{d\tau}{dt} = 0$$

$$\Rightarrow \qquad \nabla^2 R = -\left(\frac{m}{D}\right)R \quad , \quad \frac{d\tau}{dt} = -m\tau$$

where m is a separation constant to be determined. The time equation is simply $\tau = \tau_0 e^{-mt}$ where τ_0 is arbitrary. Solving the space equation in cylindrical polars

$$rR'' + R' + \left(\frac{m}{D}\right)rR = 0$$

Bessel's Equation

$$\Rightarrow \qquad R(r) = B_m J_0\left(\sqrt{\frac{m}{D}}\, r\right)$$

Hence, the general solution can be expressed as a series

$$T(r,t) = T_R + \sum_m B_m J_0\left(\sqrt{\frac{m}{D}}\, r\right) e^{-mt} \qquad (2.37)$$

where Bm are arbitrary constants, fixed by the boundary conditions $T(r,t) = T_R$ at the cylinder wall and T(r, 0)

is given by Equation (2.36). First we see that

$$J_0\left(\sqrt{\frac{m}{D}}\, r\right) = 0$$

$$\Rightarrow \sqrt{\frac{m}{D}}\, a = \eta_n \quad \text{if} \quad J_0(\eta_n) = 0 \qquad (n = 1, 2, 3 \cdots)$$

and by noting that in the region $0 \leq x \leq \eta_1 = 2.41$

$$J_0(x) \approx (1 - x^2/\eta_1^2)$$

to an accuracy of 20%, the first term only in Equation (2.37) can be taken to fit the boundary condition at $t=0$, giving

$$T(r,t) \approx T_R + \frac{\dot{Q}_0 a^2}{4k}\left(1 - \frac{r^2}{a^2}\right) e^{-\frac{\eta_1^2 D t}{a^2}} \qquad (2.38)$$

with a characteristic decay time

$$\tau = \frac{a^2}{\eta_1^2 D} \qquad (2.39)$$

Summarising the calculation so far, uniform light energy absorbed by the gas has been assumed to be chopped, slowly on and off, producing a temperature profile given by Equation (2.36) while the light is on, whilst falling to room-temperature when the light is off, with each process having a characteristic response time τ given by Equation (2.39). It only remains to calculate the uniform pressure increment p caused by the temperature profile Equation (2.36) to facilitate a comparison with the zero-mode wave solution Equation (2.33). If l is the length of the absorption cell containing N molecules

$$N = n_0 \pi a^2 l = l \int_0^a 2\pi r n(r)\, dr \qquad (2.40)$$

with an equilibrium pressure of P_o and a number density n_o . The gas equations of state are

$$P = n(r) K T(r) \qquad P_o = n_o K T_R$$

where K is Boltzmann's constant and can be substituted into Equation (2.40) with some simplification to give

$$P = P_o \frac{a^2}{2} \left[\int_o^a \frac{r T_R}{T(r)} dr \right]^{-1} \qquad (2.41)$$

The integral in Equation (2.41) can be evaluated using Equation (2.38) at $t=o$, assuming the pressure increment is small compared to P_o. Carrying out the integration Equation (2.41) gives the pressure increment

$$p = P - P_o = \frac{a^2 R}{4 C_v D} \qquad (2.42)$$

assuming ideal gas behaviour. For diatomic molecules the molar specific heat at constant volume is $C_v = 7/2\, R$ per mole. $\dot{Q}_o$ will be equal to the time derivative of Equation (2.12) so that the optoacoustic signal produced by slow light variations with an amplitude of $\dot{N}$ photons per second per volume will be given by

$$p = \frac{a^2 R}{4 C_v D} (h\nu - \alpha b) \dot{N}(\omega) \qquad \omega \tau_T \ll 1 \qquad (2.43)$$

This result of the thermal diffusion equation can be compared to Equation (2.33) of the wave equation and is identical if we choose the thermal damping time τ_T to be

$$\tau_T = \frac{a^2}{4 D C_v (\gamma - 1)} \qquad (2.44).$$

Some design considerations

Since the optoacoustic pressure signal

$$p = \alpha^2 R(h\nu - \alpha b)\dot{N}/4DC_v$$

depends on the number of photons absorbed per unit volume it might seem desirable to minimise the absorption cell volume, or at least its length l. However, if a uniform photon flux F_ν (photons s^{-1} m^{-2} per $rads^{-1}$) is incident at one end of the gas tube the rate of photons absorbed in the cell volume $\pi a^2 l$ will be

$$\dot{N}_\nu = (F_\nu/\pi a^2 l) \int_{line} \pi a^2 (1 - e^{-K_\nu l})\, d\nu$$

if K_ν is the absorption coefficient and the integration is over one line. Assuming good resolution of absorption lines will be required, the gas pressure and path length should be arranged to ensure the optical depth is less than one. In that case the equation simplifies to become

$$\dot{N}_\nu = F_\nu \int_{line} K_\nu\, d\nu \qquad (K_\nu l \leq 1)$$

and is independent of the absorption path. Using equation (2.8) the resultant optoacoustic signal will be

$$p = \left(\frac{e^2}{56\varepsilon_0 mc}\right)\left(\frac{h\nu_0 - \alpha b}{D}\right) f_{i0}\, a^2 N_0 F_\nu \qquad (2.45)$$

where f_{i0} is the line oscillator strength and N_0 the molecular number density in the ground state. The expression assumes F_ν has been selected by a monochromator with a bandwidth $\Delta\nu$ greater than the line width, but excluding any other absorption lines nearby. Clearly, the best results will be obtained if the cell radius is chosen as large as that of the light beam, and the gas pressure set as high as possible, simultaneously reducing the diffusivity. The latter condition automatically implies a shorter cell length if the optical depth is to be kept less than unity. In the VUV region the radiation source must be connected via a

windowless differential pumping system to the absorption cell at wavelengths below 1200 Å ; above this wavelength thin window materials can be used. In a differential pumping system small bore connecting tubes from the monochromator to the cell, no greater than 5mm in diameter, will be necessary to keep the already very high differential pumping rates required within practicable limits. Consequently the optoacoustic cell area should also be kept close to the cross-section of the beamline differential pumping tubes, but in practice the size of the microphone must also be accommodated and will effectively determine the dimensions of the absorption cell.

Synchrotron or Storage Ring radiation has obvious advantages for VUV spectroscopy because of its high intensity and nearly parallel beam propogation. A rough estimate of the acoustic signal can be calculated assuming a typical Rydberg absorption line whose oscillator strength f is ~ 0.1 at 1000Å, based on the predicted photon flux from the Daresbury Storage Ring, mentioned in Chapter 1 (Fig.1.2). After passing through a monochromator 10^{15} photons m^{-2} $Å^{-1}$ (25 photons $s^{-1} m^{-2}$ per ($rads^{-1}$)) might enter the absorption cell along a tangent 10m away from the Storage Ring, emerging from a 5mm bore tube into a gas pressure of 1 Torr, typical for a differential pumping system. Substituting the appropriate values into Equation (2.45) a signal amplitude of 10^{-4} $N m^{-2}$ might be achieved. A typical condensor microphone sensitivity would be $\sim 10^{-2}$ volts per $N m^{-2}$ and would yield a signal-voltage of 1 μV for such an optoacoustic signal, easily detectable by a high gain preamplifier. It must be remembered that although in practice Synchrotron light is usually pulsed on and off at a frequency near 50Hz, quite convenient for these experiments, light from a Storage Ring is virtually continuous and would have to be physically chopped at a similar frequency to produce optoacoustic signals.

The estimated signal strength of 1μV deduced here suggests that optoacoustic experiments might be successful in the VUV

if major problems caused by background noise can be overcome. The statistical thermal noise in an optoacoustic cell has been discussed by (Pa 0, 1977) for a variety of configurations, but if zero-mode operation has been chosen, Pa 0(1977) suggests a major source of statistical noise will originate in the microphone cavity, given by the formula

$$\bar{p}^2_{noise} = \frac{4 \gamma p_0 KT}{\omega_m Q_m V_m} \quad \text{per } \sqrt{Hz} \qquad (2.46)$$

where ω_m, Q_m and V_m are the microphone resonant frequency its Q-factor and its volume respectively. Taking data supplied for microphones by the manufacturers Bruel and Kjaer

$$p_{noise} \approx 2 \times 10^{-8} \ Nm^{-2} \ \text{per } \sqrt{Hz}$$

at 300K and 1 Torr pressure, indicating the maximum possible signal-to-noise ratio would be 50000 with a signal bandwidth of a few hertz. It must be emphasised that such a high signal-to-noise ratio is most unlikely to be achieved in a real experiment unless the background acoustic noise, inevitably present around a synchrotron or Storage Ring can be drastically diminished. The conclusion must be that optoacoustic spectroscopy in the Vacuum Ultraviolet region offers a potentially viable experimental technique worthy of study, but that severe limitations may be encountered if the absorbtion cell cannot be acoustically isolated from its surroundings.

Oscillator Strength, Sum Rules, and Rydberg Series in the VUV

Earlier in this chapter it was shown that the frequency integrated absorption cross-section of an electronic transition is proportional to its Einstein-B coefficient. A quantity known as the oscillator strength f_{i0} was introduced using Equation (2.8) which is repeated here for convenience.

$$\int_{line} \sigma_{j\nu}\, d\nu = \frac{h\nu_{i0}}{c} B_{i0} = \frac{e^2}{4\varepsilon_0 mc} f_{i0}$$

It is easy to show from the quantum mechanical description of the B coefficient (Equation 2.5) that the oscillator strength must also depend solely on the electronic properties of the atom or molecule, with the result that

$$f_{i0} = \frac{8\pi^2 \nu_{i0}}{3h} \left| \langle \psi_j | \hat{r} | \psi_0 \rangle \right|^2 \qquad (2.47)$$

where ν_{i0} is the transition frequency and $\hat{r}$ is the electron-coordinate operator of the perturbed electron making a transition from the ground state ψ_0 to a discrete state ψ_j. In the domain of continuous absorption above the ionisation or dissociation potential the expression for the cross-section becomes

$$\sigma_\nu = \frac{e^2}{4\varepsilon_0 mc} \frac{df_{i0}}{d\nu} \qquad (2.48)$$

where the matrix element inside f_{i0} now links states in the energy continuum of the molecule with the ground state.

Classically, an N electron system has N characteristic frequencies of oscillation for each electron moving in the potential of all the others about the nucleus. When radiation interacts with the system, the model proposed was that one of the N electrons is set into forced oscillation by the radiation electric field vector and absorption takes place if the field frequency coincides with the characteristic frequency of the electron. If a fraction $f_s(\nu)$ of the electrons have a characteristic frequency ν then from such a description it is obvious that

$$\sum_s f_s = N$$

where the symbol f has been referred to as the oscillator strength. These pictorially useful but antiquated ideas must be replaced by quantum theory, which identifies a very large (normally infinite) number of energy eigenvalues for

a molecular system, in which the 'characteristic' frequencies instead correspond to transitions from the ground state to any of the others. Clearly, the possible transitions will be more numerous than just the number of electrons so if the idea of oscillator strength is to be maintained f must generally be less than one for a particular absorption line and is actually given by quantum mechanics as Equation (2.47). Berkowitz (1979) derives the Thomas-Reiche-Kuhn Sum Rule using Equation (2.47), which states that

$$\sum_j f_{j0} = N \qquad (2.49)$$

when the summation is over all possible excited states j and the matrix elements contained in f link either discrete or continuum excited states with the groundstate ψ_0. Equation (2.49) can be evaluated in practice by splitting the Sum into two parts; in particular a discrete sum over excited states lying below the ionisation potential and an integral over the continuum states above the ionisation onset.

$$\sum_j f_{j0} = \sum_S f_s + \int_{\nu=I.P.}^{\infty} \frac{df}{d\nu}\, d\nu \qquad (2.50)$$

The integration of the oscillator strength above the ionisation potential follows naturally from Equation (2.48) and when experimentally determined continuum absorption cross-sections are known this fraction of the f-sum can be evaluated for a real molecule. Below the ionisation potential the oscillator strengths must be determined by measuring each line cross-section over its profile. For many molecules the discrete sum is roughly equal to 1, with the remainder of the oscillator strength shared out in the absorption continuum above the ionisation potential (Berkowitz,1979). Since the total f-sum increases with the number of electrons in the molecular system it is

reasonable to expect that average absorption cross-sections will also increase as the electron number increases, thus Carbon monoxide and Acetylene should have similar average absorption cross-sections because they are isoelectronic with 14 electrons, but they will absorb more strongly than hydroxyl which has only 9 electrons.

Another Sum Rule can be used to relate the absorption continuum to the static dielectric polarisability of a molecule, which can be independently measured by other techniques. From quantum mechanics the dielectric polarisability of a molecule is

$$\alpha_N = \frac{e^2}{(12\pi^3 h \varepsilon_0)} \sum_j \frac{\nu_{j0} |\langle \psi_j | \hat{r} | \psi_0 \rangle|^2}{\nu_{j0}^2 - \nu^2} \qquad (2.51)$$

where the sum is over all eigenstates j of the molecule. It is simply proportional to (Berkowitz,1979)

$$\sum_j \frac{f_{j0}}{\nu_{j0}^2}$$

if only the static polarisability is required, as can be seen by comparing the form of f_{j0} given by Equation (2.47)

with Equation (2.51); hence $\alpha_N(\nu=0)$ must be proportional to the integrated absorption cross-section as a function of wavelength, through the oscillator strength.

Berkowitz (1979) expresses two useful Sum Rules of interest here as

$$S(0) = \sum_s f_s + \frac{1}{(\pi a_0 \alpha_0^2)} \int_0^{\lambda_0} \frac{\sigma(\lambda)d\lambda}{\lambda^2} = N \qquad (2.52)$$

$$S(-2) = \sum_s \frac{f_s}{E_s^2} + \frac{1}{(16\pi^3 a_0^3)} \int_0^{\lambda_0} \sigma(\lambda)d\lambda = \frac{\alpha_N(\nu=0)}{4a_0^3} \qquad (2.53)$$

where $S(0)$ and $S(-2)$ denote special cases of a general Sum Rule which is not required for our purposes. Rydberg units must be used for the discrete energy states Es ($13{\cdot}6\,eV = 1\,Ry$), a_0 is the Bohr radius, α_0 the fine structure constant and λ is the wavelength of the transitions, measured in cgs units, as are the absorption cross-sections. λ_0 is the wavelength corresponding to the ionisation potential of the molecule. Both the Sum Rules can be evaluated numerically to provide a check of the absorption coefficients measured for a particular molecule whose polarisability and electron number are already known; the rules will be used for such a purpose in Chapter 5.

Rydberg Series

In the hydrogen atom the energy levels are nearly degenerate for all quantum numbers except the principal number n. The energy levels are described by the simple Rydberg formula

$$E_n = 13{\cdot}6\,eV - \frac{R_H}{n^2} \qquad (2.54)$$

where R_H is the Rydberg constant and 13.6eV is the ionisation potential of hydrogen. For a steadily increasing photon-energy successive discrete absorption lines occur for transitions from the ground state with n=1 upto higher principle quantum values; the lines steadily crowd together in a Rydberg series and merge together near the onset of ionisation at 13.6eV as $n \to \infty$. At higher photon energies continuum absorption occurs and the electron is excited from the ground state to an unbound, continuum state, above the ionisation potential. Berkowitz (1979) discusses the behaviour of high Rydberg states for multielectronic systems both above and below the ionisation continuum and in particular indicates how

$$f_{n \to \infty} \approx \frac{df}{dn}$$

as the principle quantuum number of a Rydberg oscillator strength becomes very large near the ionisation potential showing that Rydberg absorption series will generally merge smoothly with their ionisation continua with little abrupt change in their cross-section at the ionisation potential. In atoms or molecules which have more than one electron the lowest energy 'Valence' levels will be occupied, but electrons transiting from the ground state to principle quantum states just below the ionisation potential IP., exhibit Rydberg (Hydrogen) like behaviour because these orbits are predominantly a large distance away from the complicated atomic or molecular core and will be moving in an approximately Coulombic potential well. Such unoccupied levels approximately follow the general Rydberg formula

$$E_n = I.P. - \frac{R}{(n-\delta)^2} \qquad (2.55)$$

where δ is roughly constant for any particular series and is known as the quantum defect. R is the molecular Rydberg constant, very nearly equal to R_H and proportional

to the ratio of the reduced electron masses in the two different systems

$$R = R_H \left(\frac{m_e + m_p}{m_e + M}\right) \frac{M}{m_p} \qquad (2.56)$$

where me and mp are the electron and proton masses and M is the molecular mass.

Lower lying levels, near the ground states show a marked departure from the simple Rydberg behaviour, demonstrated by the large quantum defect which is needed to fit these 'Valance' levels to higher Rydberg levels near the ionisation potential, where the quantum defect is generally smaller (less than one) and constant. A.B.Duncan (1971) discusses the theory of Rydberg series in atoms and molecules and should be consulted for a more detailed treatment of these processes.

CHAPTER 3

A trial optoacoustic experiment in the near-ultraviolet

Introduction

The initial experimental programme before using a synchrotron was to try out the optoacoustic technique with a single absorption cell containing a microphone in a region of the spectrum of hydroxyl more accessible to me here in Cambridge. An obvious choice was the $A\ ^2\Sigma \longrightarrow X\ ^2\Pi_i$ system of Hydroxyl in the region 3200Å to 3060Å which has quite strong transitions which have been measured both in absorption and emission by many observers. (Oldenberg 1935, Kaufman and Del Greco 1961, Golden and Del Greco et al 1963, and Dieke and Crosswhite 1962). This region of the ultraviolet spectrum is radiated weakly by a quartz-halogen lamp when used as a continuous background source. At such short wavelengths the lamp cuts off very rapidly due to its low filament temperature of 3000K, but in spite of the lack of a suitably intense source in this region of the spectrum and the pessimistic indications of rough calculations outlined below, it was felt that much could still be learned from a trial experiment before moving to a synchrotron source. A question of particular interest was how a highly sensitive condensor microphone might behave, when it is immersed in a 100W radio frequency electrodeless discharge, as well as how great might be the minimum background acoustic noise reaching the microphone from rotary pumps and other sources.

It is appropriate at this point to outline briefly the molecular configuration of hydroxyl in its ground and excited states. For greater detail Herzberg (1950) should be consulted, together with the work of Dieke and Crosswhite (1962) who present a detailed analysis. The diatomic molecule consists of both an oxygen and an hydrogen nucleus bonded together by 9 electrons in an open shell configuration

$$(1s\sigma)^2\ (2s\sigma)^2\ (2p\sigma)^2\ (2p\pi)^3$$

in its ground state. If we denote the electronic orbital angular momentum $\underline{L}$ and spin angular momentum $\underline{S}$, it can be seen that hydroxyl has a coupling scheme close to Hunds case (a), represented in Fig.3.1. In this scheme both $\underline{L}$ and $\underline{S}$ are quantised along the internuclear axis by strong spin-orbit coupling, with eigenvalues Λ and $\Sigma (= \pm 1/2)$ respectively. The total angular momentum along the internuclear axis is $\Omega = \Lambda + \Sigma$. For the electronic ground state $|\Lambda| = 1$ and the spin-orbit interaction causes a splitting into two states designated as $^2\Pi_{1/2}$ and $^2\Pi_{3/2}$ which correspond to $|\Omega| = 1/2, 3/2$. For the first excited electronic state $A\,^2\Sigma_{1/2}$ the quantum number $\Lambda = 0$ and $|\Omega| = 1/2$ with the spin $\underline{S}$ decoupled from the internuclear axis.

In Hund's case (a) Ω couples with the angular momentum $\underline{K}$ of the nuclear rotation to the total angular momentum $\underline{J}$. Both $^2\Pi_\Omega$ states have their own rotational energy levels characterised by the J quantum numbers $J = |\Omega|, |\Omega|+1, \ldots$ etc. The two-fold degeneracy of each rotational state (states with $+\Omega$ and $-\Omega$ have the same energy) is lifted by an interaction between the electronic orbital angular momentum and the nuclear rotation. By this interaction each rotational state is split into two levels, forming a Λ-doublet and each Λ-doublet is split into two hyperfine states by an interaction with the spin $I = 1/2$ of the hydrogen nucleus. The total angular momentum is given by $\underline{F} = \underline{J} + \underline{I}$ with the eigenvalues $F = J \pm 1/2$. The resulting energy level scheme is shown in Fig.3.1 which includes the hyperfine splittings. Fig.3.2 shows schematically the doublet rotational levels of the ground $X\,^2\Pi_\Omega$ and the excited $A\,^2\Sigma_{1/2}$ states, neglecting the hyperfine interaction and depicts the strong absorption transitions possible from the ground rotational state. At room temperature higher rotation states are significantly populated but transitions from these levels have been omitted. The transition notation and their relative intensities have been assigned according to Dieke and Crosswhite (1962). The two sets of rotational levels correspond to a non-vibrating

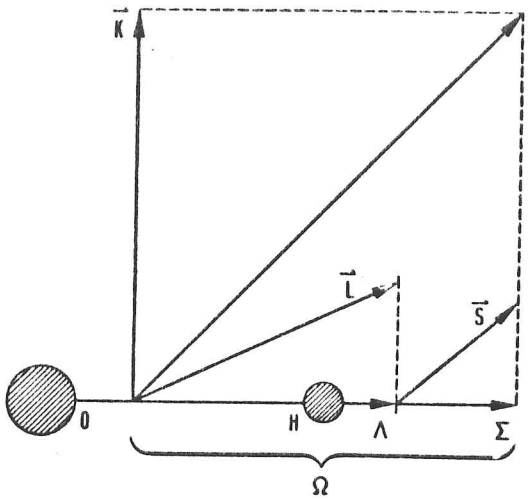

The angular momentum coupling scheme for OH according to Hund's case (a). $\vec{L}$ and $\vec{S}$ represent the electronic orbital and spin angular momentum, respectively and $\vec{K}$ stands for the nuclear end over end rotation.

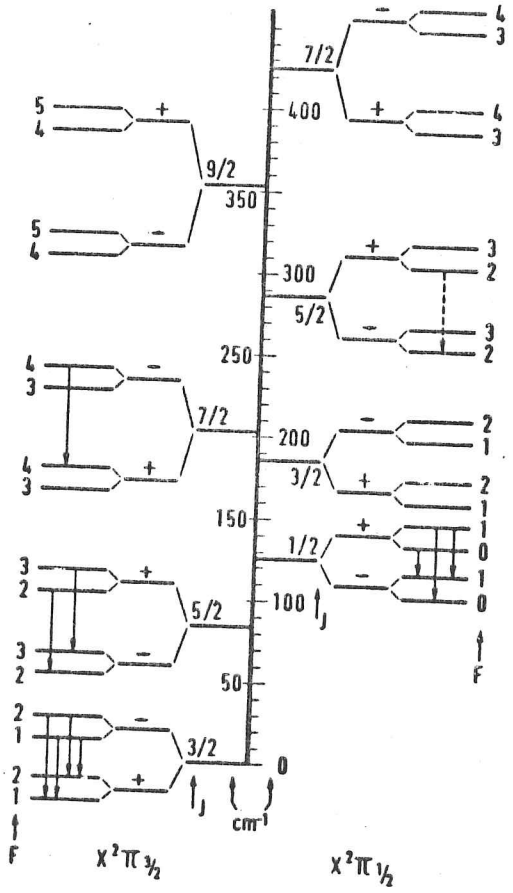

Fig.3.1

The energy level scheme of the electronic ground state $X^2\Pi$ of OH. The splittings of the Λ-doublet and hyperfine levels are not to scale. The + and - signs indicate the parity of the states. The arrows denote the observed microwave transitions from the interstellar emission sources. The observation of the $^2\Pi_{1/2}$, J = 5/2, F = 2 → 2 transition is very doubtful.

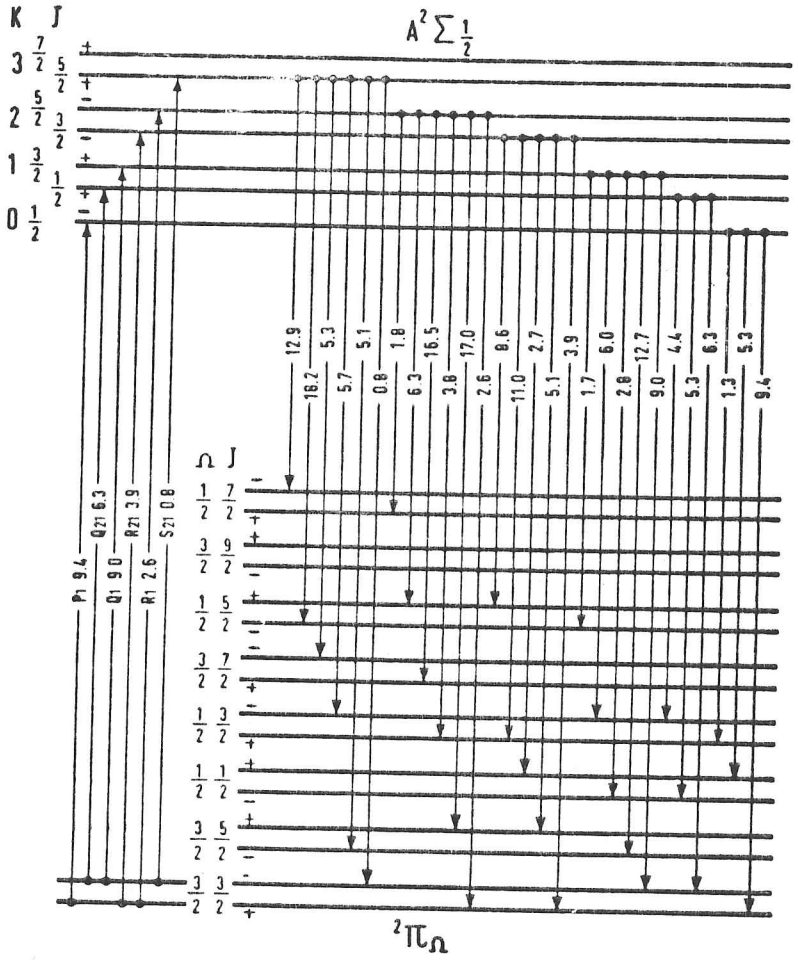

The rotational transitions from the $^2\Pi_{3/2}$, J = 3/2 state to the first excited electronic state $A^2\Sigma_{1/2}$ by UV radiation at wavelengths between 3060 and 3080 Å. The excitation is followed by fast spontaneous decay back to the rotational states of the $^2\Pi_{3/2}$ and $^2\Pi_{1/2}$ states. The cascade down the $^2\Pi_\Omega$ states involving 30 rotational transitions is not shown. The given numbers are the relative transition probabilities.

Fig.3.2

molecule with vibrational quantum $v'=0$ and $v''=0$ in the upper and lower electronic states. Each electronic configuration has a ladder of widely spaced vibrational levels each of which contains a subset of rotational levels similar to those shown in the ground vibration state in Fig.3.2, but with regard for clarity they have been omitted.

Some preliminary calculations

1) Optical depths in a hydroxyl gas at 3060Å. An electrodeless R.F. discharge in water was chosen to make the hydroxyl in concentrations of roughly 0.3% at a total pressure of 1 Torr. This technique and others are discussed in the next section. The OH is formed in the $^2\Sigma$ state which then decays radiatively after 10^{-6} sec to the rotational levels of the ground state $^2\Pi_i$. The schematic experiment is shown in Fig.3.3 A compromise had to be made between the need to have long absorption paths for the conventional absorption experiment and a small cavity volume for the optoacoustic cell. Golden and Del Greco (1963) give the following oscillator strengths for transitions from the $^2\Pi_{3/2}$ ground state to $^2\Sigma_J$ in the strongest vibrational band, $v''=0 \rightarrow v'=0$ as

$$3060\text{Å} \qquad f_{00} = 8 \times 10^{-4} \qquad (v''=0 \rightarrow v'=0)$$

$$3083\text{Å} \qquad f_{P1} = 3.74 \times 10^{-4} \qquad \text{" (Fig 3.2)}$$

The absorption cross-section σ_ν integrated over the linewidth is simply related to the oscillator strength by equation (2.8)

$$\int_{\text{line}} \sigma_\nu \, d\nu = \frac{e^2}{4\varepsilon_0 mc} f \qquad (K_\nu = n\sigma_\nu)$$

(see Ch.2)

where K_ν is the absorption coefficient and n is the OH number density. The absorption cross-section can be calculated

if the line width $\delta\nu$ is known; it is assumed to have a doppler-broadened profile in this case. From the standard formula given in Chapter 2, $\Delta\nu_D \approx (2\nu/c)\sqrt{2RT\ln 2/M}$ giving about 3×10^9 Hz or 0.01 Å at 3080Å for a temperature of 400K; thus the mean cross-section of the line is given by

$$\bar{\sigma} \approx \frac{e^2}{4\varepsilon_0 mc\,\Delta\nu_D} f_{01} = 3.3 \times 10^{-19}\ m^2$$

At a total water pressure of 1 Torr with a 0.3% yield of hydroxyl the optical depth χ of this line over the length of the 10cm absorption tube is given by

$$\chi = n_{OH}\,\bar{\sigma}\,l = p_{OH}\frac{\bar{\sigma} l}{KT} \sim 2$$

Under these conditions the light is almost totally absorbed and the line will be significantly broader than the doppler profile. Therefore, with sufficient resolution, absorption lines should be seen against a continuum source. We shall now proceed to estimate the signal voltage that might be obtained in an optoacoustic experiment employing a halogen lamp source at 3060Å.

2) Optoacoustic absorption. The optoacoustic signal voltage caused by slowly chopped light absorbed by gas in an opto-acoustic cell was given in Chapter 2 and becomes approximately

$$V \approx \frac{h\nu\,\tau_T\,Sm}{V_c}\,\dot{G}$$

if Sm is the microphone pressure sensitivity and $\dot{G}$ is the total rate at which photons of wavelength 3080Å are absorbed. τ_T is the thermal decay time, given approximately by $a^2 R/4Dc_v$ which is roughly 2×10^{-4} s for water at 1 Torr pressure at a temperature of 400K, for a 10cm long cylinder of radius 1 cm. Taking Sm to be 2×10^{-2} V/Nm^{-2} we obtain

$$V = 8.0 \times 10^{-20}\,\dot{G}$$

Fig. 3.3 shows the schematic layout of the optoacoustic experiment. $\dot{G}_o$ is the incident intensity and must be calculated from the black-body emission of the Quartz-Halogen filament with an emmitting area of .25cm^2 and placed as shown in Fig.3.3.

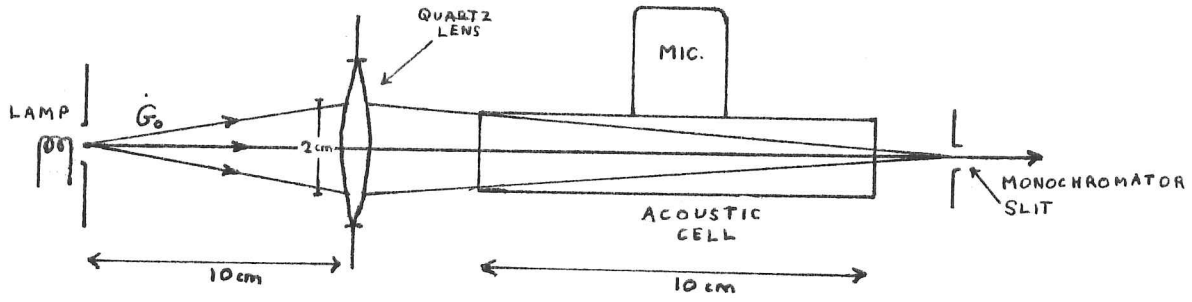

Fig. 3.3

From Thorne (1979) or Chapter 6, Equation (6.3)

$$B(\lambda,T) = \frac{2hc^2\epsilon}{\lambda^5}\,\frac{1}{e^{hc/\lambda kT}-1} \quad W m^{-2} Str^{-1} \text{ per wavelength}$$

where ϵ is the emissivity of tungsten, roughly 0.5 and T is the measured temperature, found to be 3250K (see Chapter 7) With these parameters and taking the dimensions given in Fig.3.3 $\dot{G}_o(3080\text{Å}, 3250K) = 6.0 \times 10^{12}$ photons s^{-1} Å^{-1}. If we ignore all other transitions outside the region 3060Å-3080Å and we take the optical depth of all the absorption lines inside the region to be so great that the effective line widths merge into one another, the absorbing region of the spectrum becomes 20Å wide, covering the whole band. Thus $\dot{G} = 1.3 \times 10^{14}$ photons s^{-1} and $V = 2.4\mu V$, producing a measurable signal. If we take the more realistic case of perhaps ten transitions, including some low, thermally excited rotational levels of the $^2\Pi_{\frac{1}{2}}$ ground state, each optically thick (see above) and with doppler width 0.01 Å

at 400K, then a bandwidth of roughly 0.1Å is presented to the incident continuum intensity absorbing $\dot{G} = 6.4 \times 10^{11}$ photons s^{-1} and producing an acoustic signal of 12nV. Such a voltage signal is discernable if the noise level is lower. From Chapter 2 the theoretical thermal microphone noise is given by Equation (2.46) as

$$V_N^2 = \frac{4\gamma P_0 KT}{\omega_m Q_m V_m} S_m^2 \qquad Hz^{-1}$$

Assuming Qm is dominated by viscous forces and is little affected by the ambient pressure, then the data published by the microphone manufacturers can be taken together with the conditions outlined above, giving Vnoise $\sim 2 \times 10^{-10}$ $V/\sqrt{Hz}$. This value represents the minimum signal discernible for a particular bandwidth (typically 1 Hz).

Clearly an optoacoustic detection of any groundstate absorption in hydroxyl will not be easily observed under these conditions when a quartz lamp is used as a source. Electronic transitions at longer wavelengths, from rotational levels above the ground state, could improve the signal, especially if the transitions are optically thick and the yield of OH is better than the 0.3% used in these calculations. Nonetheless, because of the uncertainty in the yield of OH and the number and strength of the absorbing transitions taking part, together with a practical interest to see how the microphone might behave when under a radio frequency discharge, an effort was made to try out the experiment.

3) <u>The production of hydroxyl</u>. Since the experiments of Oldenberg (1935), who produced hydroxyl with an high current electroded discharge through water at a few Torr, many techniques for OH production have been reported. Of these, three techniques seem to have been used more often than others. They are.

i) An electrodeless radio frequency discharge in water $H_2O + e^- \longrightarrow H + OH^* + e^-$
(Broida and Kane, 1953)

ii) The action of atomic hydrogen on NO_2
$H + NO_2 \longrightarrow OH^* + NO$
(Kaufman and Del Greco, 1961)

iii) The action of atomic hydrogen on Ozone.

$$H + O_3 \longrightarrow OH^* + O_2$$ (Bass and Garvin 1962)

The yield of OH in the first method is $\sim$ 0.3% whereas the other two techniques may produce as much as 10%. However, both NO_2 and O_3 are highly corrosive gases and O_3 is also dangerously unstable. With such properties, these gases were banned from use at Bonn. The restriction left only the first technique available for use in conjunction with a synchroton, which presented a few advantages in spite of the very low yield of OH made by a discharge. In general it is for the following reasons that the electrodeless radio frequency discharge in water has been used so frequently by other workers.

i) The radio frequency discharge is easy to make, it can be of a fairly low power and low frequency (6MHz $\longrightarrow$ 26 Hz).

ii) The discharge products continue to form hydroxyl during their passage away from the discharge source.

iii) Water is easy to handle and obtain. Some researchers who have successfully used water discharges to make OH are Broida and Kane,1952; Radford,1961; Carrington and Broida, 1958; Dousmanis, Sanders and Townes; 1955, Kaufman and Greco, 1961.

Advantage number(ii) is the most crucial one for the experiments attempted in this thesis. When OH was first studied the liftime of OH was determined to be $\sim$ 0.1sec when produced by a discharge in water (Oldenberg,1935). A controversy subsequently developed as to the true destruction mechanisms and reaction rates of hydroxyl, as later on different results were reported when different OH sources had been used. The discrepancies were resolved when Kaufman and Greco (1961) used the reaction

$$H + NO_2 \longrightarrow OH + NO$$

to study the lifetime of OH. They found it to be very short

in their experiments, of the order of a millisecond and the predominant OH removal mechanism was by collisions with the walls of their flow tube. On the other hand, they found that when a water discharge source was operated, the OH lifetime seemed to increase to about 1/3 second, similar to that found by Oldenberg and the OH concentration even showed a small increase whilst the gases moved along the flow tube before finally decaying about a metre away from the discharge. All the experiments were performed at pressures of a few Torr and the OH concentration was measured at various points along the flow tube using a small, portable OH $\Sigma \rightarrow \Pi$ emission source and a moveable monochromator.

Therefore, although a high frequency discharge in water produces a low concentration of hydroxyl the concentration persists for one to two metres downstream from the discharge area; at total gas pressures of a few Torr. Hydroxyl is destroyed rapidly by wall collisons with a lifetime of milliseconds but is continually created from the longer-lived products of a water discharge, with an apparent lifetime of about a second when this particular source is employed.

Since wall reactions were found to be predominantly responsible for the destruction of OH, workers tried various wall-coatings and treatments to prolong the existence of the molecule. (Kaufman and Greco, 1961, Radford,1961, DST, 1955). Substances which destroyed OH were:-

Cu foil, AL foil, Ni foil
Carbon,graphite
Kovar

substances which seemed to have no effect were:-

Apiezone wax
Teflon, glyptal and KCL

Various workers pretreated the glass flow tubes with either detergent followed by 20% HF and distilled H_2O or Phosphoric acid and H_2O, but neither treatment appeared to have much advantage as long as the glassware had been thoroughly

cleaned with detergent.

Bearing all the above points in mind a decision was made to use a 20MHz electrodeless discharge in water with an absorption tube constructed out of ordinary "quick-fit" Pyrex Glass.

4) The optoacoustic experiment. Fig.3.4 shows the construction of the optoacoustic absorption cell and the glass/metal seals and plugs used to connect the microphone to an external signal cable whilst maintaining good screening and vacuum-tight connections. The 1mm bore capillary tubing was employed to reduce the effective acoustic volume of the chamber to just that of the discharge and microphone regions and to dampen out any acoustic pump noise which might attempt to travel either along the tubing itself, or through the gas medium. Vibrations carried by the tubing and clamps etc. turned out to be the predominant sources of background acoustic noise, most of which originated from the rotary pump. The pirani guage was placed on the pump side of the capillary tubing so that its large internal volume would not add to that of the cell. This had the disadvantage that the rotary pump had to be isolated using the glass-tap, to gain an indication of the true pressure within the cell, via the capillary tube.

Fig.3.5 shows the schematic experimental arrangement used to measure either the ordinary absorption of monochromatised light or the broad-band optoacoustic signal produced by absorption of non-monochromatic light during its passage through the cell, emitted by the quartz halogen lamp. The discharge coils were wound on either side of the microphone area such that their fluxes reinforced each other across the small gap which remained in between, and were wired as shown in the circuit diagram. When the chopper unit had been positioned in between the cell and the "Monospek" entrance slit, the ordinary emission spectrum of the discharge could be recorded when the halogen lamp was turned off.

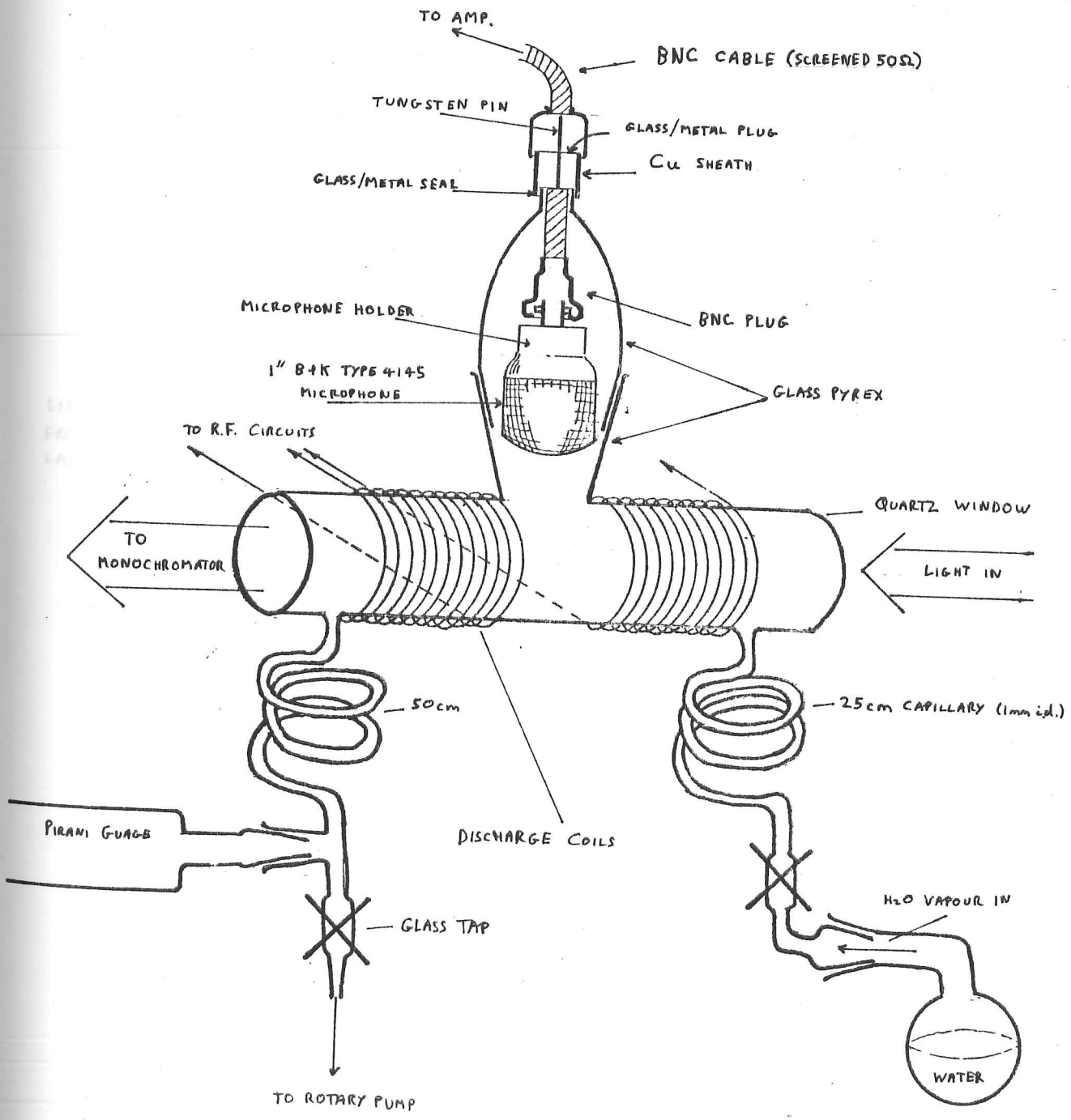
TO AMP.
BNC CABLE (SCREENED 50Ω)
TUNGSTEN PIN
GLASS/METAL PLUG
Cu SHEATH
GLASS/METAL SEAL
MICROPHONE HOLDER
BNC PLUG
1" B+K TYPE 4145 MICROPHONE
GLASS PYREX
TO R.F. CIRCUITS
QUARTZ WINDOW
TO MONOCHROMATOR
LIGHT IN
50cm
25cm CAPILLARY (1mm i.d.)
PIRANI GUAGE
DISCHARGE COILS
H2O VAPOUR IN
GLASS TAP
WATER
TO ROTARY PUMP

Fig. 3.4

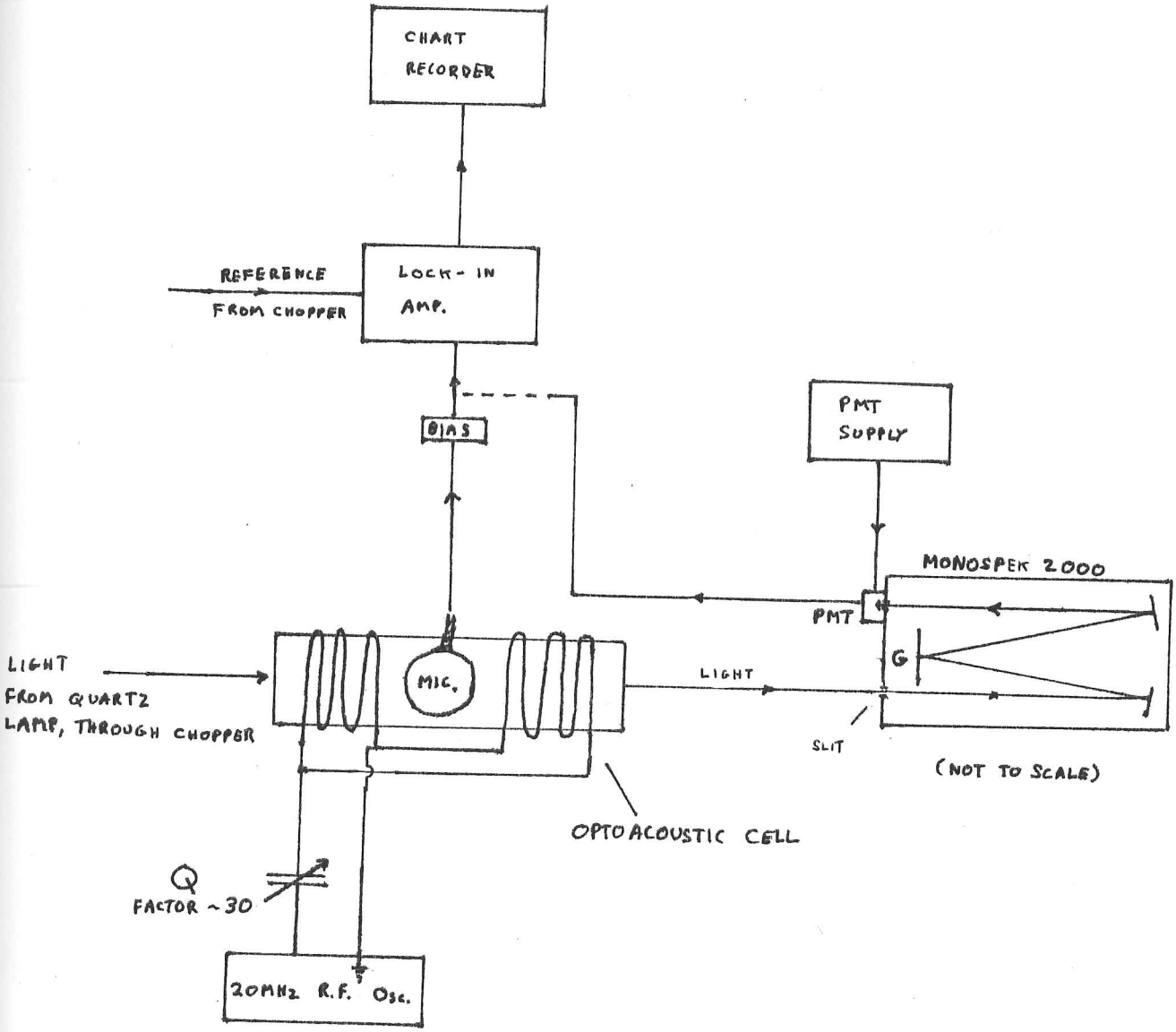
CHART
RECORDER
REFERENCE
FROM CHOPPER
LOCK-IN
AMP.
BIAS
PMT
SUPPLY
MONOSPEK 2000
PMT
G
LIGHT
FROM QUARTZ
LAMP, THROUGH CHOPPER
MIC.
LIGHT
SLIT
(NOT TO SCALE)
OPTOACOUSTIC CELL
Q
FACTOR ~30
20MHz R.F. Osc.

Fig. 3.5

5) Results The experiments were largely unsuccessful. Although good emission spectra of the OH Σ-π system were obtained (see Fig. 3.6) both the absorption and optoacoustic parts of the experiment produced mostly noise beneath which signals that might have been present could only be imagined. Small fluctuations of the direct current supply to the lamp caused large fluctuations in the emitted light at 3080Å, since its black-body characteristics depended exponentially on the electric power consumption in that spectral region. These fluctuations, together with comparable variations caused by air currents, resulted in a stability at 3080Å no better than ± 10%. Without a ratiometer system to monitor variations of the continuum source, absorptions of less than 10% were unlikely to be detected when consecutive wavelength scans of photomultiplier intensity were made with or without gas in the absorption cell and subsequently compared. Therefore 10% represented a practical lower limit to any detectable absorptions using the halogen source. This limitation, which compounded with the low resolution of the monchromator equal to 0.1Å and the typical doppler widths of the OH lines being 0.01Å at 400K meant that the greatest possible change in measured intensity would be 10% even if the optical depths were large. Clearly any OH absorption lines present could not have been discerned much above the noise. The monochromator might have been used successfully if another water discharge had been employed as a background source, since then the source line-widths would have been determined by the doppler broadened OH emission lines; with the monochromator only serving to isolate groups of lines under low resolution.

Backgound acoustic and electrical noise at the light chopper frequency of 150Hz, admitted by a bandwidth of 1Hz on the lock-in-amplifier was roughly 1 μV with the radio frequency discharge off and the cell at a water pressure of 1 Torr. The rotary pump was isolated acoustically by alternating rubber and glass tubing to produce impedance mismatches. Another serious source of acoustic noise was low frequency

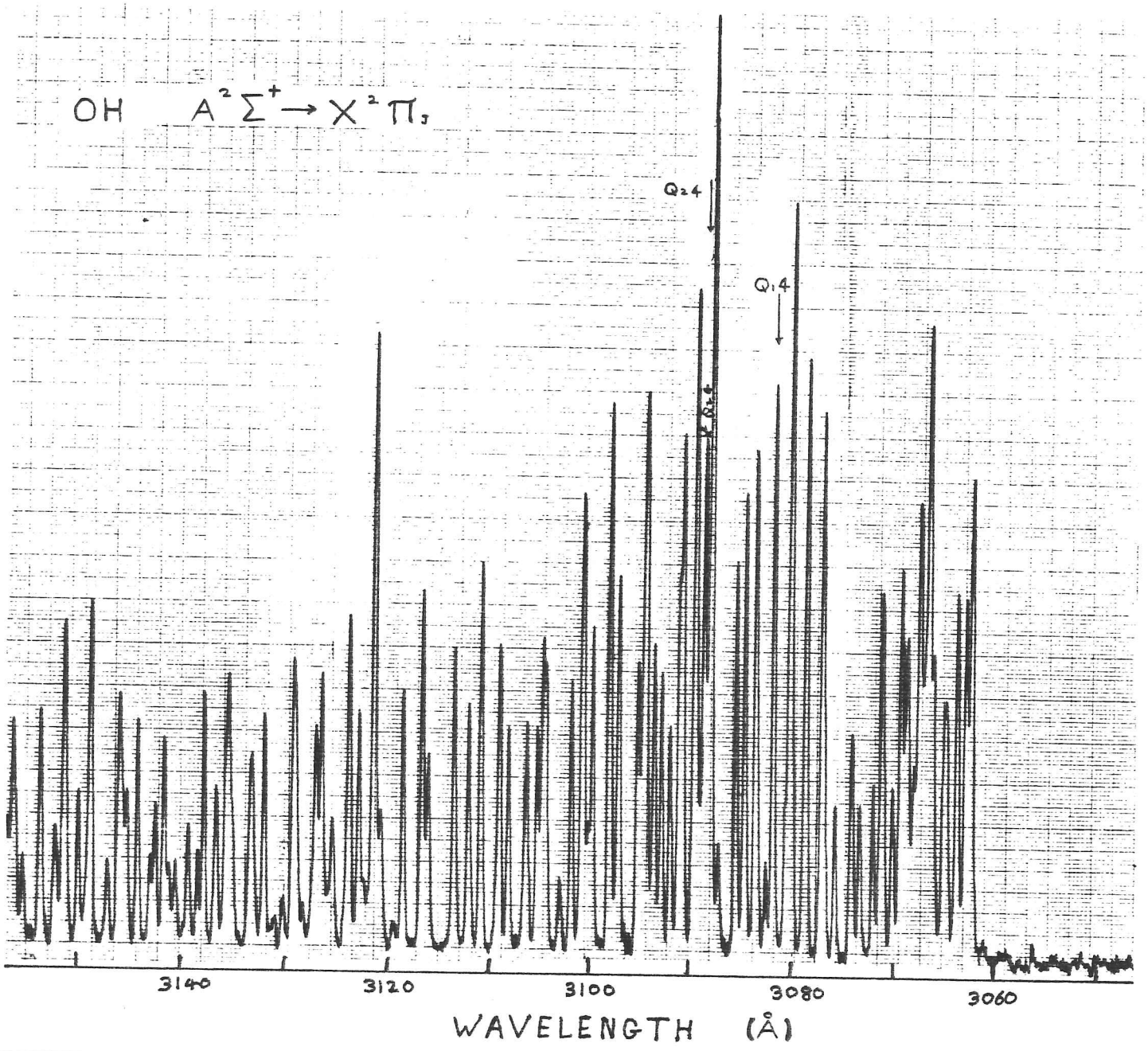
OH $A^2\Sigma^+ \rightarrow X^2\Pi_i$
Q_{24}
Q_{14}
3140
3120
3100
3080
3060
WAVELENGTH (Å)

Fig.3.6

sound from elsewhere in the Cavendish Laboratory which had to be reduced by surrounding the acoustic cell with expanded polystyrene, enclosed by an aluminium box, and placing the retort-stands on rubber mats, which then supported the whole apparatus. The mats also helped to prevent chopper sound reaching the microphone, which otherwise might have detected a coherent but interfering signal.

The radio frequency discharge produced many problems. It was found that by maximising the intensity of emission lines from the $OH\ \Sigma \rightarrow \pi$ band water pressures of a few Torr and an oscillator anode voltage of approximately 500V produced the most hydroxyl, assuming the OH emission intensity was a good indication of its concentration. This was the only measure of the hydroxyl concentration available without a recourse to absorption measurements. However, under such conditions an overloading acoustic signal which contained 100Hz and 50Hz harmonics was observed, detected by the microphone. It was caused both by earth loops in the R.F.50 Ω transmission line and some modulation of the radio frequency by the alternating-current valve heater supplies, together with unstabilised, badly smoothed and variable high-tension supplies employed to supply the anodes of valves in the 20MHz oscillator. After electronically smoothing and actively stablising all the power supplies in the oscillator, the radio frequency modulation was reduced to a level such that the acoustic signal detected by the microphone in its cell was less than the background noise of 1 μV.

Frustratingly, no optoacoustic absorption signal was ever observed; in hindsight this might have been seen from the preliminary calculations described earlier, the most optomistic of which predicted an acoustic signal of 2.4 μV. It should be noted that the background noise was a thousand times greater than the theoretical noise limits calculated, based on thermal statistical processes.

Overall, the experiments described in this chapter were dis-

satisfying but they brought out some important points for consideration before attempting an optoacoustic experiment with a synchrotron. The primary reason for their failure was the low light intensity available from the halogen lamp and the large amount of background acoustic noise detected by the microphone. Generally, optoacoustic techniques can be very powerful if a sufficiently intense light source, such as a laser or a high-current synchrotron can be employed. In an attempt to reduce background noise, twin optoacoustic cells were constructed and the two acoustic signals subtracted from each other in an arrangement which left only the optoacoustic absorption signal unbalanced. This experiment is described in the next chapter.

C H A P T E R 4

The Photoabsorption spectroscopy of H_2O, H_2O in a Discharge (OH), D_2O, C_2H_2 and CO in the region 400Å-1200Å using synchrotron light.

Introduction

Professor Alex Bradshaw at the Fritz-Haber Institute, Berlin kindly offered to let me carry out an experiment using his group's Vacuum Ultraviolet monochromator placed in a beamline of the 2.5GeV electron synchrotron at the Physikalisches Inst. BonnI. The aim of the work carried out on the synchrotron was to study various common molecules of astrophysical interest in the VUV. Of major interest was the tentative assignment of absorption lines to hydroxyl in the region 800-1000A by Viney (1980), who used a 1m vacuum spectrograph in conjunction with a radio frequency discharge in water between the entrance slit and a.5GeVelectron synchrotron, also at Bonn.

Reliable, high resolution absorption cross-sections for water have already been measured by a group at the Deutshes Elektronen-Synchrotron (DESY) in Hamburg. Gurther, Saile and Koch reported in a 1977 DESY preprint, measurements of water and D_2O from 1240Å-620Å with 0.03Å resolution. These accurate photoabsorption coefficients were published after the work of Viney(1979) who undertook his VUV work on a water-discharge at about the same time. Nonetheless, below 600Å there are fewer photo-absorption measurements. Weak photoelectron-spectroscopic measurements (Berkowitz, 1979) of the $2a_1$ state at 380Å reported by Tan et al (1978) and an inner-shell excitation at 415Å predicted by A.Baig (1981) stimulated me to study these structures in photoabsorption.

Berkowitz (1979) shows hitherto unpublished photo-electron spectra of acetylene from 600Å-1000Å, with structure not observed by Metzger and Cook (1964) in photoabsorption. Professor Bradshaw's group in Berlin have made recent calculations of the molecule's electronic structure at similar wavelengths

and they believed photoabsorption cross-sections of C_2H_2 in the region would be useful to provide both a check of the calculations and the photoelectron data of Berkowitz. Because of that emphasis the molecule was studied carefully from 400Å-1200Å.

Carbon monoxide has been observed extensively in the VUV but Berkowitz (1979) reports some discrepancies. Because of this and renewed interest in the molecule's astrophysical behaviour near hot, OB type stars (Wynn-Williams,1981) and its widespread abundance in interstellar matter within the Galaxy, carbon monoxide was also looked at briefly, over the whole 400Å - 1200Å range of wavelengths.

All the observations carried out in Bonn were made using a 1m Seya-Namaioka monochromator (Sam son, 1967) with a maximum resolution of 1.5Å, which corresponded to an exit slit-width of 150 μm. The detection system employed photo-multipliers sensitive to the scintillation of Sodium Salicylate, the phosphor used to detect the VUV light passing through a windowless differential pumping scheme.

The Design of the Experiment

Originally it was intended that this work should be under-taken at the new British Storage Ring at Daresbury (BSRS) but this was completed only recently, too late for experi-ments to be attempted there. It was explained in Chapter 2 that an optoacoustic experiment might be successful if undertaken at BSRS but would probably fail at BonnI where the VUV light intensity is much lower. For a long time we were uncertain which light source would eventually be used. The uncertainty meant that the conventional photoabsorption part of the experiment had to be compromised somewhat to enable optoacoustic measurements to be made in the event that the BSRS should have become available. As it was, we learned only one month before completion of the apparatus that BonnI was to be the source of VUV light, when it was impossible to modify the design of the experiment at so late

a stage in its development by dropping plans for opto-acoustic components and building a better photometric system.

The results of Chapter 3 suggested the following points should be considered for the optoacoustic synchrotron experiment:-

1. Background acoustic noise must be kept to a minimum, as this is the predominant source of interference.
2. Great care is needed in connecting and running a radio frequency discharge to keep down both electrical and acoustic interference.
3. A high-quality needle valve should be used to control more accurately the gas pressure in the absorption-cell(s) together with a gas-regulator mounted on the supply cylinders.
4. The water vapour pressure, when used, should not be allowed to rise higher than about to 2 Torr, as condensation of vapour can occur between the microphone diaphram and the opposing electrode, causing it to 'short'. Once water has condensed in the gap, a long period is needed to pump it all out.
5. An extremely steep differential pumping is essential to keep the effective acoustic cell volume small.
6. A wide beam line should be incorporated to admit the most light from the monochromator; a requirement which is at odds with point 5.
7. Size constraints: the whole apparatus, from the light entrance to the furthest photomultiplier had to be no greater than 1.2m, in order to fit in the restricted area available inside the synchrotron Hall at BonnI.

Clearly, the narrower the interconnecting beamline, the better is the differential pumping. However, a narrow beamline restricts the amount of light which can be accepted by the experiment and thus a compromise must be made to keep

the size of the vacuum pumps within practicable and economic limits. The physical size of the microphone cavity had to be at least 1" in diameter to accommodate the microphone selected, effectively fixing the cross-section of the optoacoustic cell. Its length was chosen to be roughly 5cm, a path over which most VUV light was expected to be absorbed at pressures of 0.1 Torr. The synchrotron radiation polar-diagram (see Fig. 1.2) was expected to have a vertical extent of about 5mm, 10m away from the electron orbit, where the experiment could be conveniently placed. The beam width was also taken as 5mm and it was assumed to have a circular cross-section. To ensure all the VUV photons emitted into such a solid angle could be absorbed in the absorption cell it was essential that the differentially pumped beamline had a minimum diameter of 5mm. This fixed the tube cross-section of the differential pumping segments, in between the areas where fast diffusion pumps were connected. The general performance of the three differential pumping stages employed is described below.

As well as the points listed above a highly effective differential pumping system is required normally for most gas absorption experiments in the VUV. The reason for this is that Storage Rings and Synchrotrons operate at high vacuums ($< 10^{-9}$ Torr and $< 10^{-6}$ Torr respectively). The ultraviolet light produced is strongly absorbed by both air and window materials at wavelengths shorter than 1200Å. Thus it is necessary to isolate the experiment which may be at a high gas pressure of roughly 1 Torr, from the very high vacuum required in the radiation source. This can be achieved by employing windowless differential pumping techniques (Samson, 1967) which rely on the rapid evacuation of the beamline connecting the experiment to the sources at intervals along its length, which can establish a relative pressure gradient of many orders of magnitude from one end to the other.

The construction of the apparatus chosen is shown in the

plate 4.1

plate 4.2

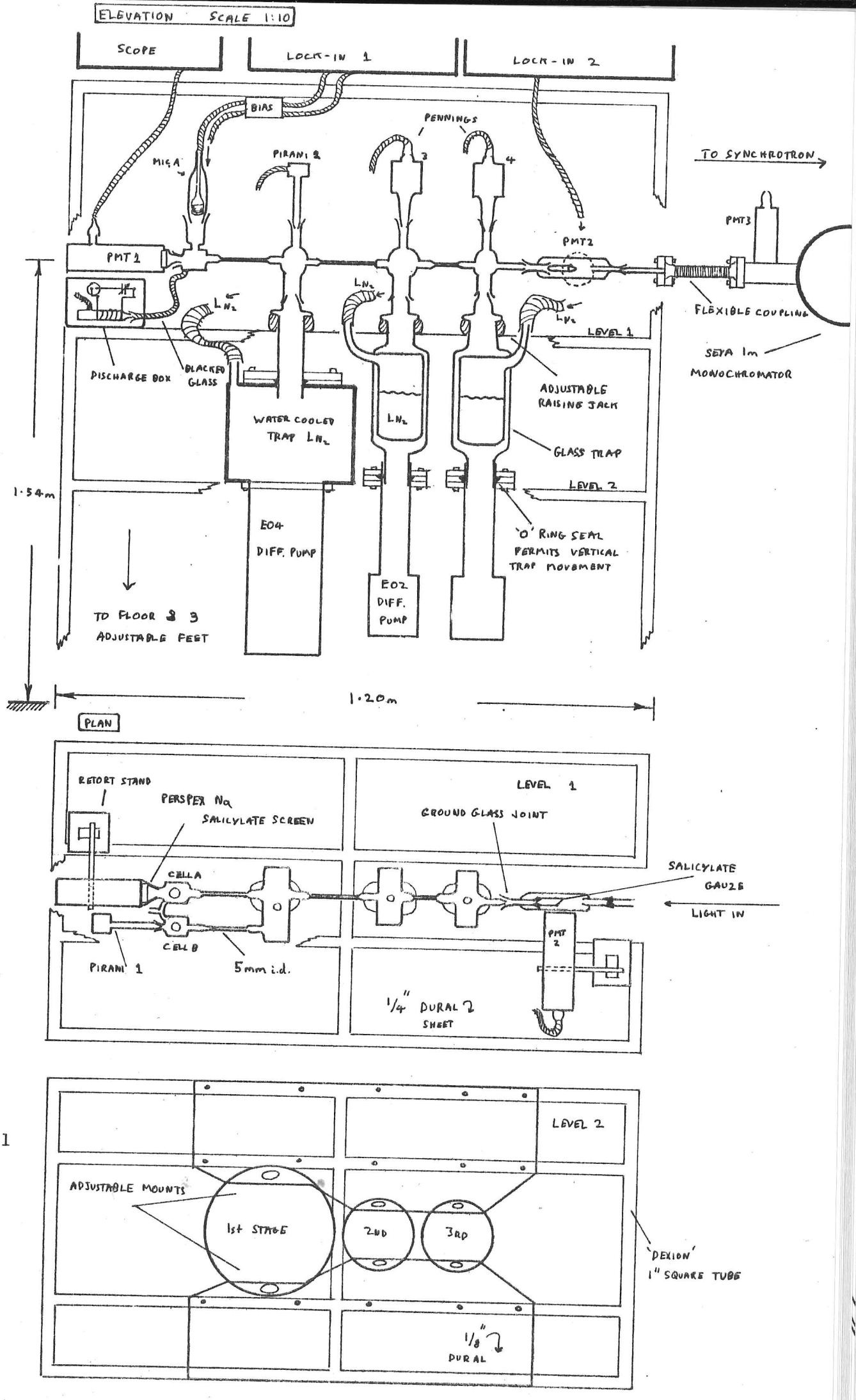
ELEVATION SCALE 1:10
SCOPE
LOCK-IN 1
LOCK-IN 2
BIAS
PENNINGS
MICA
PIRANI 2
3
4
TO SYNCHROTRON
PMT3
PMT2
PMT1
FLEXIBLE COUPLING
SEYA 1m MONOCHROMATOR
LN2
LEVEL 1
DISCHARGE BOX
BLACKED GLASS
ADJUSTABLE RAISING JACK
WATER COOLED TRAP LN2
GLASS TRAP
1·54m
LEVEL 2
E04 DIFF. PUMP
'O' RING SEAL PERMITS VERTICAL TRAP MOVEMENT
E02 DIFF. PUMP
TO FLOOR 2 3 ADJUSTABLE FEET
1·20m
PLAN
RETORT STAND
PERSPEX Na SALICYLATE SCREEN
LEVEL 1
GROUND GLASS JOINT
SALICYLATE GAUZE
LIGHT IN
CELL A
CELL B
PMT 2
PIRANI 1
5mm i.d.
1/4" DURAL SHEET
LEVEL 2
ADJUSTABLE MOUNTS
1st STAGE
2ND
3RD
'DEXION' 1" SQUARE TUBE
1/8" DURAL

Fig.4.1

photographs, Plates 4.1 & 4.2 and Fig.4.1. Twin optoacoustic cells were connected to the first differential pumping stage, only one of which was illuminated with synchrotron light. With gas connections to the cells nearly identical in all other aspects, a subtraction of the 'dead' microphone signal from the 'live' one in line with the synchrotron beam left, at least in theory, only the signal caused by the absorption of synchrotron light, since all other noises should have been common to both cells in amplitude and phase and cancelled each other. The system was fed by gas from an electrically balanced and screened radio frequency discharge box which was totally light-proof, through a blackened tube. The gas entered the discharge unit after being introduced upstream via an Edwards needle valve mounted lower down on the frame.

Three differential pumping stages were monitored by a Pirani and two Penning guages respectively and the absorption-cell pressure by means of a pirani guage mounted on the 'dead' cell B side (see Fig.4.1). Each stage was separated by a roughly 10cm length of 5mm internal bore tubing. Except for the vacuum pumps themselves and the water-cooled Liquid Nitrogen trap, the system was constructed from Glass-Pryex, blown by Mr. R. Flaxman at the Cavendish and connected together with 'quick-fit' ground glass joints. A fair amount of freedom was designed into the mountings of the various pumps and traps, permitting both horizontal and vertical displacements of each pumping stage to ease the alignment of the line. All the equipment was dismantled, except for the frame, before transporting it to Germany in a large van. Each glass pumping stage was carried over separately in its own box to Bonn, where Mr. Flaxman and I then reassembled and aligned the system. The two tubes connecting the differential pumping stages together were rejoined by the glass-blower, after we were sure everything was in the correct position. Obviously, the frame from level 2 upwards had to be light-tight. This was accomplished by covering all of that level with black rubber sheeting, carefully tailored to fit snugly

around the pumps and traps. The sides of the frame were covered by 1/32" Aluminium sheet and the top covered with 1/8" Dural sheet. Where the panels joined with the frame 'draught excluding' tape was attached so that, as the sheet was pulled into the frame by tightened self-tapping screws, the 'draught-excluder' compressed and made the experiment completely light-tight (and draught proof!)

The liquid-nitrogen hoses passed through the side panels of the light-tight frame where they were terminated with large funnels to catch the liquid, poured from portable dewar flasks. All pressure guages and photomultiplier high-tension supplies, including the radiofrequency power inputs, were mounted on a side-panel near the bottom of the frame and connected to their respective units via light-tight holes in the rubber sheet of level 2. The signal cables passed up through the roof-plate to the electronics sitting above.

The first two pumping stages were backed by a single ES330 Edwards rotary pump and the third stage by a ED220 pump. The arrangement ensured that the high vacuum third stage was completely separated from any larger flow of gas pumped by the first two stages, and the rotary pumps were placed on the concrete floor adjacent to the frame and connected via rubber hoses to heavy, carefully suspended, metal gate-valves, which in turn were connected via more hoses to the diffusion pumps. This seemingly awkward arrangement contained large acoustic impedance changes which reflected most of the pump vibrations and left the frame free from low frequency pump noise.

The whole apparatus was mounted on three adjustable metal feet supported on nylon pads, giving some freedom for alignment with the monochromator via a short, flexible metal coupling.

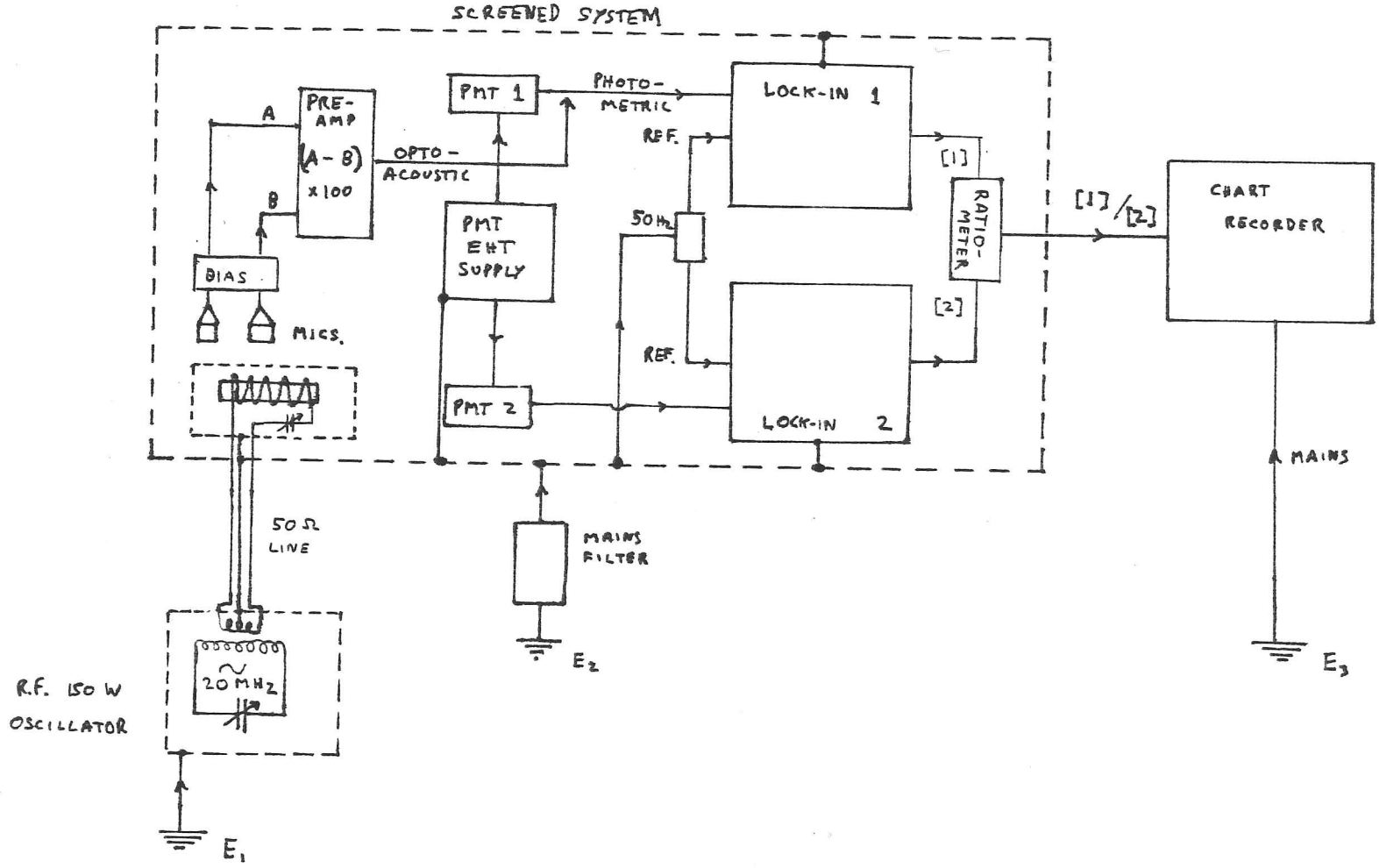
SCREENED SYSTEM
PRE-AMP
A
B
(A - B) x100
OPTO-ACOUSTIC
PMT 1
PHOTO-METRIC
LOCK-IN 1
REF.
[1]
RATIO-METER
[1]/[2]
CHART RECORDER
50Hz
PMT EHT SUPPLY
BIAS
MICS.
REF.
[2]
PMT 2
LOCK-IN 2
MAINS
50 Ω LINE
MAINS FILTER
R.F. 150 W OSCILLATOR
~20 MHz
E1
E2
E3

Fig.4.2

The Electronics and earthing system

Three separate and earthed mains supplies were used and are shown in Fig.4.2 as E_1, E_2, E_3. Highly sensitive equipment was supplied and earthed via a radio frequency mains filter from E_2 and the signals monitored on an oscilloscope, omitted from the diagram.

When the experiment was in the optoacoustic mode the microphone preamplifier was connected to Lock-In 1 in place of of Photomultiplier 1 (PMT 1). The signal from PMT2, representing the incident intensity, was derived from scattered synchrotron light which had not passed through any absorbing gas. It was used to divide all absorption signals recorded at PMT1 in real time, allowing the chart-recorder response to become nearly independent of variations in the synchrotron emission. Dividing was found to be essential as the synchrotron light intensity could be extremely erratic, sometimes rising and falling over a minute or less. A storage ring, on the other hand, would not have caused the same problems as the emitting electron current would have remained fairly constant over longer periods.

The reference signal for the lock-in amplifiers was derived from the 50Hz. mains supply. This gave extremely satisfactory results since radiating electrons were injected into the synchrotron in 5msec bursts with a full period of 20msec directly synchronised with the mains voltage.

Preliminary testing of the apparatus in Cambridge

Apart from granting peace of mind before journeying to Germany, tests of the whole experiment were essential to make plans for work with the synchrotron. A major assumption in the design of the discharge box, supported well by calculations of the flow speed was that the hydroxyl would be present long enough for the gas to pass the 20cm leading to the absorption cell. After the unsatisfactory

attempts to measure hydroxyl in absorption discussed in Chapter 3, a fresh photometric attempt was made with the new equipment. This time a portable 70 watt radio frequency water-discharge was used as a source; the chopped light was passed through the 1m 'Monospek' Hilger and Watts monochromator and out the exit slit into the light-tight flexible coupling of the new system, simulating the proposed VUV experiment, but at 3090Å. Golden and Greco (1963) describe in detail the principle of the technique. Even though the resolution of the monochromator was no better than 0.2Å with 20 μm slits, the narrower widths of the hydroxyl lines selected ensured that the monochromator was not an important limitation in this respect. Unfortunately, other problems arose. Light from the discharge box manufacturing the hydroxyl tended to leak into the absorption-cells by reflection up the glass walls of the black-covered 'S' tube leading to the twin complimentary absorption cells. With a sufficiently bright source of probing radiation this would not have prevented measurements being made, as the Lock-In amplifiers could pick out the chopped signal from the continuous background, locked in as they were to the mains supply and hence the pulsed synchrotron light. However, the long path lengths from the OH light source to the receiving photomultiplier PMT1 of about 3m meant the OH line emission was severely attenuated, even with the quartz lenses used to collimate the light from the exit slit down the length of the system. Another inhibiting factor, not fully appreciated at the time, but far more serious, was the conclusion that reactive radicals created by the discharge were destroying the sodium salicylate screen of PMT1. The phosphor had been dissolved in methanol and sprayed with an atomiser onto the perspex screen immediately behind the 'live' absorption cell, adjacent to the gas inlet. The low light intensity and the slow destruction of the phosphor combined to produce a very noisy detection signal when the discharge was on, the mean of which steadily decreased with time over an hour of operation whilst the H_2O pressure in the cell was 0.1 Torr and the hydroxyl

source remained quite bright with 500V of radio frequency across its tuned circuit. The salicylate might also have been scintillating due to the reactive radicles colliding with it, adding to the interfering stray light. However, through all the noise the OH emission spectrum of the source could still be seen, but it was stable to no better than 10% while looking at the Q_2-4 transition (Dieke and Crosswhite, 1961) at 3090.4Å, with insufficient monochromator resolution to keep out the adjacent Q_2-4′ and Q_2-1′ satellite emission lines (see Chapter 3).

An attempt was made to calculate an upper limit to the hydroxyl concentration produced by the discharge box on the basis of these observations. The two satellite lines were weak compared to the central Q_2-4 line so only one oscillator strength had to be considered in the following estimate.

Golden and Del Greco (1963) give a value of $5.9 \times 10^{-4} \pm 10\%$ for the oscillator strength f_{Q_1-4} at 3083.3Å. Thus using calculated relative transition probabilities, (Dieke and Crosswhite, 1961) f_{Q_2-4} must be 4.6×10^{-4}. To keep the calculation simple the conditions of Golden and Del Greco are taken to apply. These were that both the emission and absorption temperatures of the hydroxyl lines were 450 K and 320K respectively and that the oscillator strength was related to the partial pressure of hydroxyl by the expression

$$f_{J''J'} = \frac{m e c R^{3/2} T_A^{3/2}}{\pi^{1/2} M^{1/2} N_A} \left(1 + \frac{T_E}{T_A}\right)^{1/2} \frac{\omega_0 Q_{rot}}{\ell (2J''+1)} \exp\left(\frac{E_{J''}}{K T_A}\right) \frac{\ln(I_0/I)}{P_{OH}}$$

$$= 3.44 \times 10^{-5} \left[\log_{10}(I_0/I)\right] 1/P_{OH}$$

where Qrot was the rotational partition function, ω_0 the frequency and ℓ the length of the absorption path. P_{OH} was given in torr. TA and TE were the absorption and emission temperatures of the hydroxyl radicals produced.

K is the Boltzmann constant, M is the molecular mass, and NA is Avogadro's number and E_j is the energy of the J th rotational level in the relevant electronic state.

For the two lines:

	ω_0/Hz	l/cm	J"	$E_J"/cm^{-1}$
(This experiment) Q_2 -4:-	9.71×10^{14}	20	3½	390.80
(Golden et al) Q -4:-	9.73×10^{14}	9	4½	316.96

Table 4.1

Hence we have

$$p_{OH} = 2.2 \times 10^{-5} \frac{\log_{10}(I_0/I)}{f_{Q_2-4}}$$

Inserting an absorption no better than 10% with f_{Q_2-4} from above, the averaged partial pressure of hydroxyl along the 20cm length must have been

$$p_{OH} < 2.2 \times 10^{-3} \text{ Torr}$$

at an averaged total water pressure of 0.15 Torr. Therefore, on the basis of this calculation, the yield of OH could have been no better than 1.4%.

The differential pumping performed well in the final configuration. Typical pressures for three different gas mixtures with liquid nitrogen in the cold traps at -77 C were

	H_2O	H_2O and 300V Discharge	He
(absorption cell) P_1/Torr	1×10^{-1}	1×10^{-1}	1×10^{-1}
(1st stage) P_2/Torr	7.7×10^{-3}	8×10^{-3}	1.1×10^{-2}
(2nd stage) P_3/Torr	1.5×10^{-5}	1×10^{-4}	1.5×10^{-4}
(3rd stage) P_4/Torr	3×10^{-6}	3×10^{-5}	5×10^{-5}

Table 4.2

The Pirani gauges were calibrated using the He absorption edge at 504Å in synchrotron light (see below); the calibrated pressure readings have been given above. It is apparent from the table that water on its own was pumped very effectively by its freezing onto the cold-traps. The figures for Helium were representative of pumping performance for gases which do not condense or freeze at liquid nitrogen temperatures and suggested the high 2nd and 3rd stage pressures for water when the radio frequency discharge was on must have been caused by the presence of new, uncondensible gases or radicles manufactured in the discharge box. A tentative conclusion as to the concentration of new gases in the discharge mixture can be drawn if we look at the ratios of the water discharge and He pressures which are 1.0, 0.73, 0.67, 0.6 for the absorption cell and the three stages respectively. If the steady decrease in ratio is inferred to be due to a progressively lower concentration of H_2O at each stage, then the limiting ratio of 0.6 would suggest the fraction of new gases in the original discharge mixture was roughly 60%. This seems surprisingly large but Golden et al (1963) and Kaufman et al, (1961) report as much as 40- 50% of atomic hydrogen produced in water discharges, with very little atomic oxygen or OH. Indeed, it is well known that 'wet' H_2 in a discharge is a good source of hydrogen atoms. They suggest the low yield of OH produced (0.1-0.3%) could be due to the more rapid dissociation of OH than H_2O in the discharge followed by the swift reaction $O + OH \rightarrow O_2 + H$ which removes oxygen atoms and greatly decreases OH. However, as mentioned in Chapter 3, OH is also steadily being formed by the reactions

$$H + O_2 + M \longrightarrow HO_2 + M$$

$$H + HO_2 \longrightarrow H_2O_2^* \longrightarrow 2OH$$

and thus remains in low concentration wherever atomic hydrogen and a little oxygen is abundant.

From the circumstantial evidence provided by the high upper limit for the yield of OH and the presence of large amounts of atomic hydrogen a long way down the absorption tube, an optomistic person would believe that hydroxyl was also present in the previously observed concentrations of $\sim$ 0.3%. The aim of these preliminary laboratory tests in Cambridge was to grant peace of mind before travelling to BonnI. They were to no avail, however, and only served to emphasise how small a concentration of hydroxyl would be seen against the far larger amounts of atomic hydrogen and water in the photoabsorption experiments to be attempted.

Work at the 2.5 GeV Synchrotron in Bonn

After transporting and reassembling the differential pumping frame at the Physikalisches Institute with the aid of Mr. Flaxman, a total of five weeks were spent aligning and operating the photoabsorption experiments. The layout of the synchrotron is shown in Fig.4.3 with the synchrotron Radiation User area outlined in red. Under normal operating conditions the radiation in the user-area was never great enough to prevent people working on their equipment . However, even though the machine was on almost continuously this did not mean that the synchrotron light was useable for most of the time, due to the often conflicting requirements of Particle Physicists, who wished to extract electrons from the ring, and Radiation Users, who wished to keep as many electrons as possible circulating in the Synchrotron. As can be seen from Fig.4.4 in more detail, a gold-coated glass 'pre-mirror' was used to focus the softer VUV radiation towards the SEYA monochromator, filtering out hard VUV and X-Ray radiation not reflected by the gold. At nearly grazing incidence (10°) the wavelength cut-off of gold is roughly 30Å (Samson, 1967). However, if the lead beam-shutter, which admitted radiation from the synchrotron to the mirror box was opened when the electron energy was greater than about 1.3GeV the extremely hard XUV and X-Ray radiation would rapidly crack any oils inevitably present in the mirror box onto the gold mirror surface, reducing its reflectivity by 90% within a day of continuous operation and compelling its replacement. Severe radiation damage of the glass substrate would also result. For these reasons light users took few measurements for any length of time when the synchrotron was dedicated to High Energy Physics. At lower electron energies, down to 0.5GeV measurements could be taken parasitically if the current was sufficiently steady and near 20mA. The most efficient approach to working with the synchrotron was to align and adjust the equipment during parasitic time but to do actual wavelength scans when the machine was dedicated wholly as a synchrotron

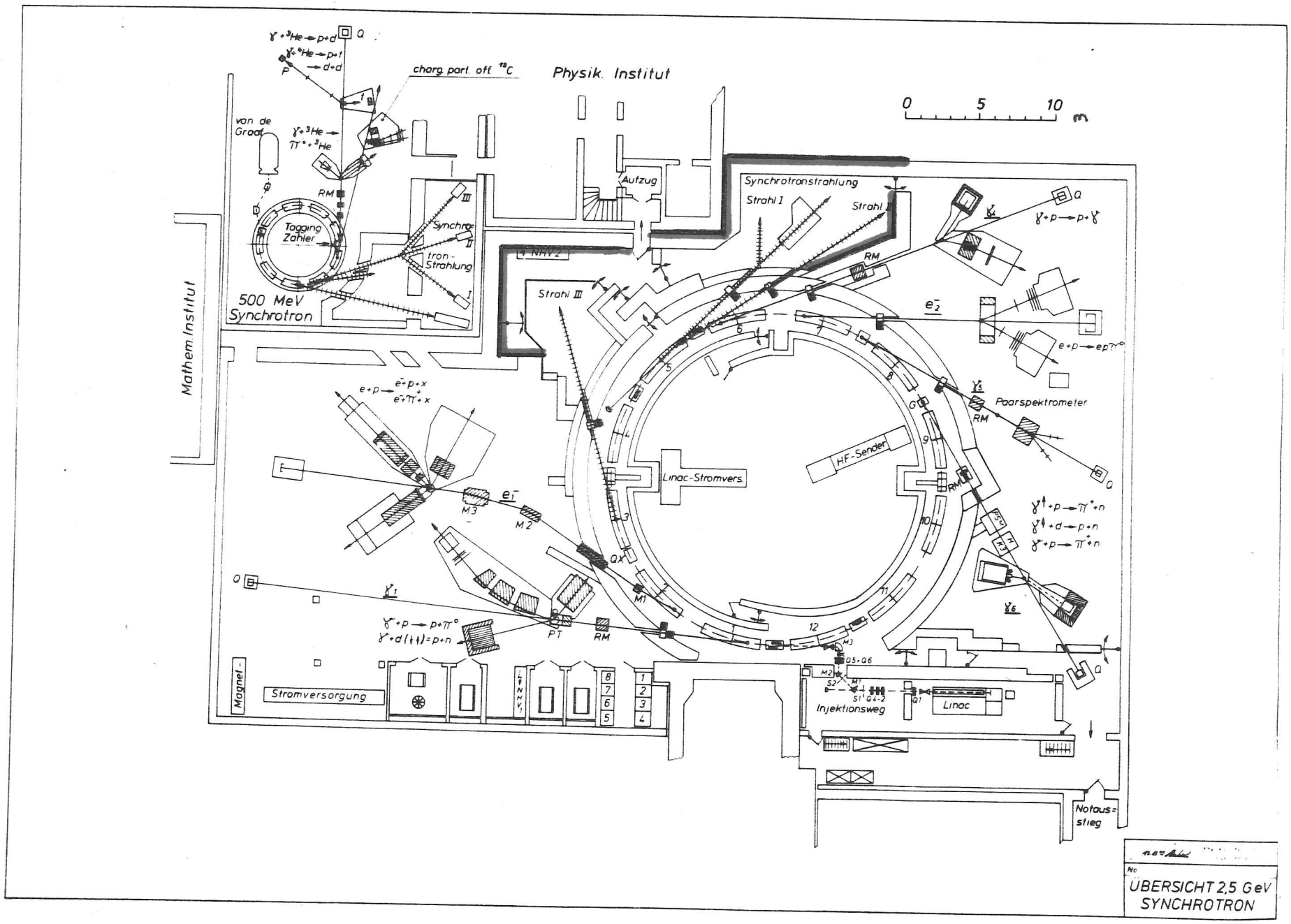
Physik. Institut
0 5 10 m
charg. part. off ^{12}C
von de Graaf
Tagging Zähler
RM
Synchro-tron-Strahlung
500 MeV Synchrotron
Mathem. Institut
Aufzug
Synchrotronstrahlung
Strahl I
Strahl II
Strahl III
Linac-Stromvers.
HF-Sender
Paarspektrometer
Stromversorgung
Magnet-
Injektionsweg
Linac
Notaus-stieg
UBERSICHT 2,5 GeV SYNCHROTRON

Fig. 4.3

Fig. 4.4

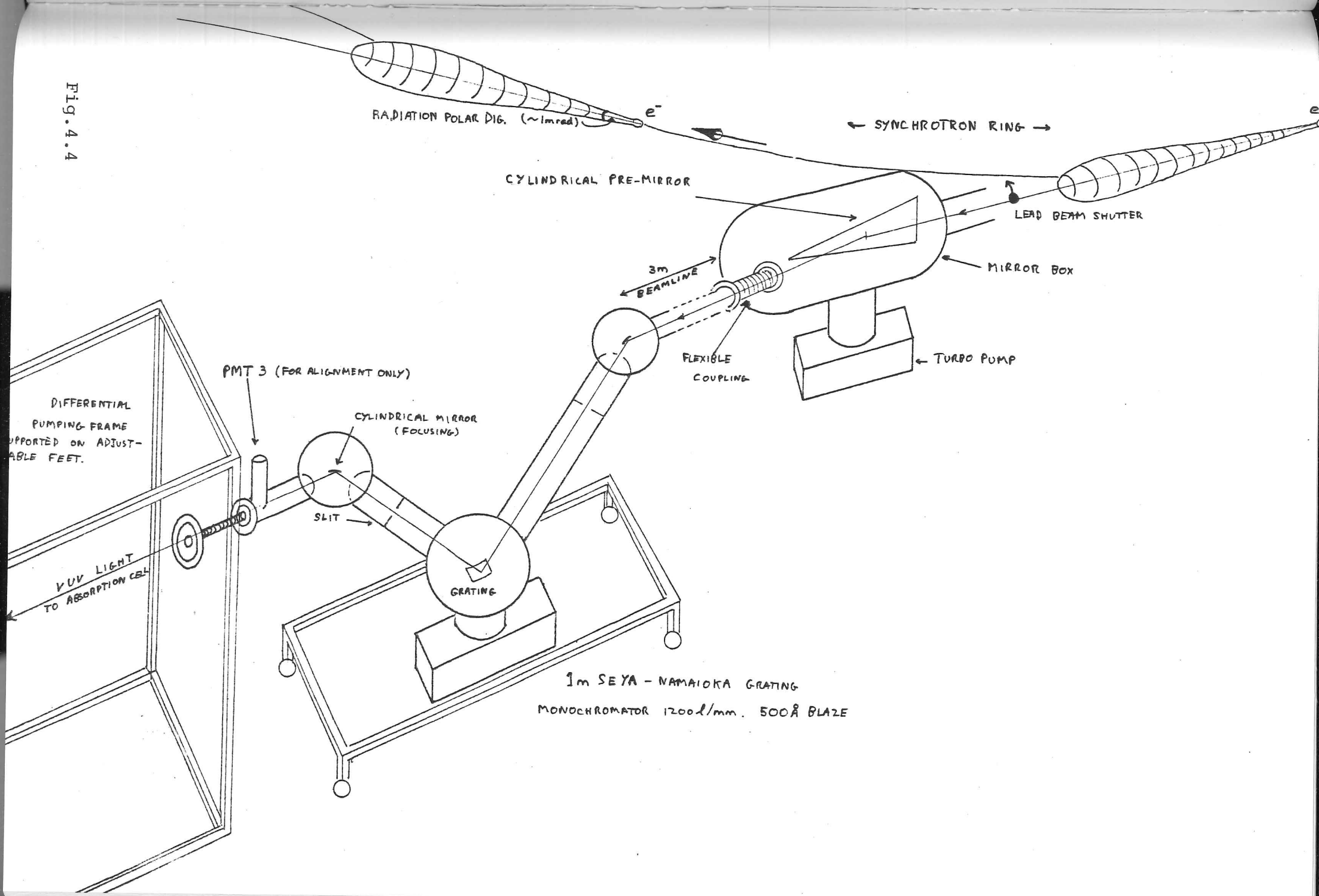
RADIATION POLAR DIG. (~1mrad)
e⁻
← SYNCHROTRON RING →
e
CYLINDRICAL PRE-MIRROR
LEAD BEAM SHUTTER
MIRROR BOX
3m BEAMLINE
FLEXIBLE COUPLING
← TURBO PUMP
PMT 3 (FOR ALIGNMENT ONLY)
DIFFERENTIAL PUMPING FRAME
UPPORTED ON ADJUST-
ABLE FEET.
CYLINDRICAL MIRROR (FOCUSING)
SLIT
VUV LIGHT TO ABSORPTION CELL
GRATING
1m SEYA - NAMAIOKA GRATING
MONOCHROMATOR 1200 l/mm. 500Å BLAZE

Radiation source. The dedicated periods accumulated to a week over the five weeks the experiment was operational.

Alignment of the Optical components

Alignment of the pre-mirror, the beamline, the monochromator and finally the differential pumping frame was a time consuming process made difficult by the large degrees of freedom allowed in each piece of equipment. The major items involved are shown schematically in Fig.4.4. No attempt was made to refocus or realign the Seya internally, as this would have required far more time than that available. Once alignment had been achieved satisfactorily the Seya did not have to be moved again and its feet were locked in position. On the two subsequent occasions when the pre-mirror had to be removed, recoated and replaced the correct mirror focusing and deflection were obtained by adjusting its mounts alone.

Both the entrance and exit flanges of the Seya had vacuum valves with built-in LiF windows, permitting the visible synchrotron light to be viewed directly with the naked eye when the grating had been rotated to allow zero-order radiation through the exit slit. A technique was developed whereby the differential pumping frame could be first aligned by sighting down the tube from the position of PMT1 (Fig.4.1) at the synchrotron light until a uniformly illuminated 'tunnel ring' with a bright centre had been attained and then by replacing the salicylate screen, PMT1 as the detector. This last stage of the process was performed when the whole line, including the differential pumping frame, was under vacuum with the SEYA valves open, so that VUV light at 600Å could be used for the final photometric adjustments.

Wavelength Calibration and Use of the Monochromator

The diffraction grating was a gold-coated 1200 l /mm holographic grating blazed at 500Å. To scan wavelengths over the total range 300Å-1400Å the grating was rotated by a stepping motor/counter arrangement in conjunction with a sine drive

(Samson, 1967), such that 20 pulses to the motor were needed to move the grating one wavelength division. This system was built by the Fritz-Haber Institute. From subsequent calibration 1Å was found to be equivalent to 1.842 $\pm$ .002 divs. The procedure was to find the zero-order (pure reflection) position of the grating, setting this as the zero-wavelength origin, and then increasing the counter reading by an amount proportional to the wavelength required. Scans were always taken in the direction of increasing wavelengths. The zero-order position was 7298.2$\pm$.2 divs, found from many separate measurements.

All wavelength scans were recorded using a Bryan's continuous-drive stepped chart recorder, included schematically in Fig.4.2. Synchronisation between the Seya counter reading and the chart-paper was ensured by me by using the internal 200Hz digital 5V pulses which drove the chart motor to trigger the grating stepping motor via a 2^N digital divider, allowing a variety of relative paper and wavelength scanning speeds to be selected.

This system could be overridden to increment the Monochromator counter reading either more or less without shifting the chart-paper. The complete arrangement was extremely flexible and easy to use, permitting any wavelength region to be scanned and recorded at a variety of speeds and time-constants set on the Lock-In amplifiers.

The calculated resolution of the monochromator, determined solely by the slit widths was roughly 1.4Å per 100 μm slit. However, when a careful scan was made of the sharp Inner Shell Argon excitation at 466Å in absorption (Berkowitz,1979), a width of 1.5Å was observed with 150 μm slits, implying a slightly better resolution of about 1Å/100 μm slits. (see Fig.4.5). However, unless the synchrotron light intensity was sufficiently strong and steady, slit widths of 200 μm (2Å resolution) were normally employed and 1.5Å resolution seemed to present a practical limit to the maximum resolution

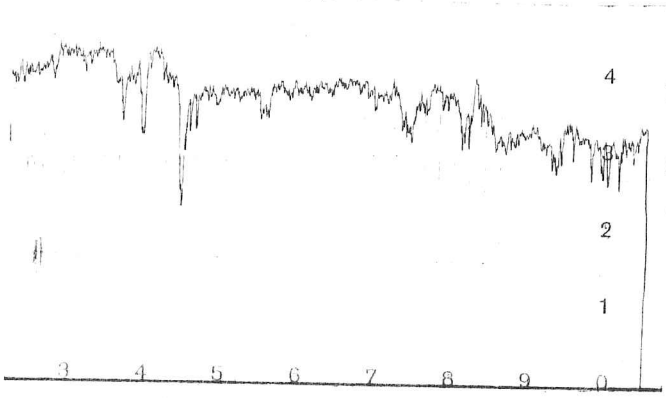

Synchrotron output during the scan of the Ar ionisation edges. (See below). The t-scales of the two charts are slightly different but correspond to the same period.

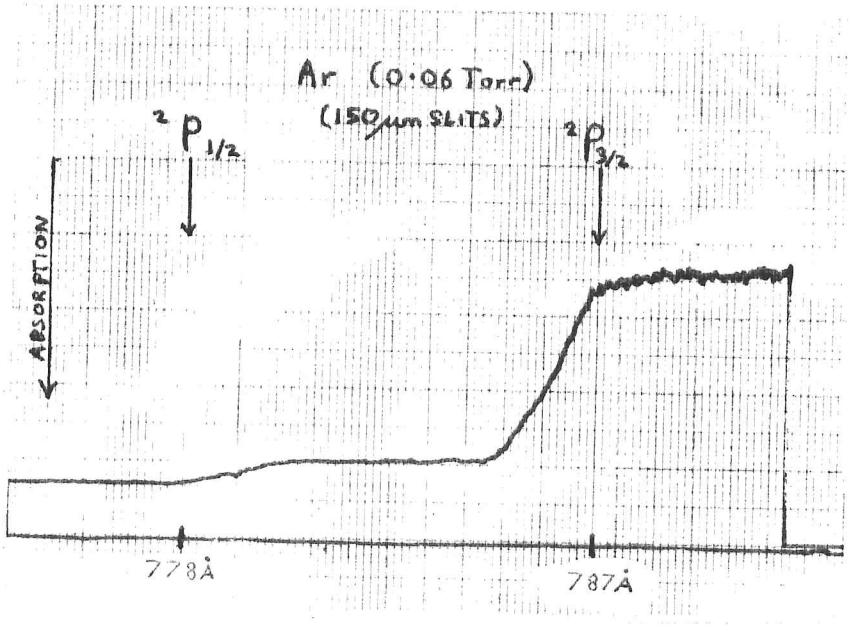

The Ar ionisation edges; the signal is from the ratiometer (see text)

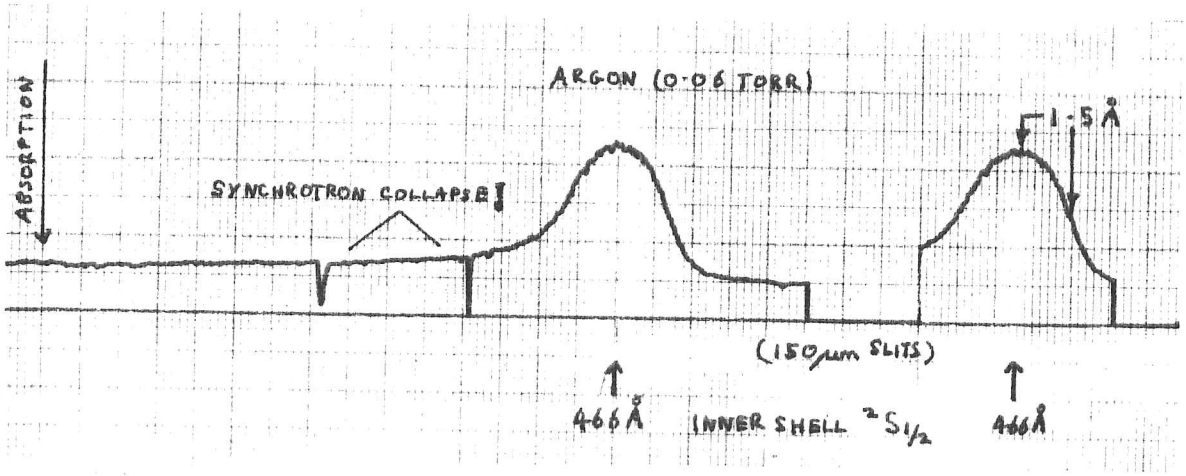

Resolution checks of the Argon Inner shell excitation at 466A.

Fig.4.5

attainable with the Seya; smaller slit widths seemed only to decrease the signal and not the width of the sharp absorption features. The wavelength-per-division calibration quoted above was found from measurements of the Argon $^2P_{3/2}$ $^2P_{1/2}$ (787Å and 778Å) edges, the He $^2S_{1/2}$ (504Å) edge and the Inner-shell $^2S_{1/2}$ excitation at 466Å (Fig.4.5) taken together with the mean position of zero-order (oÅ). A linear regression was performed on the 5 data points giving a standard Error in the slope of 0.1%, and hence a similar error in the wavelength determinations. For example at 1000Å the absolute wavelength error was about $\pm$ 1Å, less than the maximum resolution attainable of about $\pm$ 1.5Å. The extremely good linear variation of grating counter reading with wavelength was entirely due to the efficient operation of the 'sine drive' built in.

Measurement Procedures and Wavelength Scans

The system was let up to air pressure as infrequently as possible and pumped overnight, if necessary, before a wavelength scan was undertaken of a particular gas. The two glass cold-traps had to be filled with liquid nitrogen every 3 hours, whereas the water-cooled trap could be left overnight without refilling. This meant a good vacuum could still be maintained by at least one diffusion pump running continuously, with the advantage that the glass cold traps were cleaned out by the first pump when they warmed up to room termperature. It was important to prevent the accumulation of too much condensible gas which could interfere with the pumping performance. When the differential pumping was running efficiently synchrotron light was admitted by opening the beam-shutter. To make sure a high and reproducible intensity was used for each run, the light level detected by the photomultiplier at 600Å was recorded at the beginning of each day, using the same slit sizes and PMT voltages for each measurement. If the daily system check showed signals much lower than expected, time would have to be spent readjusting the pre-mirror or the frame until the standard performance had been regained.

Wavelength scans were taken of H_2O, H_2O in a discharge at different voltages, D_2O, C_2H_2, CO, and He all over a range of pressures. Simultaneous with the initiation of a scan, a second chart recorder was set running, recording the incident light level at PMT2 before it was absorbed by any gas nearer the absorption cell. This hard-copy record of the synchrotron performance was always at hand to discern when photoabsorption measurements should be disregarded because of low or rapidly fluctuating incident light. Generally the ratiometer coped remarkably well, even with sudden changes, as long as the input signals of the two Lock-In amplifiers had been accurately phased with the mains reference signal. It was, of course, essential to have identical integration time-constants set on each amplifier to prevent transient signals being displayed. In Fig.4.5 the synchrotron output is also shown for a scan of the Argon ionisation edges, illustrating how the fluctuating incident intensity was almost completely corrected.

Normally, wavelength scans were made at the lowest possible speed of 0.02A/second, and the time constants were chosen just small enough to show the noise without compromising the resolution. A typical run from 800Å-1200Å took five hours with a time-constant of 3 or 10 seconds, but these figures were often changed by a factor of two depending on the synchrotron conditions.

A Rough Pressure Calibration

An attempt was made to calibrate the pirani-guage attached to the absorption cells to gain an indication of the integrated number density of molecules along the absorption tube, using the Helium $^2S_{1/2}$ absorption edge and the known cross-section of its onset at 504Å. Scans were made across the He absorption edge at six different readings of absorption cell pressure.

The ratio of the absorption at wavelengths just greater

than 504Å to that at wavelengths just less than 504Å is given by the expression

$$\frac{I(>504\text{Å})}{I(<504\text{Å})} = e^{\sigma \int_0^L n\,dx}$$

(Beer-Lambert Law)

where σ is the He $^2S_{1/2}$ cross-section (7.5 Megabarns), n the number density and L the absorption length. If n_0 is the density at the beginning of the absorption cell then

$$\int_0^L n\,dx = n_0 \int_0^L f(x)\,dx = n_0 \ell_e \qquad [f(0) = 1]$$

where f(x) is a steadily decreasing function representing the differential pumping gradient and ℓ_e is an effective absorption length. Hence, if a guess of 15cm is made for ℓ_e at 293Kelvins

$$p = \frac{KT}{\sigma \ell_e} \ln\left(\frac{I_>}{I_<}\right)$$

$$= 0.273 \ln(I_>/I_<) \text{ torr.}$$

Thus a rough calibration curve of p versus pirani pressure p_1 can be drawn dependent entirely on ℓ_e and is shown in Fig.4.6. Included on the diagram are the appropriate guage sensitivity constants for a variety of gases which had to be used when one gas was compared to another. Water and Argon were also measured to provide a check of the calibration; their respective points have been marked as such on the graph after adjustment has been made for their different sensitivitie constants.

The precision of the calibration (ie. its scatter) is clearly no better than 20% and the accuracy (ie. how close to truth) only as good as the choice of the effective

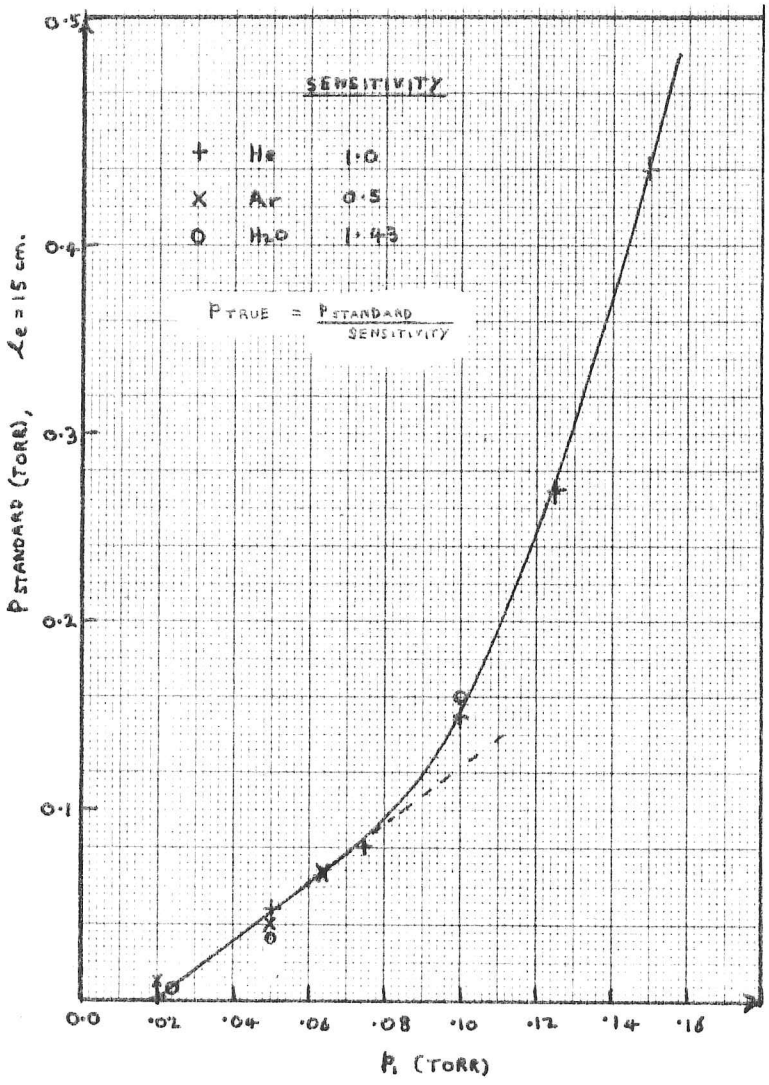
SENSITIVITY
+ He 1·0
X Ar 0·5
O H₂O 1·43
P TRUE = P STANDARD / SENSITIVITY
P STANDARD (TORR), Le = 15 cm.
0·5
0·4
0·3
0·2
0·1
0·0
·02
·04
·06
·08
·10
·12
·14
·16
P₁ (TORR)

Fig. 4.6

absorption length ℓ_e . It is quite likely the length was a function of pressure, becoming shorter at high pressures and hence leading to the striking non-linearity of the curve. More important would be the variation of ℓ_e from one gas to another; but this could not be checked since not all the gases studied later had accurately known absorption cross-sections which could be used for pressure calibrations.

Photometric Results of conventional absorption measurements

Calculation of Rough Absolute Cross-sections

All the data necessary, at least in principle, for calculating the absolute photoabsorption cross-sections of the molecules under study was recorded throughout the experiments at Bonn. However, the data included measurements of absorption cell pressures using a Pirani guage, known to be quite inaccurate unless great care had been taken with its implementation; this potential source of error, compounded with the differential scattering of light along the thin absorption tube due to progressive absorption of gas and the additional uncertainty inherent in the gradient f(x) of the very rapid differential pumping suggested that not too much emphasis should be placed on measuring absolute cross-sections. Nonetheless, for want of a relative absorption scale against which to plot the data, the calculations were made in an attempt to get within an expected factor of two of the true cross-sections.

As was outlined in the preceding section, optical depth measurements for a variety of indicated pressures were made on Helium, which could then be used to calibrate optical depths measured for other gases, using the Helium absorption as an absolute standard. This comparison does not depend on the effective length l_e of the absorption cell. Fig.4.7 shows schematically the radiation intensities I, Io, and Io′ at hypothetical points along the differential pumping line. Io′ is the light intensity entering the differential pumping line and a measure of it was detected by PMT2. Io is the intensity incident at the beginning of the effective absorption tube of length l_e, having passed through a hypothetically gas-free differential pumping line. I is the emergent intensity detected at PMT1, after absorption by gas in the cell at pressure p. For reasons discussed below, some attenuation of light occurred while passing down the

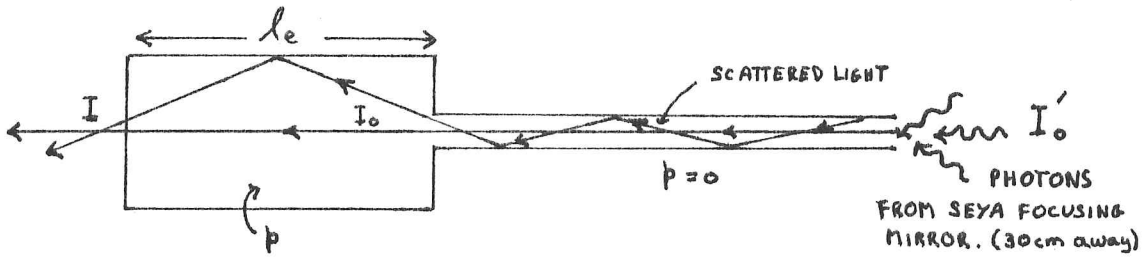

Fig.4.7.

tubes, even without gas present in the main cell; the attenuation was a slowly changing function of wavelength and was measured by making absorption scans under a good vacuum over the whole wavelength range. From the Beer-Lambert Law, using quantities already defined above and in the previous section

$$\sigma(\lambda) = \frac{1}{n_o l_e} \ln I_o/I$$

$$= \frac{KT}{p l_e} \ln I_o/I$$

$$= \frac{2.05 \ln I_o/I}{p} \quad \text{Megabarns}$$

where p is measured in Torr. In this expression the same temperature and effective length have been used as in the pressure calibration of the Pirani guage, using He as a standard; the expression represents a direct comparison of the He absorption of 7.5 Mbarns at 504Å with the absorption of a gas at a relative pressure p found from the calibration curve Fig. 4.6 with a suitable sensitivity constant. By

following this procedure only optical depths and precise, but inaccurate pressure measurements are compared to produce an absolute cross-section of the gas. However, the method is only accurate if the pressure gradient function f(x) which defines the effective length l_e is of the same form for all gases and for all pressures. This is probably true to a first approximation but quite clearly breaks down in extreme cases.

Let Fig.4.8 represent a typical chart-recording of some photoabsorption spectra, taken from the output of the ratiometer to make it insensitive to variations of synchrotron light intensity Io . The y-axis is a measure of the

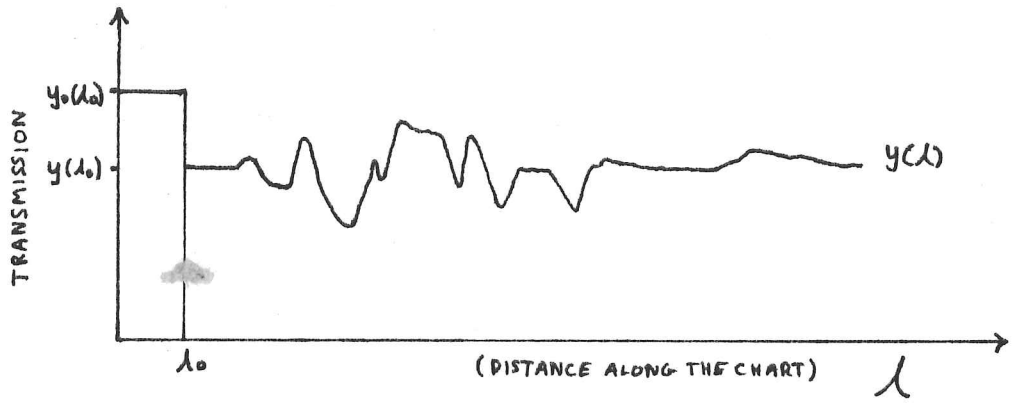

Fig.4.8

ratiometer output voltage equal to the ratio of the signal at PMT1 to that at PMT2. λ_0 was the wavelength at which the scan began and Yo(λ_0) was the transmission measured without any gas let into the absorption cell. Referring to Fig.4.7 we can define

$$T(\lambda) = I_o / I_o'$$

so that if y is proportional to I (a linear detection system) then

$$\frac{I(\lambda)}{I_0(\lambda)} = \frac{y}{y_0(\lambda)} = \frac{y}{y_0(\lambda_0)} \frac{T(\lambda_0)}{T(\lambda)}$$

and hence

$$\sigma(\lambda) = \frac{2.05}{p} \ln\left[\frac{y_0(\lambda_0)\, T(\lambda)}{y\, T(\lambda_0)}\right] \quad \text{Megabarns}$$

containing quantities all of which have been measured for each gas scanned.

Differential Scattering of Light

Ideally $T(\lambda)$ should have been unity for all wavelengths, but because the light leaving the exit slit of the monochromator was focused some 30cm down the 1m absorption line, subsequent scattering of certain rays off the glass walls occured inevitably. (See Fig.4.12). At longer wavelengths the reflectivity was fairly uniform and high, but at wavelengths shorter than about 800Å the glass reflectivity slowly dropped, probably due to its own dielectric properties and some absorption by materials and gases which were permanently adsorbed onto the glass surface. The latter mechanism almost certainly was the cause of the observed, but temporary decrease in $T(\lambda)$ towards long wavelengths, measured after a lengthy scan with gas in the absorption tube. After a few hours under vacuum, which were needed to outgas the tube walls, a reproducible scan of $T(\lambda)$ could be regained. This temporary absorption effect was of no consequence during a run, however, as any temporary reduction in $T(\lambda)$ merely became an extension of the same absorption of light taking place in the bulk of the gas present simultaneously.

Data Reduction

The long chart-recordings of molecular photoabsorption spectra were digitised at a resolution slightly greater than the noise of the traces, using a Ferranti digitising table which sent x-y coordinates to a casette tape whenever a measurement was desired, while slowly tracing the spectra with the machine's crosshair pointer unit. The data points recorded on casette were entered into files on the Cambridge IBM

370/165 computer. The data were plotted in a more convenient form using the wavelength and pressure calibration already discussed, which required they be divided by a digitised 'best trace' scan of $T(\lambda)$. The complete absolute absorption cross-sections for all the molecules studied over the whole wavelength range available are shown in the following figures. For the reasons given above the absolute cross-sections should be treated as accurate (ie. true) to within about 100%, but contain relative random variations probably less than 20%, reflecting the inaccuracy of the calibration against the Helium absorption edge used as a standard.

Key to the Figures

Fig.4.9 Acetylene: Each curve represents a separate chart. The two longest scans were taken sequentially, as were the three other plots at short wavelengths. The spectra from 1050Å-1100Å were taken immediately after the long scan from 600Å-1200Å. It demonstrates clearly how additional absorption due to adsorption of gas onto the glass walls depressed the calibrating value $T(\lambda)$ used to calculate the absolute cross-section. This interpretation is supported by the similar ranges of relative cross-section within a particular trace, even though the separate traces are considerably displaced from each other by large differences in absolute cross-section. Thus the trace with the largest absolute cross-section could be taken as most accurate if a choice is presented.

Fig.4.10 Carbon Monoxide: Only one long scan was made for this molecule. As the chart was made after the absorption tube had been outgassed overnight the values of cross-section are more likely to be accurate.

Fig.4.11 Water and Deuterium Oxide: Five traces of water spectra are shown from 800Å-1000Å, made with little regard to any outgassing of the system between runs. However, the five spectra of D_2O and H_2O taken at short wavelengths show less displacements relative to each other although a similarly casual attitude was applied to the outgassing. The closer agreement of the traces was due to the much lower absorption of water and D_2O at 380Å, where $T(\lambda)$ was measured. Thus additional adsorption of water onto the glass had little effect and yielded cross-sections which were more consistent than those calibrated at longer wavelengths where adsorption was much more important. The green spectra are those of a water-discharge and contain some features which do not correspond to those of the water spectra in red. The comparison is shown more clearly in Chapter 5 where summed 'average' spectra are presented for water and for water in a discharge. The three discharge traces are much noiser than those of water without a discharge, because of slow destruction of the Salicylate detector by the discharge products (see earlier) and pressure fluctuations in the partial pressures of the absorbing radicles or molecules.

Fig.4.12 Gas-Free Scan: This gave the smoothed function $T(\lambda)$ taken to calculate the absolute absorption cross-sections using the procedure outlined above (Fig. 4.8, and discussion).

Analysis of the molecular absorption spectra is considered in Chapter 5, where the cross-sections are presented as graphs in greater detail or in certain cases as tables of cross-sections against wavelengths. This section concludes the results obtained by conventional photometric absorption techniques at Bonn.

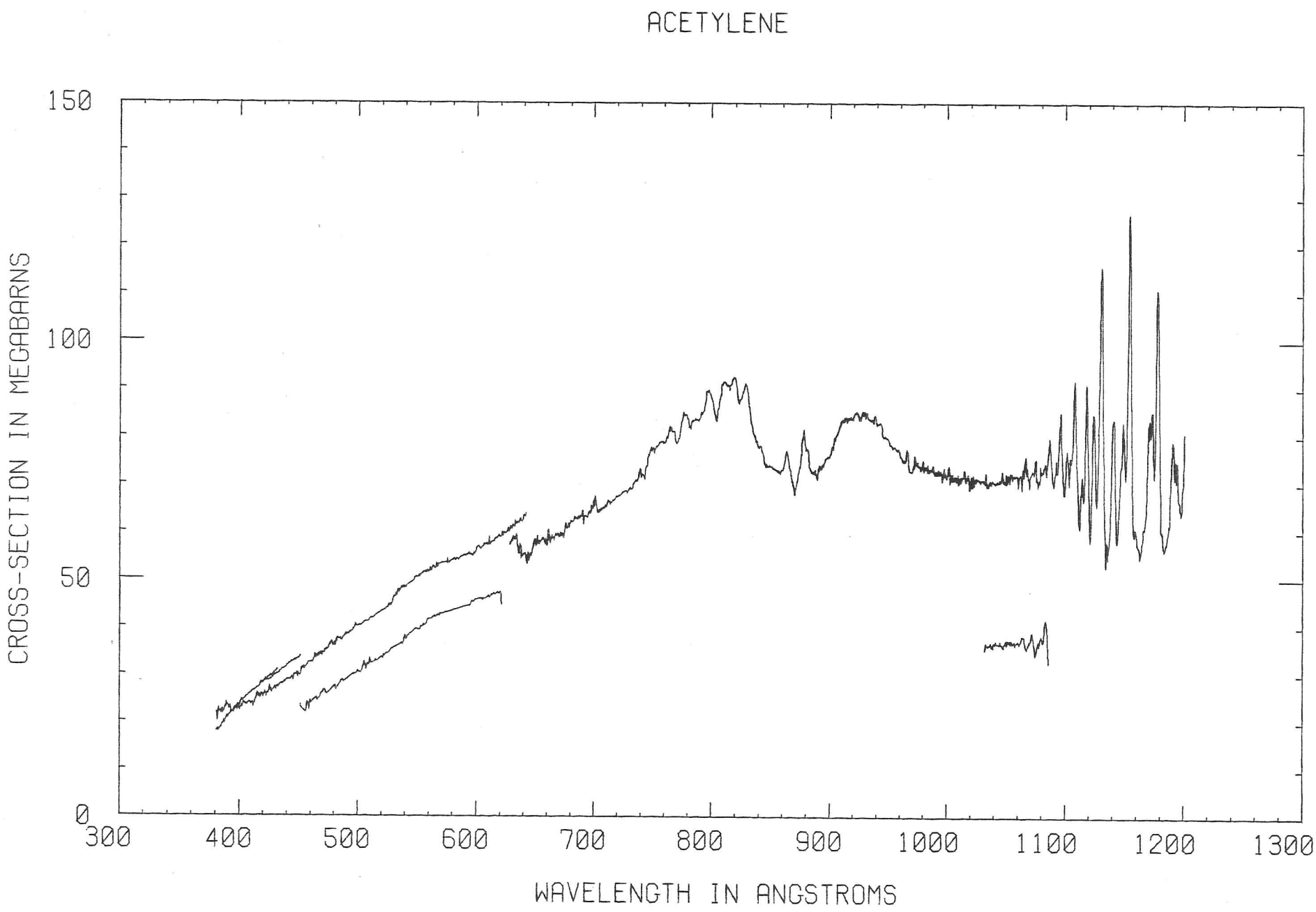
ACETYLENE
150
100
50
0
CROSS-SECTION IN MEGABARNS
300
400
500
600
700
800
900
1000
1100
1200
1300
WAVELENGTH IN ANGSTROMS

Fig.4.9

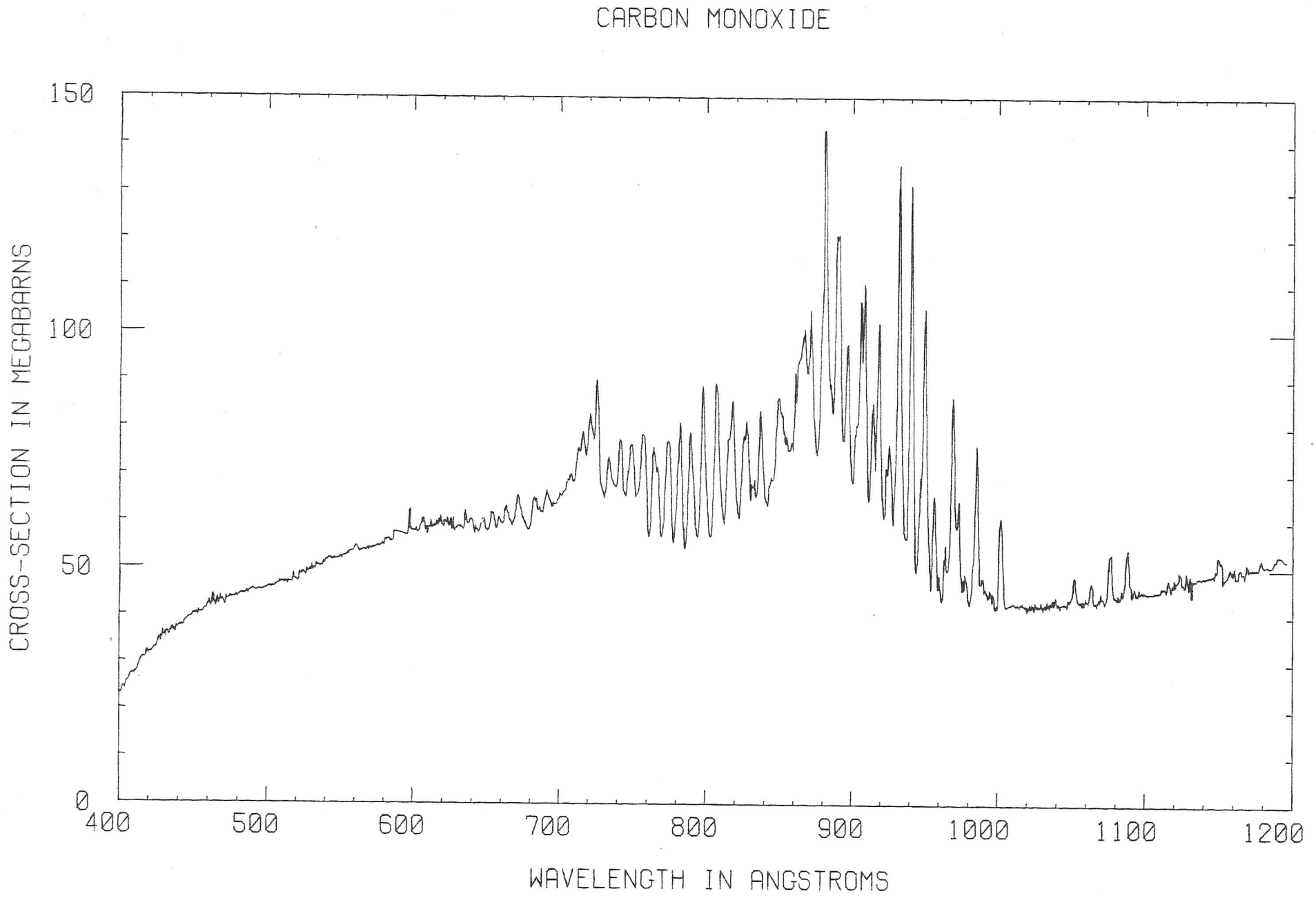
CARBON MONOXIDE
150
100
50
0
CROSS-SECTION IN MEGABARNS
400
500
600
700
800
900
1000
1100
1200
WAVELENGTH IN ANGSTROMS

Fig.4.10

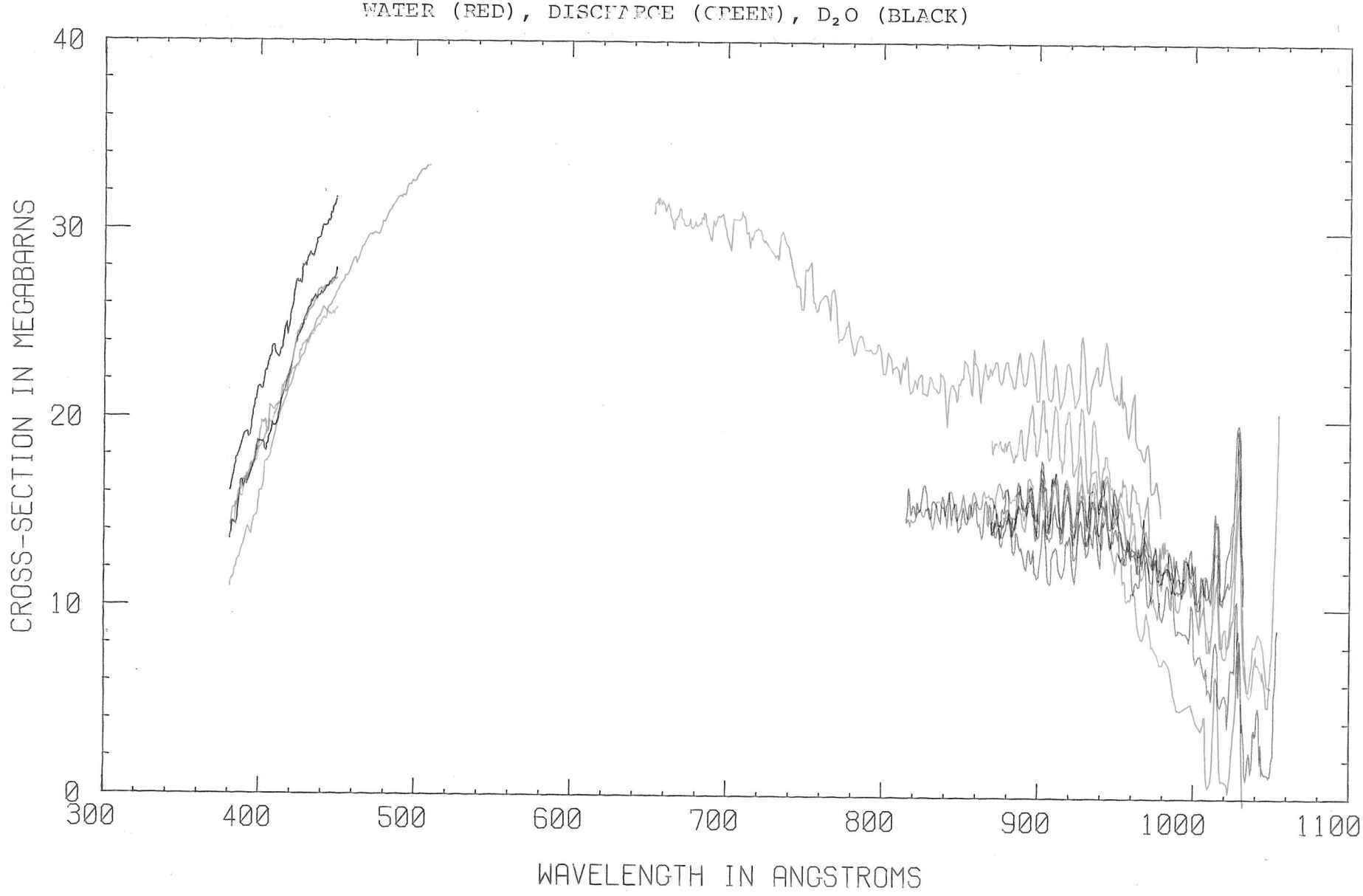
WATER (RED), DISCHARGE (GREEN), D_2O (BLACK)
CROSS-SECTION IN MEGABARNS
40
30
20
10
0
300
400
500
600
700
800
900
1000
1100
WAVELENGTH IN ANGSTROMS

Fig. 4.11

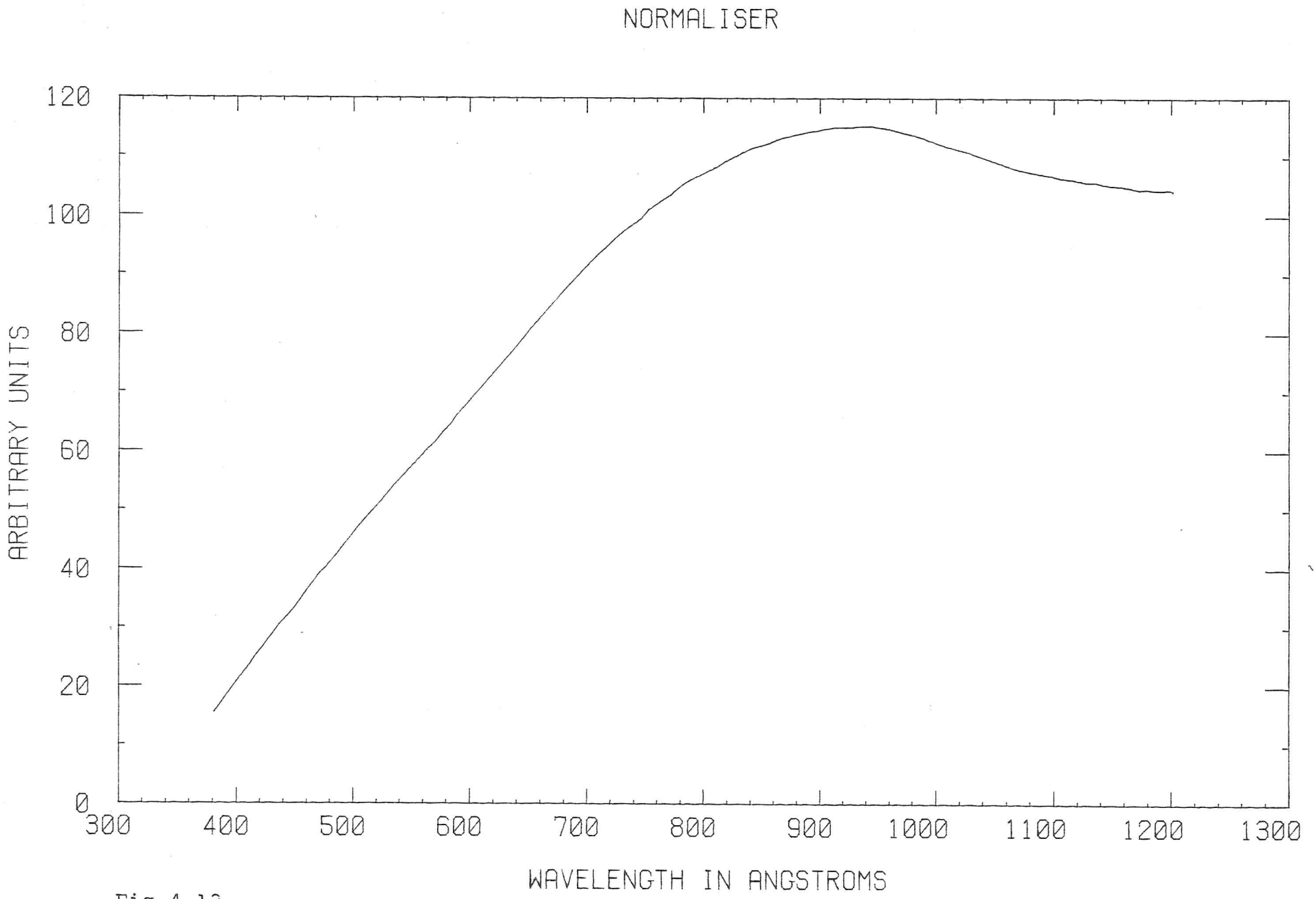
NORMALISER
120
100
80
60
40
20
0
ARBITRARY UNITS
300
400
500
600
700
800
900
1000
1100
1200
1300
WAVELENGTH IN ANGSTROMS

Fig.4.12

Optoacoustic experiments at Bonn

These were attempted as outlined in the first sections of this chapter. Employing slit-widths of 2Å equivalent resolution set on the monochromator at 600Å wavelength no optoacoustic signal could be detected above the acoustic background noise in the Synchrotron Hall, even though photo-ionisation processes in (eg. H_2O) at a pressure of 0.1 Torr caused roughly 90% of the incident synchrotron light to be absorbed in the optoacoustic cell. In a test to see if any optoacoustic signal could be detected, the zero-order light (multi-chromatic) from the monochromator was let into the absorption-cell but still no signal was seen above the background noise, although the number of photons potentially absorbed by such an increase in bandwidth should have provided a great improvement of signal over that of the more monochromatic beam used at 600Å.

The performance of the twin-cell complementary microphone system was seen to reduce detected back-ground acoustic noise by a factor of ten compared to single-cell operation without background subtraction. However, the acoustic background levels observed at the BonnI synchrotron were at least a hundred times greater than those seen in Cambridge (mentioned in Chapter 3); much of the noise was due to 'rumbling' of the synchrotron Bending magnets which caused the elctrons to follow their circular orbits. Unfortunately, the rumble frequency had, inevitably, strong 50Hz acoustic harmonics corresponding to the pulsed 50Hz synchrotron light, which was to be optoacoustically detected by one lock-in amplifier also tuned to this frequency. It was hardly surprising such a specific background harmonic could be detected by the microphones, even after electronic subtraction of their signals from each other to leave only the optoacoustically driven signal.

It was predicted in Chapter 2 that the BonnI synchrotron would not produce enough light to ensure the success of an optoacoustic experiment in the VUV. This proved correct.

However, the potential of the technique remains and if an optoacoustic experiment is attempted at a quieter, brighter radiation source, such as BSRS, the outcome of the experiment might well be different.

CHAPTER 5

Some spectra and absolute cross-sections of H_2O, H_2O in a Discharge (OH), D_2O, C_2H_2, and CO, from 400Å-1200Å.

Introduction

In Chapter 4 the vacuum ultraviolet spectroscopy of the molecules above was described, with the experimental arrangement at the 2.5GeV synchrotron in Bonn outlined in detail. Photoabsorption cross-sections with an absolute accuracy (ie. truth) of $\pm$ 100% and a precision (ie. relative random variations) of $\pm$ 20% in the absorption scales were plotted using the Cambridge IBM 370/165 computer and were presented briefly at the end of the previous chapter.

The spectra obtained from work at Bonn were of variable quality and emphasis, reflecting the particular areas of interest pertaining to each molecule studied. As accurate photoabsorption measurements had been taken already of H_2O over large parts of its spectrum by Gurther et al, (1977), no further effort was made to remeasure the cross-sections. Similarly, interest in the possible assignement of hydroxyl lines in the spectra of a radio frequency discharge in water did not require anything better than relative rather than absolutely correct photoabsorption coefficients. Thus for all the spectra of H_2O and D_2O, which will be presented fully and expanded upon below, there has been no computer readjustment other than that already described to draw the cross-sections. On the other hand, a more general interest in the VUV spectra of C_2H_2 and CO led to the production of a few long and continuous recordings of their photoabsorption cross-sections over the whole wavelength range of the Seya monochromator used. As that region of the spectrum contributes a large part to the summed oscillator strengths of each molecule, the Thomas-Reiche-Kuhn sum-rule (see Chapter 2) could be used to normalise the easily integrated data, which had been digitised already for presentation. Thus for C_2H_2 and CO a Sum Rule analysis has been performed, which includes the ensuing calculation of static dielectric polarisabilities of

both molecules and allows a comparison with other, non-spectroscopic dielectric determinations to provide a check of the data adjustments. Hence, absolute photoabsorption cross-sections are presented in detail for C_2H_2 and CO, to an estimated accuracy of $\pm$ 20%.

The spectra of water and water in a radio frequency discharge: A Rydberg series in OH?

The aim of this particular part of the experiment was to see if features attributed to the hydroxyl radicle by Viney (1980) in the region 800Å-1000Å might be seen in the photoabsorption spectra of water which had been passed through a radio-frequency discharge. The conditions and probable yields of OH were discussed at length in Chapters 3 and 4. The tentative conclusion was that for this experiment an R.F. voltage of about 300V across a tuned, electrodeless discharge in water at pressures of the order 0.5 Torr produced approximately 0.3% hydroxyl along the absorption line, together with almost 50% atomic hydrogen. From very general considerations of oscillator strength and the Thomas-Reiche-Kuhn rule (Chapter 2)

$$\sum_s f_s + \frac{1}{\pi \alpha_0^2 a_0} \int_0^{\lambda_{I.P.}} \frac{\sigma(\lambda)}{\lambda^2} d\lambda = N$$

where f_s are the discrete oscillator strengths, N is the total number of electrons in the system and $\lambda_{I.P.}$ is the 1st ionisation potential, the average absorption cross-section of hydroxyl should be very roughly equal to that of water in the continuum region of the spectrum, where predissociation and autoionisation play a major part in broadening its structure. On the basis of this prediction alone, when taken with the very low yield of hydroxyl present in the absorbing water-vapour, only extremely strong transitions of hydroxyl could possibly have been seen against the already strong absorption of water in the wavelength region referred to by Viney,

above the first ionisation potential of water. These points should apply to all attempts to measure hydroxyl produced from a water discharge by VUV photoabsorption spectroscopy in this wavelength region.

The spectra obtained over many separate wavelength scans from 800Å-1000Å at 2Å resolution are shown in Fig.5.1. The spectra in green were produced with the R.F. discharge in operation; all the scans were made with water pressures of about 0.1 Torr. It is immediately apparent that a large amount of variation and noise was present when the discharge was on, the possible causes of which have already been discussed in Chapter 4. Even the spectra of water alone (red) show marked variation from one scan to the next. Nonetheless it is quite clear that many peaks and valleys occur in the same places from one scan to the next and on this basis certain conclusions can be drawn. To ease their comparison Fig. 5.2 presents the summed red and green traces respectively and Table 5.1 compares the wavelengths of these lines with those seen by other workers for O_2, H_2O and OH.

The wavelength calibration is good to within an angstrom, as is evident from the strong Rydberg $1b_1 \rightarrow nd$ transitions of water when compared to those reported by Gurther et al (1977). Other water transitions published elsewhere by various workers and employing photoabsorption or photoelectron spectroscopy can be seen in Fig.5.2 and occur at the correct wavelengths (Table 5.1). Therefore, it is surprising that the transitions tentatively assigned by Viney (1980) as OH seem to be generally unrelated to those shown here, even though a similar system was used to produce the radicle.

The resolution quoted for Viney's spectra of 0.005Å is almost certainly too good (A. Baig, 1981) and nearer to 0.05Å, but this is of little consequence here. More important is that these lines were assigned on the basis

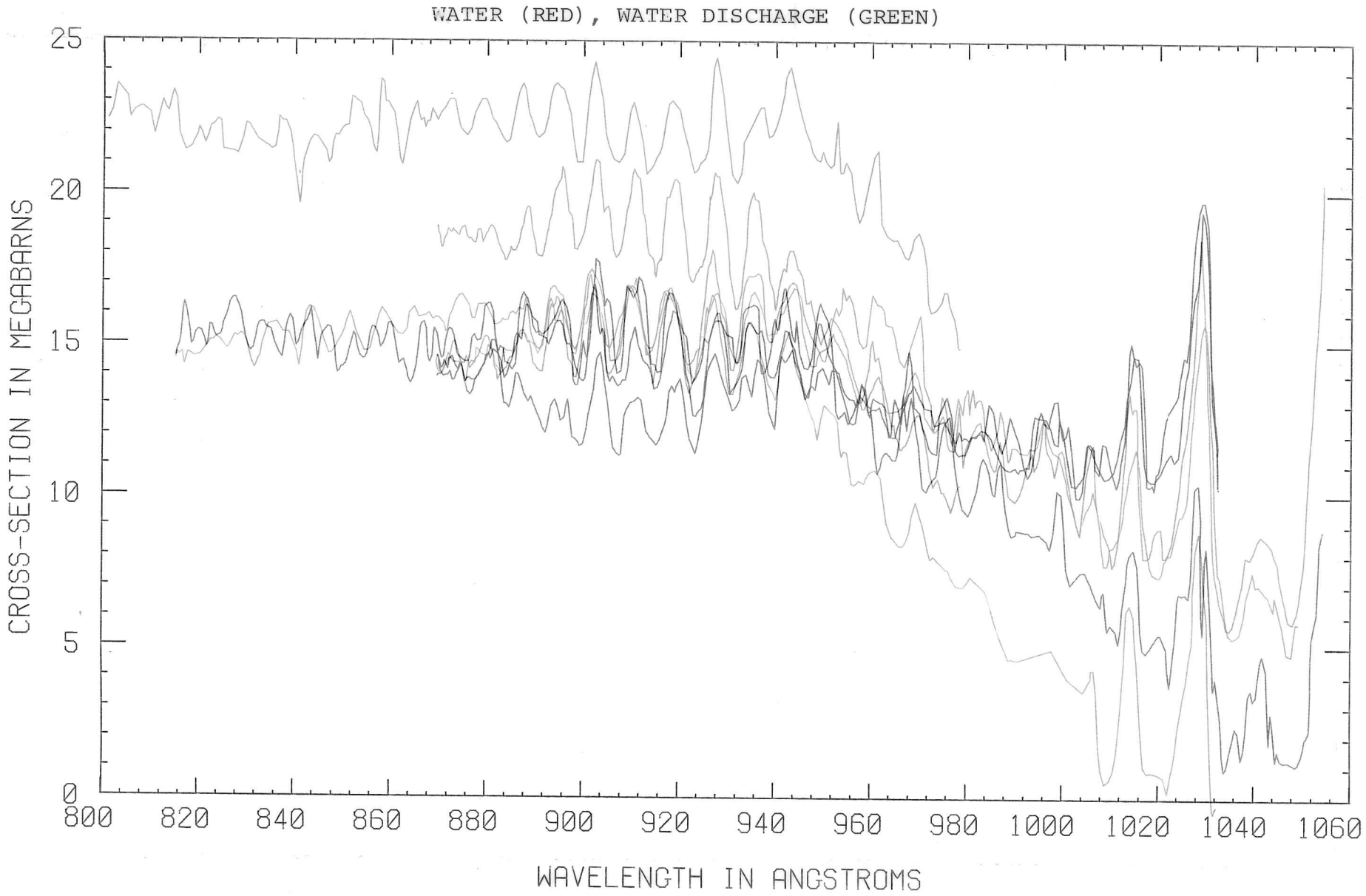
WATER (RED), WATER DISCHARGE (GREEN)
CROSS-SECTION IN MEGABARNS
0
5
10
15
20
25
800
820
840
860
880
900
920
940
960
980
1000
1020
1040
1060
WAVELENGTH IN ANGSTROMS

Fig.5.1

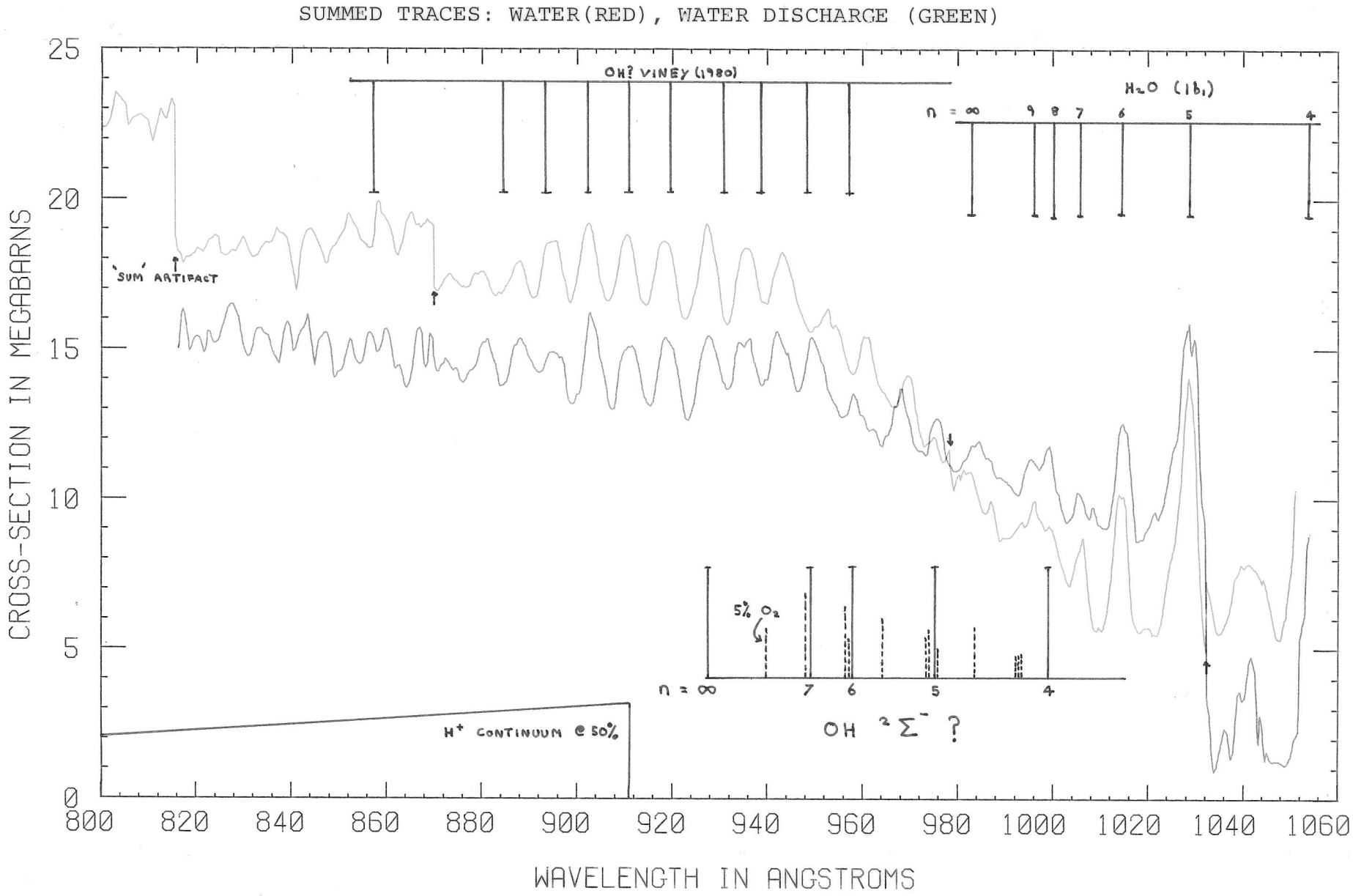
SUMMED TRACES: WATER(RED), WATER DISCHARGE (GREEN)
OH? VINEY (1980)
H₂O (1b₁)
n = ∞ 9 8 7 6 5 4
'SUM' ARTIFACT
5% O₂
n = ∞ 7 6 5 4
OH ²Σ⁻ ?
H⁺ CONTINUUM @ 50%
CROSS-SECTION IN MEGABARNS
0 5 10 15 20 25
800 820 840 860 880 900 920 940 960 980 1000 1020 1040 1060
WAVELENGTH IN ANGSTROMS

Fig. 5.2

H_2O (I.P.982.41Å)					H_2O Discharge (OH)?		O_2 (I.P.1027Å)	
(Å)	(Mb)	(Å)	(Mb)		(Å)	(Å)	(Å)	(Mb)
This work		Gurther et al (1977)			This work	Viney (1980)	Matsunaga et al (1967)	
1028	14.0 (5d)	1028	18	(5d)				
1014	10.2 (6d)	1013	15	(6d)				
1006	8.8 (7d)	1005	15	(7d)	1008			
999	9.0 (8d)	1000	11	(8d)	998 (OH?n=4) A		993.5	24.5
996	10.0 (9d)	996	9	(9d)			993.2	21.6
987	9.9	de Reilhac et al (1977)					992.9	23.4
981	10.8	980.6	16.7		984		983.3	46.1
975	12.1	973.6	15.0		975 (OH?n=5) B		972.9	42.8
969	14.2	968.3	17.7				965.5	51.0
961	15.3	959.7	19.4		958 (OH?n=6) C	956.32	957.0	35.3
953	16.2	952.1	20.2		949 (OH?n=7) D	947.96	955.9	54.7
943	18.2	942.6	24.1				947.7	56.2
935	18.3	934.8	23.5			938.12	939.3	45.0
		933.7	24.3					
927	19.2	926.2	25.4			929.52		
918	18.5	917.5	24.1			918.71		
		916.6	25.7					
910	18.7	910.0	23.2			910.63		
		909.0	24.2					
		908.1	24.0					
902	19.1	900.4	24.2			901.13		
894	18.6	894.4	22.8			892.54		
		892.9	23.7					
887	17.8	885.8	22.6			883.63		
879	17.5	879.0	21.7					
873	17.4	872.3	20.6					
						855.91		

Line Wavelengths and Cross-sections of H_2O, OH? and O_2 (see text). Cross-sections from this work should be used as a comparative guide only. Spectroscopic assignments are shown in parenthesis.

Table 5.1.

that they appeared with a discharge on; but were not present without one. Neither were many of the water lines seen which also lie in this wavelength region, but at the time Viney undertook his work the very clear results of Gurther et al had not been published, so these lines may not have been suspected. Thus, as most of Viney's proposed hydroxyl lines do not seem to easily line up with either the water or the discharge features presented here, their nature and origin must remain obscure.

In fact there are only a few features from this experiment at Bonn which can unambiguously be assigned to the water-discharge alone, because of the large amount of probably random variation. Four peaks which can be picked out above the water valleys when only the discharge was on look much like a Rydberg series. They are indicated as such in Fig. 5.2 with possible alternative strong O_2 absorptions marked alongside. From Chapter 2 a Rydberg series can be expressed by the formula

$$E_n = E_\infty - R/(n-\delta)^2$$

where n is the principle quantum number of a transition, E_n is its engery, δ is the quantum defect, E_∞ is the Series Ionisation potential and R the Rydberg constant. When a calculator 'Best Fit' linear regression program was used to find the ionisation potential of this proposed series, a value of 13.357 ± 0.009eV for the series limit and a selected quantum defect of 0.26 was obtained to give the best line of E_n versus $1/(n-\delta)^2$ (see Fig.5.3). This agrees almost exactly with the only independent measurements of hydroxyl's 1st ionisation potential, by electron impact techniques, the average of which has been given by Wilkinson (1963) as 13.36 ± 0.2eV. The computer programme operated by taking a value of quantum defect , which was then used to calculate the R.M.S. error in the line best representing E_n versus $1/(n-\delta)^2$. The value of δ =0.26, which gave the smallest error in the line was taken to find the I.P. Table 5.2 lists the quantum defects of each transition, required to fit the series perfectly, for the

A possible Rydberg Series for OH and the necessary quantum defects to fit perfectly each line to an I.P. of 13.36+ .01eV, derived from the four lines A,B,C and D. The band system seen by Douglas (1974) near 1222Å with T_o=1222.52Å for his assignment

$$A\,^2\Sigma^- \text{——} X\,^2\Pi$$

is included to show the quantum defect it should have if it is the first member of the series with n=3.

	n	λ(A)	E(eV)	$n-\delta$	δ
I.P.	∞	928.2	13.357	∞	-
A	7	949	13.064	6.814	0.19
B	6	958	12.942	5.726	0.27
C	5	975	12.716	4.604	0.39
D	4	998	12.423	3.817	0.18
$^2\Sigma^-$	3	1222.52	10.142	2.057	0.94

Table 5.2

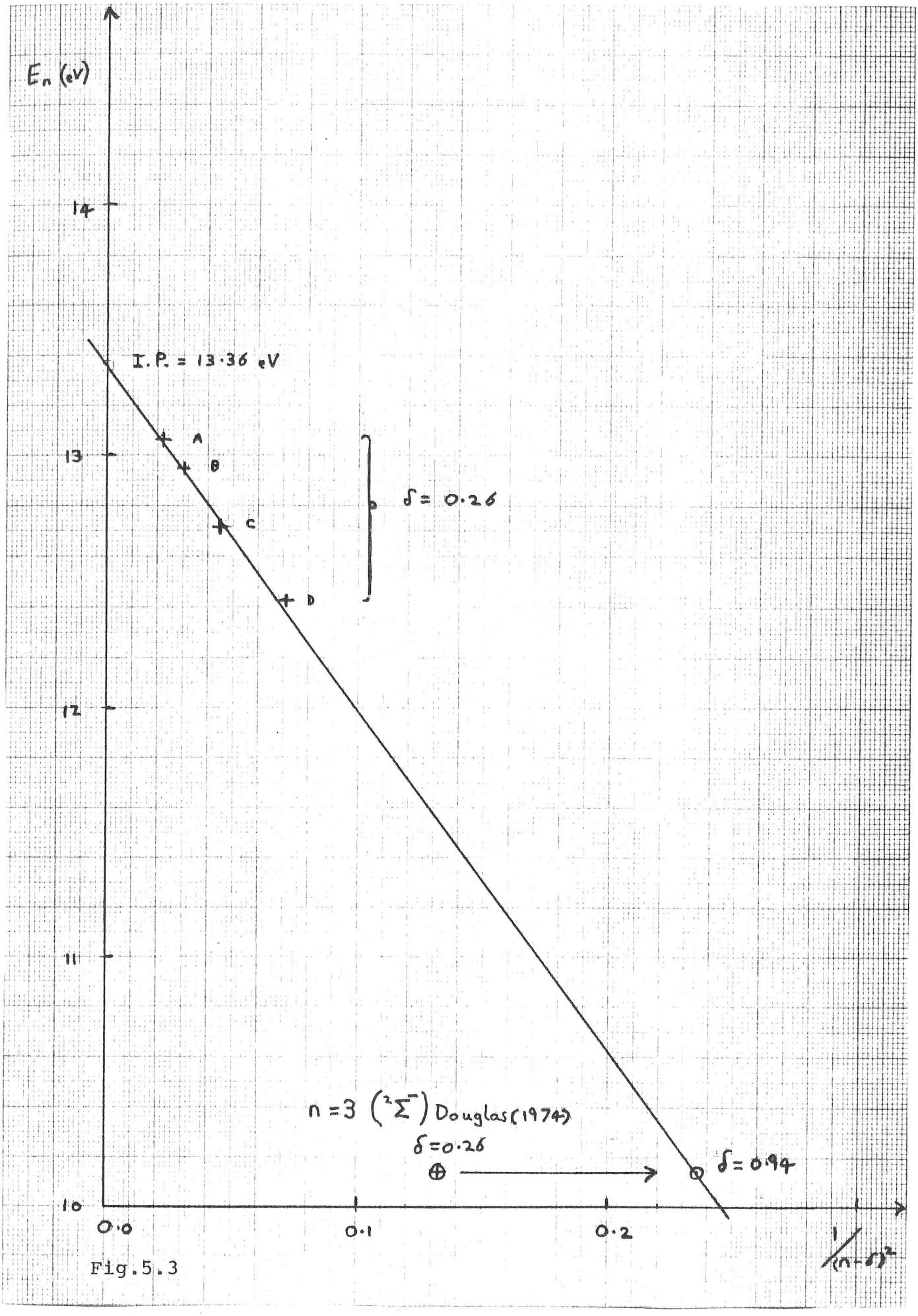
E_n (eV)
14
13
12
11
10
I.P. = 13·36 eV
A
B
C
D
δ = 0·26
n = 3 ($^2\Sigma^-$) Douglas (1974)
δ = 0·26
δ = 0·94
0·0
0·1
0·2
$\frac{1}{(n-\delta)^2}$

Fig.5.3

ionisation potential 13.36eV.

Can these features be due to Hydroxyl?

Douglas (1974) identified strong absorption bands of OH near 1222.5Å in high resolution and assigned the upper electronic state as a $^2\Sigma^-$ Rydberg orbital. He reported that the spectra were visible in absorption when the strong $A^2\Sigma - X^2\Pi$ (3060Å) band system could not be observed spectrographically, implying that the oscillator strength of the new state was much larger than the value of about 0.001 measured elsewhere for the A-X system. Therefore, it is possible that the $^2\Sigma^-$ state, consisting of a Rydberg orbital built on the $^3\Sigma^-$ core of OH^+ is the first member of the necessarily strong Rydberg series suggested by Fig. 5.2. The Rydberg lines assigned here are tabulated in Table 5.2, together with the Rydberg band seen by Douglas (1974); no attempt was made to include the n =3 $^2\Sigma^-$ state in the 'best fit' procedure described above. Using the ionisation potential of 13.3eV Douglas's band must have a quantum defect of 0.94 to fit the series given here.

From Table 5.2 it can be seen that the quantum defect generally decreases with increasing n except for an anomaly at n=4, with a fairly typical quantum defect of 0.9 for the lower lying n=3 state seen by Douglas; a similar defect had already been guessed by him when he assigned the $^2\Sigma^-$ state. Overall, the justification for a Rydberg series is quite good, but certainly not perfect when the non-uniform quantum defects are considered. However, this non-ideal situation is quite common to molecular Rydberg systems where many multi-electronic interactions can occur near the core of the molecule's non-Central Field, consequently disturbing the otherwise simple Rydberg behaviour of low lying energy levels with low principle quantum numbers. (Lu and Fano, 1970).

By far the most likely alternative to the assignment of the meagre lines seen in Fig.5.2 is that another, more abundant discharge product is causing the absorption. Atomic hydrogen is probably the most abundant product, as discussed in Chapter 4, and may be present in a concentration of nearly 50%, but surprisingly its absorption edge cannot be seen in Fig.5.2, starting at 911Å. With an abundance of 50% the threshold continuum absorption of hydrogen should been seen at an equivalent level of about 3Mb in Fig. 5.2 (allowing for the water normalisation of the cross-sections), trailing off from the ionisation threshold of 911Å towards shorter wavelengths; however neither has the edge been seen by other workers (Berkowitz, 1979 or Viney, 1979). Molecular hydrogen was observed by Viney (1979) in water discharge products below 835Å, but H_2 is not a strong absorber at longer wavelengths and therefore can be ruled out as a possible absorber in the region above 920Å. After atomic hydrogen and water, the most abundant species could be O_2; it is known that very little atomic oxygen can be present (Kaufman et al,1961) because of the absence of an air glow further down-stream. Viney (1979) recognised O_2 absorption from 1000Å-965Å in his water discharge products and quite clearly some of these lines lie very close to the 'discharge transitions' spotted in Fig.5.2. Only a rough estimate of O_2 concentration can be made, if its production from the decomposition of H_2O_2 is assumed to be the major source (Oldenberg, 1935). When no metal is present H_2O_2 can form as much as 50% of the discharge products (Rodebush, 1933); this was not the case here and a lower concentration due to its catalytic decomposition probably held. If a guess of 5% O_2 is assumed then the anticipated equivalent oxygen absorption cross-sections can be plotted, using other published data for O_2 (Matsunaga and Watanabe, 1967).

The strongest lines are shown to scale dotted-in alongside the identified discharge features in Fig.5.2. It appears that three of the features, assigned as n=5, 6, 7 might at least be broadened by strong O_2 lines, but the lines do not

coincide exactly with the discharge peaks. With some imagination other O_2 features can also be identified in the discharge spectra through all the noise, but the exercise is risky and might be misleading. As well as O_2, H_2O_2 or HO_2 might also have to be considered, but at present their spectra are not known below 1200Å.

Finally, a rough estimate of the oscillator strength can be deduced as a check if the line designated as n=4 really does arise from hydroxyl and has not been overlaid by other absorbers.

From Chapter 3 the oscillator strength of a transition f is roughly related to its width $\Delta\nu$ and cross-section $\bar{\sigma}$ by the expression

$$f = \left(\frac{4\,\varepsilon_0\, m\, c}{e^2}\right) \bar{\sigma}\,\Delta\nu$$

In this case σ must be about (2/0.3%) Mb when a yield of 0.3% OH is assumed. Hence we obtain $f \sim 0.15$ for a width of 2Å at a wavelength of 1000Å. The value is typical of strong, discrete transitions in molecules below the ionisation potential, where the discrete sum $\sum_i f_i$ over all the sub-ionisation states is generally between 1 and 2 for most simple molecules. It should be noted that if the n=4 line is assigned to hydroxyl it is likely to be broadened by predissociation ($D_0 = 4.395_{eV}$ Herzberg, 1957), as is supported by its apparent width and its vibration-rotation structure determined for the n=3 $^2\Sigma^-$ state by Douglas. Unfortunately, the spectrographic work of Douglas gives us little indication of his Rydberg level's oscillator strength to make a comparison with the estimate above; only his observation that the new state was visible in absorption when the $^2\Sigma^+ - ^2\Pi$ system was not, suggests that the Rydberg oscillator strength must be much greater than 0.001 corresponding to the $^2\Sigma^+ - ^2\Pi$ absorption.

Broad structure in the ionisation continuum of D_2O near 400Å.

Tan et al (1978) have reported photoelectron excitation spectra of the ($2a_1$), inner shell of water, producing an onset of ionisation at about 30eV (413Å) and increasing to a maximum at 32.2eV, , corresponding to the vertical ionisation potential. However, the ($2a_1$) excitation does not appear to have been studied in photoabsorption. This fact, together with the tentative proposal that a two-electron or inner shell excitation might be visible in the region at 415Å (Baig, 1981) suggested a brief look at water near these wavelengths might prove productive, especially as the Seya monochromator at the Bonn 2.5GeV synchrotron still passed sufficient radiation intensity for measurements to be made down to 390Å, at which point the grating and mirrors began to seriously diminish the reflected light.

The water molecule has in its electronic ground state C_{2v} symmetry and an electron configuration $(1a_1)^2$ $(2a_1)^2$ $(1b_2)^2$ $(3a_1)^2$ $(1b_1)^2$.

The first two orbitals $(1a_1)^2$ $(2a_1)^2$ are essentially the filled $(1S)^2$ $(2S)^2$ inner shells of atomic oxygen, while the three remaining orbitals have O 2p character. Transitions from the three outermost orbitals occur up to energies of 17eV (730Å) and have been studied carefully in photoabsorption by Gurther et al (1977). Table 5.3 summarises the experimentally observed energies for single excitation of each of these orbitals (Berkowitz, 1979).

Orbital	Adiabatic I.P/(eV)	Vertical I.P.(eV)
$1b_1$	12.615	12.615
$3a_1$	13.839	14.745
$1b_2$	17.189	18.51
$2a_1$	~ 30	32.2
$1a_1$		539.7

Table 5.3

Possible two electron excitations above 390Å are

$(3a_1)^{-1}\ (1b_1)^{-1}$	26.45eV	(469Å)
$(1b_2)^{-1}\ (3a_1)^{2}\ (1b_1)^{-1}$	29.804eV	(416Å)
$(1b_2)^{-1}\ (3a_1)^{-1}\ (1b_1)^{2}$	31.028eV	(400Å)

The spectra obtained for H_2O and D_2O between 380Å and 450Å are displayed in Fig. 5.4 and the summed spectra in Fig.5.5. The expected position of the $(2a_1)^{-1}$ state and its onset have been dotted in Fig. 5.5. What appears to be a 'window' in the ionisation continuum lies between 410Å-420Å in the spectra of the heavy molecular isotope D_2O, whereas no obvious shape can be associated with H_2O, or in the region of the $(2a_1)^{-1}$ vertical ionisation potential. Since the spectra are quite noisy any further identification of features would probably be misleading.

A possible explanation for the diminished absorption at 415Å in D_2O is that it might be the consequence of a strong continuum interaction with the $(1b_2)^{-1}\ (1b_1)^{-1}$ excited state, in conjunction with a weak transition matrix element between these states and the ground configuration with the ensuing repulsion of nearby rapid transitions to the continuum, thus forming a resonance 'window'. A good example of this mechanism was shown in Chapter 4 for Argon, where a single inner shell excitation from the (3S) shell to the 4_p Rydberg level caused a deep window in the ionisation continuum at 466Å (Fano,1961). In the tentative analysis suggested here a strong configuration or correlation interaction is also required between the $(1b_2)^{-1}$ and the $(1b_1)^{-1}$ excited states to account for the initial two-electron excitation and in this respect the heavy-water case is distinctly different from the example taken from Argon. It is strange that the same considerations do not apply to the spectra of light water, which seem to show a smooth continuum at 415Å compared to those of D_2O.

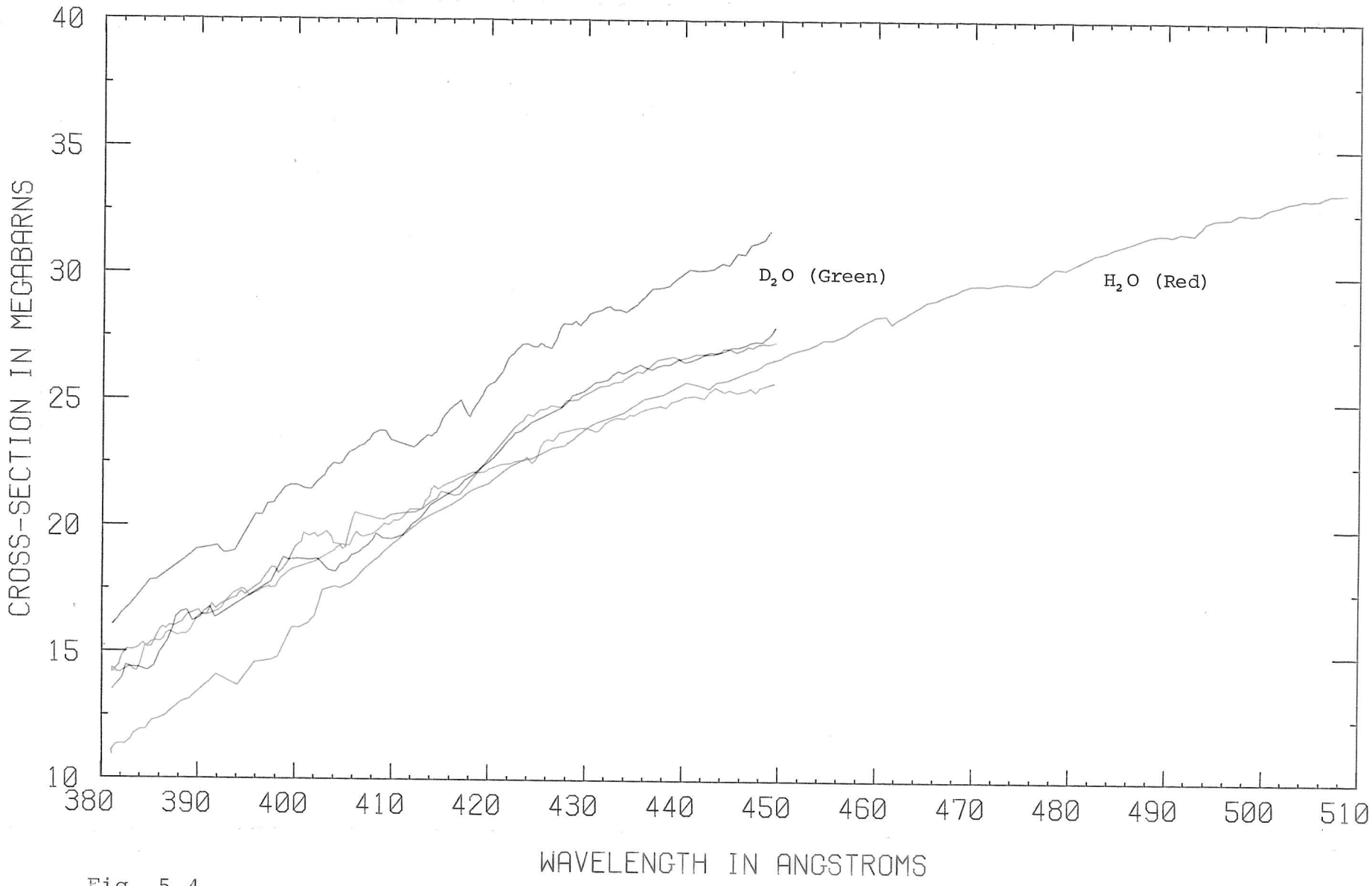
40
35
30
25
20
15
10
CROSS-SECTION IN MEGABARNS
D_2O (Green)
H_2O (Red)
380
390
400
410
420
430
440
450
460
470
480
490
500
510
WAVELENGTH IN ANGSTROMS

Fig. 5.4

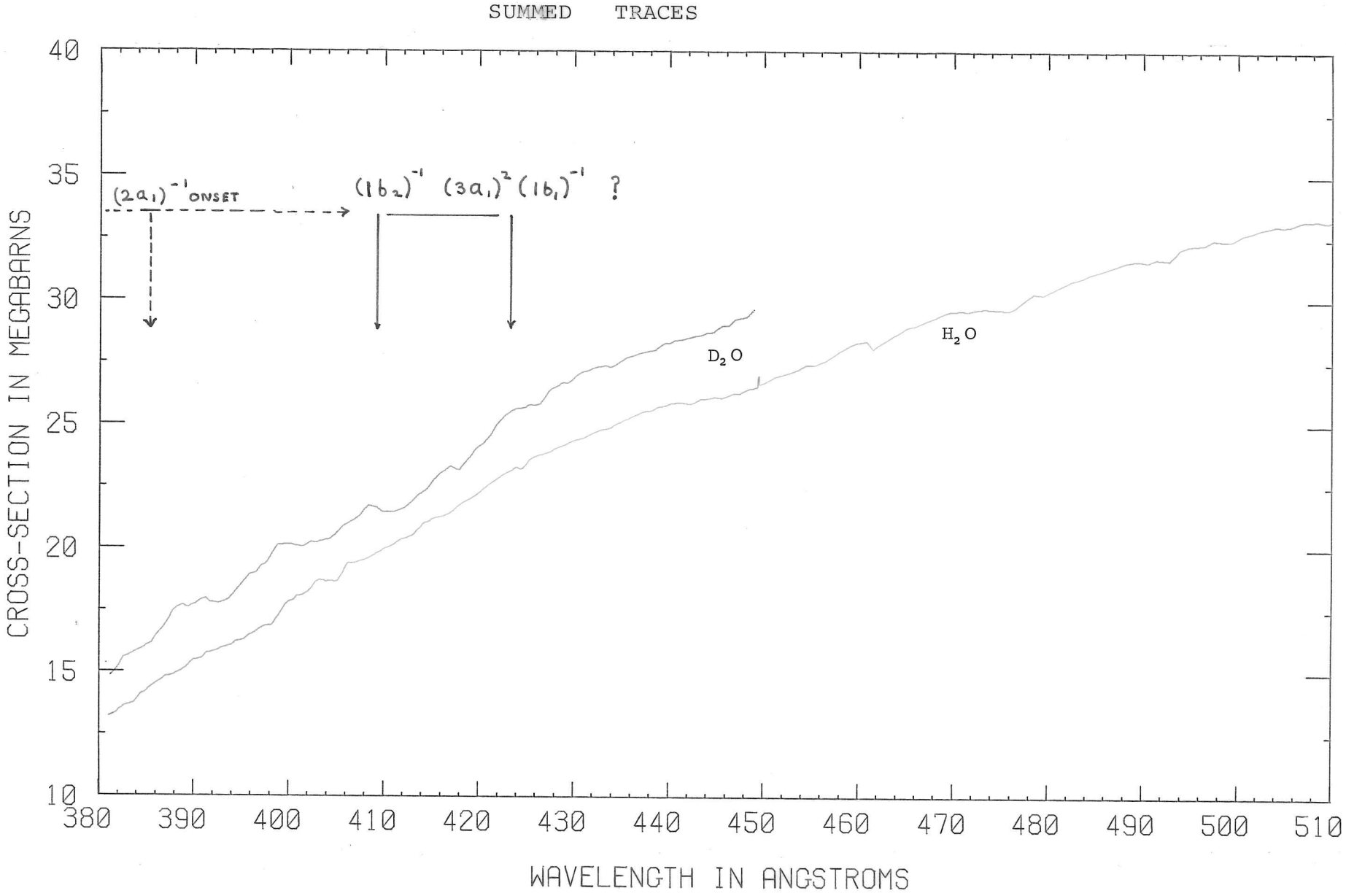
SUMMED TRACES
40
35
30
25
20
15
10
CROSS-SECTION IN MEGABARNS
$(2a_1)^{-1}$ ONSET
$(1b_2)^{-1}$ $(3a_1)^2$ $(1b_1)^{-1}$?
D_2O
H_2O
380
390
400
410
420
430
440
450
460
470
480
490
500
510
WAVELENGTH IN ANGSTROMS

Fig. 5.5

Sum Rule normalisation of C_2H_2 and CO photoabsorption spectra

The photoabsorption spectra of C_2H_2 and CO displayed briefly in the previous chapter are generally larger in absolute cross-section than overlapping values reported by Metzger and Cook (1963), Lee et al (1969) and Berkowitz (1979). The discrepancy is as much as a factor of two, as had been anticipated earlier, since the pressure gradient of the differential pumping used at Bonn could not be easily calibrated, but there seems to be no reason why the relative cross-sections should be much less accurate than $\pm$ 20% if pressure variations during a wavelength scan are considered to be the major source of error. It therefore seems reasonable that the data can be normalised using the measured cross-sections of C_2H_2 and CO above their 1st ionisation potential, together with the Thomas-Reiche-Kuhn rule, if the cross-section sums in the remaining regions of the spectrum are already known to a similar degree of accuracy, as happens to be the case. Berkowitz (1979) defines the following sum Rules (in c.g.s. units); for their discussion see Chapter 2.

1) $$S(0) = \sum_s f_s + \frac{1}{\pi \alpha_0^2 a_0} \int_0^{\lambda_0} \frac{\sigma(\lambda)\, d\lambda}{\lambda^2}$$

$$= N$$

2) $$S(-2) = \sum_s \frac{f_s}{E_s^2} + \frac{1}{16 \pi^3 a_0^3} \int_0^{\lambda_0} \sigma(\lambda)\, d\lambda$$

$$= \frac{\alpha_N}{4 a_0^3}$$

In the formulae α_0 is the fine-structure constant, a_0 the Bohr radius, λ_0 the 1st Ionisation Potential of the

molecule and f_s the oscillator strength of discrete states below the 1st I.P.

The first sum S(o) represents the Thomas-Reiche-Kuhn Rule and is probably the most familiar one. It is straight forward to show (see Chapter 2) that the sum of the discrete and continuum oscillator strengths is equal to the total number of electrons in the molecular system. The second sum S(-2) is directly proportional to α_N the static dielectric polarisability of the molecule, which can be deduced from a variety of experiments, including the Stark effect by microwave and radiofrequency spectroscopy, and dielectric constant or molar refraction determinations.

Clearly, the S(o) sum is most suitable for normalising experimental cross-sections above the 1st I.P., assuming the resolution is sufficient to pick out the generally broader autoionised or predissociated peaks and valleys of the spectra, since the sum is given simply by the number of electrons in the molecule. The procedure is to integrate $\sigma(\lambda)/\lambda^2$ from the 1st I.p. up to the highest energy (shortest wavelength) at which measurements were made. The remaining wavelength region is then integrated to zero wavelength using x-ray and XUV data already given in the literature. In this high-energy region $\sigma(\lambda)$ drops very quickly towards shorter wavelengths, much faster than $1/\lambda^2$, making the integrand tend rapidly to zero. At long wavelengths,below the 1st Ionisation energy, the oscillator strengths are discrete and have been measured quite accurately by many workers in this more accessible part of the spectrum so published data can be used to complete the evaluation of the Sum.

A computer program has been written to evaluate the two Sums for the molecules C_2H_2 and CO, which were measured continuously over the wavelength range 400A-1200A. The results of the calculations are shown in Tables 5.4 and 5.5 using published cross-sections of spectra shown in Berkowitz

Acetylene - C_2H_2

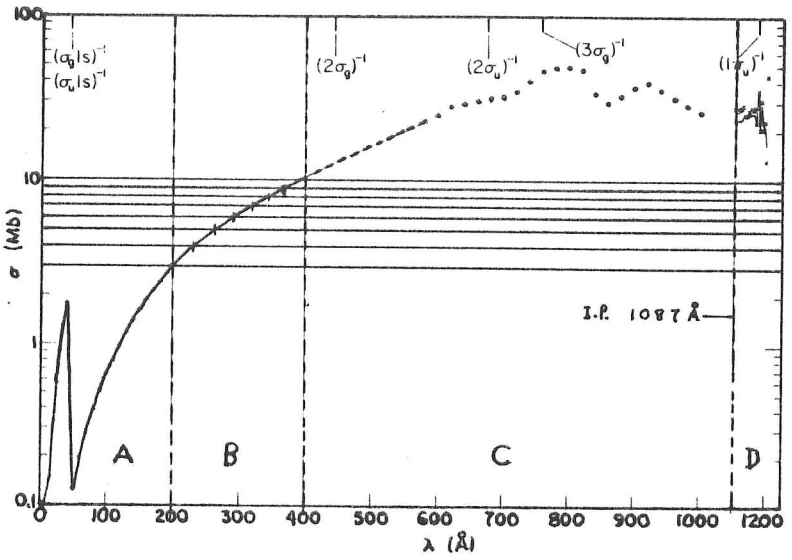

Fig. 5.6
(Berkowitz, 1979)

S(o) and S(-2) are evaluated from data given by Berkowitz (1979) for the regions A and D; with trapezium integration of the data presented in Fig. 5.6 in B. Region C contributes at least 50% to the Sums, which are evaluated there by numerical integration of the measured absorption spectra shown in Fig. 4.9.

Table 5.4

	Wavelength Region	S(o)	S(-2)
A	0 - 200Å	4.9215	0.0294
B	200 - 400Å	1.5776	0.1736
C	400 - 1087Å(I.P.)	10.1889 (6.5446)	6.4780 (4.1608)
D	(discrete) 1087Å(I.P.)	0.9563	1.9576
TOTAL SUMS		17.6443 (14 in theory)	8.6386 (6.3214)

Assume Sums in Region C are too large. If S(o) is adjusted to equal 14 (no. of electrons), the contribution in region C should be scaled by 0.6423 to become 6.5446. To be consistent the measured cross-sections in Fig.4.9 must be reduced by 0.6423 and are then 'Normalised' (see Fig.5.8). Similarly, S(-2) in C reduces to 4.1608 with normalised cross-sections; the new total S(-2) = 6.3214 implies

$$\alpha_N = 3.7 \times 10^{-24} \text{ cm}^3 \text{ (c.g.s.units)}$$

Carbon Monoxide - CO

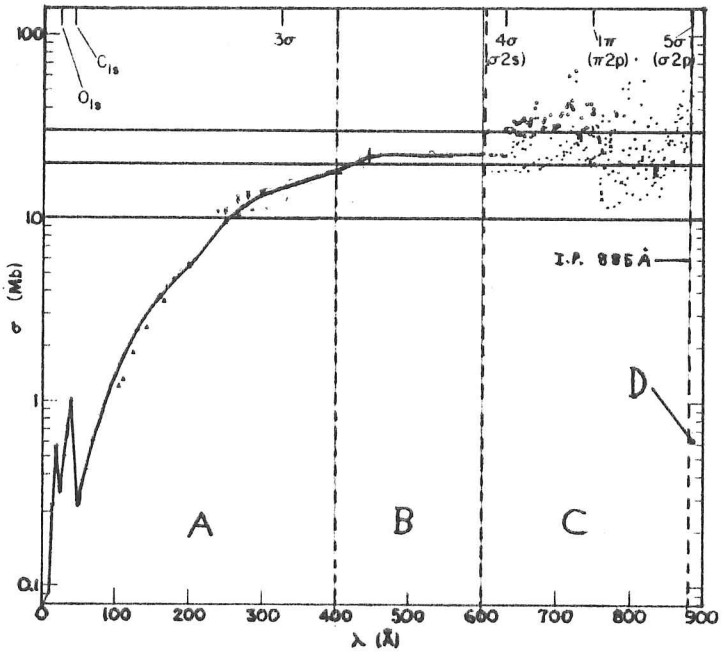

Fig. 5.7
(Berkowitz, 1979)

S(O) and S(-2) sums are evaluated from data given by Berkowitz (1979) for the regions A & D, using trapezium integration of the region B in Fig.5.7 to derive the sums in A, as only sums published for the region 0-600Å are given. Regions B+C are evaluated by numerical integration of the measured spectra shown in Fig. 4.10.

Table 5.5

	Wavelength Region	S(o)	S(-2)
A	0.400Å	9.0557	0.3598
B+C	400-885Å (I.P.)	8.1636 (3.6618)	3.9262 (1.7613)
D (discrete)	> 885Å(I.P.)	1.2825	1.725
	TOTAL SUMS	18.5018 (14 in theory)	6.011 (3.846)

Assume Sums in Region B+C are too large. If S(o) is adjusted to equal 14 (no. of electrons), the contribution in region B+C should be scaled by 0.4486 to become 3.6618. The measured cross-sections in Fig.4.10 are scaled by 0.4486 to become normalised (see Fig.5.13). S(-2) in B+C reduces to 1.7613 with normalised cross-sections; the new total S(-2)= 3.846 implies

$$\alpha_N = 2.2 \times 10^{-24} \text{ cm}^3 \quad \text{(c.g.s.units)}$$

(1979)over the wavelength regions shown in Fig.5.6 and Fig.5.7. It is immediately apparent that the S(o) sums of both CO and C_2H_2 in the region 400Å-1000Å, from measurements at Bonn, are too high by the roughly predicted factor of 2. As this error most likely lies within the pressure measurements and calibrations, and not in the adjustment for selective scattering of synchrotron light, the remedy is to scale the recorded data (rather than use subtractions) by the ratio of the calculated and measured S(o) sums found for this wavelength region. The measured, but now normalised S(-2) Sums in the region 1200Å-400Å lead to the quantities

C_2H_2 : $N = 3.7 \times 10^{-24}$ cm^3 (c.g.s.units)

CO : $N = 2.2 \times 10^{-24}$ cm^3

compared to non-spectroscopic determination for C_2H_2 of 3.33×10^{-24} cm^3 (Hirschfelder,1954); 3.95×10^{-24} cm^3, (Maryott et al,1953); 3.46×10^{-24} cm^3 (Landolt-Bornstein, 1963), and for CO a value of 1.97×10^{-24} cm^3 (Landolt-Bornstein, 1963).

The static dielectric polarisability obtained for C_2H_2 is within 10% of all the experimental values quoted, which were determined by the alternative techniques mentioned above. The good agreement suggests that an absolute accuracy of 20% for the normalised absorption cross-sections of C_2H_2 is a reasonable estimate. In the case of CO, the polarisability derived here is 11% higher than the quantity determined by Landolt and Bornstein (1963), but again the normalised photoabsorption spectra seem to be within 20% of the absolute values. A fair degree of confidence can be placed in the conclusions drawn from these comparisons of polarisability measurements, since the spectra given here contribute 50% or more to the S(-2) sums over the whole wavelength range. Thus normalised and continuous photoabsorption spectra are presented in the next Figures for CO and C_2H_2 with an error of ± 20% in their absolute cross-sections.

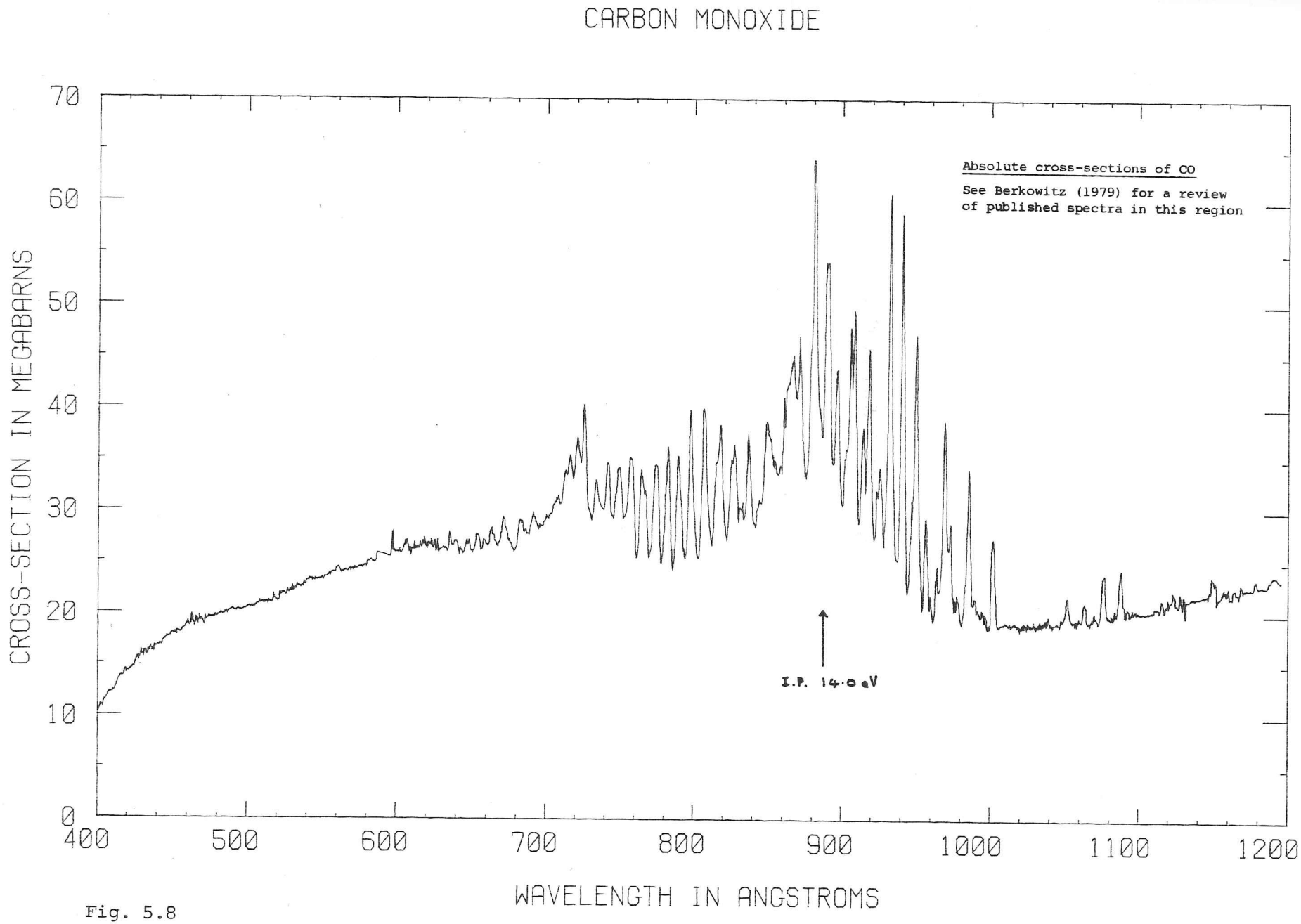
CARBON MONOXIDE
CROSS-SECTION IN MEGABARNS
70
60
50
40
30
20
10
0
400
500
600
700
800
900
1000
1100
1200
WAVELENGTH IN ANGSTROMS
Absolute cross-sections of CO
See Berkowitz (1979) for a review
of published spectra in this region
I.P. 14.0 eV

Fig. 5.8

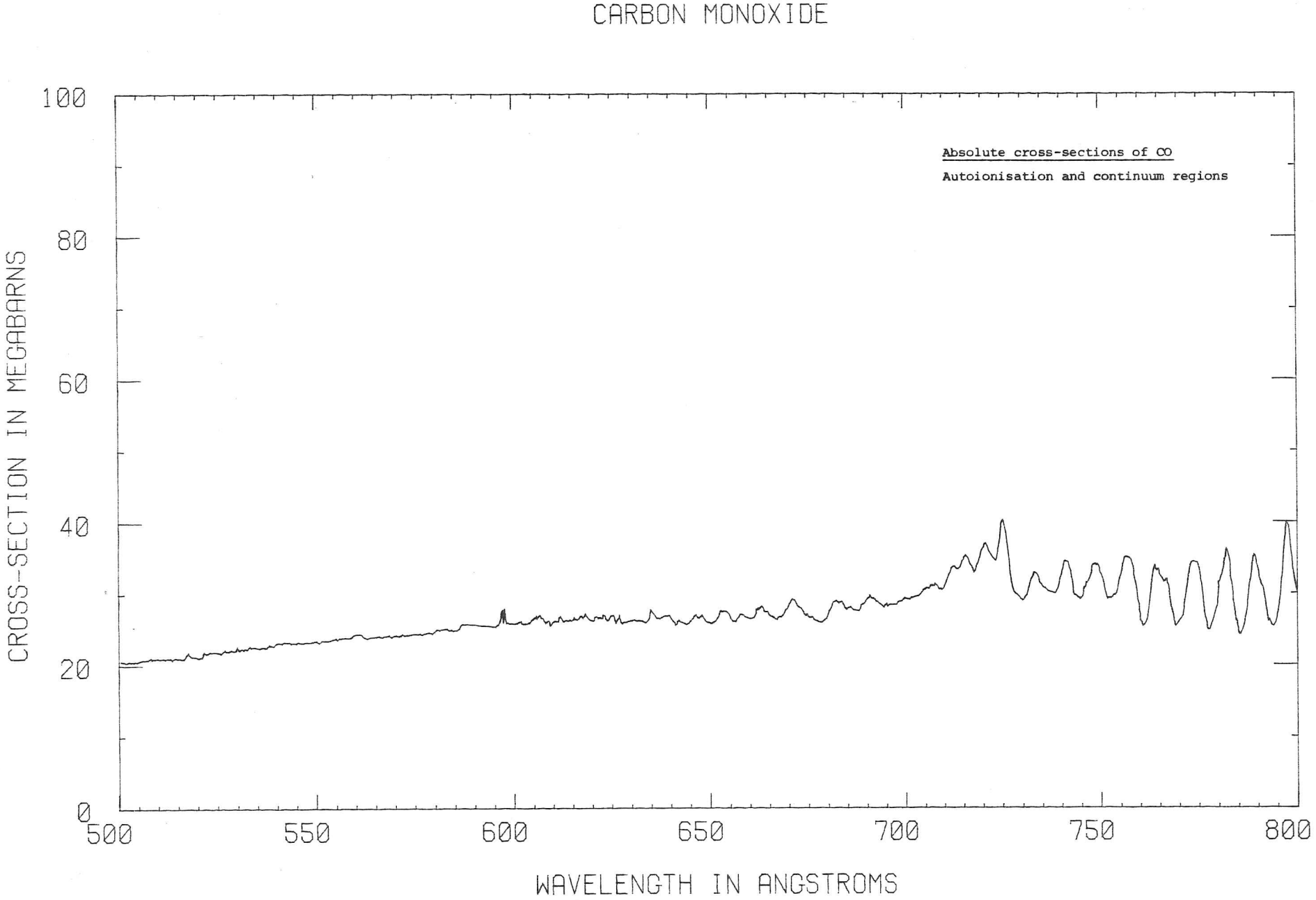
CARBON MONOXIDE
Absolute cross-sections of CO
Autoionisation and continuum regions
CROSS-SECTION IN MEGABARNS
100
80
60
40
20
0
500
550
600
650
700
750
800
WAVELENGTH IN ANGSTROMS

Fig. 5.9

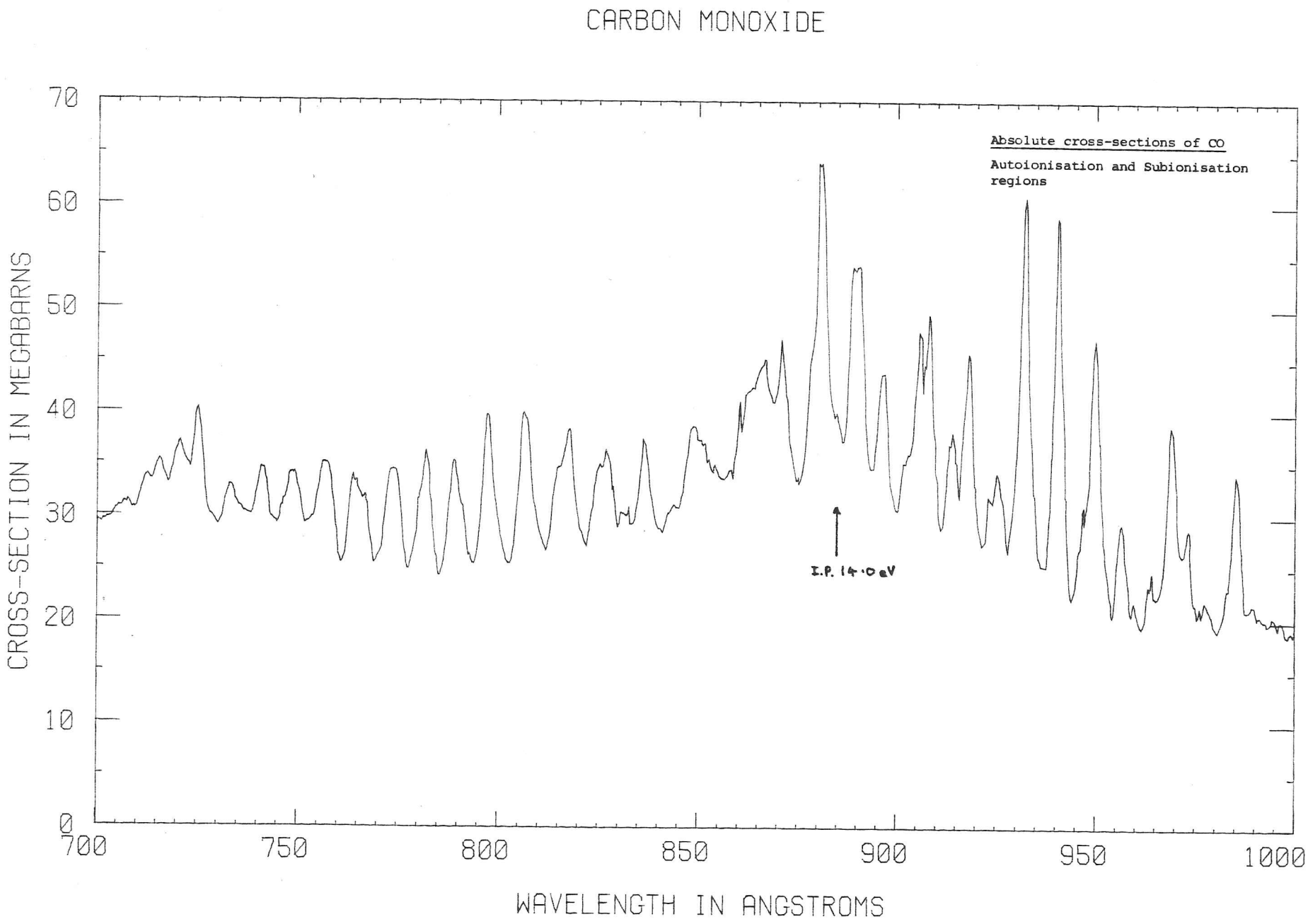
CARBON MONOXIDE
Absolute cross-sections of CO
Autoionisation and Subionisation regions
I.P. 14·0 eV
CROSS-SECTION IN MEGABARNS
WAVELENGTH IN ANGSTROMS
0
10
20
30
40
50
60
70
700
750
800
850
900
950
1000

Fig. 5.10

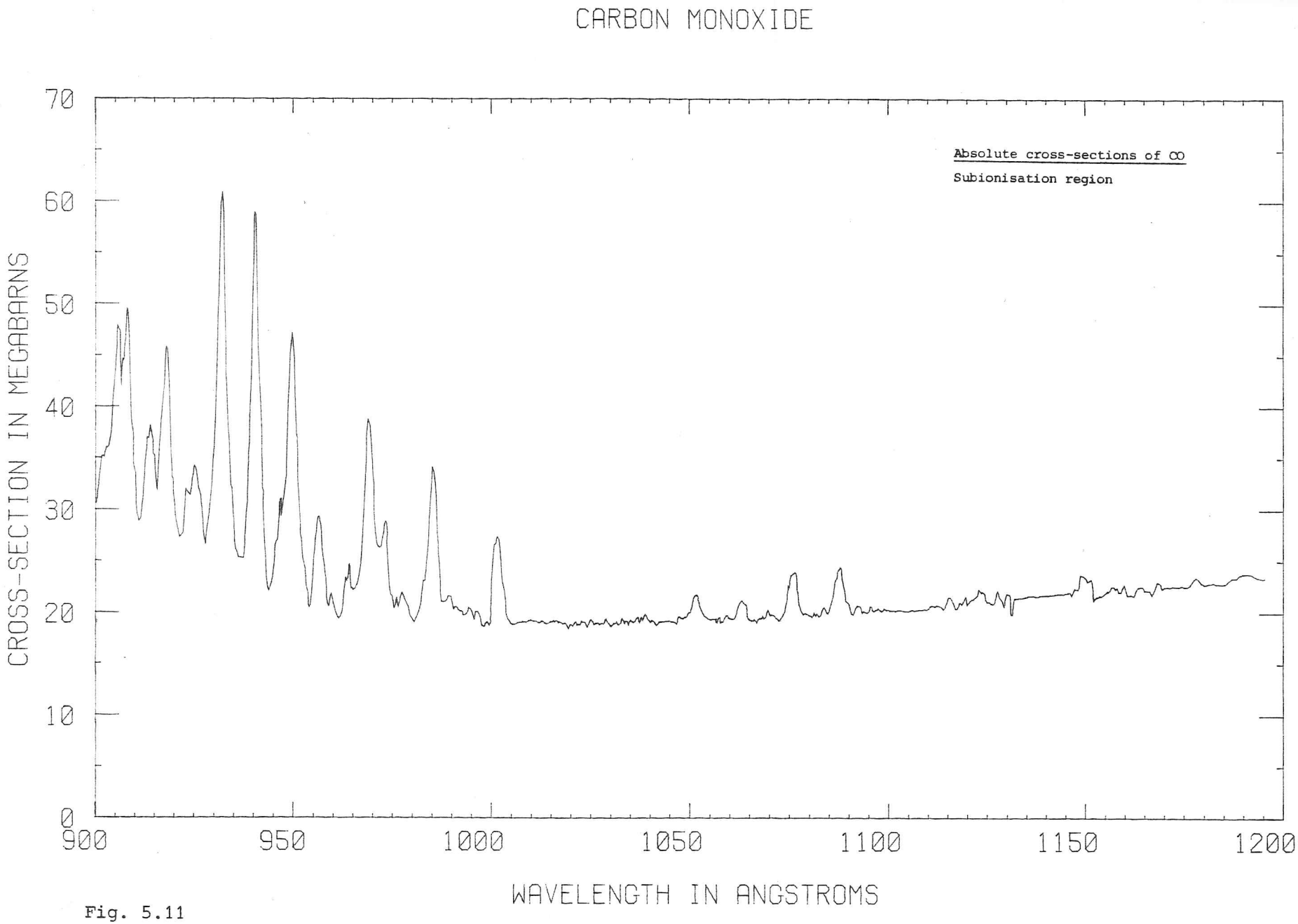
CARBON MONOXIDE
Absolute cross-sections of CO
Subionisation region
CROSS-SECTION IN MEGABARNS
0
10
20
30
40
50
60
70
900
950
1000
1050
1100
1150
1200
WAVELENGTH IN ANGSTROMS

Fig. 5.11

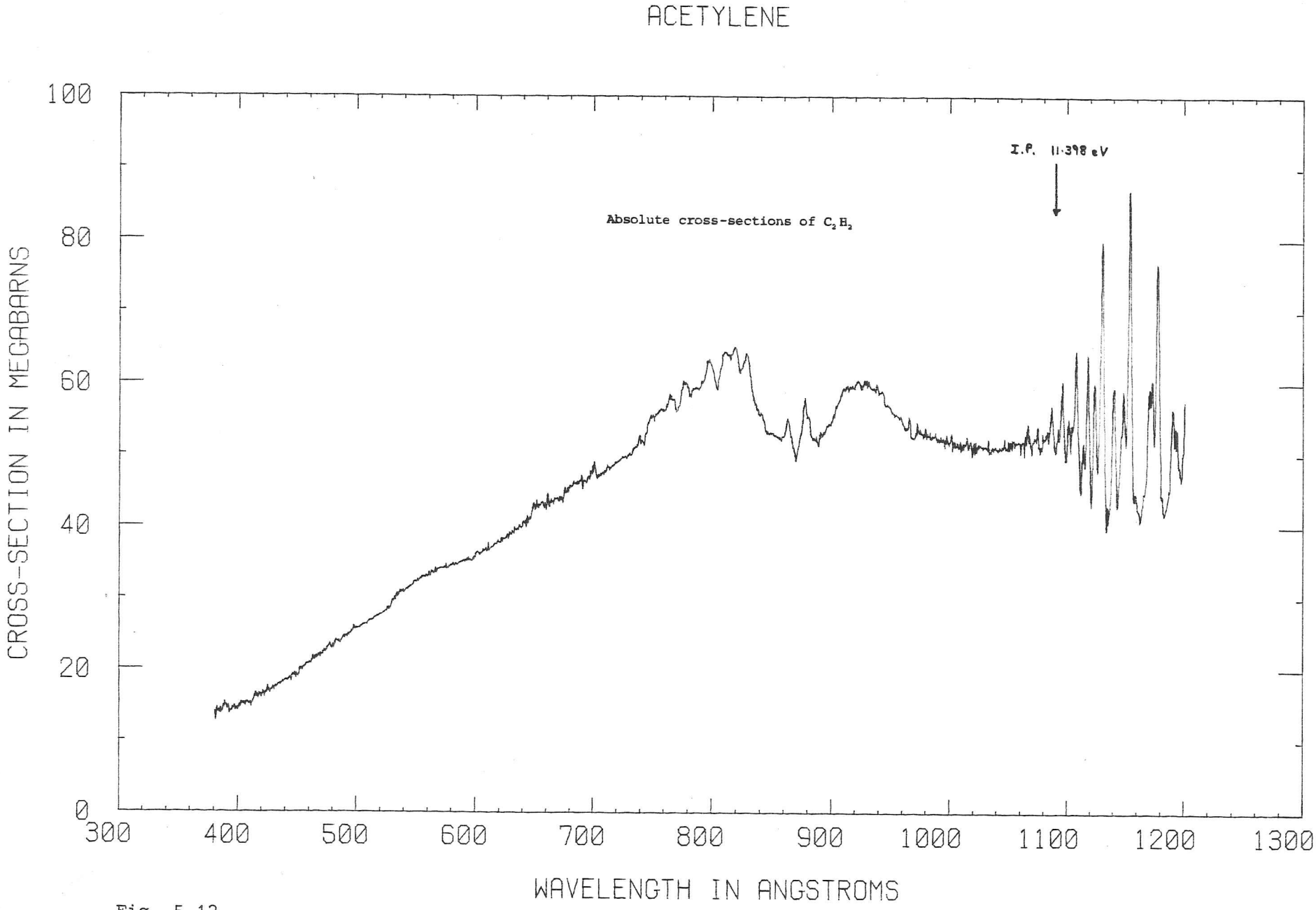
ACETYLENE
I.P. 11.398 eV
Absolute cross-sections of C_2H_2
CROSS-SECTION IN MEGABARNS
0
20
40
60
80
100
300
400
500
600
700
800
900
1000
1100
1200
1300
WAVELENGTH IN ANGSTROMS

Fig. 5.12

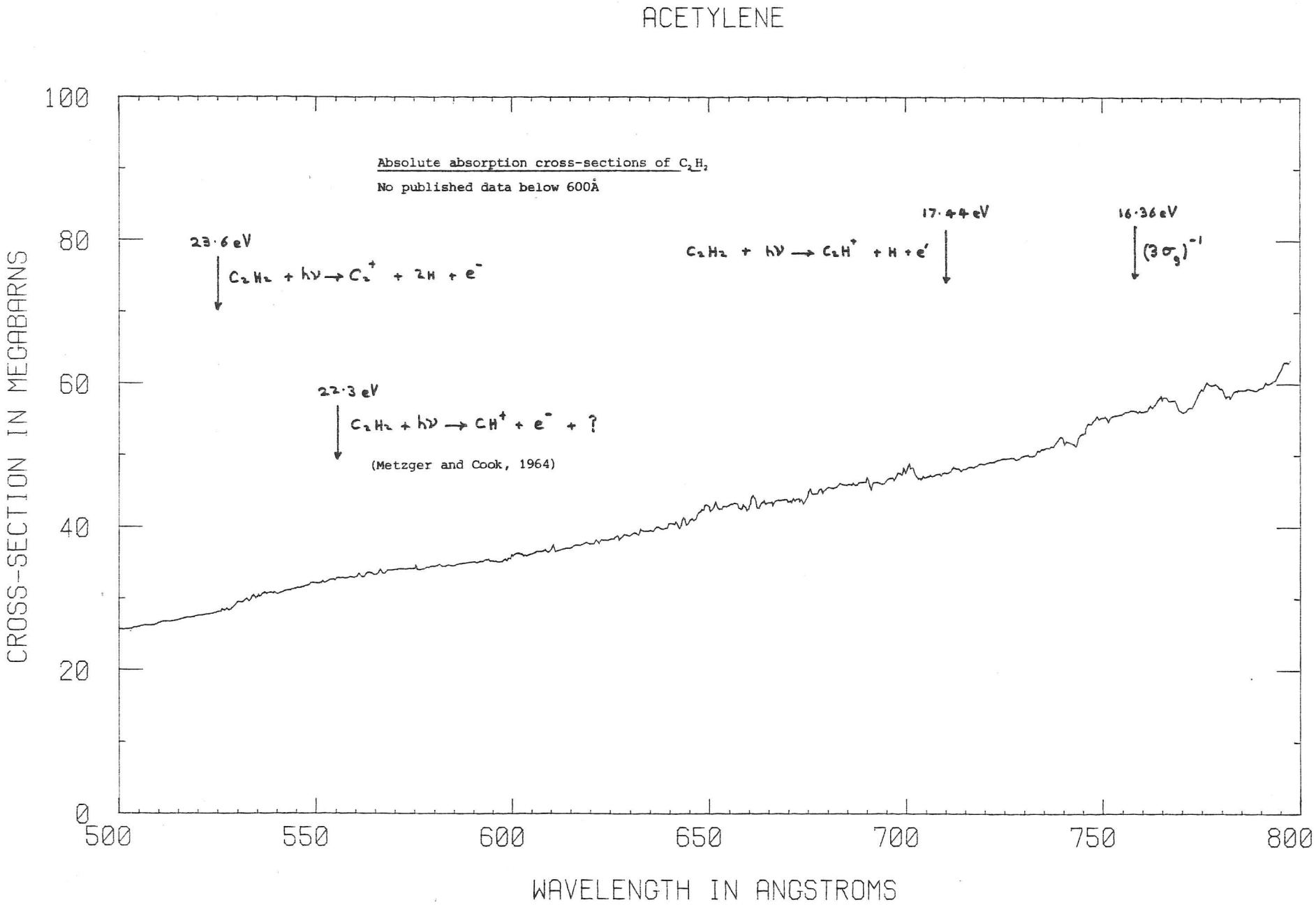
ACETYLENE
Absolute absorption cross-sections of C_2H_2
No published data below 600Å
23·6 eV
$C_2H_2 + h\nu \rightarrow C_2^+ + 2H + e^-$
22·3 eV
$C_2H_2 + h\nu \rightarrow CH^+ + e^- + ?$
(Metzger and Cook, 1964)
17·44 eV
$C_2H_2 + h\nu \rightarrow C_2H^+ + H + e'$
16·36 eV
$(3\sigma_g)^{-1}$
CROSS-SECTION IN MEGABARNS
0
20
40
60
80
100
500
550
600
650
700
750
800
WAVELENGTH IN ANGSTROMS

Fig.5.13

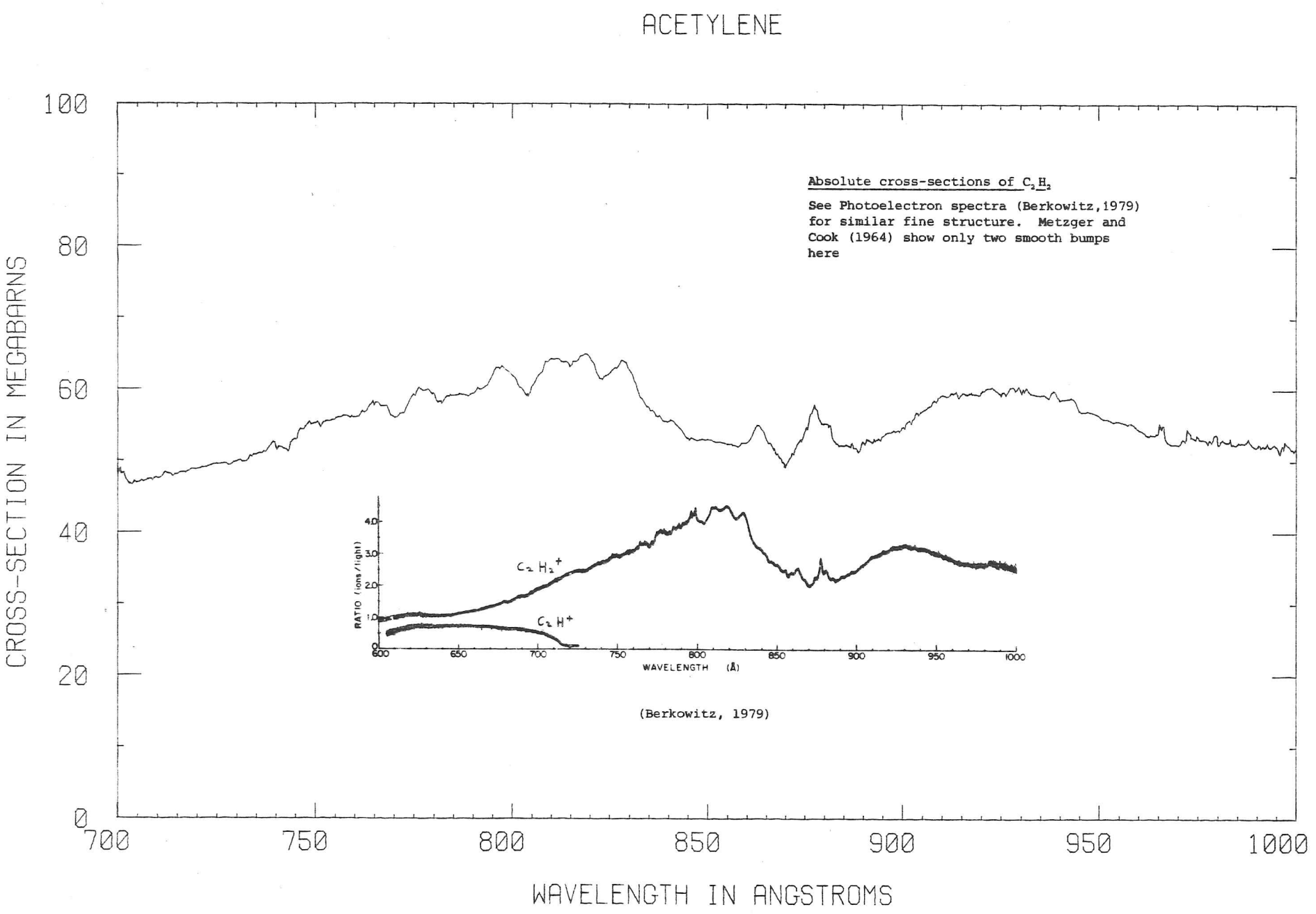
ACETYLENE
CROSS-SECTION IN MEGABARNS
100
80
60
40
20
0
700
750
800
850
900
950
1000
WAVELENGTH IN ANGSTROMS
Absolute cross-sections of C_2H_2
See Photoelectron spectra (Berkowitz,1979) for similar fine structure. Metzger and Cook (1964) show only two smooth bumps here
RATIO (ions/light)
$C_2H_2^+$
C_2H^+
WAVELENGTH (Å)
(Berkowitz, 1979)

Fig. 5.14

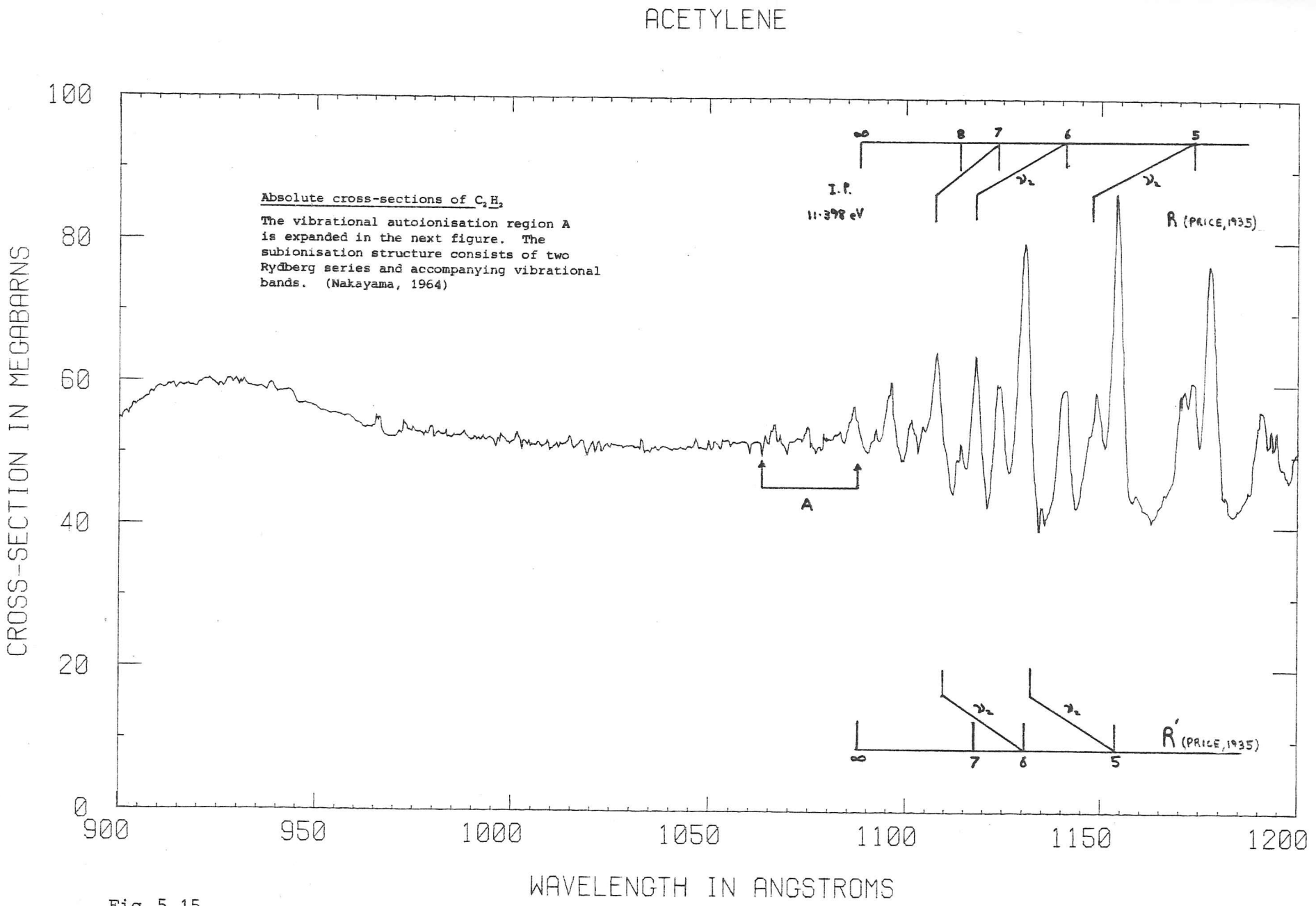
ACETYLENE
Absolute cross-sections of C_2H_2
The vibrational autoionisation region A is expanded in the next figure. The subionisation structure consists of two Rydberg series and accompanying vibrational bands. (Nakayama, 1964)
I.P. 11·398 eV
∞ 8 7 6 5
ν_2
R (PRICE, 1935)
A
R′ (PRICE, 1935)
CROSS-SECTION IN MEGABARNS
0 20 40 60 80 100
900 950 1000 1050 1100 1150 1200
WAVELENGTH IN ANGSTROMS

Fig. 5.15

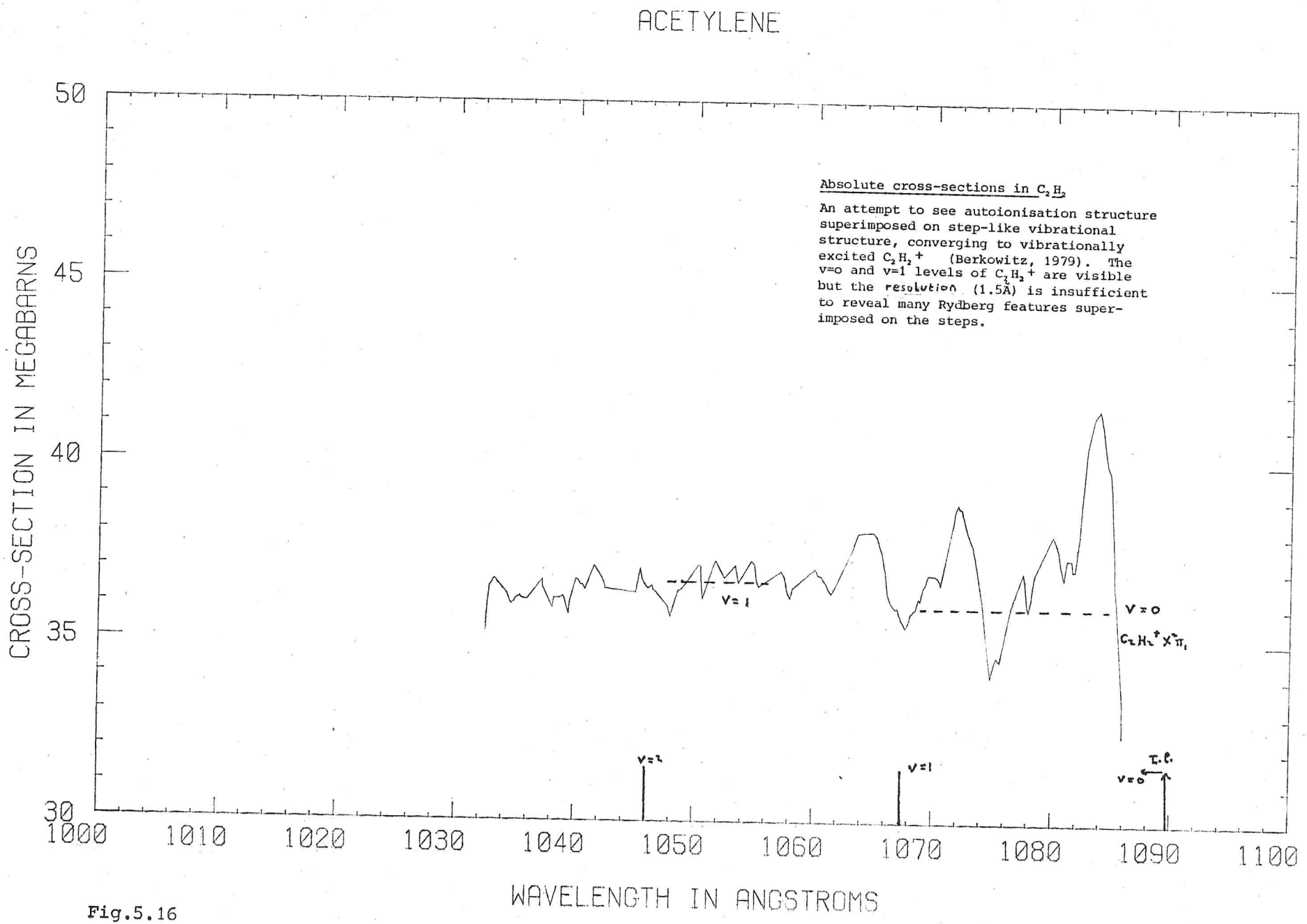
ACETYLENE
Absolute cross-sections in C_2H_2
An attempt to see autoionisation structure superimposed on step-like vibrational structure, converging to vibrationally excited $C_2H_2^+$ (Berkowitz, 1979). The v=0 and v=1 levels of $C_2H_2^+$ are visible but the resolution (1.5Å) is insufficient to reveal many Rydberg features superimposed on the steps.
CROSS-SECTION IN MEGABARNS
50
45
40
35
30
1000
1010
1020
1030
1040
1050
1060
1070
1080
1090
1100
WAVELENGTH IN ANGSTROMS
v=1
v=0
$C_2H_2^+ X^2\Pi_u$
v=2
v=1
I.P.
v=0

Fig.5.16

CHAPTER 6

The potential use of laser-produced plasmas as continuum VUV sources and some related theoretical aspects

Introduction

Previous chapters have described the Vacuum Ultraviolet Spectroscopy of a few simple molecules using an electron sychrotron as a background continuum source. The advantage of synchrotron radiation as a light source was outlined in Chapter 1 and it was concluded that if such a piece of equipment is readily available to a spectroscopist excellent results can be achieved throughout the VUV and XUV wavelength regions. Unfortunately, electron synchrotrons or Storage Rings are not always readily available and on such occasions an alternative source must be found. It was explained in Chapter 1 that because of the initial uncertainty as to when a synchrotron would become available for my use, an alternative VUV scurce, in this case a laser-produced plasma, had to be studied in some detail.

Briefly, the principle of the source lies in the formation of a small, highly dense fireball of material which becomes sufficiently opaque at high temperature to emit continuum radiation like a black body, although in reality large departures from this ideal behaviour have been observed. The small blob of plasma is created by focusing a high power, Q-switched laser onto a metal target with a large atomic number, for example Ytterbium (Z = 70). Usually, energies of the order of 1 Joule have been deposited onto a $0.1mm^2$ focal area of target during a typical pulse time of 50 nanosecs, implying incident laser fluxes between 10^{14} and 10^{15} Wm^{-2}. High electron temperatures can be produced, greater than 10^6 K in Local Thermodynamic Equilibrium, so that if anything like black body emission occurs then Wien's Law with λ max corresponding to greatest emission

$$\lambda_{max} T = 2.9 \times 10^{-3} (mK) \qquad (6.1)$$

should also apply, suggesting that wavelengths as short as 300Å or less will be radiated strongly. One of the most complete spectrographic surveys of laser-produced plasma sources has been reported recently by Carroll et al (1980) who shows that with appropriately chosen targets, essentially line-free continua suitable for absorption spectroscopy from 40-2000Å can easily be obtained using a moderately powered Q-switched Ruby laser. In their quite straightforward experiments the target was mounted a few centimetres from the entrance slit of a Normal or Grazing Incidence Vacuum Spectrograph. Other experiments by Mahajan et al (1979) found that higher continuum intensities near 1000Å could be obtained by focusing the plasma spot onto a spectrograph slit in conjunction with a gold coated concave mirror mounted behind the target but in front of the spectrograph. Both Carroll et al and Mahajan et al reported photometric measurements of intensity with high reproducibility, from one laser shot to the next and showed that the time-resolved emission of the plasma essentially followed that of the exciting laser pulse, except towards longer wavelengths where emission persisted beyond the cessation of the pulse. These results were taken to indicate that the shot-to-shot reproducibility and long-term stability of laser-plasma sources are good enough for accurate photoelectric scanning over large wavelength ranges or for time-resolved fluorescence studies.

The first report of VUV radiation from laser produced plasmas employed as sources for spectroscopy came from Ehler and Weissler (1966), who used a 10MWatt 0.4 J Ruby laser focused onto a tantalum target to produce the densitometer trace shown in Fig.6.1. Much later Breton et al (1973) studied the absolute intensity emission at 1216Å and the surrounding continuum radition produced in the range 1000Å-2000Å, also on tantalum, and found 3×10^{13} photons str^{-1} $Å^{-1}$ were emitted per 10J 60ns laser pulse. Their densitometer trace is shown adjacent to that of Ehler et al in Fig.6.1 and shows a basically similar spectral response. In contrast,

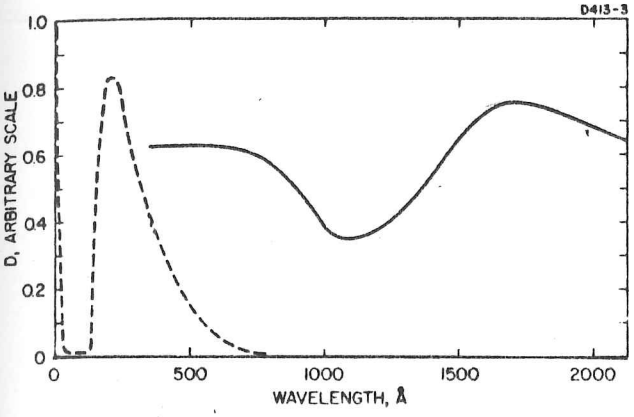

Densitometer trace of grazing and normal incidence vacuum spectrograms. Solid line: Continuum radiation from tantalum plasma observed with normal incidence spectrograph. Dashed line: Continuum radiation from tungsten plasma observed with grazing incidence spectrograph. (Ehler et al, 1966).

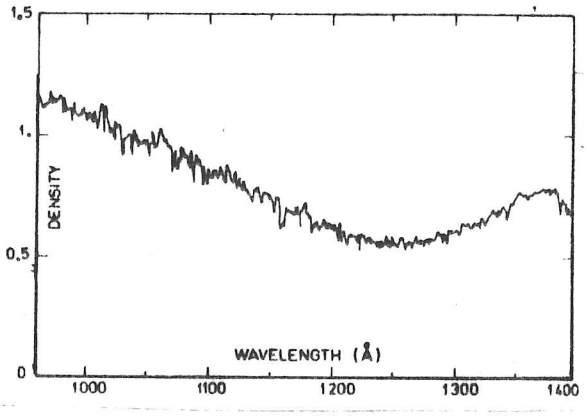

Microdensitogram of the source spectrum; five shots superposed; tantalum target; irradiation: 4 J; Nd laser, ψ =45°, ϕ =45°; entrance slit width: 0.1mm. (Breton et al, 1973)

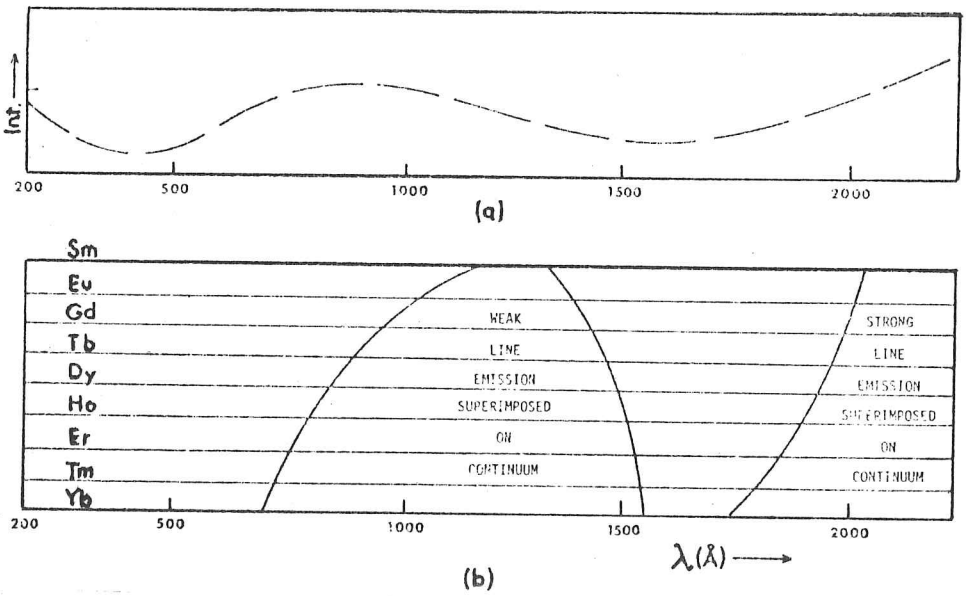

Carroll et al (1980).

(a) Approximate intensity distribution in rare earth continua (samarium to ytterbium) in the 200-2000A region. (b) Regions where line emission is superimposed on rare earth continua.

Fig.6.1

qualitative spectrographic intensity curves deduced by Carroll et al are also shown for comparison, but these are from plasmas produced on target materials other than tantalum.

The essentially line-free continua described by these researchers encouraged me to consider seriously a plasma source as an alternative to synchrotron radiation, especially since a rather old, but serviceable Ruby laser was at hand. However, the bulk of the reports mentioned above offered little explanation of the absorption and emission processes present during the space-time histories of the laser plasmas. Considering that the photodensitometer traces displayed in Fig.6.1 are at best time-integrated intensities measured from laser plasmas, care must be taken before trying to fit black-body behaviour to these diagrams, since the emission peak indicated by Wien's Law will have swiftly decreased and moved towards longer wavelengths concurrent with the plasma expansion and consequent cooling, contributing more to the response of longer wavelengths when time-integrated measurements have been made. With the meagre information available concerning the optical depths of laser plasmas at different wavelengths, only an informed guess could possibly be made to estimate the total photon emission from a particular laser plasma throughout the VUV region. One other absolute measurement of the photon emission at 1215Å was made by Mahajan et al (1979), who deduced that 2×10^{11} photons Str^{-1} $Å^{-1}$ were emitted by a 2J 20ns Ruby laser pulse, incident on a copper target, a striking two orders of magnitude less than that found by Breton et al. With such an uncertainty as to the possible continuum emission that might be obtained from a laser-plasma I attempted to make some preliminary absolute measurements of the emission from an Ytterbium target before embarking on any VUV spectroscopy. These experiments are described in Chapter 7, including a comparison with the results of Mahajon et al and Breton et al and the prediction of a computer model described later in this chapter.

Experimentally deduced properties of laser-plasmas

In order to understand the continuum emission of these plasmas measurements of both the density and temperature are needed over times spanning the laser pulse duration. The simple numerical model to be described later has to assume an initial plasma density similar to that of the solid target itself. Before attempting an analysis of the laser-plasma history the experimental observations from Chapter 7 and separate experiments by other workers will first be summarised. A description of Ruby laser operation can be found in Lengyl (1962) or very briefly in Chapter 7.

Ready (1971) shows Streak Camera photographs of plasma production by a free-running Ruby laser which demonstrate a virtual synchrony of the plasma plumes emitted from a target with the succession of 1 μs pulses which constituted the laser output, similar to observations mentioned in Chapter 7, which implied that the radiative emission has a response time less than 10^{-6} sec. Typical free-running laser pulses containing approximately a thousand individual spikes of 1 μs duration usually bore deep holes in metal targets with energies of about 1J, extending to a few millimetres in some cases, whereas single Q-switched laser spikes of similar total energy, but much higher intensity produce only shallow holes, never excavating more than one or two microns depth. The difference in behaviour between the modes of laser operation can be ascribed to the very different mean laser intensities involved for the two cases and are described for the particular targets of Aluminium and Ytterbium in Chapter 7.

Low laser intensities produce target vapourisation at a temperature not much greater than the boiling point with the vapour never becoming opaque enough to shield the target from the almost continuous train of low power, but numerous laser spikes. At high intensities, with all the laser energy in one short 50nsec pulse, vapourisation

occurs to a depth of a micron or so after which the plasma apparently becomes opaque, absorbing the remaining laser radiation to heat up the fireball, rather than the target. Ready (1971) shows evidence for the theory that the rate of plasma expansion increases rapidly just after the Q-switched laser pulse has begun and he describes the work of many researchers who have reported very high ionisation stages present in the subsequently heated laser-plasma. For example, Burgess et al (1967) report C(V) excitation produced by a fairly modest Ruby laser power of 50MWatts, and deduce excitation temperatures up to 100eV as well as showing strong continua produced at less than 100Å. Bearing all these points in mind, emphasis will henceforth be placed on Q-switched laser-plasma production where the very high excitation temperatures possible are most likely to produce the strong VUV and XUV continua of particular interest here.

Apart from many temperature determinations electron densities have also been inferred using the established techniques of Plasma Spectroscopy. For a good account of the subject see Griem (1964) or an introduction by Thorne (1979). In the same paper mentioned above Burgess concluded that electron densities in excess of 10^{20} cm^{-3} were present, deduced from the stark broadening of emission lines in the XUV, as might be expected in a plasma whose substance was originally at a density of 10^{22} cm^{-3} when in the solid state. However, interferometric probe techniques, similar to those of Mach-Zehnder and employing laser light, all seem to indicate electron densities of only 10^{19} cm^{-3} or less when applied to laser-produced plasmas. Many such experiments reported in the literature and discussed by Ready (1971) were time-resolved and also showed higher neutral atom concentrations than those of the electrons, including the respective decay times at various distances up to a few millimetres away from the target surface.

I found it puzzling that no electron densities greater than 10^{19} cm^{-3} were ever seen in these experiments, since it

is most likely that at some early stage in the laser-plasma history higher free-electron densities must have been present. As the degree of ionisation within the plasma has been seen to be high, neutral atom densities greater than 10^{20} cm^{-3} are then apparently incompatible with those observed for electrons, suggesting only 10% ionisation was present in these experiments. In an effort to gain more knowledge of the electron densities in laser-plasmas an attempt was made to measure the Faraday Rotation of a He/Ne laser probe passed through the fireball in the presence of a longitudinal magnetic field. The experiment, together with its background, is discussed fully in Chapter 7 but its conclusion was that an average electron density of the order 10^{21} cm^{-3} was present in a laser produced plasma formed on an aluminium target.

The conclusions drawn from all the experimental work described above and suggested by Ready(1971) were that Q-switched laser pulses with powers greater than a few Megawatts can be focussed to produce very high temperature and, at least in some cases, very highly ionised and dense plasmas on metal targets. Most of the material vapourised by such a laser pulse then comes from a hole a few microns deep, distributed over the focal-area of the laser condensing lens and primarily generated in the early stages of the plasma history. As the plasma develops it becomes opaque to the laser radiation, shielding the target surface and absorbing the energy itself, while its temperature and expansion rate rapidly increase until the laser pulse has begun to diminish. At some point, further target vapourisation occurs by heat from a now hot and expanded plasma, over an area larger than that of the focusing lens, deepening relatively little the hole formed earlier on. Employing this picture for the space-time history of laser-plasmas, a fairly simple mathematical model has been pieced together, which attempts to predict the total continuum emission from a given target metal, partly vapourised by a fully specified high intensity laser pulse.

Theorectical aspects of laser-produced plasmas

A good treatment of a whole variety of radiation processes in plasmas has been written by Bekefi (1966), in which the early introduction of Kirchoff's Laws, the black-body source function and the equation of transfer form the basis for a subsequent discussion of plasma emission. Unfortunately, no texts seem to have covered the radiation processes present in the very dense plasmas of special interest here. Some essential points will be discussed below, using Bekefi as the main source of reference.

For a solid or gas in thermodynamic equilibrium a temperature T can be defined for the body. The density of radiation in the gas or a cavity within the solid is given by Planck's formula

$$U_o(\omega) = \frac{\hbar\omega^3}{\pi^2 c^3} \frac{1}{e^{\frac{\hbar\omega}{kT}} - 1} \quad J\,m^{-3}\,\text{per rads}^{-1} \tag{6.2}$$

and includes the two possible transverse polarisations of radiation. ω is the angular frequency and c is the speed of the light. The flux of radiation escaping from a small hole of unit area into unit solid angle defines the luminance or bightness of the source and the formula has often been referred to as the Source or Ergiebigkeit function, playing a central role in the analysis of the emission from hot media. It is given by the expression

$$S_\omega = \frac{\hbar\omega^3}{4\pi^3 c^2} \frac{1}{e^{\frac{\hbar\omega}{kT_r}} - 1} \quad W m^{-2} Str^{-1}\,\text{per rads}^{-1} \tag{6.3}$$

for two polarisaitons where T_r is the radiative equilibrium temperature, normally equal to the thermodynamic temperature if thermodynamic equilibrium is present. An absorption coefficient α_ω can be defined in the usual way by the expression

$$I_\omega(l) = I_o e^{-\int_o^l \alpha_\omega dx} \qquad W m^{-2} \text{ per rads}^{-1}$$

(6.4)

for radiation I_ω travelling through a lossy medium over a distance l. The optical depth of the radiation path l into the medium is defined by the integral

$$\chi = \int_o^l \alpha_\omega d\omega \qquad \text{(Optical depth)}$$

(6.5)

If χ is much greater than 1, substantial attenuation of the radiation will occur over a path length l whereas if χ is much less then 1 only an amount

$$\delta I_\omega \approx \chi I_\omega \qquad \chi \ll 1$$

(6.6)

will be absorbed by the medium. A gas or solid at temperature T_r can emit no more radiation at a frequency ω than that given by the source function. In that case the body is called 'black'. If a lower emission occurs the body may be called 'grey' if the emission function is less than the Source function by a constant factor ϵ, the emissivity. For a hot gas or plasma ϵ is nearly one when the optical depth at all frequencies is much greater, but if the medium is optically thin, corresponding to small values of χ the emissivity becomes approximately the same value as the optical depth in the limit χ going to zero.

For a solid surface the emission function B is given by

$$B(\omega, T_r) = \varepsilon S_\omega(T_r) \qquad (6.7)$$

For a gas or plasma

$$B(\omega, T_r) = \varepsilon S_\omega(T_r)$$

optically thick

$$\approx S_\omega(T_r)$$

optically thin

$$\approx \chi S_\omega(T_r) .$$

The general case, when the optical depth varies arbitrarily as a function of frequency or other parameter, can be deduced using the equation of transfer

$$\frac{d}{d\chi}\left(\frac{I_\omega}{n^2}\right) = \frac{I_\omega}{n^2} - S_\omega \qquad (6.8)$$

where n is the plasma refractive index, which for most purposes is nearly equal to one. Its departure from free-space behaviour will be discussed below. It is shown in many texts on Electromagnetic theory (eg. Panofsky and Phillips, 1955) that an isotropic-free electron gas has a dispersion relation given by the simple formula

$$\omega^2 = \frac{k^2 c^2}{\left(1 - \frac{\omega_p^2}{\omega^2}\right)} = \frac{k^2 c^2}{K_T} \qquad (6.9)$$

for transverse electromagnetic waves of wave number k propagating at an angular frequency greater than the critical plasma frequency ω_p. This frequency is simply related to the electron number density N and is given by

$$\omega_p = \sqrt{\frac{Ne^2}{m\varepsilon_0}} \qquad (6.10)$$

where e is the electronic charge and m the electron mass. The quantity K_T can be identified as the dielectric constant of the medium and related to the refractive index by the expression

$$n = \sqrt{K_T} \qquad (6.11)$$

At frequencies less than the plasma frequency the dielectric constant becomes negative. Since ω is taken to be a real quantity the wave number must become imaginary below the plasma frequency, preventing the propagation of the radiation, which instead is evanescent. At very high frequencies much greater than ω_p propagation occurs normally at a phase velocity close to light in vacuo with a refractive index near to unity.

In the presence of collisions the dielectric constant is modified by the inclusion of a collision frequency ν in the general expressions given by Bekefi; further modifications are needed if a magnetic field is present to make the electron gas anisotropic and in these cases the dielectric constant K_T has to be described as a tensor of rank 2. Generally the dielectric tensor

$$\underline{\underline{K}} = \begin{pmatrix} K_{xx} & K_{xy} & K_{xz} \\ K_{yx} & K_{yy} & K_{yz} \\ K_{zx} & K_{zy} & K_{zz} \end{pmatrix} \qquad (6.12)$$

must satisfy the dispersion relation described from Maxwell's equations,

$$\underline{k} \wedge (\underline{k} \wedge \underline{E}) + (\omega/c)^2 \underline{\underline{K}}.\underline{E} = 0 \qquad (6.13)$$

where $\underline{E}$ is the electric field vector of either a longitudinal or transverse wave (or both). Since we are only considering transverse waves which are able, eventually, to leave the

plasma $\underline{B} \cdot \underline{E} = 0$ must apply. For a magnetic field $\underline{B}$ along the Z-axis the components of $\underline{\underline{K}}$ are given approximately by

$$K_{zz} = 1 - \frac{\omega_p^2}{\omega(\omega - i\nu)} \qquad \omega_c = \frac{eB}{m_e}$$

$$K_{xx} \pm iK_{xy} = 1 - \frac{\omega_p^2}{\omega(\omega \pm \omega_c - i\nu)}$$

$$K_{xx} = K_{yy}, \quad K_{xy} = -K_{yx}, \quad K_{zx} = K_{xz} = K_{yz} = K_{zy} = 0$$

(6.14)

ω_c is the cyclotron frequency of circular electron motion in the magnetic field, e/me is the electron charge/mass ratio and ν the collision frequency. The relations are strictly true for a cold electron gas but will hold well for warm plasmas if electron and ion speeds remain non-relativistic. From the definition of refractive index

$$n = \frac{c}{\omega} Re(k)$$

(Re=Real part of)
(6.15)

and the isotropic dispersion relation for transverse waves

$$k^2c^2 = K_T \omega^2 \qquad K_T = K_{xx} = K_{yy}$$

the refractive index in the presence of collisions has been calculated to be roughly

$$n(\omega) \approx \left[\left(1 - \omega_p^2/\omega^2\right)^2 + (\nu/\omega)^2 \right]^{\frac{1}{4}}$$

(6.16)

and can be used if ν is only known approximately. In Chapter 7 expressions which have been calculated are given

for the anisotropic refractive index in a magnetic field, where a linearly polarised wave is considered as split up into left and right handed circular components treated separately to find a Faraday rotation of a linearly polarised light-beam propagating along the Z-axis.

Keeping the theory outlined above in mind the emission mechanisms of real, highly ionised laser plasmas can now be discussed, considering always whether local thermodynamic equilibrium adequately defines the temperature. As the plasma is so compact and dense, heat conduction occurs very rapidly over typical times of 10^{-11} s (Ready, 1971) so the assumption of at least LTE is not unreasonable. The assumptions of Ready (1971) and David et al (1966) that free-free electronic transitions constitute the dominant absorption mechanisms in laser plasmas at the Ruby laser wavelength led me to presume that free-free Bremsstrahlung systems should also dominate the continuous absorption throughout the visible and VUV spectral range. The picture developed here assumes free-electrons and ions form the major constituents of a laser plasma, interacting with each other through Bremsstrahlung collision processes to provide a means by which continuum light is either emitted or absorbed. When the optical depth of the Bremsstrahlung absorption mechanism is greater than about unity, at any particular wavelength, the plasma will radiate at the same wavelength, a black body continuum radiation corresponding to the plasma temperature, assuming the presence of LTE. Conversely, when the Bremsstrahlung process cannot provide an optical depth much greater than unity the plasma will radiate like a grey body, with an emissivity no longer one, but instead approximately equal to the optical depth, again assuming LTE. Because the optical depth and therefore the emissivity of the hot plasma may alter drastically as a function of wavelength the observed intensity spectrum is unlikely to look anything like that of a theoretical black body, even though the source function will still implicitly be causing the emission. The absorption coefficient produced by Bremsstrahlung collision processes

is given by Bekefi to be

$$\alpha\omega = \frac{1}{n_r}\frac{\pi}{\sqrt{3}}\left(\frac{Z^2e^6}{6\pi\varepsilon_0^3 c m^2}\right)\left(\frac{m}{2\pi KT}\right)^{1/2}\frac{N_e N_i}{\hbar\omega^3}\left(1-e^{-\frac{\hbar\omega}{KT}}\right)\bar{g}$$

$$\Rightarrow \alpha_\nu = \frac{1}{n_r}\frac{\pi}{\sqrt{3}}\left(\frac{e^6}{48\pi^4 c\varepsilon_0^3 m^2\hbar}\right)\left(\frac{m}{2\pi K}\right)^{1/2}\frac{Z^2 N_e N_i}{\nu^3 T^{1/2}}\left(1-e^{-\frac{h\nu}{KT}}\right)\bar{g}$$

(6.17)

where stimulated emission and dispersion have been included. Ni is the ion concentration, Ne the electron concentration, n_r the anisotropic or isotropic refractive index and $\bar{g}$ a Gaunt factor which for most cases is approximately unity, both above and below the plasma frequency. Z is the stage of ionisation reached in the plasma; generally $N_e = Z N_i$ if the species are conserved in equilibrium.

Therefore, if the plasma temperature T, density N and optical path length X are known at a particular time then the Bremsstrahlung absorption coefficient can be calculated to find the optical depth. Solving the equation of transfer for rays originating in the plasma and emerging at its surface the continuum emission should be given completely by the relation

$$I_\omega = \left[1 - e^{-\chi_\omega}\right] S_\omega(T_r) \qquad W m^{-2} Str^{-1} per rads^{-1}$$

(6.18)

with any discrepancies in behaviour being ascribed to non-Bremsstrahlung transitions not included into the optical depth χ_ω. After finding I_ω at an early time in the plasma history, further values can be calculated subsequently to deduce the total photon emission E_ω, evaluated by integrating I_ω over the plasma lifetime. E_ω is the desired function which will indicate theroretically the absolute continuum

emission that could be obtained from a particular laser plasma. However before these calculations can be performed a model of the laser plasma space-time history must first be chosen to provide the essential functions $T(t)$ and $N(t)$ for even the simplest case, a one dimensional plasma of size $X(t)$, driven by a high intensity laser pulse which must be specified exactly.

A simple model of the plasma expansion

The qualitative behaviour of the laser-plasma history deduced experimentally has been discussed and is depicted in Fig. 6.2

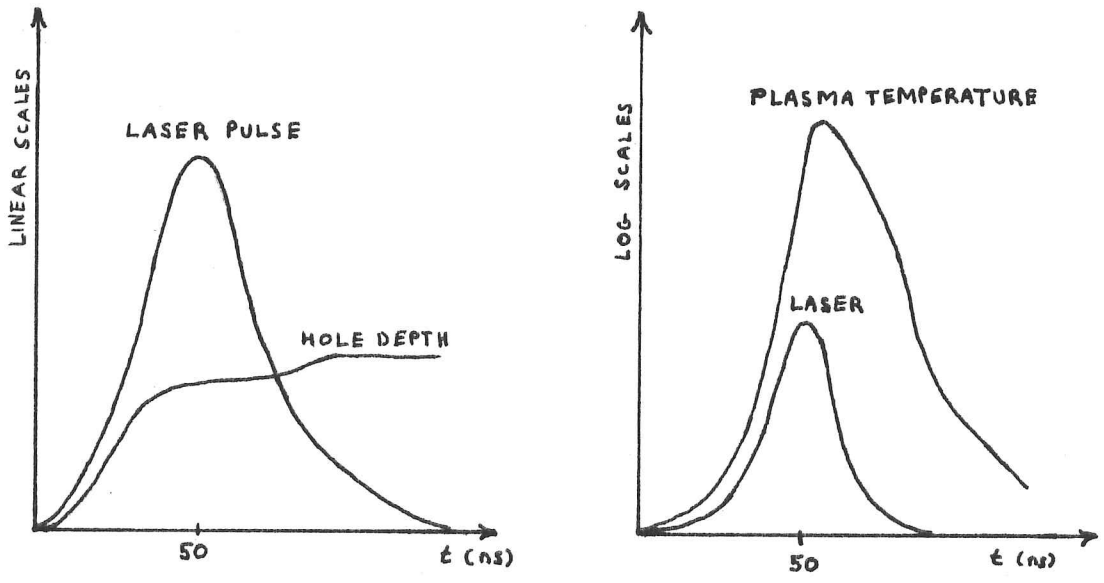

Fig.6.2

Given a fixed number of atoms N_o within the plasma gas the subsequent hydrodynamic expansion under the influence of absorbed radiation can be solved fairly easily if the initial boundary conditions are known and no further target material is added to the plasma. A one dimensional treatment discussed by Ready (1971) will be described below and is used as part of a computer model for the plasma history. A greater problem, which to my knowledge has not yet been

solved completely is the very early behaviour of the vapourised material, before the boundary conditions needed for the hydrodynamic expansion have been achieved. Phenomenologically, the plasma seems to become nearly opaque at an early stage during the high intensity laser pulse, at which point the continuous removal of target material ceases to add to the bulk of the plasma. It is at this time t_o that N_o becomes fixed and hydrodynamic equations must take over to describe the ensuing expansion and laser heating. Prior to the time t_o the model described here assumes the plasma was transparent, allowing unimpeded laser radiation to strike the target surface and cause a steady vapourisation of material. This assumption can only be qualitatively correct, for any vapour in front of the target will have probably caused the laser radiation to be at least slightly attenuated before the time t_o. It is likely that this assumption constitutes the major weakness in the computer model derived here. The point at which surface vapourisation will cease and the plasma becomes opaque can be determined in the model by integrating the surface-recession velocity V_{ss} with respect to the laser pulse-time from its beginning at $t=0$ until $t=t_o$ at which point the integral equals the hole depth created by a single Q-switched laser pulse. If the hole depth has been measured empirically, t_o can be evaluated using a suitable model for V_{ss} as a function of the incident laser flux. Therefore, what is needed initially is a description of the vapourisation and the surface recession V_{ss} caused by the laser pulse.

Again the treatment to be described here has been taken from Ready (1971), although the author himself does not mention its possible use to find the boundary conditions for the hydrodynamic expansion. To determine the steady-state condition for high intensity laser vapourisation a limiting velocity of propagation of the retreating surface is assumed. The temperature T of the surface is taken to be greater than the normal boiling point of the material. Conservation of energy yields

$$F = v_{ss}\,\rho\,(cT' + L) \qquad Wm^{-2}$$

(6.19)

where F is the quasi-static flux density absorbed at the surface, ρ is the target density, C its specific heat and L the specific Latent heat of vapourisation. The velocity v_{ss} can be expressed in terms of dN/dt, the rate at which the number density of the target atoms is removed to form the plasma vapour and is given in statistical Mechanics by the relation

$$\frac{1}{N}\frac{dN}{dt} = \nu_D\, e^{-\frac{LM}{RT'}}$$

(6.20)

where ν_D is the Debye frequency ($\sim 10^{13}$ Hz), M is the target molar weight and R the gas constant. The equation gives essentially the rate at which atoms at the surface can escape from their potential wells and leave the target. Combining the two equations above

$$F = h_a\,\nu_D\,\rho\,[cT' + L]\; e^{-\frac{LM}{RT'}}$$

(6.21)

where h_a is approximately the thickness of an atomic layer at the target surface. By solving this equation for T' as a function of F(t) the surface velocity can be calculated and then integrated to find the time t_0 at which the hole depth observed will be produced by the model. In solving for F as a function of time the quasi-static assumption will still be maintained since the equilibrium time for the process should be approximately the reciprocal of the Debye frequency, much less than the time scale of the laser pulse F(t). Taking data for Ytterbium, T' and v_{ss} were calculated numerically for increasing values of F. Table 6.1 lists the values obtained using a programmable calculator.

	Laser Flux F (Watts cm^{-2})	Surface Velocity (ms^{-1})	Surface Temperature (K)
(Free-running)	10^6	1.0	3000
	10^7	9.0	4300
	10^8	68	8300
	10^9	320	25,000
(Q-switched)	10^{10}	590	160,000
	10^{11}	660	1,500,000

Table 6.1

For an estimated focal area of 2×10^{-3} cm^2 the laser fluxes obtained during experiments, mentioned in Chapter 7 are indicated in the table for the free-running or Q-switched case. In order to find the boundary conditions at t_o, the hole depth d is given explicitly by the integral

$$d = \int_0^{t_o} \frac{F(t)}{\rho(cT'+L)}\, dt \qquad (6.22)$$

from which t_o can be deduced since all the other functions and quantities can be measured. Fig.6.3 shows schematically the point at which the laser pulse is no longer absorbed at the target surface with the plasma concentration depicted as a linear function of distance from the target x, for a total size $X(t_o) = X_o$.

$$N = N_o(1 - x/X) \qquad (6.23)$$

The choice of the profile was fairly arbitrary and the simplest reasonable case was chosen; Ready (1971) reports that models of the subsequent hydrodynamic expansions do not depend critically on the exact density gradient model employed.

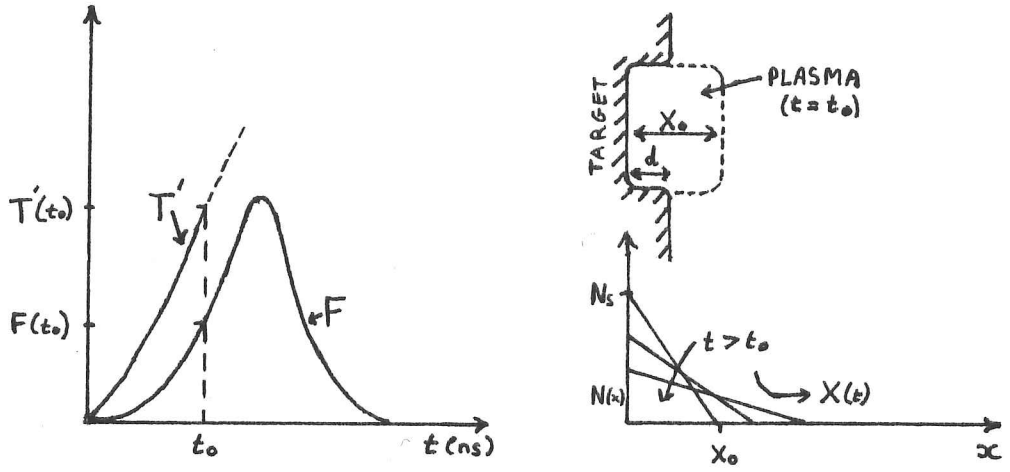

Fig. 6.3

Using the linear density gradient, the total number of atoms at $t = t_0$ must be equal to N_0, the number to be used in the hydrodynamic expansion. Therefore, by integrating the profile with respect to x

$$N_0 = \frac{A N_s X_0}{2} = A N_s d \qquad (6.24)$$

where N_s is the number density at the surface and is set equal to the atomic number density in the target at t_0. A is the focal-area of the laser condensing lens. Thus the choice of a linear density gradient has constrained the plasma size X_0 to be simply twice the hole depth at t_0. Because the laser flux at t_0 is also known, the plasma temperature must be $T'(F)$, given by the model above, if the plasma is in LTE. Hence the expansion velocity of the plasma dX/dt at $t = t_0$ can be deduced assuming the atoms move away from the target at a velocity proportional to their mean thermal speeds at the leading edge. From Kinetic Theory the flux of atoms across a surface within a gas is $\frac{1}{4} N \bar{c}$ for a number density N and mean thermal speed $\bar{c}$; it is reasonable to assume that the diffuse plasma boundary will expand outward at a roughly similar speed. The inclusion of the factor $\frac{1}{4}$ is probably unjustified, but is retained nonetheless, so that

$$\left.\frac{dX}{dt}\right]_{t_0} \approx \frac{1}{4}\bar{c} \approx \left(\frac{KT}{2\pi m}\right)^{\frac{1}{2}} \qquad (6.25)$$

where m is the atomic (or ionic) mass and a Maxwellian velocity distribution has been assumed. It is worth noting here that the electrons and ions are presumed to expand together, with no charge separation; Ready (1971) presents some experimental evidence for this, but in any event the electrostatic interaction between charges is so strong that any imbalance from neutrality will be swiftly nullified.

The required boundary conditions for the subsequent hydrodynamic expansion of the opaque plasma can now be found. They are t_0, X_0, $[dX/dt]_{t_0}$ and T_0 and N_0, corresponding to the time, size, expansion velocity, temperature, and total number of atoms pertaining respectively when surface vapourisation ceases. The remaining task must be to calculate the plasma history at all other times after t_0. This will be done following a procedure given by Ready in his book (1971) which assumes a one dimensional expansion, a linear density gradient at all times, the boundary conditions given above, and radiation energy losses from the hot plasma to be negligible.

The rate W at which the laser beam deposits energy in the plasma must be equal to the rate at which the plasma does work in its expansion, plus the rate at which the thermal energy of the plasma increases. Thus for a pressure P and area A

$$-A\int_0^x \frac{\partial P}{\partial x}\left(\frac{dx}{dt}\right)dx + \frac{A}{2}\frac{d}{dt}\int_0^x (N_i + N_e)KT\,dx$$

$$= W = FA\int_0^x K_\nu e^{-K_\nu x}\,dx. \qquad (6.26)$$

where N_e and N_i are the electron and ion densitites and K_ν is the Bremsstrahlung absorption coefficient given by α_ω (Equation 6.17) for the Ruby laser frequency 4.3×10^{14} Hz. Since the plasma boundary is diffuse little reflection of laser light will occur. It should be noted that K_ν includes the refractive index of the plasma and is a complicated function of x, $X(t)$ and $T(t)$. From the plasma equation of state

$$P = (N_i + N_e)KT \tag{6.27}$$

and

$$N_i = N_{is}(1 - x/X) \qquad N_e = N_{es}(1 - x/X) \tag{6.28}$$

where N_{is} and N_{es} denote the ion and electron surface concentrations, which will steadily drop if target vapourisation has really ceased. Assuming the density profile does not change with time then the velocity of the plasma increases linearly with distance from the surface and

$$\frac{dx}{dt} = \frac{x}{X}\frac{dX}{dt} \tag{6.29}$$

Inserting Equations (6.27)-(6.29) into the left-hand side of (6.26) gives

$$A\int_0^X \frac{P_s x}{X^2}\left(\frac{dX}{dt}\right)dx + \frac{1}{2}A\frac{d}{dt}\int_0^X (N_{is} + N_{es})\left(1 - \frac{x}{X}\right)KT\,dx$$

$$= A\frac{P_s}{2}\frac{dX}{dt} + \frac{1}{2}A\frac{d}{dt}(N_{is} + N_{es})\frac{X}{2}KT = W \tag{6.30}$$

remembering that T is independent of spatial position due to the high thermal conductivity in the plasma. The total number of ions is given by the expression

$$N_{io} = A\int_0^X N_{is}\left(1 - \frac{x}{X}\right)dx = \frac{A N_{is} X}{2} \tag{6.31}$$

with a similar expression for the total number of electrons N_{eo}. Substituting these equations, Equation (6.30) becomes

$$\frac{A P_s}{2} \frac{dX}{dt} + \frac{1}{2} K (N_{io} + N_{eo}) \frac{dT}{dt} = W \qquad (6.32)$$

The rate at which work is done by the plasma in its expansion is equal to the rate of increase of the plasma Kinetic energy so

$$-A \int_o^X \frac{\partial P}{\partial x} \left(\frac{dx}{dt}\right) dx = \frac{1}{2} \frac{d}{dt} \int_o^X (N_i m_i + N_e m_e) A \left(\frac{dx}{dt}\right)^2 dx \qquad (6.33)$$

where M_i and M_e are the ionic and electronic masses. Using Equations (6.27-6.29) and (6.31). Equation (6.33) can be simplified and integrated to yield

$$\frac{A P_s}{2} \frac{dX}{dt} = \frac{1}{12} \frac{d}{dt} \left(\frac{dX}{dt}\right)^2 (N_{io} m_i + N_{eo} m_e) \qquad (6.34)$$

substituting (6.27) and (6.28) into (6.34) gives, after some manipulation

$$T = \frac{(N_{io} m_i + N_{eo} m_e)}{6 K (N_{io} + N_{eo})} \times \frac{d^2 X}{dt^2} \qquad (6.35)$$

If Equation (6.34) is substituted into (6.32) we obtain

$$\frac{1}{12} \frac{d}{dt} \left(\frac{dX}{dt}\right)^2 (N_{io} m_i + N_{eo} m_e) + \frac{1}{2} K (N_{io} + N_{eo}) \frac{dT}{dt} = W \qquad (6.36)$$

which can be rewritten by differentiating Equation (6.35) and substituted for dT/dt to give, finally

$$\frac{d^3 X^2}{dt^3} = \frac{24}{(N_{io} m_i + N_{eo} m_e)} W \qquad (6.37)$$

The two coupled differential equations (6.37) and (6.35) can be solved numerically using the boundary conditions already described to produce the required time and space history of the plasma for a specified (measured) laser pulse shape.

Before proceeding to the actual numerical calculations, some consideration had to be applied to both the degree of ion-

isation and to the collision frequency within the expanding plasma. Very high ionisation stages have been reported in some experiments, such as the work of Burgess et al (1967). Generally, however, lower temperatures have been estimated than the 100 eV implied by that work, especially for the more modest laser intensities near 10^{10} Wcm^{-2} considered in this thesis, similar to those used by Ehler and Weissler (1966) who determined an empirical temperature of 10 eV for their laser plasmas. Their value fits well with the elevated surface temperature T' calculated from a Q-switched flux of 10^{10} W cm^{-2} shown in Table 6.1 for an early stage of the plasma history.

Thorne (1979) discusses Saha's equation for electron-ion equilibria with an introduction as to its use. Its relevance is also discussed in the next chapter. In this case Saha's equation can be used to indicate the ionisation stage at a temperature near 10eV(100,000K). The equation is

$$\frac{N_e N_{z+1}}{N_z} = \frac{2(2\pi m_e kT)^{3/2}}{h^3} \frac{U_{z+1}(T)}{U_z(T)} e^{-\frac{I}{kT}} \qquad (6.38)$$

where I is the ionisation energy needed to excite the Z^{th} stage to the $(Z+1)^{th}$. U_{z+1} and U_z are the respective partition functions of the two related ion stages and their ratio is normally of the order unity at temperatures less than 10 eV. Inserting numerical values Saha's equation becomes

$$\frac{N_e N_{z+1}}{N_z} \approx 4.8 \times 10^{21} T^{3/2} e^{-\left(1.16 \times 10^4 \frac{I}{T}\right)} \qquad (6.39)$$

where the number densities are in m^{-3} and I is the ionisation energy in electron volts. The first two ionisation potentials of Ytterbium (Goodfellow Metals Ltd) are 6.2eV and 12.1eV

respectively. The third and fourth potentials had to be estimated, however, and rough values of 20eV and 40eV were chosen. The electron density can be assumed to be of the order 10^{21} cm^{-3} during the laser pulse, but this may be too high towards the end of the forced hydrodynamic expansion (See an earlier discussion above). Inserting these estimated values into (6.39) it can be shown that at a temperature of 100,000K Z=4 is the dominant ionisation stage but that at 50,000K the third stage takes over to dominate the plasma. Lower electron densitites tend to increase Z, whereas only a small drop in temperature can reduce the stage of ionisation quite sharply. It was decided that since most of the plasma properties of interest occur at the highest temperatures, when the large value Z=4 is present then such a value should be chosen, but the decision is really rather arbitrary and has little effect on the results of the numerical calculations.

The collision frequency within the plasma was derived using an impact approximation applied normally to calculations of pressure broadening in Plasma Spectroscopy. The approximation holds when considering the predominant electron-ion collision process if the plasma frequency is much greater than the collision frequency. For highly dense laser plasmas this criterion is just obeyed. Thorne (1979) gives an impact parameter for electron-ion collisions to be

$$\rho_0 \approx \left(\frac{2\pi C_4}{\bar{v}}\right)^{1/3} \qquad (6.40)$$

where C_4 is an interaction constant for stark type collisions and $\bar{v}$ the average velocity of the electrons. The number of collisions per second for which the impact parameter is less than ρ_0 is approximately the collision frequency given by

$$\nu_c \approx \pi \rho_0^2 \bar{v} N \qquad (6.41)$$

if N is the ion number density. Using a rough value of C_4 taken from Thorne (1979) for ions

$$C_4 \approx \frac{1}{h}\frac{\alpha e^2}{(4\pi\varepsilon_0)^2} \approx 8 \times 10^{-25}\ \mathrm{J\,m^4}$$

where α is the ionic dielectric polarisability, we obtain

$$\nu_c \approx \pi\left(\frac{2\pi C_4}{\bar{v}}\right)^{2/3}\bar{v}\,N$$

$$\approx 2 \times 10^{-14}\,T^{1/6}\,N \qquad (6.42)$$

if $\bar{v}$ is assumed to be the velocity of thermal electrons. At a temperature of 100,000K and a density of $10^{27}\ \mathrm{m^{-3}}$ for Ytterbium the collision frequency is about 10^{14} Hz, half the plasma frequency. The expression (6.42) for the collision frequency was used by the computer model to calculate the modified refractive index in the plasma (see above), preventing it from becoming zero, as would have applied in a cold,collisionless electron gas, but which is not the case here.

The calculated laser plasma history and continuum emission

Two computer programs have been written to calculate the laser-plasma history and the integrated continuum emission The essential metal data for Ytterbium in S.I. units are shown in Fig.6.4 together with information concerning the laser pulse required to solve the plasma history. The figure constitutes the first few lines of printer output produced by the 'Laser Plasma Temperature and Space History' program. The only purely empirical piece of information supplied to this particular program was the hole depth created by a real laser pulse, which had been obtained by measuring the amount of target mass removed over roughly 50 shots, during experiments described in Chapter 7. On average a focal depth of 2.4 μm was removed from the target for each 0.5J laser pulse incident on the Ytterbium. The value agrees well with

typical depths produced by Q-switched pulses on other metals shown in Ready (1971).

```
LASER PLASMA TEMPERATURE AND SPACE HISTORY

METAL DATA IN S.I. UNITS

ATOMIC THICKNESS  0.3300D-09
DEBYE FREQUENCY  0.2700D+13
DENSITY  0.6972D+04
SPECIFIC HEAT  0.1450D+03
LATENT HEAT  0.9210D+06
ATOMIC MASS NO.  0.1730D+030HOLE DEPTH  0.2400D-05

LASER PARAMETERS

FOCAL AREA  0.2000D-06 PULSE TIME  0.3920D-06
PULSE ENERGY  0.5000D+00
FREQUENCY  0.4320D+15

CALCULATION PARAMETERS

TIME RANGE  0.1000D-05
STEP NO.300
INTEGRATION EVEN NO. 10
TEMPERATURE ERROR0.10D+02
TOLERANCE0.10D-02

NO. OF FLUX POINTS29

COLLISION INTERACTION CONSTANT  0.1700D-13

DIMENSION IS  0.6207D-05HOLE IS  0.2400D-05SURFACE SPEED  0.3123D+03
PLASMA SPEED  0.4042D+03TEMPERATURE  0.1826D+05TIME  0.3333D-07STEP
```

Fig.6.4

The 'calculation parameters' are relevant only to the details of the numerical calculations, which are discussed fully in the descriptions of the computer programs to be found in the Appendix. The 'History' program was usually used to produce only the first microsecond of the plasma expansion, as later times contributed an insignificant amount to the time-integrated photon emission of the plasma, calculated with the second program. The 1 μs time interval was divided by the 'History' program into 300 evenly spaced intervals and plasma conditions were output at each of these 301 points, covering the most important heating and expansion

phases. The 301 size and temperature values were to be used subsequently by the Continuum Emission program. The real laser-pulse profile had been photographed using a Storage 'Scope camera (see next chapter) and digitised at 29 'Flux Points' using an arbitrary scale. The flux points representing the laser-pulse were input to the 'History' program, together with the metal data, and integrated and normalised to have S.I. units using the known pulse energy and pulse time. The collision interaction constant is the collision-frequency-constant used in the formula Equation (6.42). The last two lines of Fig.6.4 show the boundary conditions on the plasma calculated to exist at t_o and which then were employed to evaluate the subsequent hydrodynamic expansion of the plasma when target vapourisation had stopped.

The appropriate graph-plotter output of the 'History' program is shown in Figs.6.5-6.7 for three different Ruby laser pulses, whose energies were 0.25J, 0.5J, and 1.0J respectively. The program always used the same pulse shape, as drawn schematically in green on the figures, and the same hole depth, which had been measured only for 0.5J laser pulses. Thus the picture for a 0.5J pulse is most consistent with the model, but the other two can be taken to indicate roughly the important effects of doubling or halving the pulse-energy, when keeping all other parameters constant and assuming the hole depth actually observed does not depend much on the energy. It should first be pointed out that the oscillation of the temperature at an early time is an artifact due to the model suddenly changing from a transparent to an opaque plasma system. Immediately apparent from the pictures is the rapid response of the temperature to changes of laser flux intensity; the artificially produced digitisation discontinuities of the laser time-profile can be seen synchronously with changes in the Temperature curve; implying the response time of the model is fast, at most a few nanoseconds, and supporting the important assumptions of local Thermodynamic Equilibrium. More interesting, however,

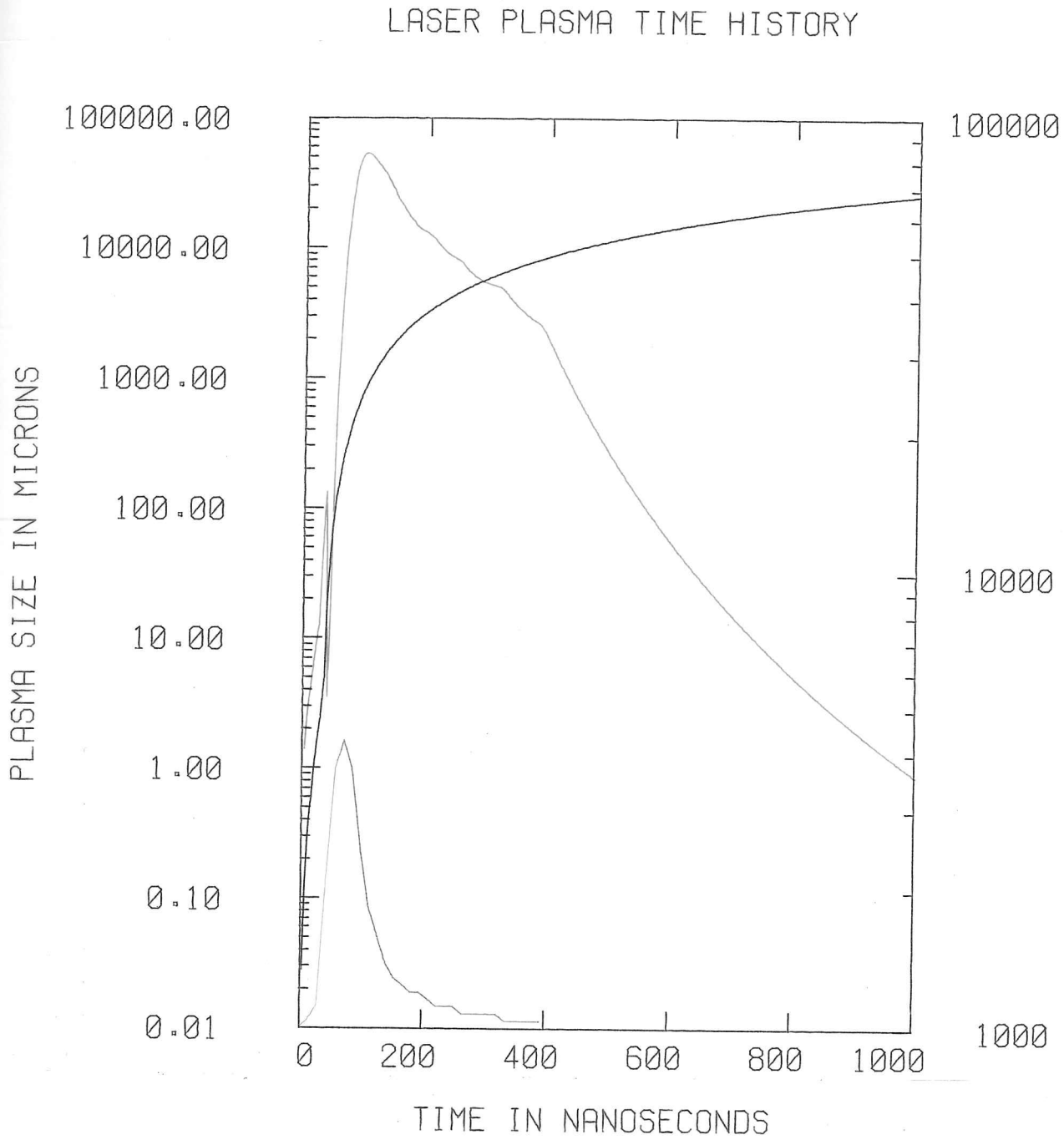

Fig.6.5 PULSE ENERGY 0.25J

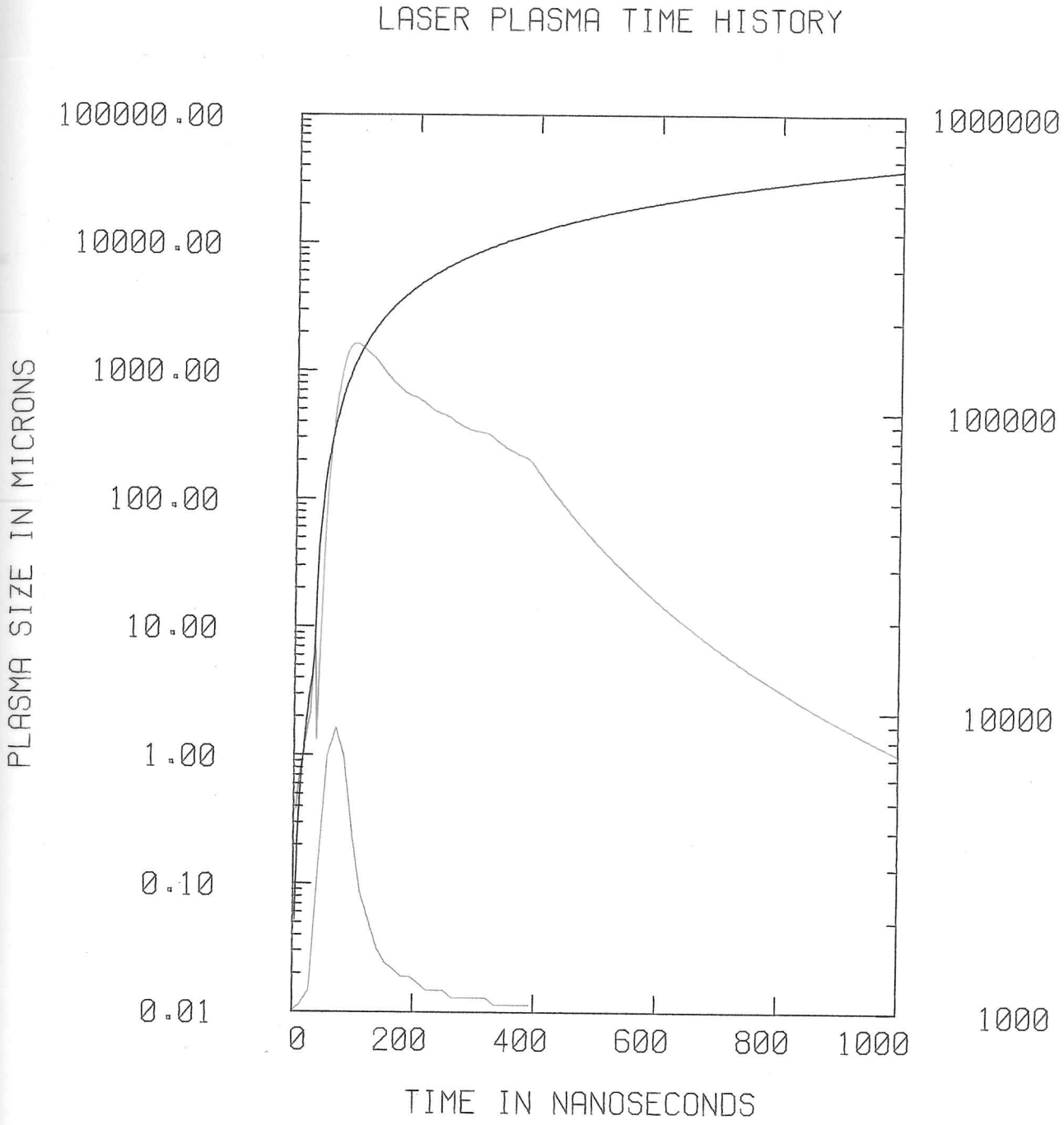

Fig.6.6 PULSE ENERGY 0.5J

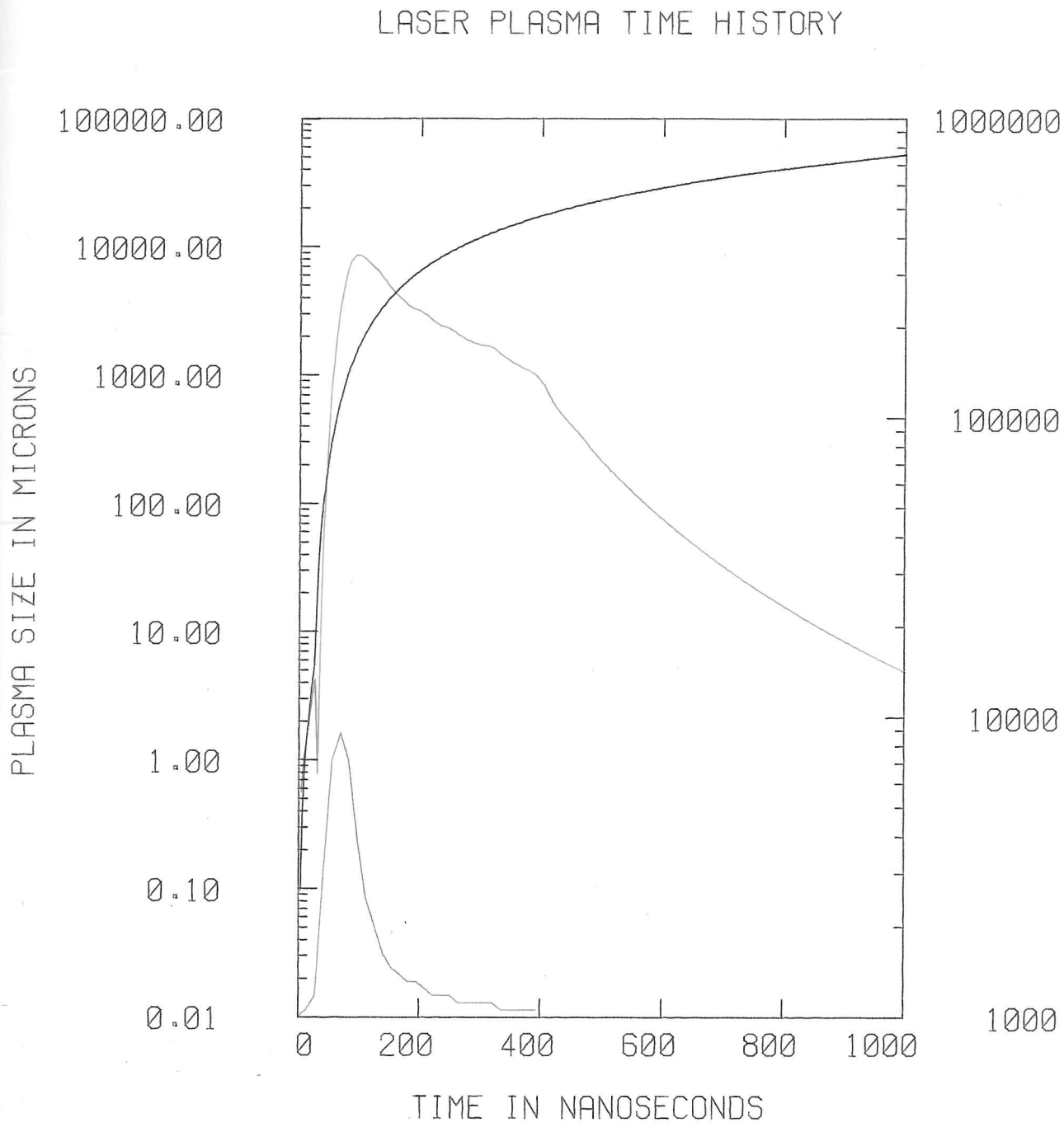

Fig.6.7 PULSE ENERGY 1.0J

is the almost direct proportionality of the temperature at any one time to the laser energy, as is apparent from the figures. These results are enumerated in Table 6.2 below.

The ionisation stage chosen to best represent the plasma under these conditions was Z=4, based on calculations employing Saha's equation. At 0.5J laser energy only the temperatures were sensitive to changes in Z by plus or minus one, leaving the size history unaffected by alteration of the ionisation stage. The different calculated temperatures are found to be simply scaled by $1/(1+Z)$ as can be seen from Equation (6.35) if the plasma acceleration is presumed insensitive to variations of the ionisation stage. Using this result, Equation (6.37) then implies that the total laser flux absorbed is just equal to that in the laser pulse, which must, by implication be completely absorbed by the plasma. The conclusion is that the optical depth for Bremsstrahlung processes of the laser light, although a function of Z and temperature, must at all times be greater than one under the circumstances. This was confirmed to be the case when intermediate numerical evaluations of the optical depth were output by the 'History' program during some runs. A large optical depth does not always apply at higher frequencies, as is explained below.

The Continuum Emission calculations were performed by the second computer program, using the temperature and space history data supplied by the 'History' program, together with all the data for Ytterbium and some fundamental constants. Essentially the continuum emission calculations involved the integration of Equation (6.18) over the plasma history at a number of discrete frequencies. The total photon emission per steradian per Angstrom was then calculated, assuming the emitting area of the plasma, where the primary heating occurred, to be equal to the focal area of the condensing lens. However, an inspection of the Ytterbium target area revealed a shallow crater with a rim of 2mm diameter, at variance with

the 1-dimensional model used here which assumed a constant cross-sectional area equal to the small focal area of the laser beam. Because of this discrepancy it is likely the model produces an underestimate of the total photon emission towards longer wavelengths where the cooler, but apparently much wider, real plasma at late times contributes predominantly to the continuum time-integration. The results of the calculations by the Emission program are shown in Figs.6.8-6.10 for the three laser-energies 0.25T, 0.5J and 1.0J respectively and some relevant numerical values have been listed in Table 6.2. The numbers in brackets represent the ratios

Laser Energy (Joules)	Tpeak (Kelvins)	λ peak (Angstroms)	E(7000A) (GIGA Photons str^{-1} A^{-1})	E(1215)	E(300A)
0.25 (1)	85,000 (1)	1000	50 (1)	1650	100
0.5 (2)	170,000 (2)	800	100 (2)	3300	1400
1.0 (4)	350,000 (4)	600	200 (4)	4400	4700

Table 6.2

of quantities corresponding to the 3 laser energies, demonstrating in particular the apparently simple linear behaviour of the calculated peak temperature mentioned earlier. However, the wavelength λ peak at which maximum continuum emission occurs seems to show far less sensitivity to the laser pulse energy and was found to be insensitive to changing the ionisation stage used by the

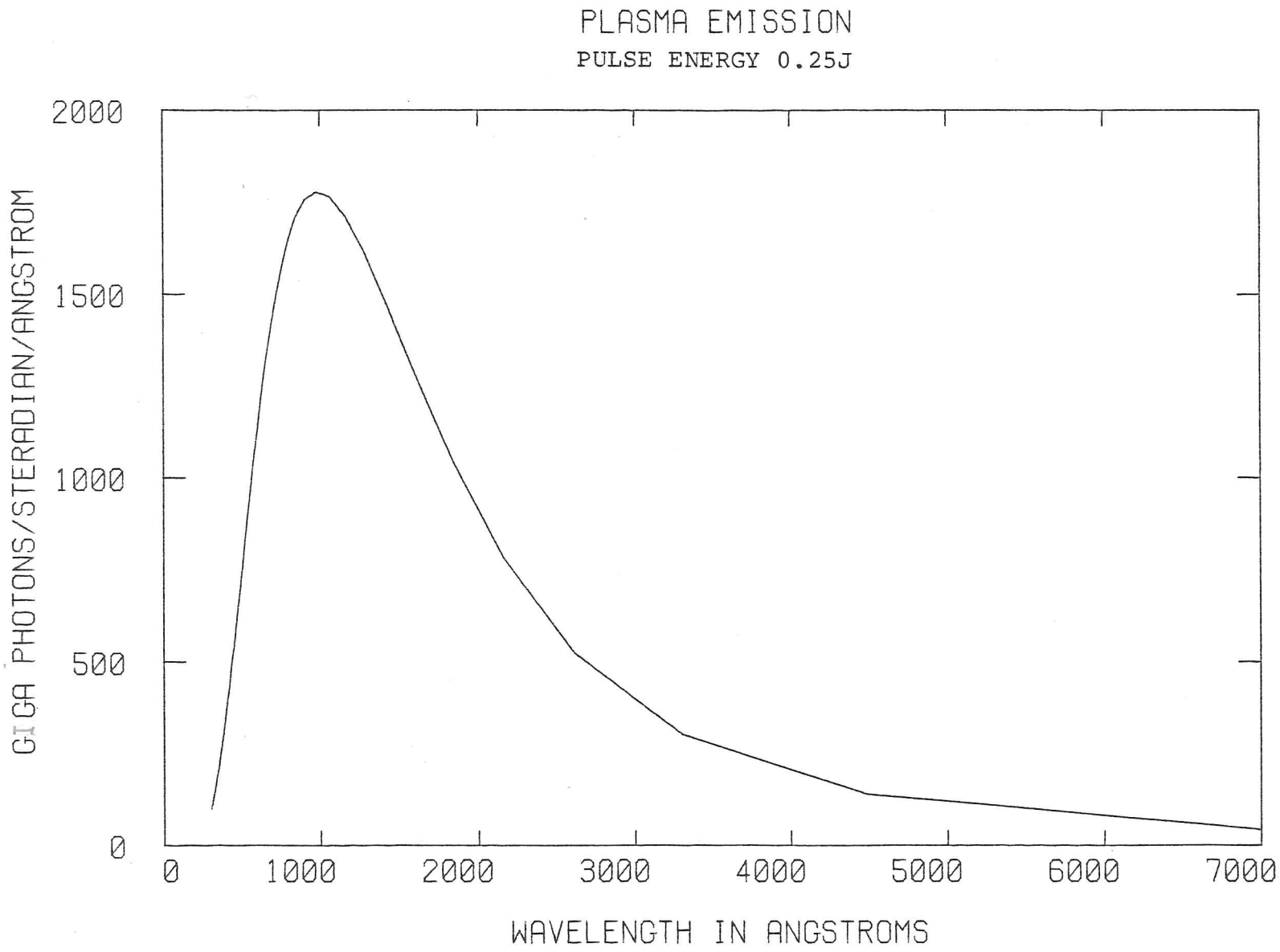
PLASMA EMISSION
PULSE ENERGY 0.25J
GIGA PHOTONS/STERADIAN/ANGSTROM
2000
1500
1000
500
0
0
1000
2000
3000
4000
5000
6000
7000
WAVELENGTH IN ANGSTROMS

Fig.6.8

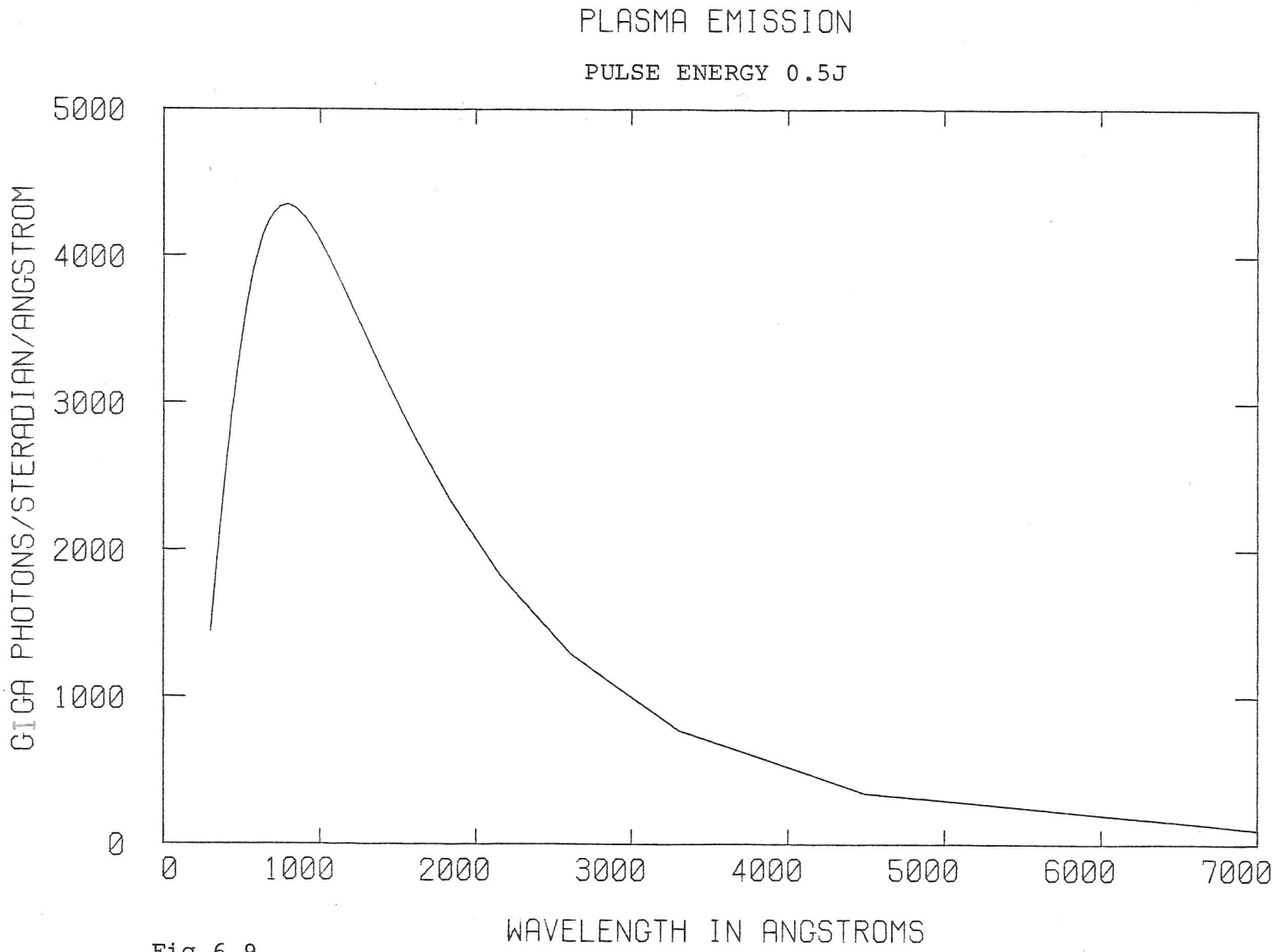
PLASMA EMISSION
PULSE ENERGY 0.5J
GIGA PHOTONS/STERADIAN/ANGSTROM
5000
4000
3000
2000
1000
0
0
1000
2000
3000
4000
5000
6000
7000
WAVELENGTH IN ANGSTROMS

Fig.6.9

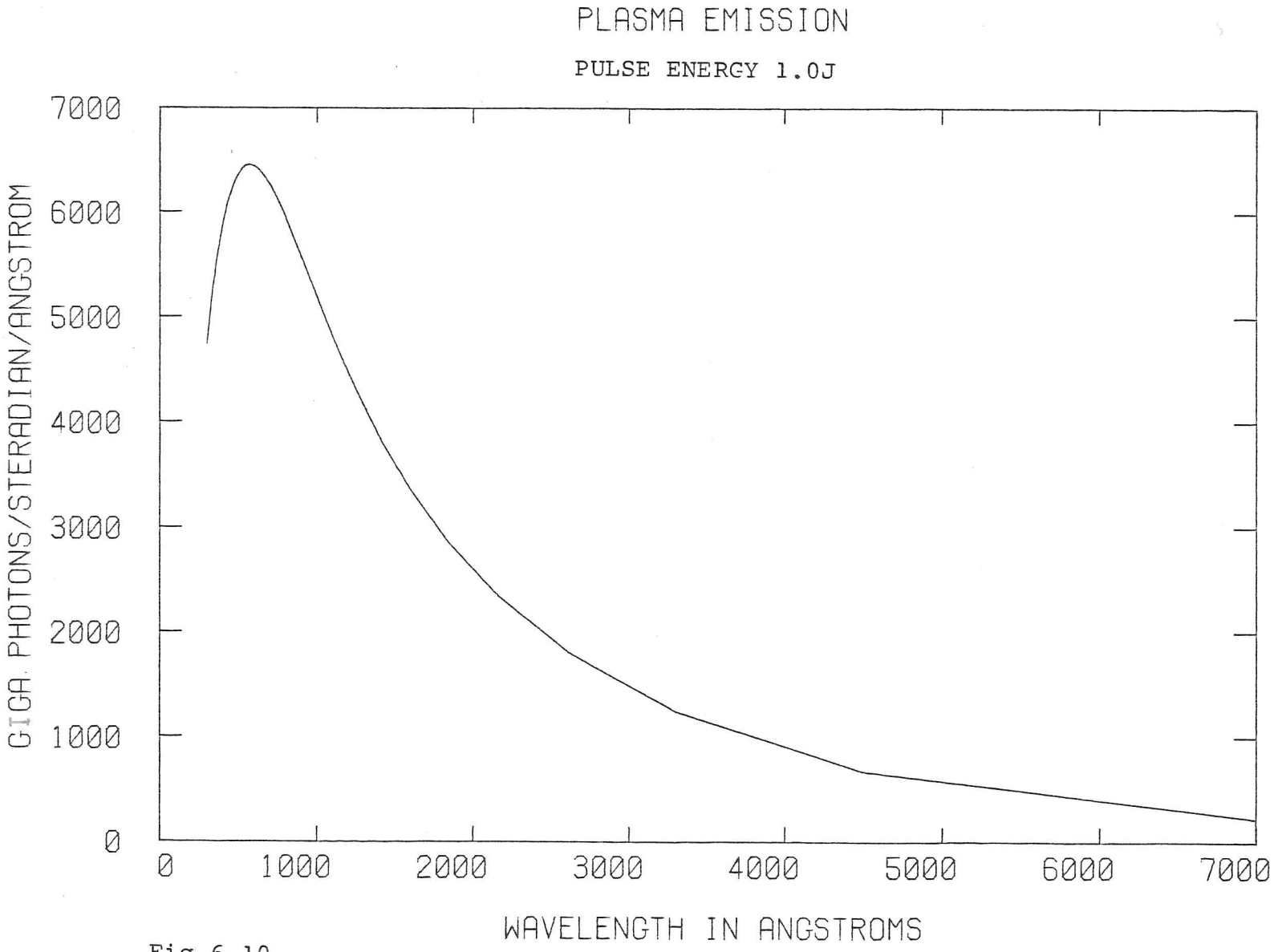
PLASMA EMISSION
PULSE ENERGY 1.0J
GIGA PHOTONS/STERADIAN/ANGSTROM
7000
6000
5000
4000
3000
2000
1000
0
0
1000
2000
3000
4000
5000
6000
7000
WAVELENGTH IN ANGSTROMS

Fig.6.10

computer programs. Interestingly, the emission at long wavelengths shows a rough proportionality to the incident laser energy, when assuming a constant emitting area (see discussion earlier), but the emission behaviour becomes less simple below ~ 1000Å where the photon emission climbs very rapidly towards shorter wavelengths with greater pulse-energies. It has been mentioned that the optical depth at the Ruby wavelength of ~ 7000Å was always greater than one; this is confirmed by the result that the emission calculated in this region was found to be insensitive to variations in Z and, by implication to changes in the absorption coefficient (Equation 6.17). However, towards shorter wavelengths the optical depth is less than one at certain times in the plasma history, falling off as $(Z/\nu)^3$ at these frequencies. This means that when the ionisation stage is increased a fairly small increase in the short wavelength emission will be calculated by the Emission program, although conversly the temperatures also drop a little, being proportional to $1/(1+Z)$ under these particular conditions.

Reviewing the contents of this chapter, it is clear that the dynamics of laser plasmas is complicated and one must draw on a large range of Physics to achieve even a fairly simple picture of the behaviour. One particular example of the limitations of this computer model was the way in which the one-dimensional nature of the initial problem is seen to break down most obviously at later times in the plasma's development. Another serious problem which could not be adequately solved was the transition from a transparent to an opaque plasma, determining the hole depth created by the laser. The next chapter shows that the absolute continuum emission of an Ytterbium laser plasma measured experimentally (Fig. 7.6) does not behave much like the computer model at long wavelengths, but at 1200Å a photon flux is observed similar to that calculated by the model for the same laser energy of 0.5J. At shorter wavelengths the model and the photographs of Chapter 7 are in better agreement with one another. It can be seen from Fig.6.1 that

the rare-earth continua seem to be exceptionally intense at long wavelengths compared with those produced on Tungsten or Tantalum; nonetheless the actual emission of a laser plasma does not always follow too closely the emission predicted by a model based on a Bremsstrahlung absorption process alone. Giant resonances or free-bound transitions may play important roles in determining the relative intensities of the continua at different wavelengths (Carroll et al,1980). What is quite clear, however, is the fact that a laser-produced plasma can produce a substantial amount of continuum radiation in the VUV, the absolute order of magnitude of which can be calculated using the fairly simple computer model described in this chapter.

CHAPTER 7

Experimental characteristics of laser-produced plasmas

Introduction

It was explained at the beginning of the previous chapter that the major interest in laser-produced plasmas lay in their possible use as strong, continuous Vacuum Ultraviolet Sources, either for optoacoustic or photoabsorption spectroscopy. However, an important item of information crucial to their use, namely the absolute intensity spectrum, could not be found easily in any literature which reported the use of these sources for VUV spectroscopy. Although Carroll et al(1980) mention that between one and a hundred laser shots were required in their arrangement for adequate exposure of the spectrograph plate, it was very hard to predict from this what number of shots might be required if a rather different experiment were to be undertaken. Breton et al (1973) studied a laser-plasma source at 1216Å as a possible diagnostic probe for the density distribution of neutral hydrogen atoms in thermonuclear machines. At such a wavelength they concluded 3×10^{13} photons $Å^{-1}$ Str^{-1} per pulse were emitted when a Nd- Glass laser-energy of 10J was incident on a tantalum target for a duration of about 65 ns. A similar arrangement used by Mahajan et al (1979) indicated a continuum flux of 2×10^{11} photons $Å^{-1}$ Str^{-1} per Ruby laser pulse of 2J and 20ns duration. Thus the emission at 1216Å seemed to vary considerably from one laboratory to the next, even when comparable laser irradiances (but different targets), had been used. Clearly, before attempting any serious VUV spectroscopy with a plasma-source, more quantitative information as to the emission intensity at other wavelengths would be very useful.

In order to make complete quantative measurements of the laser plasma over a large range of wavelengths a VUV photometric system is needed, in conjunction with a vacuum monochromator. However, such an instrument was unavailable for use in Cambridge and consequently experiments had to

be restricted to the visible and near ultraviolet wavelengths, employing equipment readily to hand.

The Laser

The high power laser used throughout the experiments described in this thesis was an old 'NELAS' Ruby laser manufactured by International Research and Development Ltd and purchased in 1965. The active cavity was a 6" pink ruby rod, 15/32" in diameter with a front reflector, quartz Fabry-Perot cavity giving approximately a 12% reflectance. The rear reflector consisted of a quartz right-angled prism, similar to a 'corner cube' in its function. For a general description of pulsed ruby lasers and their operation see Lengyl (1972).

The laser was operated in either the free-running or Q-switched mode. Free-running operation was the easiest mode to attain and employed only the laser-cavity mentioned above, with no additional intra-cavity devices. It produced a series of 0.5 μs duration pulses every 5 μs on average, over a total pumping time of 2ms. See photographs 7.1 and 7.2 for typical outputs in the free-running and Q-switched modes respectively.

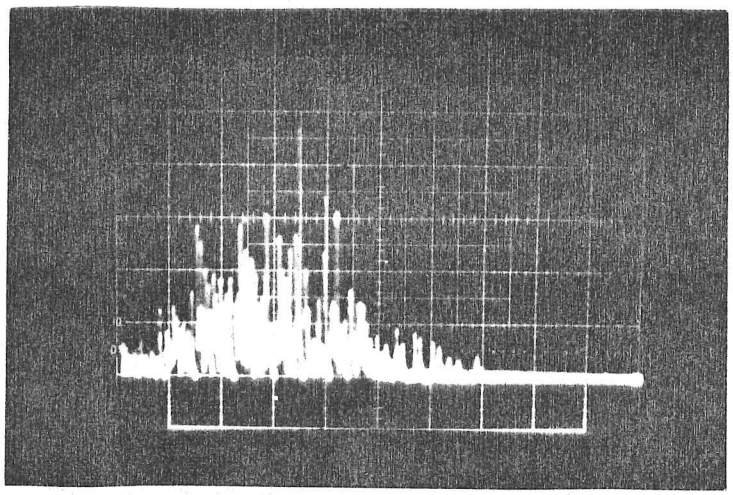

Photograph 7.1 Free-running Ruby laser output.
(timebase 100 μs/Div)

The laser energy was adjusted to be 0.8J per pulse in the free-running mode when fired every two minutes. (A 'pulse' in this context refers to the whole lasing time of about 2ms; in the Q-switched mode it refers to a single, 50ns spike). A more rapid repetition rate caused the ruby rod to overheat with a consequent progressive loss of gain, because only rather slow forced air cooling could be used to remove excess heat from the Ruby. High power commercial lasers with much shorter duty cycles can now be purchased. In the Q-switched mode a fused-quartz flask with optical flats was placed in the cavity, containing Vanadyl Phthalocyanine dye dissolved in nitrobenzene to act as a passive Q-switch. The concentration of the dye was adjusted to produce a 0.5J pulse with a half-powerwidth of 60ns, firing every 5 minutes (photograph 7.2).

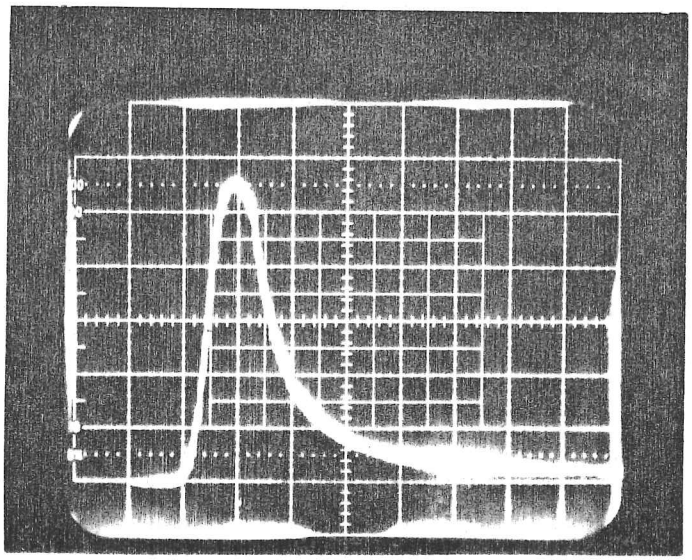

Photograph 7.2 Q-switched Ruby laser output
(timebase 50ns/Div)

In both modes of operation, whether Q-switched or free-running, the laser pulse-energy could be maintained constant to 5% if the repetition rate (in effect the ruby temperature) was kept steady. In all the measurements above, a laser calorimeter together with a fast photo-diode and Tektronix Storage 'scope were employed to find the respective pulse energies and time profiles.

Preliminary Spectrographic Investigations of the laser-plasma emission

As a preliminary to using a 1m. monochromator in conjunction with a photomultiplier to make quantitative measurements, a quartz prism-spectrograph was employed to study the general characteristics of the laser plasma emission throughout the visible and near ultraviolet spectrum. Both Aluminium and Ytterbium metals were used as targets so that a comparison of the extent of line emission for two widely differing atomic numbers (Z = 13 and Z = 70) might be made. The experimental arrangement used is shown in Fig. 7.1.

The 5mm diameter metal target rod was mounted on 6BA Brass studding so that it could be screwed up and down to present a fresh target surface to the incident ruby light whenever necessary. Similarly the photographic plate holder could be moved vertically to enable multiple exposures to be taken on one piece of Ilford FP4 film. The plate-holder arrangement meant the plasma spectra could be easily calibrated for wavelength versus horizontal plate position by taking adjacent exposures using a mercury discharge lamp, placed just in front of the spectrograph entrance slit. Typical spectra of both free-running and Q-switched laser plasmas are shown for Ytterbium and Aluminium in plates 7.1 - 7.4 with their respective microdensitometer scans.

In all cases a large 50μm slit was used to enable spectra from only one laser shot to be photographed, with a consequent resolution of 5Å at 3000Å. The resolution improved rapidly towards shorter wavelengths where the dispersion of the quartz prism increased.

In the free-running mode approximately 400 five kilowatt spikes of ruby radiation were produced each shot, whereas a single Q-switched laser pulse had an average power of 8 megawatts. However, both modes of operation deposited similar amounts of energy onto the target surface, 0.8J and 0.5J respectively. It is apparent from the plates 7.1-7.4

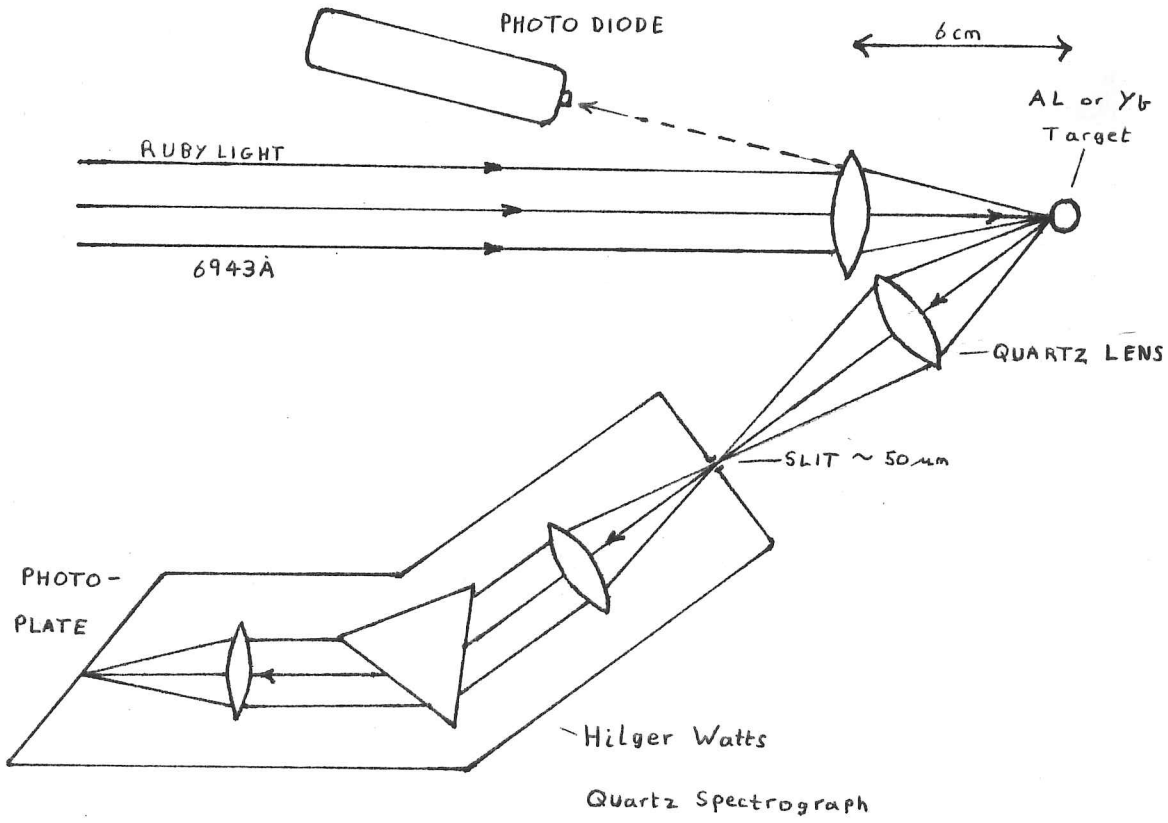

Fig. 7.1 (PLAN VIEW)

1

2

3

4

Plates 7.1 - 7.4

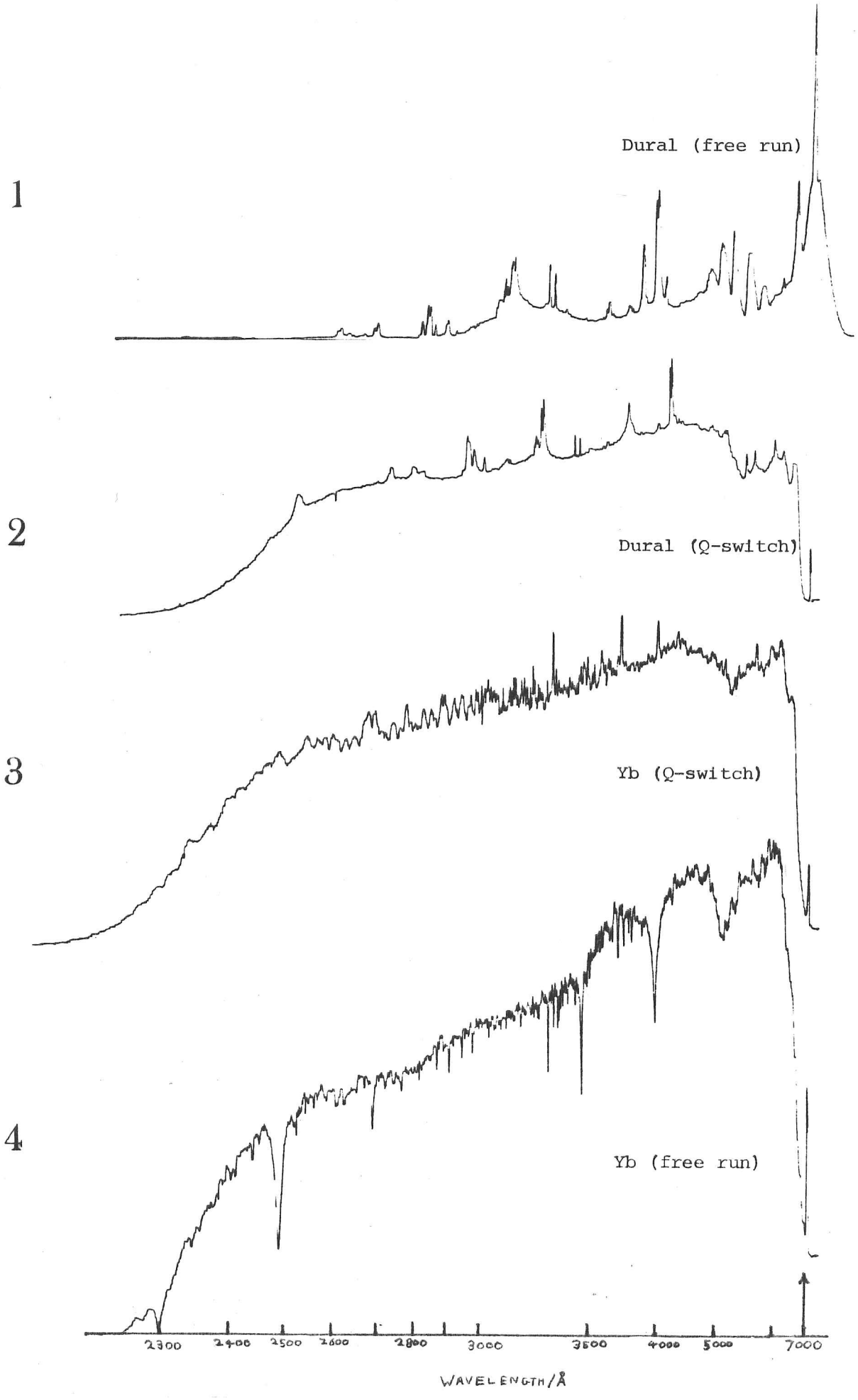

Plates 7.1 - 7.4
(densitometer)

and the densitometer scans that the emission from both Aluminium and Ytterbium is more continuous, with less obvious line structure, when a very high power, but short pulse is incident on the target. The focal area of the laser focusing lens was estimated to be 2×10^{-3} cm^2 (see below) implying an average laser irradiance of 4×10^{10} Wcm^{-2} and probably high electron energies of order 10eV. In the case of a high laser intensity, it is likely a large degree of ionisation was present within the plasma so that bound-free and free-free transitions will have dominated the optical depth of the source, leading to strong continua with little line emission; which would have applied especially towards the longer wavelength where the bound-free and free-free absorption coefficients increase as λ^3 in that limit.(See Chapter 6). Nonetheless, stark broadened emission lines are also visible, making up 10% of the integrated intensity at many discrete wavelengths and in this respect there are some noticeable differences between the spectra for the two elements. The Aluminium Q-switched plasma seems to have a fairly small number of strong, very broad lines with particularly smooth continua in between, whereas the Ytterbium plasma shows numerous lines, but which are weaker and more narrow.

The spectra of the two elements, when under rather low laser irradiances of 3×10^{6} Wcm^{-2} show some startling dissimilarities. In the case of Ytterbium a strong continuum radiation is still produced but shows mostly deep and very broad absorption features within it. On the other hand Aluminium seems to emit relatively little continuum radiation at such a low laser irradiance, showing only very broad emission features dominating the spectrum. A tentative conclusion could be that as the free-running Ytterbium continuum is similar in shape to that produced by a high laser irradiance, then at least the first stage of ionisation must have been reached to provide a bound-free and free-free absorption mechanism, but with many cooler, less excited atoms forming a "Corona" around the plasma

which consequently absorbs continuum light, coming out from the interior. In Aluminium the lack of a strong continuum and the presence of powerful emission lines suggest the first stage of ionisation has not been reached with the low laser irradiance. It is likely that strong continuum emission occurs only if both the temperature is large enough and the first ionisation potential sufficiently low, for any particular target, so that large numbers of free electrons can be produced to take part in continuum-forming transitions. This criterion is expressed succinctly by Saha's equation (Chapter 6).

$$\frac{N_e N_i}{N_o} = \frac{2(2\pi m kT)^{3/2}}{h^3} \frac{U_i(T)}{U_o(T)} e^{-\chi/kT}$$

where Ne and Ni are the electron and ion number densities respectively, Ui and Uo are the appropriate ionic and neutral atom partition functions, generally of order one, T is the temperature of the plasma and χ the first ionisation potential. Using the equation N_o can be estimated for any temperature if $N_{TOT} = Ni + N_o$ is also known. Since the laser-plasma material is effectively lifted off from the target surface and heated, with little time to expand, N_{TOT} will be of the same order as the number density of atoms in the solid target. Thus the fraction N_o/N_{TOT} can be calculated from a model-prediction of the temperature (see Chapter 6) indicating a large number of free electrons when the ratio becomes much less than one. The equation is dicussed more fully in Chapter 6. It must be pointed out that in normal plasma spectroscopy the Saha equation is used the other way round from that proposed here. By identifying the presence of characteristic spectral lines for a particular stage of ionisation, the temperature can roughly be deduced, as in general only adjacent ionisation stages are present at any one time; Burgess et al (1967) show that this may be misleading in some laser-plasmas as high ionisation

stages can be "frozen in" while the plasma expands and subsequently cools.

So far in the preceeding discussion no consideration has been given to the amount of laser energy used up during the initial vapourisation of the target and lost as latent heat. Quite clearly, if the mean laser irradiance is very low the dominant process will be a steady removal of material from the target at its boiling point, with little excess power available to heat the vapourised material any further (see Chapter 6). If the duration of the low laser intensity is also long (eg. 1 ms), deep holes a few millimetres long can be formed in the target; this was found to occur when the free-running mode was employed in the experiments described here, with the consequent serious disadvantage that targets were rapidly destroyed after only a few laser shots. By measuring the diameter of a hole produced by one free-running pulse, an upper-estimate for the focal area of the condensing lens was obtained.

To summarise, it appears that high laser irradiances of 10^{10} Wcm^{-2} cause substantial heating of the vapourised target material, leading to a high degree of ionisation and a fairly uniform continuum with few line spectra superimposed. Because the plasma becomes rapidly opaque it consequently screens the target surface from any further laser induced vapourisation, resulting in very little target damage from shot to shot. With lower laser irradiances of 10^{6} Wcm^{-2}, but with similar total pulse energies, a low temperature plasma is formed near the boiling point of the target. The degree of ionisation and hence the strength of the continuum emission then becomes critically dependent on the target material used and strong line spectra are likely to be seen. As the plasma will be insufficiently ionised to become opaque to the exciting laser radiation, continuous vapourisation of the target material results, leading to substantial laser damage.

The absolute photon emission of a laser-plasma in the range 2500Å - 6500Å.

The qualitative aspects of laser produced plasmas were briefly described in the previous section, with the conclusion that high-power laser fluxes of 10^{10} Wcm^{-2} on both Aluminium and Ytterbium targets produced fairly line-free continua. The aim of all these investigations was to understand the intensity distribution of the continua throughout the spectrum, but with a particular emphasis towards the VUV. As Carroll(1980) pointed out, Ytterbium seems to produce the most uniform and line-free spectra in the VUV region, making this metal an obvious choice for the rather inaccurate, but tricky experimental determination of the photon flux from its plasma.

Although the spectrographically determined continua of Ytterbium produced either by free-running or Q-switched laser pulses were of similar structure and extent, the strong, broad absorption lines also present when the free-running mode was used could have given peculiar results if intensity measurements were to be made at only a few discrete wavelengths. For this reason, together with the ultimate aim to use "hot" continua in the VUV, it was decided that Q-switched operation should be employed for the experiment, with the spectrographic results suggesting that any flux determination found in this mode should also apply to free-running operation with the differences noted above. The experimental arrangement used to measure the emission is shown in Fig. 7.2.

In contrast to the damage produced by a free-running laser pulse of similar energy, only a shallow hole (1 μm) was created by the Q-switched operation. This meant it was unnecessary to alter the target surface very often, (it could be done by screwing the Yb up or down its brass studding), because the plasma intensity remained reproducible to within 20% over many tens of laser shots at any particular

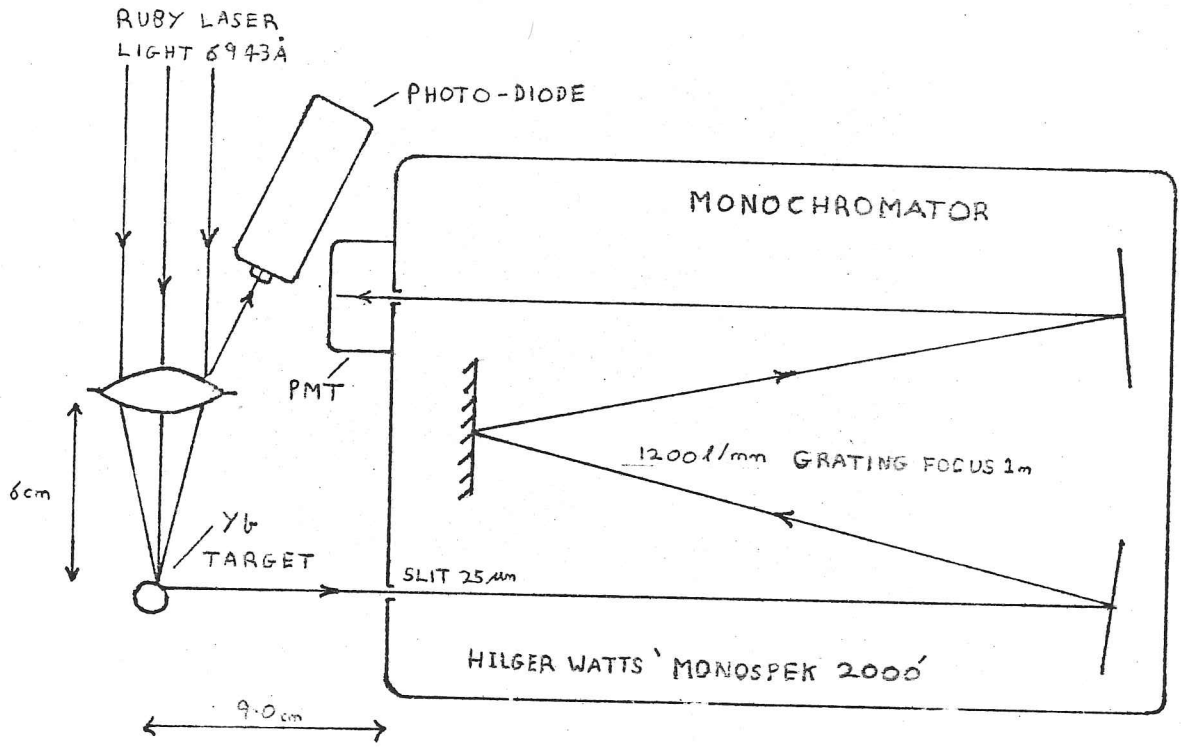

Fig. 7.2 (PLAN VIEW)

wavelength. Except for the laser focusing lens, no other glass optics were used, to ensure that subsequent black-body calibrations of the monochromator/PMT system would be reliable, which depended on all the optics being filled to a predictable and predetermined amount. The photomultiplier current was integrated over 1.5 μs by a fast operational amplifier circuit which displayed the integrated PMT charge and its subsequent decay on a Tektronix 466 Fast Storage Oscilloscope. Correct 'scope triggering was arranged by taking a trigger pulse from a fast photodiode monitoring scattered laser light off the focusing lens. The multi-chromatic continuum emission monitored by a photo-diode placed between the target and the monochromator entrance slit is shown in photo 7.3 from which it can be implied that the power emission of the plasma was comparable to that of the laser pulse and was present for about 500 ns, a factor of ten greater than the duration of the laser excitation (photo 7.2). Therefore a photomultiplier integration time of 1.5 μs was chosen, long enough to sum the total photon flux arriving at the photomultiplier.

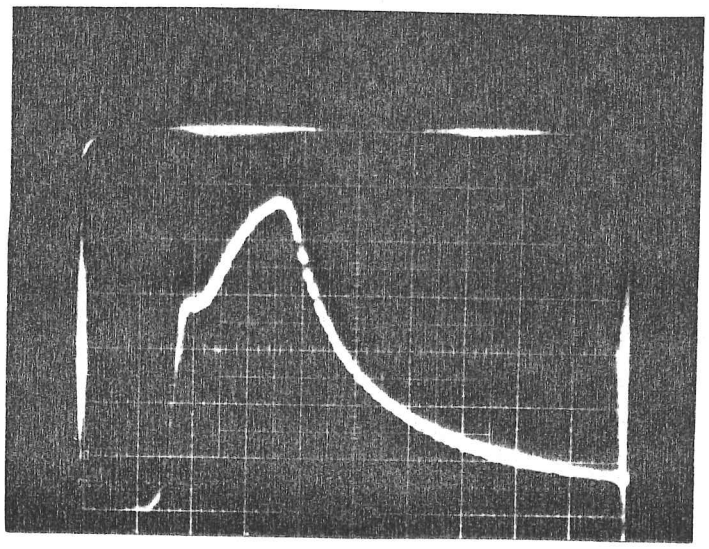

Photograph 7.3 Q-switched multichromatic plasma emission (timebase 50nsecs/div)

Measurements were taken at five minute intervals with a Q-switched laser energy of 0.5J per pulse. Before the laser fired, the storage 'scope was cleared, reset and when necessary a new discrete wavelength was selected on the monchromator. During the experiment the entrance slit was kept at 25μm and a total of three readings were taken for every wavelength selected, demonstrating a reproducibility of 20% over the range 2500Å-6500Å.

Black-body calibration of the detection system

Some means was required by which the very non-uniform response of the monochromator/photomultiplier system could be calibrated for absolute intensity as a function of wavelength. Non-uniform wavelength response was removed after relative transmission measurements of the monochromator at various wavelengths had been made to correct for second order wavelengths detected in the first order of the grating. Following this adjustment the monochromator transmission could be considered uniform with wavelength, with subsequent justification. By far the most important cause of non-uniformity was the

quantum efficiency of the EMI photo-tube used. After all the signals had been divided by the published quantum efficiencies, a roughly uniform response was obtained over the middle and shorter wavelengths; which left only the difficult task of absolute calibration to be undertaken.

The simplest solution to this problem was to use a quartz-halogen lamp with a fairly well known and uniform emissivity which behaves like a black-body source over the wavelength region 2500Å-6500Å. The principles can be outlined in the following way. Thorne (1979) gives the total radiation power (including two polarisations) emitted by a black-body source at temperature T as

$$B_o(\lambda,T)\,d\lambda = \frac{2hc^2}{\lambda^5}\,\frac{1}{e^{hc/\lambda kT}-1}\,d\lambda \quad Wm^{-2}Str^{-1}$$

For a 'grey' body $B(\lambda,T) = B_o(\lambda,T)\,\varepsilon(\lambda,T)$ where $\varepsilon(\lambda,T)$ is the emissivity of the hot body. If we denote the wavelength at which $B(\lambda,T)$ is a maximum to be λ_m then Wien's law states

$$\lambda_m T = \text{Const} = 2.9 \times 10^{-3}\ mK$$

At any particular wavelength $I(\lambda)$ $[V\,str^{-1}\,Å^{-1}]$ measured by a linear detection system should be proportional to $B(\lambda,T)$. Thus if a is the emitting area of the black body source and $\Delta\lambda$ and $\Delta\Omega$ are the respective wavelength and solid angle increments perceived by the detection system

$$a\,B(\lambda,T)\,\Delta\lambda\,\Delta\Omega \approx K_o\,I(\lambda)\,\Delta\lambda\,\Delta\Omega$$

(Watts)

where K_o is a calibration constant to be determined, and is independent of λ if the system response is uniform. Since $(hc/\lambda kT)$ is much greater than one in the spectral range con-

sidered, the voltage $V(\lambda)$ measured by the system as a function of wavelength is well approximated by the expression

$$V(\lambda) = I(\lambda)\Delta\lambda_B\Delta\Omega_B \approx \frac{(2hc^2\varepsilon\alpha\Delta\lambda_B\Delta\Omega_B)}{K_o}\frac{e^{-\frac{hc}{KT\lambda}}}{\lambda^5}$$

$$= \frac{A\, e^{-\frac{hc}{KT\lambda}}}{\lambda^5} \quad \text{Volts}$$

where $K_o = 2\alpha\varepsilon hc^2\Delta\lambda_B\Delta\Omega_B/A$ and the subscript B refers to the black-body source. Taking logarithms

$$F(\lambda) = \ln(V\lambda^5) = \ln A - \left(\frac{hc}{KT}\right)\frac{1}{\lambda}$$

and a plot of $F(\lambda)$ versus $(1/\lambda)$ for a uniform detection system should give a straight line of slope hc/KT with an intercept $\ln A$, which will in turn yield the respective black-body source temperature and system calibration constants. Thus $P(\lambda)$, the power emitted by the plasma (or any other source measured with the detection system), which has units of $(W\ str^{-1}\ \text{Å}^{-1})$ is given by

$$P(\lambda)\Delta\Omega_p\Delta\lambda_p = K_o I(\lambda)\Delta\Omega_p\Delta\lambda_p = K_o V(\lambda)$$

$$P(\lambda) = \frac{(2\alpha\varepsilon hc^2)}{A}\left(\frac{\Delta\lambda_B\Delta\Omega_B}{\Delta\lambda_p\Delta\Omega_p}\right)V(\lambda)$$

where the subscripts B and P refer to quantities determined by the dimensions of monochromator entrance slit, subtended at the black-body and plasma sources respectively.

Figure 7.3 shows schematically the quantities $\Delta\Omega$ and $\Delta\lambda$ which have to be measured. If the pinhole source of area S uniformly fills the whole entrance slit with light both vertically, as well as horizontally, only the slit width

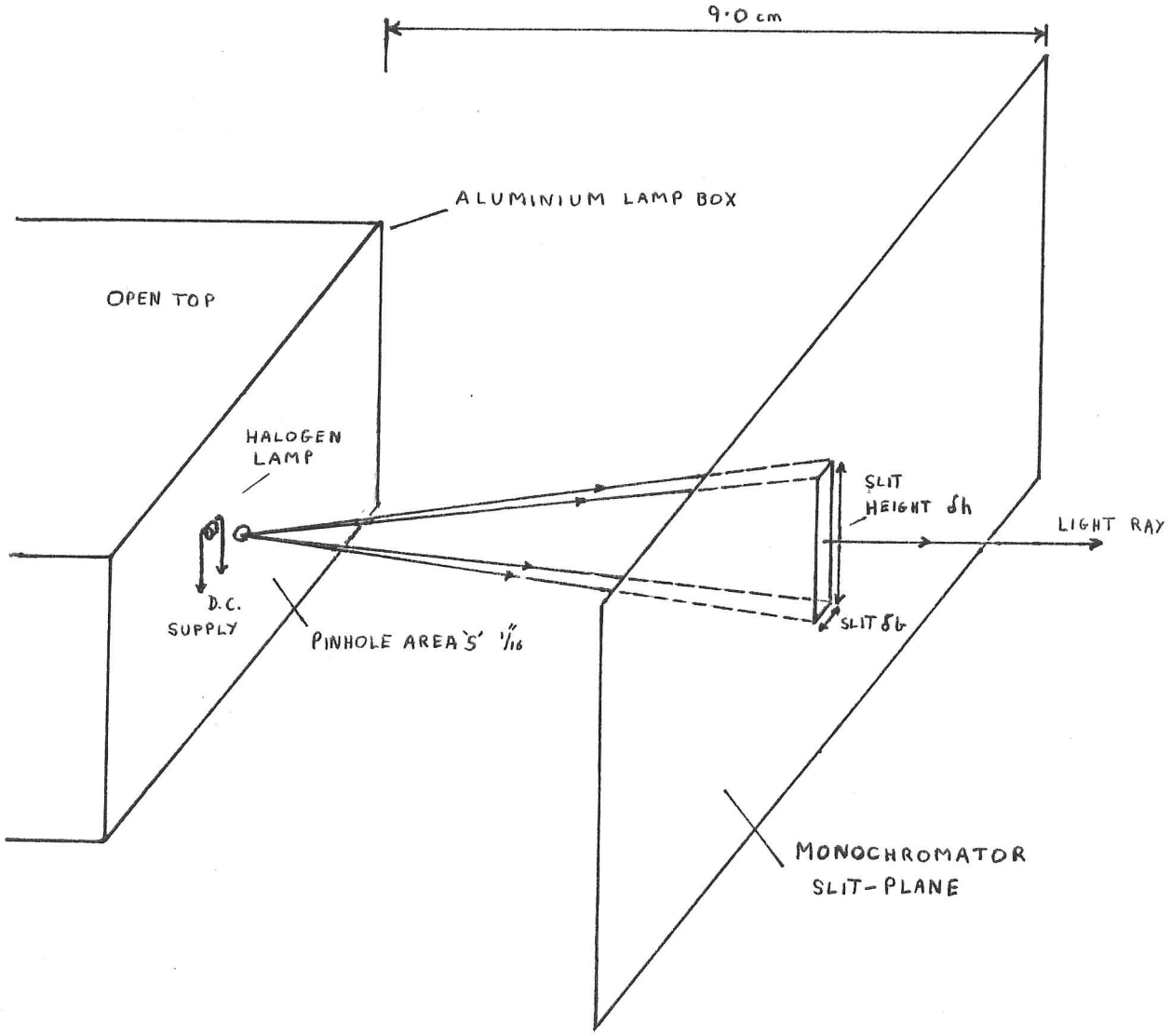

Fig. 7.3

$$\Delta\Omega = \frac{\delta h\, \delta b}{r^2} \qquad \Delta\lambda \propto \delta b$$

will determine the solid angle of light accepted by the monochromator.

The quartz-halogen lamp was placed so that the densely wound filament was about 3mm from the pinhole, in an aluminium screening box as close to the wall as the glass bulb would allow. This arrangement permitted the approximation to be made that the pinhole area S was roughly the same as the emitting area a of the filament, radiating out into a hemisperical solid angle based on the pinhole. It is likely the largest systematic error came from this approximation and may have caused the final, calculated, absolute intensity to be in error by a factor of two. The lamp assembly was placed with the pinhole in the same position as the plasma source had been, in front of the monochromator entrance slit and operated on a direct-current, current-limited power supply to ensure reproducibility and to minimise any systematic fluctuations of the light intensity. To measure the light intensity detected on a Tektronix Storage 'scope, a light-chopper was introduced between the pinhole and the slit, which gave the advantage that none of the electronic coupling had to be adjusted when moving from the plasma to the calibration source.

As mentioned above, adjustments had to be made to the voltages recorded as a function of wavelength. First, 2nd Order signals present in the 1st Order were considered and dismissed as insignificant. (When measuring the plasma, 2nd Order grating components could not be ignored due to the much higher ultraviolet intensity). Next, the voltages were divided by quoted EMI values of quantum efficiency for the photomultiplier and finally a graph of $\ln(V\lambda^5)$ versus $(1/\lambda)$ was plotted (Fig.7.4). The points at wavelengths shorter than 6000Å all fit well onto a straight line, but the scatter noticeably increases towards 2000Å where the detected light is very small. The deviation from linearity at wavelengths greater than 6000Å implies the quantum efficiency quoted by EMI in the wavelength region is too low by

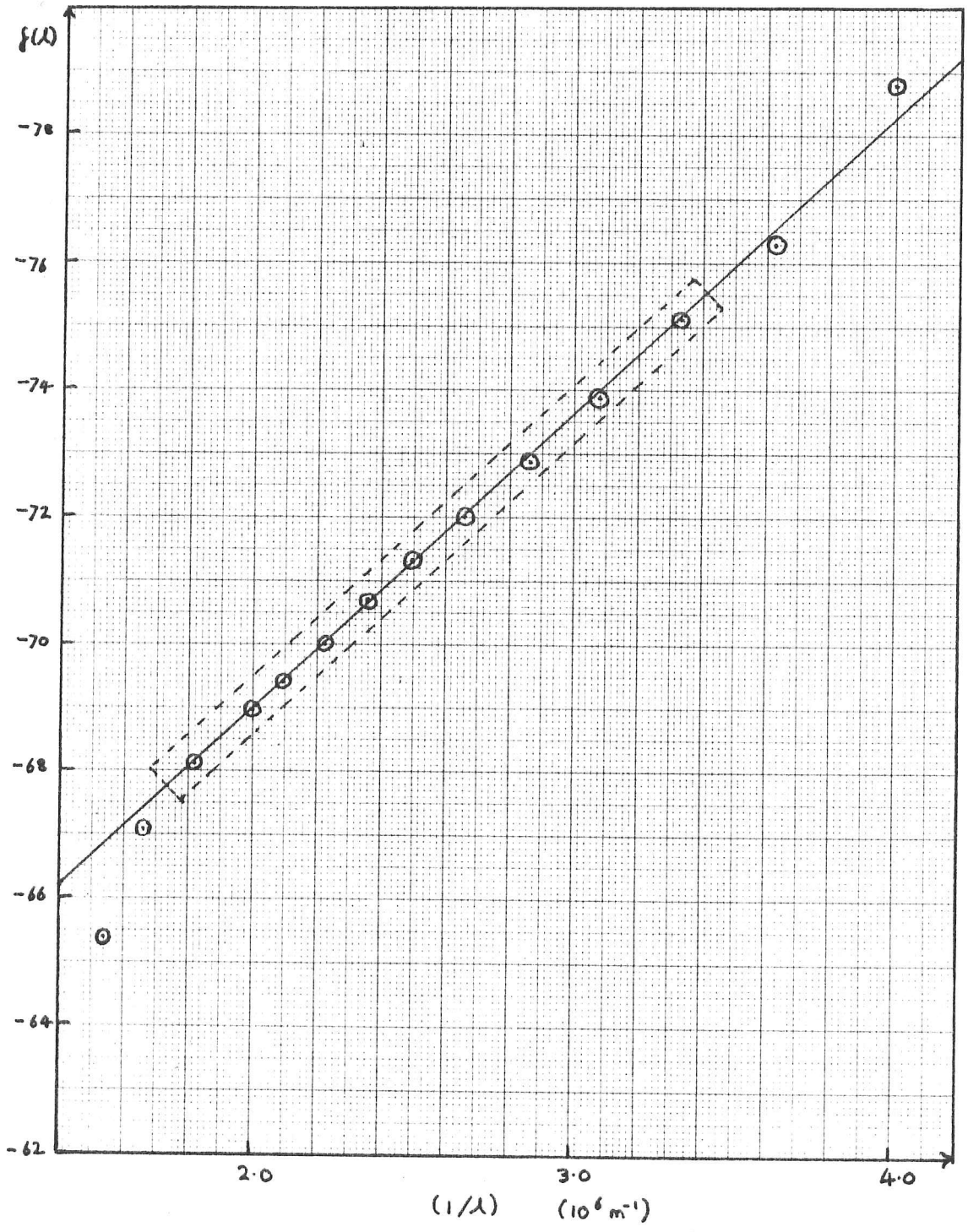

Fig.7.4

a steadily increasing factor. The discrepancy was allowed for in later calculations to permit extrapolation up to 6500Å. From the slope of the graph, a black-body temperature of 3080 ± 60K for the quartz halogen lamp has been deduced and the intercept $\ln A$ is -59.6 ± .2. Because the graph drawn (Fig. 7.4) was linear and it indicated a realistic temperature, the data adjustments described were considered satisfactory and the procedure was used to calibrate time-integrated intensity measurements of the laser-plasma emission.

During the calibration procedure a constant K_o was obtained which related the emitted power to a time independent signal voltage recorded on the 'scope (ignoring the low-frequency light-chopper). On the other hand, during measurements of the plasma, the maximum of a 'decay-spike' voltage was recorded, proportional to the integral of the time-dependent emission. These two different types of voltage-recording had to be reconciled if the steady-state calibration procedure was to be applied to time-integrated measurements. The calibration constant K_o was found such that $K_o V = P \Delta\Omega_p \Delta\lambda_p$ (Watts).
The circuit diagram of an equivalent charge source (the PMT) and its input is shown schematically in Fig.7.5, together with the light and voltage pulses received and transmitted by the circuit. The time constant $\tau = RC'$ has already been mentioned; it is the 1.5μs integration time, which was long compared to the light pulse. Thus when the PMT received a 100ns light pulse it nearly instantaneously dumped an amount of charge q , proportional to the total number of photons in the pulse, onto the capacitor; which then slowly decayed through the resistor, producing an exponentially decaying voltage displayed on the Storage scope. The peak of the decay pulse Vmax was recorded during all measurements of the plasma emission and was related to the total energy E ($J\ sr^{-1}\ Å^{-1}$) of the light pulse, by the following argument

(see over)

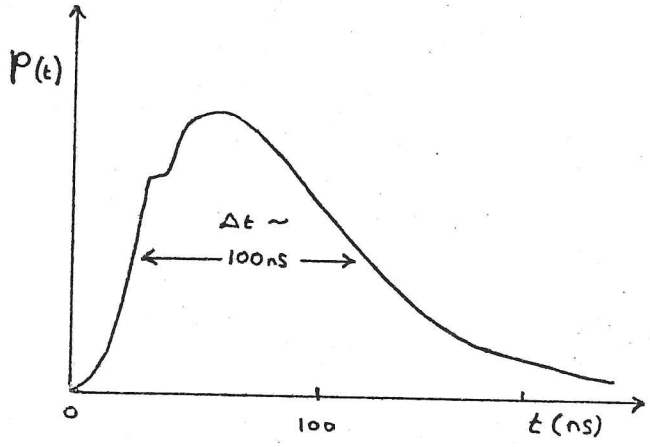
P(t)
Δt ~
100nS
0
100
t (nS)

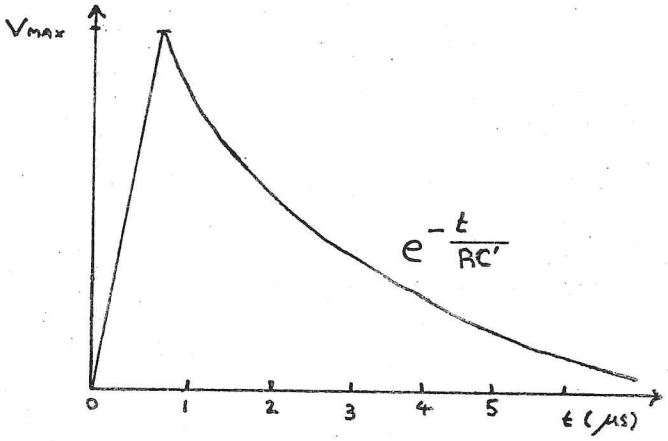
Vmax
e^{-t/RC'}
0
1
2
3
4
5
t (μs)

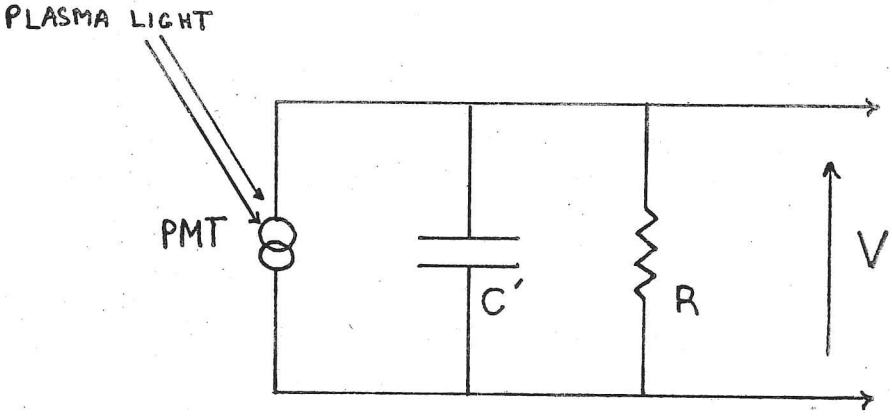
PLASMA LIGHT
PMT
C'
R
V

Fig. 7.5

$$V_{max} = \frac{q}{C'} = \int_0^t \frac{I(t)\,dt}{C'} = \int_0^t \frac{V_p(t)\,dt}{RC'}$$

$$= \int_0^t \frac{P \Delta\lambda \Delta\Omega\, dt}{K_o RC'} = \frac{E \Delta\lambda \Delta\Omega}{K_o RC'} .$$

Hence

$$E(\lambda) = \frac{K_o RC'}{\Delta\lambda_p \Delta\Omega_p} V(\lambda)$$

$$= \frac{(2a\varepsilon hc^2)RC'}{A} \frac{\Delta\lambda_B \Delta\Omega_B}{\Delta\lambda_p \Delta\Omega_p} V(\lambda)$$

or more conveniently

$$N(\lambda) = \frac{E(\lambda)}{h\nu} = \frac{(2a\varepsilon c)\,RC'}{A} \frac{\Delta\lambda_B \Delta\Omega_B}{\Delta\lambda_p \Delta\Omega_p} \lambda V(\lambda) \text{ photons str}^{-1} \text{Å}^{-1}$$

All the above quantities were known or had been measured; $\left(\frac{\Delta\lambda_B \Delta\Omega_B}{\Delta\lambda_p \Delta\Omega_p}\right)$ was simply equal to the ratio of the squares of the slit widths used for the two different parts of the experiment, because the slit height was kept constant. After manipulating calibration and laser plasma measurements Fig. 7.6 was drawn, which displays the total photon output (Photons Str^{-1} Å^{-1}) as a function of wavelength caused by a 0.5J Q-switched laser pulse with a 60ns half-power width. The error bars on the graph denote an estimated random error caused mostly by variations of the plasma emission over the three shots fired at each wavelength. As mentioned earlier, the estimation of the emitting area of the quartz-halogen lamp may have held a systematic error, but was probably no greater than a factor of 2.

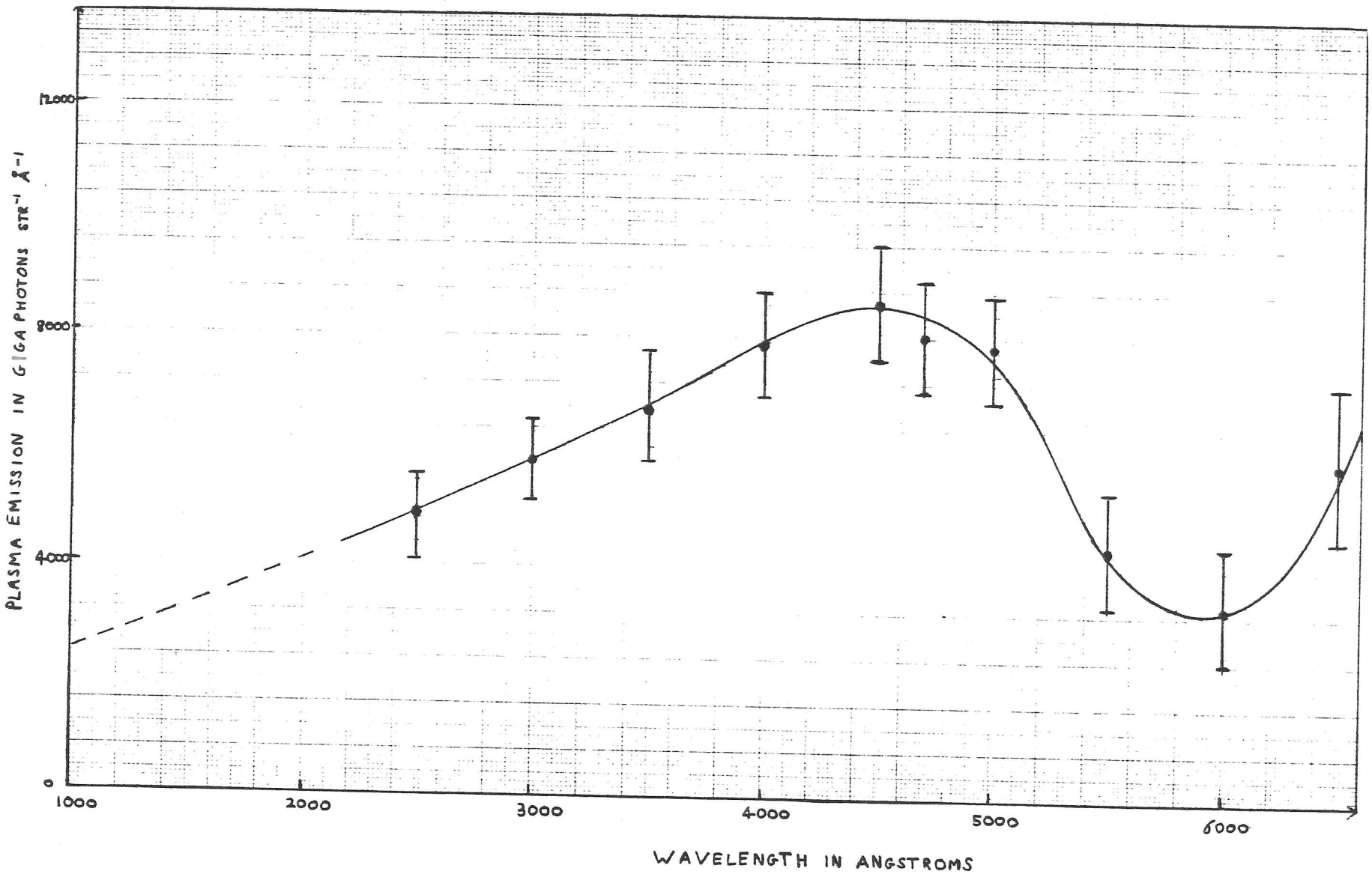
PLASMA EMISSION IN GIGA PHOTONS STR⁻¹ Å⁻¹
12000
8000
4000
0
1000
2000
3000
4000
5000
6000
WAVELENGTH IN ANGSTROMS

Fig. 7.6

It is reassuring to note that Fig. 7.6 has the same characteristics as the spectrograph plates of the Ytterbium laser plasma (Plates 7.1 - 7.4), assuming the photographic emulsion darkens in proportion to the incident number of photons. Allowance has to be made for the cut off of the film emulsion, outside the range 2300-7000A, but when this is taken into consideration, together with the non-linear wavelength scale, a fairly good match can be seen.

By extrapolating the curve of Fig.7.6 to 1216A a flux of 3×10^{12} photons $Str^{-1} A^{-1}$ might plausibly have been measured in an evacuated experiment. This extrapolation should be compared with the quantities measured by Breton et al (1973) and Mahajan et al (1979) in Table 7.1. (All the measurements refer to 1216A).

Researchers	Target	Focal area (mm^2)	Pulse Energy (J)	Pulse time (ns)	Photon Emission ($Ster^{-1}$ A^{-1})
Breton et al (1973)	Tantalum	5×10^{-2}	10 (Nd Glass)	65	3×10^{13}
Mahajan (1979)	Copper	3×10^{-2}	2 (Ruby)	20	2×10^{11}
This work	Yb	2×10^{-1}	0.5 "	60	3×10^{12}
This work	Yb	2×10^{-1}	0.8 (free running)	500	4×10^{12}
Theoretical model in (Chapter 6)	Yb	2×10^{-1}	1	60	4×10^{12}
	Yb	2×10^{-1}	0.5	60	3×10^{12}

Table 7.1

It is interesting that experiments with such widely differing laser parameters all seem to produce photon fluxes of the order 10^{12} photons str^{-1} $Å^{-1}$ at 1216Å including a rough agreement with the crude model described in Chapter 6. The free-running entry in the table is derived by scaling the Q-switched extrapolated emission found above by the ratios of the densitometer scans at long wavelengths shown in Plates (7.1 - 7.4). The ratio happens to be that of the free-running laser energy to the Q-switched energy ie. 0.8/0.5, but it is probably naive to deduce from this that the photon emission from a laser plasma is solely proportional to the pulse energy. However, a similar behaviour was observed at long wavelengths in Chapter 6, using the computer model described; such a deduction would cause the largest value shown in the table to fit better with the others.

From these results and those of others, it is clear that a high photon emission can be obtained easily from a variety of laser-plasma sources; given a suitable selection of target materials the radiation will form clean continua over most of the visible and VUV wavelengths.

Faraday rotation of a He/Ne laser passed through the plasma

When studying the continuum emission of a laser produced plasma it can be seen from Fig. 7.6 that the intensity apparently increases towards longer wavelengths. The same behaviour was visible in Plates 7.1 - 7.4, followed by a very sharp cutoff at 7000Å. It has been stated that the cutoff was almost certainly due to an insensitive emulsion, but when first seen it stimulated speculation that an average plasma frequency might occur near the wavelength of the exciting Ruby laser, at which point continuum emission would first increase and then diminish towards longer wavelengths. The free-electron density within the target was about 10^{22} electrons cm^{-3} and could be connected

to a plasma frequency cutoff ω_p in the metal using the expression (Chapter 6)

$$\omega_p = \sqrt{\frac{Ne^2}{m_e \varepsilon_0}}$$

yielding a value of 10^{15} Hz or about a 2000Å wavelength cutoff. The hypothesis was that during the initial vapourisation of the target surface, material was probably lifted off at a density near to that of the metal and the laser pulse only coupled strongly to heat the vapour when the plasma frequency was below that of the laser radiation, at which point it would no longer have been reflected but instead was able to penetrate and heat up the fireball, accelerating its expansion. This picture could only be qualitatively correct as a very high collision frequency $\sim 10^{13}$ Hz within the dense material will cause large amounts of damping with a consequent absorption mechanism for the laser light below the plasma's critical frequency. Experimental evidence of an electron density, near to that of the metal in the early history of the plasma was required to substantiate this speculation. However, most researchers employing either spectroscopic or probe-techniques to determine the electron density report no more than 10^{19} cm^{-3} (Ready, 1971), in a region about 1mm in front of the target. One exception was that of Burgess et al (1967), who used pressure broadening of spectral lines at 100Å to deduce electron densities of 10^{21} cm^{-3} near to 2.4×10^{21} cm^{-3} which corresponds to Ruby laser radiation. Unfortunately, at these densities the pressure broadening at visible wavelengths would have created spectral widths of many tens of Angstroms which could not have been seen on top of the underlying continuum in the spectrographic observations described above. It is true that many lines in Plates 7.1-4 have obvious Lorentzian, pressure broadened profiles of 20Å width, but these lines imply electron densities of only 10^{18} cm^{-3} (Thorne, 1979) and most

likely provide information about a later stage in the plasma development. Hence a probe technique was needed which would be sensitive to high electron densities close to the target, early on in the plasma history.

The Faraday rotation of radio waves passing through long columns of ionised gas in magnetically permeated interstellar space has been a useful tool for some time, providing Astronomers with an estimate of the longitudinal magnetic fields or path integrated number densities in HII regions within our galaxy. The quantities involved are usually so small that a rotation of the plane of polarisation of a radio wave by one degree typically occurs over many light years of travel through ionised gas columns. But, if the ionised gas is sufficiently dense, near to that of a laser plasma, the path lengths required to rotate a linearly polarised He/Ne laser beam a few degress in a magnetic field of 1 Tesla shorten considerably, becoming a centimetre or less. When the approximate rotation formula used by Astronomers is adjusted for the special case where the probe radiation is near to the plasma frequency of the gas the required path length can be shortened further by a factor

$$\left(1 - \frac{\omega_p^2}{\omega^2}\right)^{1/2}$$

For the He /Ne laser the criterion should certainly be satisfied when electron densities of 10^{21} cm^{-3} are present in the laser plasma. Because of this it was decided that an attempt could be made to probe the laser plasma by looking for Faraday rotation of a lower power, He /Ne laser passed just in front of the target, parallel to a magnetic field of roughly 1 T, produced by an electromagnet.

Bekefi (1966) discusses many radiation processes in plasmas and gives expressions for the dielectric constant in a cold, anisotropic plasma when collisions at a well defined frequency ν are also present (See Chapter 6). From the

dielectric constant an expression for the anisotropic refractive index correct to 2nd order terms in (ν/ω) can be obtained, in turn yielding the amount of Faraday rotation produced as a function of the magnetic path, near the plasma frequency ω_p.

$$n_\pm \approx n_0 \left[\left(1 + \frac{\nu^2}{\omega^2} \frac{(1+3n_0^2)(1-n_0^2)}{8 n_0^4} \right) \pm \frac{(1-n_0^2)}{2 n_0^2} \frac{\omega_c}{\omega} \right]$$

$$\text{if} \quad n_0^2 = 1 - \frac{\omega_p^2}{\omega^2} \qquad \omega_c = \frac{eB}{m_e} \qquad \frac{\omega_c}{\omega} << \frac{\nu}{\omega} << 1$$

For Left (+) and Right (-) circularly polarised radiation propagating along the magnetic field $\underline{B}$.

$$|\theta_F| = \frac{(n^+ - n^-)}{2} k_0 x = \frac{x}{2c} \frac{(1 - n_0^2)}{n_0} \omega_c$$

$$\Rightarrow \qquad |\theta_F| \approx \frac{l}{2c} \left(\frac{\omega_p}{\omega} \right)^2 \frac{1}{(1 - \omega_p^2/\omega^2)^{1/2}} \omega_c$$

where the cyclotron frequency ω_c is proportional to the uniform magnetic field $\underline{B}$ and l is the path length. Surprisingly, when considering terms of order $(\nu/\omega)^2$ or greater, the collision frequency does not enter into the expression for θ_F. Presumably the singularity at $\omega = \omega_p$ can be avoided by the inclusion of higher order damping terms. This behaviour should be compared to that of the refractive index for left and right handed circularly polarised radiation in a magnetic field derived from the dielectric constants given by Bekefi (1966) for a cold, anisotropic plasma and shown as $n_\pm$ above.

For a field of 1T n_0 is altered by a fraction $\omega_c/\omega \sim 10^{-4}$ if ω corresponds to He /Ne laser radiation at 6328Å suggesting that the application of a magnetic field to the light beam passing through the plasma should not produce a

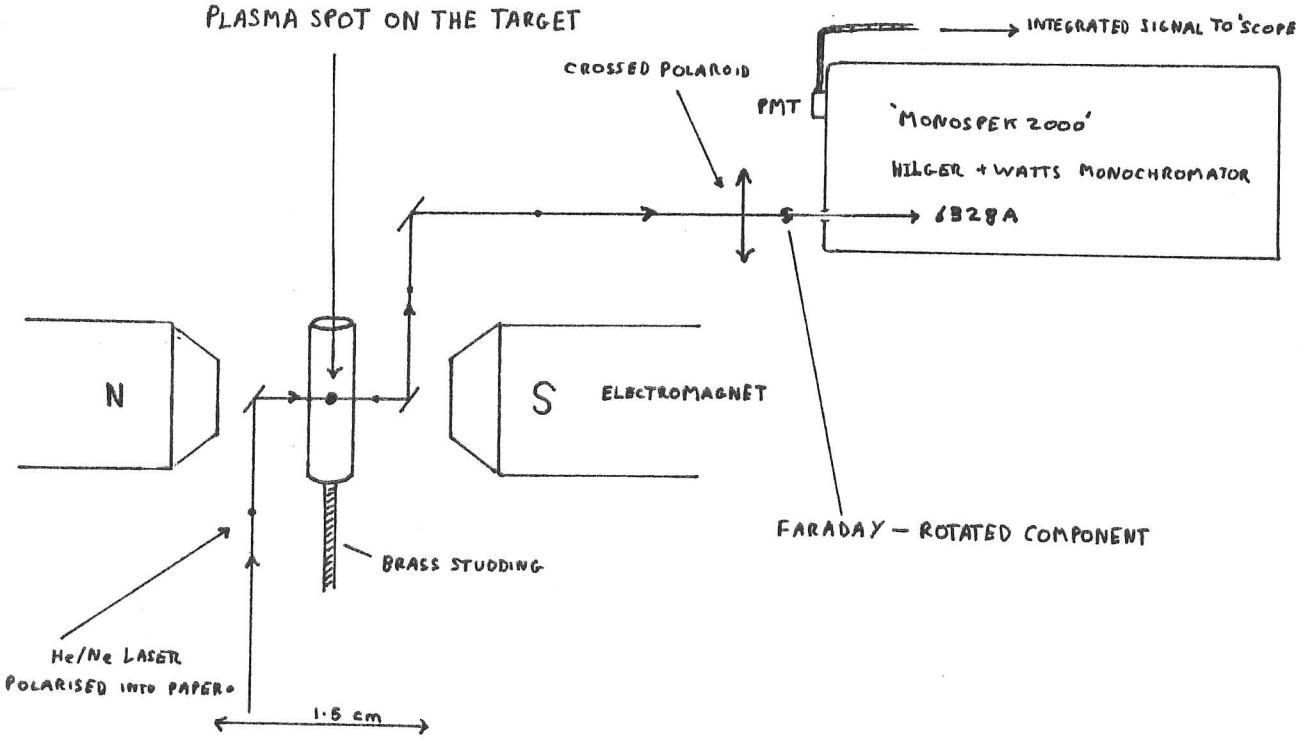
PLASMA SPOT ON THE TARGET
INTEGRATED SIGNAL TO 'SCOPE
CROSSED POLAROID
PMT
'MONOSPEK 2000'
HILGER + WATTS MONOCHROMATOR
6328A
N
S
ELECTROMAGNET
FARADAY – ROTATED COMPONENT
BRASS STUDDING
He/Ne LASER
POLARISED INTO PAPER
1·5 cm

Fig.7.7

measurable change in the transmitted intensity, considering the optical depth which is inversely proportional to n, hardly effects the black body emission except in the optically thin case and even then only by a fraction ω_c/ω (See Chapter 6). Without this complication use can be made of crossed polaroids to measure any Faraday rotation caused by the anisotropic plasma. The experiment attempted is shown schematically in Fig. 7.7.

The initially polarised He/Ne laser light was passed by means of a 'periscope' in front of the target, grazing the surface where the laser plasma was formed, with the light beam parallel to the field produced by the eletromagnet pole pieces. The beam next passed through a 'crossed' polaroid whose transmission line was set at right angles to the beam polarisation, normally preventing laser light from reaching the monochromator slit. When a Q-switched laser plasma was formed on the target the probe beam polarisation became briefly Faraday rotated, so that its emerging polarisation was no longer completely crossed relative to the polaroid filter. A fraction $\sin^2\theta_F$ was able to travel through to the monochromator entrance, where the brief pulse of light was subsequently time-integrated and its energy displayed on a storage scope. The simultaneous emission of unpolarised continuum light by the plasma itself made the use of a monochromater essential to select the laser beam from the very bright background. Indeed, even with such substantial filtering, the transmitted laser light constituted only 5% of the integrated intensity detected.

To unravel an average value for R = $\sin^2\theta_F$ from the measurements careful attention had to be given to the continuum light simultaneously detected and the appropriate integration time of the detector circuit. The integration circuit connected to the photomultiplier was shown in Fig. 7.5. From this figure an expression can be derived for the total energy E received (ignoring the solid angle and bandwidth, which were kept constant).

$$\int_0^{t=t_p<\tau} p(t)\,dt = \int_0^{t_p<\tau} K_0 V(t)\,dt = E = K_0 V_{max}\tau \quad \text{(Joules)}$$

where $P(t)$ is the power received, K_o a system constant, V the voltage detected, τ the integration time RC, and t_p is the duration of the laser plasma. Let Fig.7.8 show schematically the quantities involved.

$R = \sin^2\theta_F$ is the Faraday rotation factor introduced above and α is the transmissivity of the plasma, both of which last only as long as the plasma lifetime, reverting back to zero and one respectively in the steady state. $P(t)$ is the unpolarised continuum emission and the quantities in parenthesis refer to transmission through an uncrossed polaroid, rotated by 90°. In the steady state there was no light detected when the polaroid was crossed, so V_{mx} equalled zero. When a plasma was formed for a time t_p V_{mx} became

$$V_{mx}(B) = \int_o^{t_p} \frac{P(t)\,dt}{2K_o\tau} + \int_o^{t_p} \frac{\alpha R(B) I_o\,dt}{K_o\tau}$$

$$\simeq \frac{\bar{P}\,t_p}{2K_o\tau} + \frac{I_o t_p}{K_o\tau}\,\bar{\alpha}\bar{R}(B)$$

where $\bar{R}(B)$ and $\bar{\alpha}$ were time averaged functions. When the polaroid was uncrossed the steady state threshold voltage V_{mu} was no longer zero, but equal to $V_{TH} = I_o(f+1)/K$. With the magnetic field off no rotation should have occured and V_{mu} became a signal diminished by the partial obscuration of I_o due to the plasma and increased by the unpolarised continuum pulse $P(t)$.

$$V_{mu} = \frac{1}{2K_o\tau}\int_o^{t_p} P(t)\,dt - \frac{1}{K_o\tau}\int_o^{t_p}(1-\alpha)I_o\,dt$$

$$= \frac{\bar{P}\,t_p}{2K_o\tau} - \frac{I_o t_p}{K_o\tau}(1-\bar{\alpha}) \quad \text{(above } V_{TH}\text{)}$$

After manipulation the following expressions were derived.

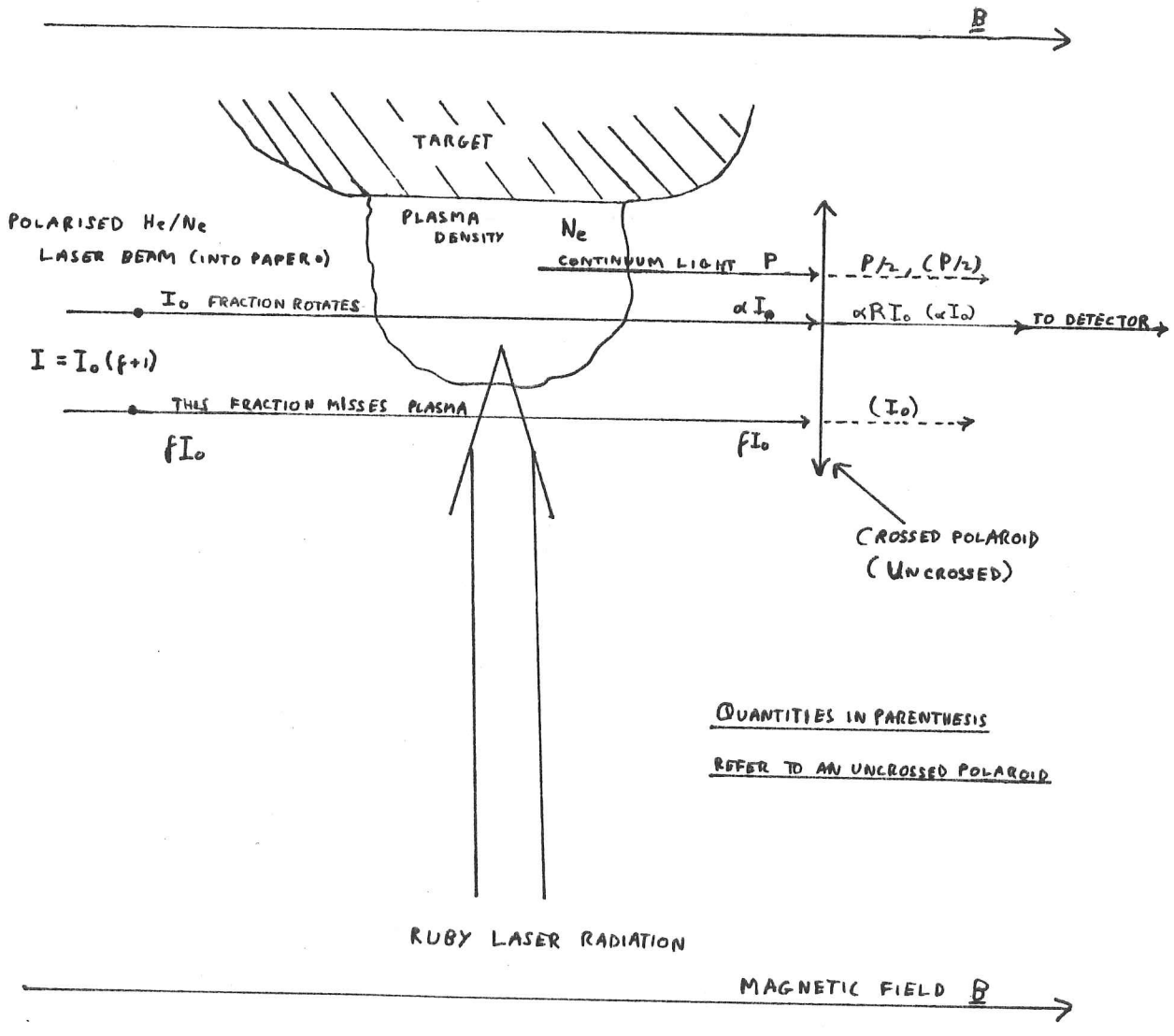
B
TARGET
POLARISED He/Ne
LASER BEAM (INTO PAPER)
PLASMA
DENSITY
Ne
CONTINUUM LIGHT P
P/2, (P/2)
I_0 FRACTION ROTATES
$\propto I_0$
$\propto R I_0$ ($\propto I_0$)
TO DETECTOR
$I = I_0(f+1)$
THIS FRACTION MISSES PLASMA
(I_0)
fI_0
fI_0
CROSSED POLAROID
(UNCROSSED)
QUANTITIES IN PARENTHESIS
REFER TO AN UNCROSSED POLAROID
RUBY LASER RADIATION
MAGNETIC FIELD B

Fig. 7.8

$$\bar{\alpha} = 1 + \frac{\tau}{t_p} \frac{(V_{mu} - V_{mx})(1+f)}{V_{TH}}$$

$$\bar{R}(\beta) = \frac{\tau}{t_p} \frac{(V_{mx}(\beta) - V_{mx}(0))(1+f)}{\bar{\alpha} V_{TH}}$$

Two quantities in the expressions which had to be estimated were t_p and f. The pulse time was taken to be 500ns on the basis of photograph 7.3, which showed continuum emission long after the exciting Ruby laser pulse had finished. During that time the plasma would have expanded a few millimetres out from the target surface. As the breadth of the He/Ne laser beam passing in front of the target was about 0.5mm the plasma should have enveloped the probe completely after the first 40ns of development (Chapter 6). By this argument the probe fraction f not involved with the plasma could be taken as approximately zero, but such a procedure ignored the fact that at earlier times than 40ns the electron densities were also likely to have been very high, contributing substantially to the averages $\bar{\alpha}$ and $\bar{R}$. Nonetheless, to keep the complexity of analysis only within the practical error limits the unobscured probe fraction f was henceforth considered negligible, with the warning that $\bar{R}$ measured may be systematically smaller than its true value.

The Results

Many laser shots were studied and the measured voltage signals were recorded and averaged. They are summarised below in a table from which it can be seen from the Standard Errors quoted that only qualitative conclusions can be drawn from the experiment. Indeed only qualitative conclusions could possibly have been meaningful, even if much higher precision had been obtained, since the time-averaged quantities $\bar{\alpha}$

and $\bar{R}(\underline{B})$ were by their very definition imprecise. Inspite of the large errors, all the experiments gave results which indicated a large Faraday rotation, including one set of results, not shown, which provided a value for $\bar{R}(0.7)$ greater than one! Although theoretically absurd, the result is quite understandable in an experiment where large errors were present.

As a check that the increased values of $V_{mx}(\underline{B})$ were due to Faraday rotation and not just a confinement or alteration of the plasma by the applied magnetic field, attempts were made to measure an increase in the intensity when unpolarised He/Ne laser light was used as a probe. The conclusion drawn from these measurements was that within the random error, no increased or decreased continuum emission could be detected when the magnetic field was either on or off and vice-versa. A more specific check was the use of the polaroid in an intermediate position between that of crossed and uncrossed operation.

In this mode, the experiment yielded an increased $V_{mx}(\underline{B})$ signal due to rotation when the polaroid had been rotated $+45^{\circ}$, and a decreased signal for the polaroid rotated -45° from the crossed position. The assymetry corresponded correctly with the direction of twist deduced by myself (and others), given a knowledge of the magnetic field direction.

Expt	Vth/Volts	Vmu/V	Vmx(B)/V			$\bar{\alpha}$	$\bar{R}(.5)$	$\bar{R}(.7)$
			B=0 Tesla	B=.5 T	B=0.7 T		0.5T	0.7T
1	3.7	-	1.3± .1	1.5± .1	1.7± .1	-	0.4	0.8
2	3.0	1.4±.2	2.0± .1	-	2.1± .3	0.4	-	0.3
3	5.0	-	1.3± .2	-	1.6± .3	-	-	0.5
4	2.5	0.8± .2	1.4± .1	-	1.5± .1	0.3	-	0.3
5	3.0	-	2.5± .1	-	2.7± .1	-	-	0.5
					MEAN	0.4	0.4	0.5

Table 7.2

In table 7.2, if no value for $\bar{\alpha}$ can be calculated to find $\bar{R}$, 0.4 has been chosen. The magnetic field was measured using a calibrated Hall probe and found to be approximately uniform in the plasma region.

A very rough estimate of the mean plasma density during t_p can be deduced when a value of 0.5 is taken for $\bar{R}$ in a field of 0.7 Tesla, the mean of the experimental measurements. The path length l in the plasma was approximately the focal diameter which was 0.5mm. Using the formula given above

$$\bar{R} = \sin^2\theta_F \approx \sin^2\left[\frac{a x^2}{(1-x^2)^{1/2}}\right]$$

$$\text{if} \quad a = \frac{\omega_c l}{2c} \qquad x = \frac{\omega_p}{\omega} \approx 1$$

$$\Rightarrow \quad \sin^{-1}(\bar{R}^{1/2}) = y = \frac{a x^2}{(1-x^2)^{1/2}}$$

$$\Rightarrow \quad x^2 = \frac{-y^2 \pm \sqrt{y^4 + 4y^2a^2}}{2a^2}$$

Inserting the numbers picked out above $x^2 = 0.985$, implying a mean electron density of $\bar{N} = 3 \times 10^{21}$ cm^{-3}.

Although the electron density calculated here cannot be considered precise in any way, because of the large experimental and averaging errors present, the order of magnitude

probably still reflects an ability of the experiment to measure Faraday rotation; it provides independent confirmation that a high electron density near the plasma frequency of the Ruby laser may have existed for some time during the laser-plasma history. As a technique, Faraday rotation has already been used to measure magnetic fields in the much lower density plasmas produced by Tokamak Fusion reactors. A time-resolved measurement system could be combined with some fine spatial probing with laser beams to form a technique that may be just as successful elucidating the space-time history of the laser plasmas described in this thesis.

CHAPTER 8

Preliminary use of a laser plasma source with a VUV spectrograph

Introduction

The aim of this thesis was to study the far ultraviolet spectroscopy of some simple molecules known to occur in interstellar space and in particular the hydroxyl radicle which has demonstrated a strong maser action in some interstellar molecular clouds. Eventually a synchrotron continuum source became available to make an attempt on the proposed spectroscopy; the experiments using that source have already been described in earlier chapters. (see Chapter 5). However, the initial lack of a suitable continuum source had stimulated the investigation of the continuum emission from laser plasmas, with an emphasis on their possible application to VUV spectroscopy. The methods and conclusions of these experiments were discussed in the previous chapter, where it was suggested that absorption VUV spectroscopy should be possible using a laser plasma as a background continuum source. However, by the time the preliminary plasma work had been completed and a Vacuum Spectrograph had been procured for our use, the synchrotron at Bonn was available, allowing the original spectroscopy to be undertaken in a more conventional manner. After returning from Bonn less than a month of experimental time was left before completing this thesis but it was felt an effort should be made to bring the plasma work to a more tidy conclusion, with the consequence that a brief experiment was undertaken to study in absorption C_2H_2 and CO using a laser plasma source and to compare the results obtained with those from the synchrotron.

The Experiment

The apparatus used is shown schematically in Fig.8.1. As Ytterbium targets were reported by Carroll et al(1980) to provide good continua in the region 1200Å-500Å, a similar

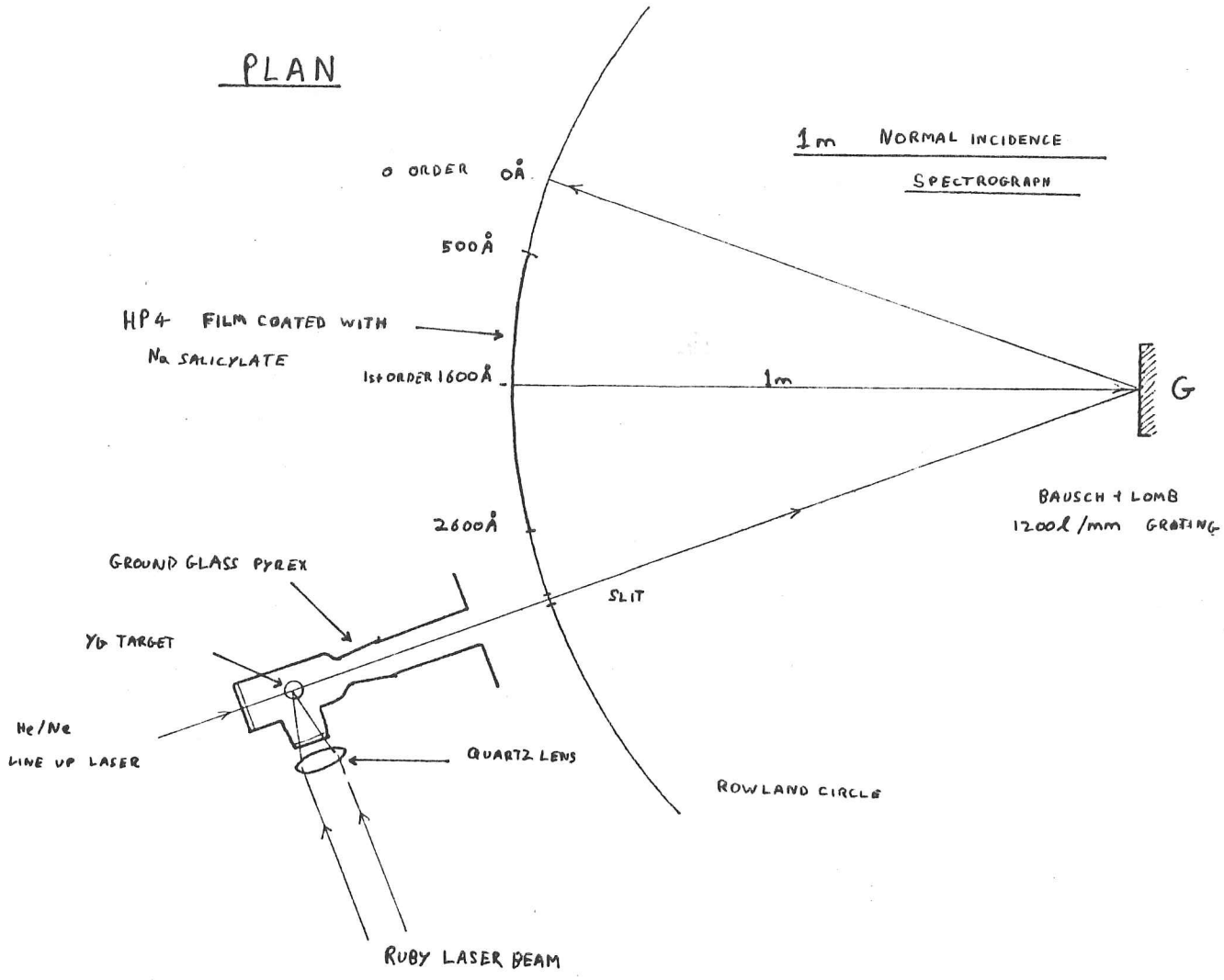
PLAN
1m NORMAL INCIDENCE
SPECTROGRAPH
0 ORDER 0Å
500Å
HP4 FILM COATED WITH
Na SALICYLATE
1st ORDER 1600Å
1m
G
BAUSCH & LOMB
1200ℓ/mm GRATING
2600Å
GROUND GLASS PYREX
SLIT
Yb TARGET
He/Ne
LINE UP LASER
QUARTZ LENS
ROWLAND CIRCLE
RUBY LASER BEAM

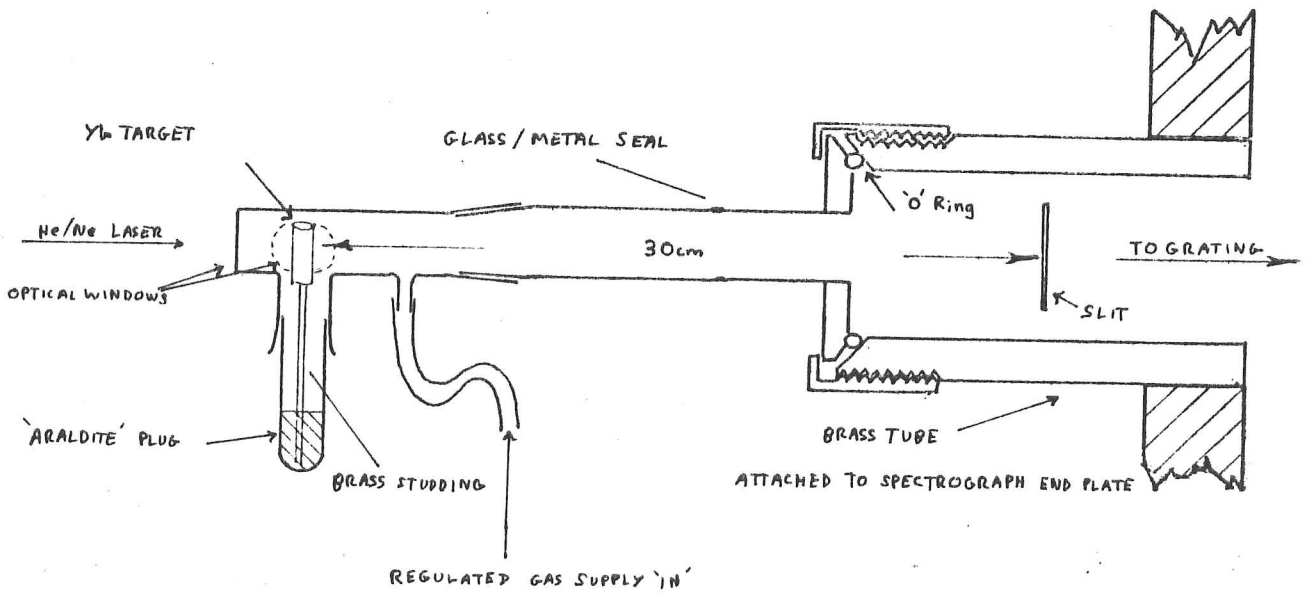
GLASS WARE - ELEVATION
Yb TARGET
GLASS / METAL SEAL
'O' Ring
He/Ne LASER
30cm
TO GRATING
OPTICAL WINDOWS
SLIT
'ARALDITE' PLUG
BRASS TUBE
BRASS STUDDING
ATTACHED TO SPECTROGRAPH END PLATE
REGULATED GAS SUPPLY 'IN'

Fig. 8.1

target was chosen for this experiment and mounted so that it could be rotated or moved up and down for adjustment. The spectrograph was a 1m normal incidence instrument (eg. Samson 1967) designed by Dr. A.B.Callear (Dept. of Physical Chemisty, Cambridge) who kindly loaned the equipment to the Cavendish Laboratory. The optical components were contained in a large vacuum-tight metal canister mounted on rails, so that it could be moved back from a large end-plate for adjustment of the diffraction grating or removal of the filmholder. The Bausch and Lomb diffraction grating used to disperse the light had a 1m radius of curvature with 1200 lines mm^{-1} blazed at 1200Å and ruled on MgF coated aluminium, backed with glass. The grating was set in an Eagle mounting so that diffraction to the normal occurred at 1500Å in 1st order, with a plate-factor of 8.4Å/mm, presenting a total wavelength span of 500Å-2600Å across the 26cm. photographic film, placed along the circumference of the Rowland circle. Line-up of the target with the spectrograph slit, grating and photographic plate was facilitated by ensuring the zero-order reflection of a fixed He/Ne laser always hit the same places on the target, when it was in position, and on the grating and Rowland circle inside the spectrograph when the target had been removed. By using the laser to find the correct position calculated for the grating only a few photographic measurements had to be made while varying the slit position to find the best focus of the slit at the plate holder.

The spectrograph itself was made from mild steel and was pumped by either a pipe connected to a rotary pump for initial roughing out or by a 4" Edwards EO4 diffusion pump via a large liquid nitrogen cold trap. Isolation of the diffusion pump from the spectrograph during the roughing stage was brought about by including a baffle valve above the cold trap and employing gate-valves to redirect the rotary pumping. The arrangement meant that the whole system could be pumped from atmospheric pressure down to 10^{-4} Torr in three hours. The pressures were monitored by

either a Pirani or a Penning guage in appropriate pressure regimes. Within the entrance tube of the spectrograph a Hilger and Watts slit and Hartmann diaphragm were mounted on a second tube, machined to fit the outer one which passed through the end-plate at an angle such that its axis passed through the centre of the grating. The slit could be racked towards and away from the grating, across the Rowland circle. Connected to the entrance port was a flange with a 2cm diameter glass/metal seal welded into its centre and jointed onto a 'quick-fit' Pyrex cone, allowing various types of glass-ware to be connected into the beamline.

The Ytterbium target assembly was made primarily out of a 'quick-fit' ground-glass Pyrex, with 'spectrosil' optical windows to introduce the He/Ne and Ruby laser light. The window through which the focused Ruby light impinged on the target was built out as near to the 6cm focusing lens as possible. This modification prevented rapid and potentially catastrophic damage of the window glass by high intensity Ruby radiation, which was found when the window was originally mounted only 1cm. away from the target, nearer the focus of the condensing lens. The target was cylindrical and threaded internally to permit controlled vertical movement up and down the brass studding on which it was mounted. Although the studding was set in 'Araldite', in a sealed glass tube with a ground-glass cone at the open end, the metal was sufficiently flexible to allow it to be slightly bent so that the target was correctly positioned across the He/Ne laser beam. The focus of the Ruby laser described in Chapter 7 was adjusted, using a movable quartz condensing lens, to produce a plasma spot based on the target, on the axis of the He/Ne line-up laser at a 45° angle of incidence to the Ytterbium target; the distance of the target area from the spectrograph slit was about 20cm.

Sample gases which were to be examined spectroscopically could be introduced into the absorption path via a tube

mounted in the bottom of the glass target assembly. The flows were regulated by an Edwards' needle valve and a gas regulator attached to the high pressure sample cylinder.

The photographic film used in the experiment was ordinary Ilford H P4 25x10cm acetate film sensitized to VUV radiation by dipping it very briefly into a 0.5 Molar solution of Sodium Salicylate in methanol and dried subsequently with a low-power hair-drier. Whilst in the dark-room the film was placed in a curved and light-tight plate holder which was shaped to follow the Rowland circle; it had been modelled on a design used in some Hilger and Watt's medium quartz spectrographs. The holder could be rotated slightly about a vertical axis and raised or lowered by a screw mechanism with a vacuum-tight shaft, which passed out through the spectrograph end-plate, enabling multiple exposures to be made on different parts of the film while the spectrograph was under a high vacuum. Because the grating focusing was astigmatic the image of the slit did not have clearly defined edges. To solve this problem a variable horizontal slit had been mounted a few cm in front of the film holder to reduce the height of each exposure to 5mm or less. To keep scattered light from darkening the film during an exposure black card and tape were positioned inside the spectrograph appropriately, with particular care taken to obstruct the zero-order transmission of the grating, which was the strongest source of spurious light.

Calibration of the plate factor and focus checks

To try out the whole system under vacuum, before using a plasma source, a radio frequency discharge tube similar to that described in Chapter 4 was inserted between the target assembly and the glass cone attached via the metal seal and flange to the spectrograph. The 'Pyrex' discharge tube was sealed using standard 'quick-fit' sockets and cones at the two ends. When Helium gas was bled into the target

assembly a bright, greeny blue discharge could be set up in front of the entrance slit when 600V of radio frequency voltage was applied to the tuned coil wrapped around the tube. Long exposure times of four hours or more were required to bring out the HeI line at 584.3Å, using a slit width of 50μm. As well as Helium lines, many impurities due to OI, HI, and NI could also be seen in the region 1400Å-500Å, facilitating the wavelength calibration of the plate factor. A densitometer scan of a Helium discharge exposure is shown in Fig.8.2, from which it can be seen that the wavelength calibration is approximately linear and sufficiently accurate for the comparison of spectrographic features with those obtained using a synchrotron. Taking a plate factor of 8.4Å /mm deduced from the calibration the resolution of the lines should be entirely determined by the slit width of 50μm, implying a resolution of 0.4Å for the calibration lines.

Photographic exposures with the laser-plasma source

Once it was established that the spectrograph vacuum system worked as a whole unit, including a sufficient sensitivity of the Sodium Salicylate coated emulsion to the VUV, experiments were attempted employing the laser plasma source without the discharge tube between it and the spectrograph slit. To ensure adequate exposure of the photographic film many laser shots were required, especially for a good continuum intensity near 500Å where the grating reflectivity started to diminish. An additional light-degrading factor was the blaze of the grating at 1200Å, which directed only little light towards much shorter wavelengths.

The first trials were made with a high vacuum of 10^{-5} Torr present in the spectrograph, using a slit width of 200μm equivalent to 1.6Å resolution. This resolution was similar to that of the Seya Monochromator used in conjunction with the 2.5GeV synchrotron at Bonn. Plate 8.1

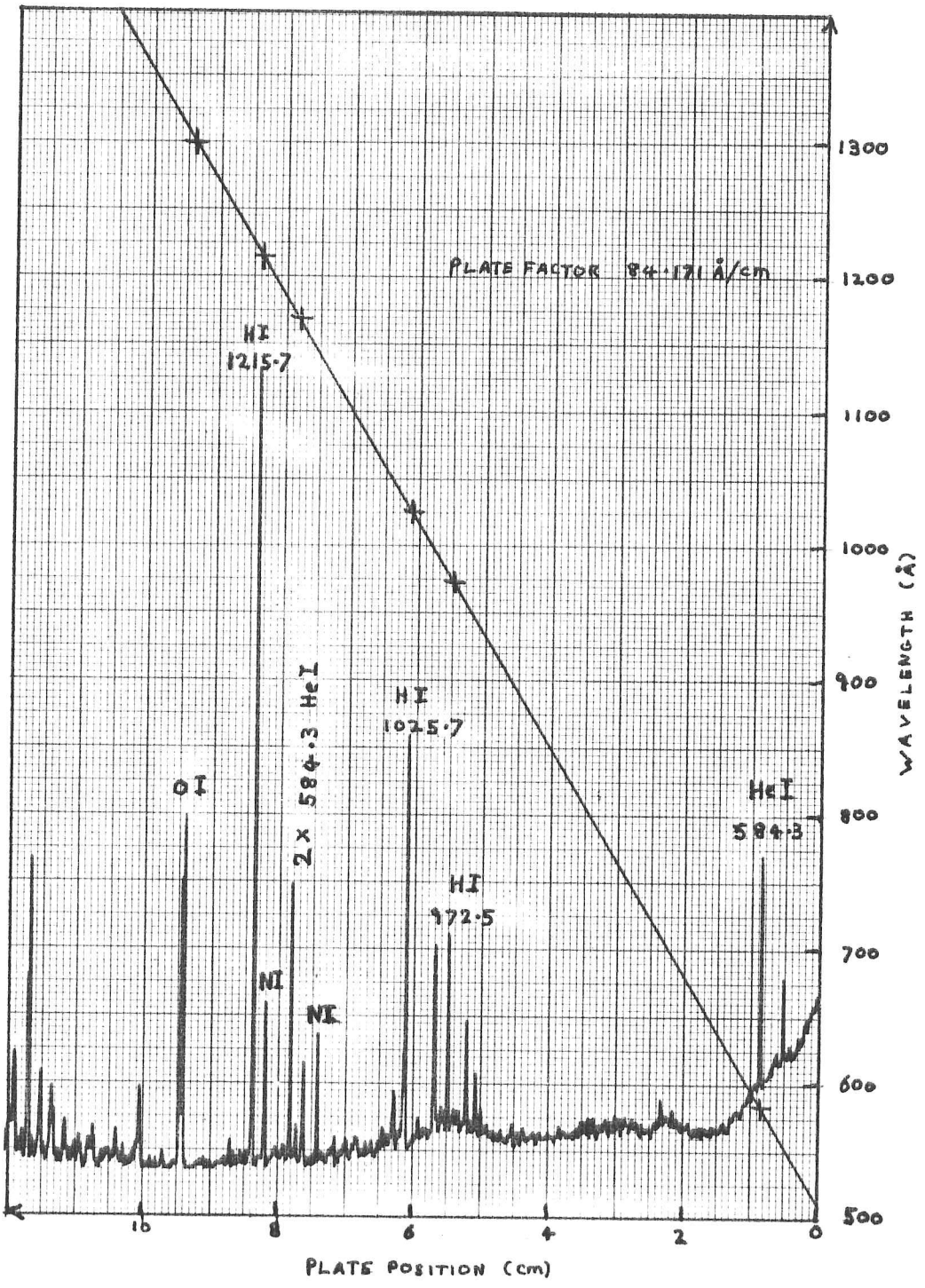
PLATE FACTOR 84·171 Å/cm
HI
1215·7
OI
NI
2x 584·3 HeI
NI
HI
1025·7
HI
972·5
HeI
584·3
1300
1200
1100
1000
900
800
700
600
500
WAVELENGTH (Å)
10
8
6
4
2
0
PLATE POSITION (cm)

Fig.8.2

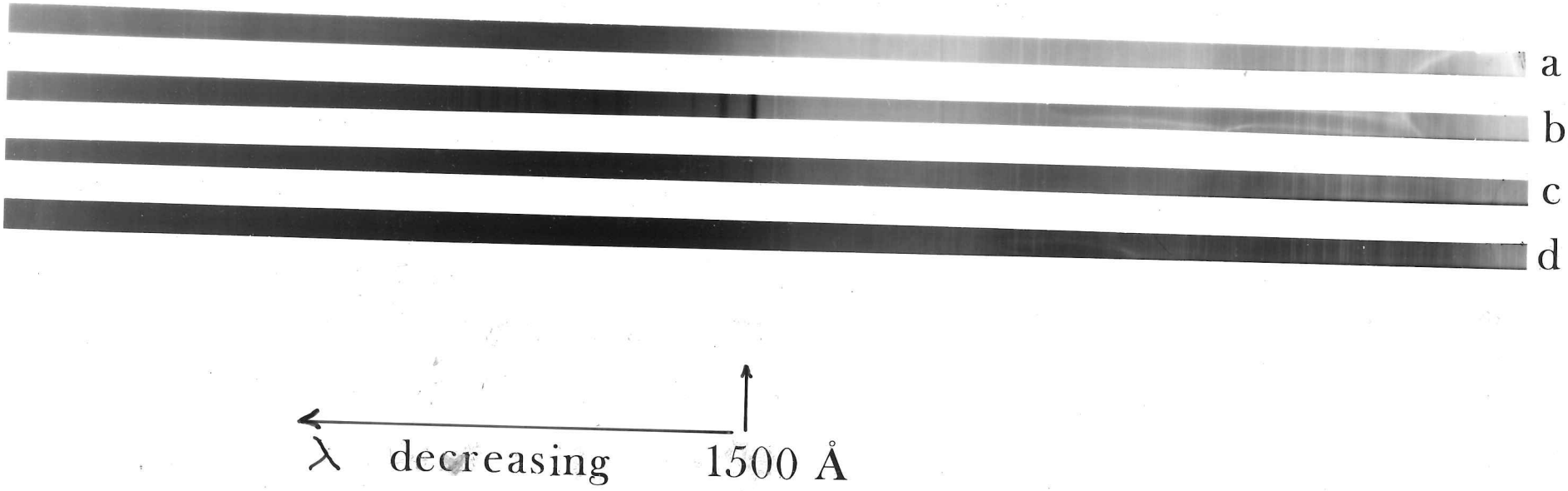

Plate 8.1

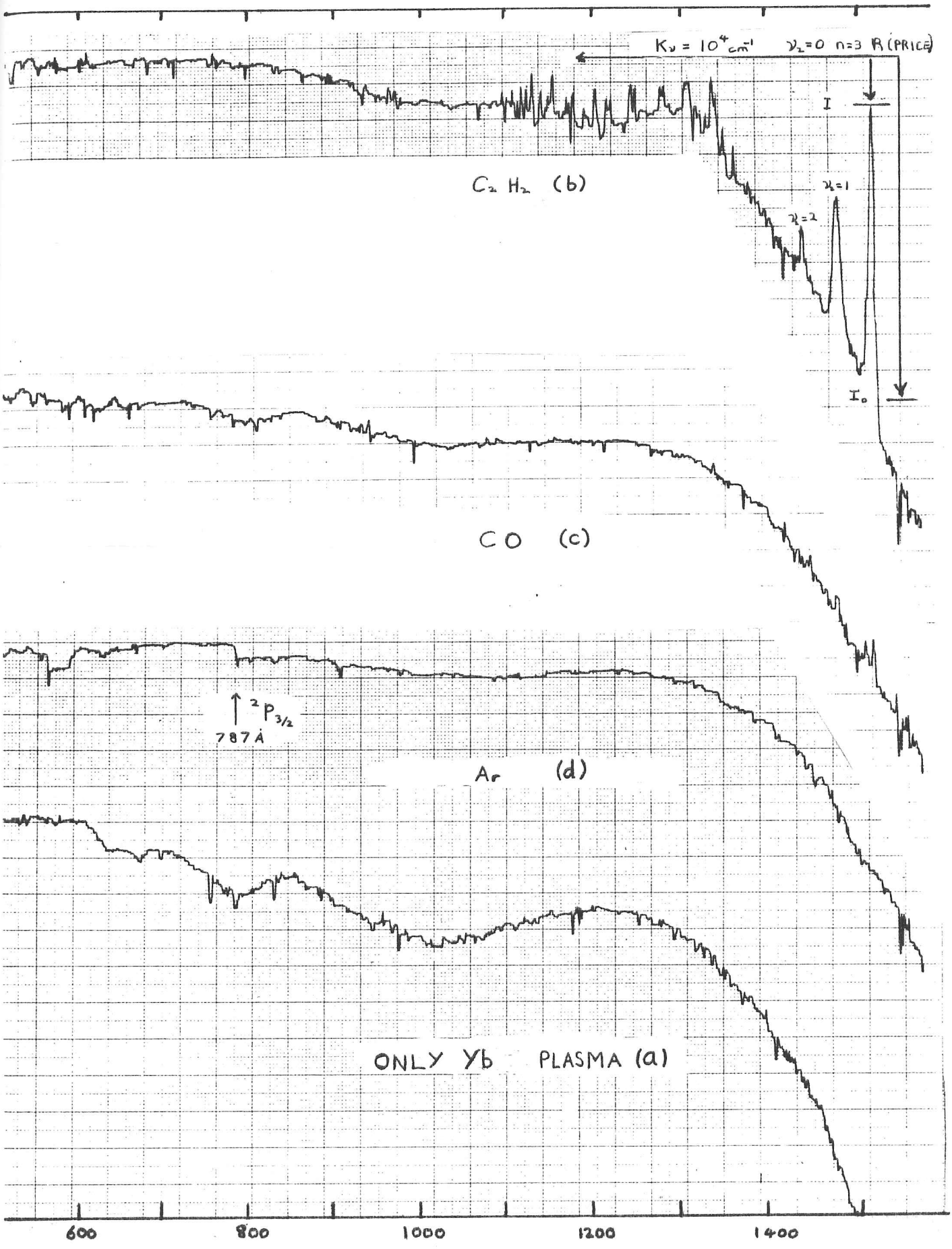
$K_\nu = 10^4\ cm^{-1}$
$\nu_2=0$ n=3 R (PRICE)
I
C_2H_2 (b)
$\nu_2=1$
$\nu_2=2$
I_0
CO (c)
$^2P_{3/2}$
787 Å
Ar (d)
ONLY Yb PLASMA (a)
600
800
1000
1200
1400
WAVELENGTH (Å)

Fig. 8.3

shows the continua obtained from 2600Å to 500Å after 60 Q-switched laser shots had been fired every five minutes with an energy of 0.5 Joules in each pulse. The continua have noticeable line emission above 1500Å where the background emission is also strong. Below 1500Å a substantial decrease in the continuum intensity appears to occur, which then decays more gradually towards the short wavelength limit of 500Å. Whether this behaviour was due to the grating and photographic film sensitivity or reflects the actual behaviour of the continuum source is not entirely clear. The blaze of the grating at 1200Å should have produced a peak in the continuum intensity, all other factors being constant but in reality a minimum can be seen, forcing the conclusion that the intensity response of the film from the spectrograph and the plasma source cannot be considered straightforward.

After establishing the conditions necessary for an adequate continuum response of the spectrograph down to 500Å, Acetylene, Carbon Monoxide, and Argon were leaked successively into the spectrograph and each gas illuminated with about 60 shots from the laser plasma source. Three gas spectra, together with one of the Ytterbium continuum alone were taken on a single film to facilitate their comparison. In between each run, after a gas had been present, the spectrograph was pumped to high vacuum for one or two hours to purge the system before introducing new samples while the target surface was readjusted slightly to prevent deep pitting of the metal. During the gas runs the pressure was kept constant at about 5×10^{-4} in the spectrograph chamber, a higher pressure may have been present between the target source and the spectrograph slit, but as the slit was not the only channel opening into the spectrograph any differential pumping that may have occurred should not have been significant in determining the total optical depth of molecular absorption lines between the plasma source and the photographic film.

The absorption spectra obtained for the three molecules C_2H_2 CO and Ar together with the unobscured background continuum are displayed in Plate 8.1 with their corresponding densitometer scans in Fig.8.3. The wavelengths of notable line features are tabulated in Table 8.1, together with corresponding features detected using the synchrotron. The acetylene ionisation threshold and the preceeding vibronic structure is clearly visible, showing the same features detected with the Bonn synchrotron (Ch.5). Above the ionisation threshold at 1085Å the continuum emission detected by the film shows some confusing variation with wavelength and suffers from diminished intensity, making it difficult to pick out the new autoionisation structure seen around 800Å in C_2H_2 with the synchrotron. Towards longer wavelengths, beyond those studied at Bonn, the n=3 vibronic Rydberg absorptions observed by Nakayama et al (1964) and Price (1935) are very noticeable. Taking the n=3 $\nu_2 = 0$ line and making a rough assumption that the photographic darkening was a linear function of light intensity the acetylene pressure derived from the optical depth was calculated to be 6×10^{-4} Torr, using the relation in Ch.4

$$P = \frac{KT}{\sigma l} \ln \frac{I_0}{I} \qquad (\text{Pascal})$$

The temperature T was 290 Kelvins and σ was taken from Nakayama et al as 450Mbarns, over a total path length 2.2m between the source and the photographic film. The quantities I and I_0 are marked on Fig.8.3 and are likely to be inaccurate but do not affect the derived pressure very greatly. The conclusion drawn was that the measured spectrograph pressure of 5×10^{-6} Torr was fairly accurate in spite of any differential pumping present over some short distances near the entrance slit.

Spectral lines observed with a Plasma source (Fig.8.3).
Corresponding features seen with a Synchrotron are shown (Ch.5).

C_2 H_2 (Å)					CO (Å)	
Plasma (Ch8)	Synch.(Ch5)	Assignment (Price,1935)			Plasma (Ch8)	Synch.(Ch5)
		n	ν_2	Branch		
1523					1521	
1484					1511	
1442					1479	
1365					1452	
1352					1419	
1344					1087	1087
1339					1076	1076
1333					941	941
1321					932	932
1310					893	890
1283						
1279						
1250						
1245						
1223						
1218						
1204						
1191						
1179						
1174						
1170	1172	5	0	R		
1156	1153	5	0	R′		
1149	1148	5	1	R		
1141	1142	6	0	R		
1132	1132	6	0	R′		
1124	1124	7	0	R		
1118	1118	6	1	R		
1114	1114	8	0	R		
1110	1108	7	1	R′		
1101	1102					
1097	1096					
876	876					

Ar (Å)	
Plasma	Synch.
786.6	786.6

($^2P_{3/2}$ Calibration feature)

Table 8.1

The Argon spectra produced show few features except for the clear ionisation threshold at 786.6Å of the $^2P_{3/2}$ excitation which was taken to help fix the wavelength calibration of the other exposures on the same film. The absorption spectra of Carbon Monoxide are rather disappointing, showing indistinctly some of the ionisation features above the ionisation threshold at 885Å, which were observed using the Bonn synchrotron (Chapter 5). During the Carbon Monoxide run the pressure fluctuated down to 5×10^{-5} Torr from an attempted setting of 5×10^{-4} Torr, the instabilities were caused primarily by the lack of a suitable low-pressure gas regulator between the high pressure gas sample cylinder and the delicate Edwards needle valve. Very soon after these experiments, when the spectra described above had just been taken, the old NELAS Ruby laser finally began to fail, developing a flaw across one end of the Ruby crystal. Because of this equipment failure and the limited time available to me, the VUV spectrographic work had to be curtailed prematurely.

There seems little doubt that the techniques described here to produce absorption spectra with a plasma source could be easily improved and with a little more time results obtained at least complimentary to those achieved with a synchrotron. In this thesis, the synchrotron work described in earlier chapters has produced clearer spectra than the spectrographic experiment above. Their interpretation and analysis are discussed more appropriately in Chapter 5, where the synchrotron results are presented.

C H A P T E R 9

Conclusions

9.1 This thesis has been concerned with both the techniques and the results of the VUV spectroscopy of H_2O, D_2O, OH, CO, and C_2H_2 in the region 1200-400Å. Much of the work described has been preoccupied with the type of continuum VUV source to be used in various experiments, specifically Synchrotron Radiation and Laser-produced plasma sources. In Chapters 6, 7, and 8 the character and properties of laser-produced plasmas were described with particular emphasis on the reproducible VUV continuum emission that can be obtained. The experiments ranged in wavelength from the visible to the VUV part of the spectrum. Although only a little time was spent doing molecular spectroscopy with the source as discussed in Chapter 8, the results were encouraging in comparison with those obtained using a synchrotron. It is most likely that laser plasma sources could be used effectively to study more molecules in the VUV, at least spectrographically if not photometrically. Although the Synchrotron or Storage Ring are good sources of continuum light, their size and complexity make them expensive machines to use and occasionally inaccessible. If limited time or budget is available the laser-plasma source could well be used as an alternative to a synchrotron for a variety of experiments.

9.2 The Laser-Plasma Source

The properties of the laser plasma sources were described and partly explained in Chapters 6 and 7. It was found that fairly line-free, continuum emission could be obtained using modest laser irradiances of 10^{10} Wcm^{-2} in the Q-switched mode on an Ytterbium or Aluminium target over visible and VUV wavelengths. However, in certain regions of the spectrum broad line emission could dominate the underlying continuum, suggesting that a variety of Rare-earth targets would be needed to provide a complete, overlapping range of line-free sources.

It was estimated by an experiment using the Faraday Rotation of a He/Ne laser with a modest magnetic field (Chapter 7) that the plasma electron density could be as high as 10^{21} cm^{-3} during the first 500ns of plasma development, implying that at wavelengths greater than 1200Å the optical depth by Bremsstrahlung processes was greater than unity. This observation, together with the observed absolute photon flux in the visible and ultraviolet (Chapter 7) of $\sim 10^{12}$ photons str^{-1} $Å^{-1}$ per laser pulse, was in rough agreement with computer programs written to predict the net photon emission and plasma properties, as described in Chapter 6. The programs might be used in future to give a lower estimate of the continuum emission from a laser plasma source, given a knowledge of the target material and the laser pulse duration,wavelength and energy.

9.3 The Molecular Spectroscopy

Best results were obtained using the 2.5GeV synchrotron at Bonn from a conventional photometric absorption experiment, described in Chapters 4 and 5. Good photoabsorption spectra of CO and C_2H_2 were obtained in the region 1200-400Å; after normalising the spectra using the Thomas-Reiche-Kuhn Sum rule absolute absorption coefficients were presented in Chapter 5 to an estimated accuracy of 20%, at a resolution of 1.5Å. Photoelectron spectra presented by Berkowitz (1979) for C_2H_2 from 600-1000Å at 0.14Å resolution seem to be in good agreement with those shown in Chapter 5 (see Fig.5.14).

H_2O and D_2O were studied near 400Å to a resolution of 2Å (Chapter 5) in an attempt to see a postulated inner shell two-electron excitation at 415Å. Although H_2O presented a smooth continuum spectrum in this region, D_2O seemed to show a resonance 'window' in its absorption continuum at 415Å, with a width of 10Å. The spectra were noisy but were improved after an average was taken of all the spectra for each molecule. It seems unlikely that the observation of a resonance in D_2O is entirely due to random variations;

it is not clear why H_2O does not demonstrate a similar effect.

A possible Rydberg series in OH approaching an ionisation limit of 13.36eV was observed in the region 920Å-1020Å, using a radio frequency discharge in water as a source of OH. (Chapter 5 and Table 5.2). Although the Rydberg lines were assigned tentatively to OH after considering alternative absorption by O, O_2 H and H_2, doubt must still remain as to their origin because other possible discharge products such as H_2O_2 or HO_2 might also absorb in this region. However, the ionisation limit agrees exactly with that determined by electron impact techniques (Wilkinson, 1963) and the series fits the $^2\Sigma^-$ Rydberg state (n=3) seen by Douglas (1974) at 1222Å, if his state has a quantum defect of 0.9, typical of such low lying, molecular Rydberg levels. The approximate oscillator strength of 0.15 calculated for the line assigned as n=4 in the Rydberg series of OH is typical of molecular Rydberg transitions; its width of 2Å almost certainly hides unresolved rotational structure. Clearly, an alternative source of OH such as the reaction of atomic hydrogen with nitrogen dioxide is needed to verify the asisgnments, especially as the reaction can produce an order of magnitude greater OH concentration for spectroscopic study, but it is unlikely to be used in conjunction with a Synchrotron or Storage Ring because of NO_2's highly corrosive properties. A laser-plasma source could be a suitable alternative for a future spectrographic experiment.

It should be pointed out that hydrogen emission lines at 949.743 and 972.537Å (Lyman - γ, δ) (Kelly's book of Standards) coincide with the broad (2Å) features assigned to hydroxyl, thus re-presenting the possibility that celestial OH masers might be pumped in the ultraviolet near hot OB-type stars (Chapter 1 and Cook, 1968) via such transitions. A higher-resolution study to discern the rotational structure of the OH Rydberg levels n=5 and n=7 is required to establish the proposal further.

Finally, a brief mention should be given to the unsuccessful attempt at optoacoustic spectroscopy in the VUV. As stated in Chapter 4, a Storage Ring producing maybe a thousand times more light than the 2.5GeV synchrotron at Bonn might produce a useable optoacoustic signal for spectroscopy at ~ 1Å resolution if background acoustic noise can be carefully isolated from the experiment; the two factors, background noises and insufficient light intensity are attributed as the major causes of failure in the optoacoustic experiments described in Chapters 3 and 4. Nonetheless, all the calculations and estimates discussed in Chapter 2 still support the potential use of optoacoustic spectroscopy as a viable technique in the VUV in spite of the practical difficulties encountered here. The advent of powerful VUV lasers would be most appropriate as sources for these types of experiment. The laser-produced plasma could conceivably be used as an optoacoustic source, due to its inherently pulsed nature and strong intensity if the pulse repetition rate could be made as great as 10Hz or more. Again, acoustic isolation of the microphones from the 'bang' which inevitably occurs when a high-power laser is fired would be necessary, but this problem might easily be solved if only low frequency harmonics could be detected by the microphone. This is because the actual optoacoustic signal mostly contains harmonics at frequencies near $1/\tau_T$ if the laser-repetition rate is slow, as is best for zero-mode operation (Chapters 2 and 3).

APPENDIX 1

The 'Laser Plasma Space and Time History' computer program (FORTRAN)

Refer throughout to Chapter 6 for a comprehensive description of the theory. The laser pulse shape in arbitrary units and its duration in seconds must be specified, together with the pulse energy in joules for the program to calculate the true laser flux intensity F(t) in Wm^{-2}. After calculating F(t) the initial laser plasma heating T(t) is calculated from Equation (6.21) which becomes

$$\ln\left(\frac{F(t)}{A(T+B)}\right) + \frac{C}{T} = 0 \qquad \text{(A1.1)}$$

with $A = h_a \nu_D \rho c \quad B = L/c \quad C = LM/R$

As F(t) is a continuous function, a linear interpolation is used between the discrete points which specify the pulse shape. T(t) is solved as a function of F(t) by calculating the roots of Equation (A1.1) using the bisection method. Equation (A1.1) is evaluated at specified intervals and when it changes sign between two points the interval is successively bisected until the requested accuracy is achieved. The surface velocity Vss is calculated from Equation (6.19) which becomes

$$Vss = F/D(T+B) \qquad \text{(A1.2)}$$

This is integrated by the trapezium method to calculate the hole depth (Equation 6.22). When the hole depth calculated is greater than or equal to the depth d actually measured the program calculates the boundary conditions for the subsequent hydrodynamic expansion.

From Chapter 6 Equations (6.35) and (6.37) can be written as

$$T = P \times \frac{d^2X}{dt^2} \qquad \text{(A1.3)}$$

$$\frac{d^3X^2}{dt^3} = Q\,W'(t,T,X) \qquad \text{(A1.4)}$$

with $P = m_i/6K(1+z)$ $\qquad Q = 24A/m_i$

Equations (A1.3) and (A1.4) can be solved over a specified time period, given the initial boundary conditions

$$X_0\,,\ \left.\frac{dX}{dt}\right|_0\,,\ \left.\frac{d^2X}{dt^2}\right|_0 \quad \text{at} \quad t = t_0$$

The equations can be written as three linearly dependent first order differential equations, which are solved using the Numerical Algorithms Group Ltd (Oxford) NAGLIB Fortran subroutine D02BBF, available with the IBM Fortran compiler FTG1CLG on the Cambridge IBM 370/165 computer. The equations become

$$\frac{dx_3}{dt} = Q\,\frac{W'(t,x_1,T(x_2,x_1))}{2x_1} - \frac{3x_2x_3}{x_1} = f_3(x_1,x_2,x_3,t)$$

$$\frac{dx_2}{dt} = x_3 = f_2(x_1,x_2,x_3,t)$$

$$\frac{dx_1}{dt} = x_2 = f_1(x_1,x_2,x_3,t) \qquad T = Px_1x_2$$

The boundary conditions at t_0 are

$$x_1 = X_0 = 2d$$
$$x_2 = dX/dt = ET_0^{1/2}$$
$$x_3 = T_0/PX_0$$

with $E = \left(\frac{3KT}{16\,m_i}\right)^{1/2}$.

The function $W'(t,T,X)$ is

$$W' = F(t) \int_0^X K_\nu e^{-K_\nu x} dx \qquad \text{(A1.5)}$$

where $$K_\nu = \frac{3.68 \times 10^{-2} Z^3}{n_r} \left(\frac{N^2}{\nu^3 T^{1/2}}\right) \left(1 - e^{-h\nu/kT}\right) \quad (m^{-1}) \qquad \text{(A1.6)}$$

The Integral is evaluated using Simpsons Rule. The refractive index n_r is given by Equation (6.16)

$$n_r(\omega) \approx \left[(1 - \omega_p^2/\omega^2)^2 + (\nu/\omega)^2 \right]^{1/4}$$

with

$$\omega_p = H N^{1/2} \quad (Hz) \qquad N(x) = G(X-x)/X^2 \quad (m^{-3})$$

$$H = \frac{Z^{1/2}}{2\pi} \left(\frac{e^2}{m_e \varepsilon_0}\right)^{1/2} \qquad G = \frac{2N_{io}}{A} = \frac{2\rho d}{m_i}$$

in the presence of collisions at frequency ν (Hz) given by Equation (6.42) as

$$\nu \approx C_f T^{1/6} N$$

where Cf is a constant specified to the program.

The program outputs to a file at regular time intervals over the specified plasma history period, values of Size and Temperature. These data points are also drawn by high level Fortran graph-plotting routines described in the file INFO.SPEC.HIGRAPH on the Cambridge IBM 370/165 computer.

The Data list for LPSTH and constants used by the program

All units read into the program should be S.I. Actual values are given for Yb and conditions in Chapter 6, in parenthesis.

Data Card 1:

A1,	A2,	A3,	A4
(3.3D-10	2.7D12	6.972D3	1.45D2)

A1 is the atomic layer thickness h_a.
A2 is the debye frequency ν_D.
A3 is the target density ρ
A4 is the specific heat capacity C.

Data Card 2: A5, A6, A7,
(9.21D5 1.73D2 2.4D-6)

A5 is the latent heat of sublimation L.
A6 is the atomic Mass No.M, changed to actual mass internally.
A7 is the hold depth d.

Data Card 3: AREA, PTIME, ENERGY, FREQ,
(2.D-7 3.92D-7 0.5DO 4.32D14)

Laser parameters: AREA is the focal area
PTIME is the total length of the pulse
ENERGY is the pulse energy
FREQ is the laser frequency

Data Card 4: TFINISH, NSTEPS, INSTEPS, TERROR, TOL
(1.D-6 300 10 1.D1 1.D-3)

Calculation parameters: TFINISH is the total time period overwhich the plasma history is evaluated.
NSTEPS is an <u>even</u> No. of time-intervals making up TFINISH.
INSTEPS is the No. of <u>even</u> integration steps used in Simpson's evaluation of Equation (A1.5).
TERROR is the temperature error allowed when calculating the initial conditions.
TOL is the number of decimal places to which D02BBF works to calculate X.

Data Card 5: NPOINTS
(29)

Pulse shape: NPOINTS is the odd no. of ordinates to be read next, describing the laser pulse shape, spanning PTIME.

Data Card 6 → 6 + NPOINTS: FLUX

FLUX are the successive (time increasing) no. of odd ordinates describing the Pulse Shape. They must be evenly spaced.

Data Card 6+NPOINTS+1: CF
(1.7D-14)

This is the last card. CF is the collison frequency constant Cf.

Constants internally assigned

$$A = h_a \nu_D \rho c, \quad B = L/c, \quad C = L(M \times 10^{-3})/R,$$

$$D = \rho c, \quad E = (3K/16 m_i)^{1/2}, \quad G = (2\rho d/m_i),$$

$$H = 1/2\pi (2e^2/m\varepsilon_0)^{1/2} \quad Z, \quad DELTA = 3.68 \times 10^{-2} Z^3$$

$$EPSILO = h/K \quad P = m_i/6K(1+Z) \quad Q = 48/m_i G$$

```
      IMPLICIT REAL*8(A-H,O-Z)
      REAL FLOAT
      COMMON/ONE/A,B,C
      COMMON/TWO/FLUX(50),PTIME,NPOINT
      COMMON/THREE/XOUT(1005),TOUT(1005),DELTAT,N
      COMMON/FOUR/FREQ,TEMPT,XONE
      COMMON/FIVE/INSTEP
      COMMON/SIX/P,Q
      COMMON/SEVEN/G,H,CF
      COMMON/NINE/DELTA, EPSILO
C   D02BBF SUBROUTINE ARGUMENTS USED
      DOUBLE PRECISION TIME, TEND, X(3), TOL, W(3,7)
      INTEGER M, IR, IFAIL
      DOUBLE PRECISION ARRAY(5)
      EXTERNAL FCN,OUT
C   THESE FUNCTIONS ARE CALLED BY D02BBF, SUPPLIED BELOW.
C   CHOOSE APPROPRIATE ERROR FLAGS IN D02BBF
      IFAIL=1
      IR=2
      M=3
C   CLEAR OUTPUT ARRAYS - SET TO MINUS ONE
      DO 4 I=1,1005
      XOUT(I)=-1.D0
4     TOUT(I)=-1.D0
C   END OF D02BBF INITIALISATION
C   START DATA READ IN
      WRITE(6,900)
      READ(5,*) A1,A2,A3,A4
      WRITE(6,901)A1,A2,A3,A4
      A=A1*A2*A3*A4
      D=A3*A4
C THE EXPECTED IONISATION STAGE Z OF THE
C PLASMA SHOULD BE INSERTED HERE.  IT IS
C PROBABLY IN THE RANGE 3-5.
      Z=4.D0
      READ(5,*)A5,A6,A7
      HDEPTH=A7
      WRITE(6,902)A5,A6,A7
      B=A5/A4
      C=A5*A6/8.31D3
      A6=A6*1.672D-27
      G=2.D0*A3*A7/A6
      P=A6/(8.28D-23*(1.D0+Z))
      Q=4.8D01/(G*A6)
      H=8.980D0*DSQRT(Z)
      DELTA=3.68D-02*(Z**3)
      EPSILO=4.801D-11
C   THE TITLE HAS BEEN WRITTEN - F900
C   ATOMIC THICKNESS, DEBYE FREQUENCEY, DENSITY, HEAT CAPACITY - F901
C   LATENT HEAT, ATOMIC MASS, HOLE DEPTH - F902
C   ALL OTHER ASSIGNMENTS ARE INTERNAL, EXCEPT Z
      READ(5,*) AREA, PTIME, ENERGY, FREQ
      WRITE(6,903) AREA,PTIME,ENERGY,FREQ
      READ(5,*) TFINI, NSTEPS, INSTEP, TERROR, TOL
      WRITE(6,904) TFINI, NSTEPS, INSTEP, TERROR, TOL
C   REAL TIME LIMIT, THE NO. STEPS TO DIVIDE IT,
C   THE NO. OF EVEN INTEGRATION STEPS, THE TEMPERATURE ERROR
C   THE DECIMAL PLACES GIVEN TO THE PLASMA DIMENSIONS

      READ(5,*) NPOINT
      WRITE(6,905) NPOINT
      FMAX=0.D0
      DO 14 I=1,50
14    FLUX(I)=-1.D0
      DO 15 I=1,NPOINT
15    READ(5,*) FLUX(I)
      READ(5,*) CF
      WRITE(6,906) CF
C   CALCULATE NORMALISING FLUX CONSTANT, ANORM
      XLIM1=0.D0
      VALUE=SIMPSO(XLIM1,PTIME,FLUX,NPOINT)
      ANORM=ENERGY/(VALUE*AREA)
C   NORMALISE FLUX TO UNITS WATTS PER SQ. METRE
      DO 1 I=1,NPOINT
      FLUX(I)=FLUX(I)*ANORM
      IF(FLUX(I).GT.FMAX) FMAX=FLUX(I)
1     CONTINUE
C   FUNCTION F(T) WILL BE USED TO INTERPOLATE FLUX
C   CALCULATE SURFACE TEMPERATURE AND VELOCITY OF
C   RECESSION AS A FUNCTION OF F(T).  EVALUATE
C   INTEGRAL OF SURFACE VELOCITY VSS UNTIL IT IS GREATER
C   THAN THE HOLE DEPTH, BY THE TRAPEZIUM RULE.
      DELTAT=TFINI/DBLE(FLOAT(NSTEPS))
      TIME=0.D0
      N=1
      XOUT(1)=0.D0
      FT=F(0.D0)
      TEMPT=TEMP(FT,TERROR)
      DEPTH=FT/(2.D0*D*(TEMPT+B))
      TOUT(1)=TEMPT
2     N=N+1
      TIME=TIME+DELTAT
      IF(TIME.LE.TFINI) GOTO 20
      WRITE(6,915) XD,HDEPTH
      STOP
20    FT=F(TIME)
      TEMPT=TEMP(FT,TERROR)
      VSS=FT/(2.D0*D*(TEMPT+B))
      TOUT(N)=TEMPT
      DEPTH=DEPTH+VSS
      XD=2.D0*DEPTH*DELTAT
      XOUT(N)=XD
      XD=XD/2.D0
      IF(XD.GE.HDEPTH) GOTO 3
      DEPTH=DEPTH+VSS
      GOTO 2
3     VSS=2.D0*VSS
      VS=DSQRT(2.588D-24*TEMPT/A6)
      WRITE(6,914) XOUT(N),HDEPTH,VSS
      WRITE(6,907)VS,TEMPT,TIME,N
      WRITE(6,802)
802   FORMAT(1H0,3X,1HN,10X,2HX1,10X,2HX2,10X,2HX3,
     &8X,4HTEMP,6X,6HRINDEX,6X,6HABSORB,2X,10HPLASMAFREQ)
C   SET UP BOUNDARY CONDITIONS FOR PLASMA EXPANSION
      X(1)=2.D0*XD
      X(2)=VS
      X(3)=TEMPT/(P*X(1))
```

```
      TEND=TFINI
C  ENTER THE NUMBER CRUNCHER!!
      CALL D02BBF(TIME,TEND,M,X,TOL,IR,FCN,OUT,W,IFAIL)
      WRITE(6,908) IFAIL
      IF(TOL.LT.(0.D0)) WRITE(6,909)
      WRITE(6,916) FMAX
916   FORMAT(1H0,16HMAXIMUM FLUX WAS,D12.4)
      WRITE(6,910) NSTEPS,TFINI
C  WRITE OUT THE PULSE, SPACE AND TIME HISTORY OF THE PLASMA
12    I=0
5     DO 6 J=1,5
6     ARRAY(J)=XOUT(J+I)
      WRITE(6,911) ARRAY
      IF(ARRAY(5).LT.(0.D0)) GOTO 7
      I=I+5
      GOTO 5
7     I=0
10    DO 8 J=1,5
8     ARRAY(J)=TOUT(J+I)
      WRITE(6,911)ARRAY
      IF(ARRAY(5).LT.(0.D0)) GOTO 9
      I=I+5
      GOTO 10
9     WRITE(6,912) G,H,CF
      WRITE(6,913) DELTA,EPSILO
C CONVERT LENGTHS TO MICRONS
      DO 30 I=1,NSTEPS
      XOUT(I)=1.D6*XOUT(I+1)
30    TOUT(I)=TOUT(I+1)
C CONVERT TIMES TO NANOSECONDS
      DELTAT=DELTAT*1.D9
      TFINI=TFINI*1.D9
      PTIME=1.D9*PTIME
C DRAW SPACE AND TEMPERATURE HISTORY WITH
C DIFFERENT SCALES ON THE SAME GRAPH.
C FIND PHYSICAL LIMITS
      CALL GRLM4D(PXL,PXH,PYL,PYH)
C SET NEW LIMITS
      PXL=PXL+2.D1
      PXH=PXH+2.D1
      PYHNEW=PYL+.8D0*(PYH-PYL)
      PXHNEW=PXL+0.54D0*(PXH-PXL)
      CALL GRLM2D(PXL,PXHNEW,PYL,PYHNEW)
C DRAW IN BLACK SPACE GRAPH LOG-LIN
C AUTO FRAME ON. SUPPRESS ANNOTATION OF MINOR MARKS
      CALL GRFT3D(2.D0,0.D0,5,5,0.D0,1)
C  SET X & Y AXIS ANNOTATIONS
      CALL GRAN3D(0,0)
      CALL GRAN2D(4,0)
C DRAW TWO AXES ONLY
      CALL GRFT2D(1,-1,1,-1)
C DRAW THE SPACE GRAPH
      CALL GRGR5D(XOUT,NSTEPS,DELTAT,TFINI)
      CALL GRAN6D('LASER PLASMA TIME HISTORY',
     &25,'TIME IN NANOSECONDS',20,
     &'PLASMA SIZE IN MICRONS',22)
C DRAW IN RED TEMPERATURE GRAPH LOG-LIN
C SET AUTO SCALE ON

      CALL GRLM6D
C SET RED GRAPHS
      CALL GRPN4D(2)
C NO X-AXIS ANNOTATION THIS TIME
C SET AUTO FRAME ON AND DRAW
C TOP RIGHT CORNER WITH ANNOTATIONS
      CALL GRFT2D(1,1,1,-3)
      CALL GRAN2D(-1,0)
C DRAW THE FRAME AND TEMPERATURE GRAPH
      CALL GRGR5D(TOUT,NSTEPS,DELTAT,TFINI)
C SET RED TITLING
      CALL GRPN5D(2)
      CALL GRAN6D('N',0,'N',0,'TEMPERATURE IN KELVIN',21)
C SET FLUX SCALES TO A THIRD OF FRAME SIZE
C FIND PHYSICAL LIMITS AND CHANGE THEM
      CALL GRLM4D(PXL,PXH,PYL,PYH)
      PYHNEW=PYL+(PYH-PYL)/3.D0
      CALL GRLM2D(PXL,PXH,PYL,PYHNEW)
C SET X AXIS SCALE
      CALL GRLM3D(0.D0,TFINI,0.D0,0.D0)
C SET GREEN GRAPH
      CALL GRPN4D(3)
      CALL GRGR4D(FLUX,NPOINT,0.D0,PTIME)
      STOP
900   FORMAT(1H ,42HLASER PLASMA TEMPERATURE AND SPACE HISTORY,
     &/1H0,24HMETAL DATA IN S.I. UNITS)
901   FORMAT(1H0,16HATOMIC THICKNESS, D12.4/1H ,15HDEBYE FREQUENCY,D12.4,
     &/1H ,7HDENSITY,D12.4/1H ,13HSPECIFIC HEAT,D12.4)
902   FORMAT(1H ,11HLATENT HEAT,D12.4/1H ,15HATOMIC MASS NO.,
     &D12.4,1H0,10HHOLE DEPTH,D12.4)
903   FORMAT(1H0,16HLASER PARAMETERS/1H0,10HFOCAL AREA,D12.4,
     &1H ,10HPULSE TIME,D12.4/1H ,12HPULSE ENERGY,D12.4/10H FREQUENCY,
     &D12.4)
904   FORMAT(1H0,22HCALCULATION PARAMETERS/1H0,10HTIME RANGE,D12.4,
     &/1H ,8HSTEP NO.,I3/1H ,20HINTEGRATION EVEN NO.,I3/1H ,
     &11HTEMPERATURE,6H ERROR,D8.2/1H ,9HTOLERANCE,D8.2)
905   FORMAT(1H0,18HNO. OF FLUX POINTS,I2)
906   FORMAT(1H0,30HCOLLISION INTERACTION CONSTANT,D12.4)
907   FORMAT(1H ,12HPLASMA SPEED,D12.4,11HTEMPERATURE,
     &D12.4,4HTIME,D12.4,4HSTEP,I4)
908   FORMAT(1H0,26HD02BBF ERROR FLAG IFAIL IS,I2)
909   FORMAT(1H0,49HBEWARE! THE TOLERANCE IS TOO LARGE FOR THIS RANGE)
910   FORMAT(1H0,38HDATA:- NO. OF STEPS & RANGE, DIMENSION,
     & 13H, TEMPERATURE,/1H ,I3,D12.4)
911   FORMAT(1H ,5D12.4)
912   FORMAT(1H ,3D12.4)
913   FORMAT(1H ,2D12.4)
914   FORMAT(1H0,12HDIMENSION IS,D12.4,7HHOLE IS,D12.4,
     &13HSURFACE SPEED,D12.4)
915   FORMAT(1H0,32HLARGEST CALCULATED HOLE DEPTH IS,D12.4,
     &28HTHIS IS LESS THAN THAT GIVEN,D12.4)
      END
      FUNCTION SIMPSO(XLIM1,XLIMN,YN,N)
      IMPLICIT REAL*8(A-H,O-Z)
      REAL FLOAT
      DOUBLE PRECISION YN(N)
      VAL=YN(1)+YN(N)
      J=N-1
```

```
      DO 1 I=2,J,2
1     VAL=VAL+4.D0*YN(I)
      J=N-2
C   THE NUMBER OF ORDINATES MUST BE GREATER THAN THREE!
      DO 2 I=3,J,2
2     VAL=VAL+2.D0*YN(I)
      VAL=VAL*(XLIMN-XLIM1)/(3.D0*DBLE(FLOAT(N-1)))
      SIMPSO=VAL
      RETURN
      END
      FUNCTION F(T)
      IMPLICIT REAL*8(A-H,O-Z)
      REAL FLOAT
      COMMON/TWO/FLUX(50),PTIME,NPOINT
C   IF T IS OUT OF RANGE, F(T) IS PUT EQUAL TO ZERO
      IF(T.GT.PTIME) GOTO 1
      DELT=PTIME/DBLE(FLOAT(NPOINT))
      NLOW=IDINT(T/DELT)+1
      NHIG=NLOW+1
      DT=T-DELT*DBLE(FLOAT(NLOW-1))
      F=FLUX(NLOW)+(FLUX(NHIG)-FLUX(NLOW))*DT/DELT
      RETURN
1     F=0.D0
      RETURN
      END
      FUNCTION TEMP(F,TERROR)
      IMPLICIT REAL*8(A-H,O-Z)
      REAL FLOAT
      COMMON/ONE/A,B,C
      ZEROFN(T,F)=DLOG(F/(A*(T+B)))+C/T
C   IF FLUX F IS ZERO, PUT TEMP = 0.D0
      IF(F.GT.(0.D0)) GOTO 1
      TEMP=0.D0
      RETURN
1     DELT=TERROR*1.D3
      TEM=1.D0
C  FIND THE ZERO OF ZEROFN(TEM,F)
2     TEMT=TEM
      SGN=ZEROFN(TEM,F)
      IF(SGN.EQ.(0.D0)) GOTO 4
      TEM=TEM+DELT
      SGN=SGN*ZEROFN(TEM,F)
      IF(SGN.GE.(0.D0)) GOTO 3
      TEM=TEMT
      DELT=DELT/2.D0
3     IF(DELT.GE.TERROR) GOTO 2
4     TEMP=TEM
      RETURN
      END
      SUBROUTINE FCN(T,X,FN)
      IMPLICIT REAL*8(A-H,O-Z)
      REAL FLOAT
      COMMON/FOUR/W,TEMPT,XONE
      COMMON/SIX/P,Q
      DOUBLE PRECISION T,X(3),FN(3)
      EXTERNAL DINTGR
      XONE=X(1)
      TEMPT=X(1)*X(3)*P

      FN(1)=X(2)
      FN(2)=X(3)
C  FIND THE LASER POWER ABSORBED
      DK=XONE*ABSORB(W,TEMPT,XONE,0.D0)
      IF(DK.GE.(5.D0)) GOTO 1
      WP=F(T)*DINTEG(0.D0,XONE,DINTGR)
      GOTO 2
1     WP=F(T)
2     FN(3)=Q*WP/(2.D0*X(1))-3.D0*X(2)*X(3)/X(1)
      RETURN
      END
      FUNCTION DINTEG(XMIN,XMAX,DINTGR)
      IMPLICIT REAL*8(A-H,O-Z)
      REAL FLOAT
      COMMON/FIVE/INTSTP
C  NOTE, THE NO. OF INTEGRATION STEPS MUST BE EVEN (CF. NSTEPS)
      VAL=DINTGR(XMIN)+DINTGR(XMAX)
      DELTAX=(XMAX-XMIN)/DBLE(FLOAT(INTSTP))
      J=INTSTP-1
      DO 1 I=1,J,2
      XV=DBLE(FLOAT(I))*DELTAX+XMIN
1     VAL=VAL+4.D0*DINTGR(XV)
      J=INTSTP-2
      DO 2 I=2,J,2
      XV=DBLE(FLOAT(I))*DELTAX+XMIN
2     VAL=VAL+2.D0*DINTGR(XV)
      DINTEG=VAL*DELTAX/3.D0
      RETURN
      END
      FUNCTION DINTGR(XV)
      IMPLICIT REAL*8(A-H,O-Z)
      REAL FLOAT
      COMMON/FOUR/W,TEMPT,XONE
      DK=ABSORB(W,TEMPT,XONE,XV)
      IF(DK.LE.(0.D0)) DK=1.D-70
      DINTGR=DLOG(DK)-DK*XV
      IF(DINTGR.GT.(-1.5D2)) GOTO 1
      DINTGR=0.D0
      RETURN
1     DINTGR=DEXP(DINTGR)
      RETURN
      END
      FUNCTION ABSORB(W,TM,X,XV)
      IMPLICIT REAL*8(A-H,O-Z)
      REAL FLOAT
      COMMON/SEVEN/G,H,CF
      COMMON/NINE/DELTA,EPSILO
C  FIND THE PLASMA DENSITY AT XV, OF TOTAL DIMENSION X
      DENSIT=G*(X-XV)/X**2
      ABSORB=DELTA*((DENSIT/W)/(W*DSQRT(TM)))*(DENSIT/W)
      ABSORB=ABSORB*(1.D0-DEXP(-1.D0*EPSILO*W/TM))
C GAUNT FACTOR PUT TO ONE
      ABSORB=ABSORB/RINDEX(W,X,XV,TM)
      RETURN
      END
      FUNCTION RINDEX(W,X,XV,TM)
      IMPLICIT REAL*8(A-H,O-Z)
      REAL FLOAT
```

```
      COMMON/SEVEN/G,H,CF
      FQ=CF*(TM**(1.D0/6.D0))*G*(X-XV)/X**2
      WP=H*DSQRT(G*(X-XV)/X**2)
C  CALCULATE THE REFRACTIVE INDEX OF THE PLASMA, INCLUDING COLLISIONS
      RINDEX=((1.D0-(WP/W)**2)**2+(FQ/W)**2)**0.25
      RETURN
      END
      SUBROUTINE OUT(T,X)
      IMPLICIT REAL*8(A-H,O-Z)
      REAL FLOAT
      COMMON/FOUR/FREQ,TEMPT,XONE
      COMMON/SEVEN/G,H,CF
      COMMON/THREE/XOUT(1005),TOUT(1005),DELTAT,N
      COMMON/SIX/P,Q
      DOUBLE PRECISION T,X(3)
      XOUT(N)=X(1)
      TOUT(N)=P*X(1)*X(3)
      RDX=RINDEX(FREQ,X(1),0.D0)
      ABS=ABSORB(FREQ,TOUT(N),X(1),0.D0)
      WP=H*DSQRT(G*(X(1)-0.D0)/X(1)**2)
      WRITE(6,900) N,X,TOUT(N),RDX,ABS,WP
900   FORMAT(1H ,I4,7D12.4)
      N=N+1
      T=T+DELTAT
      RETURN
      END
```

APPENDIX 2

Continuum Emission Program (FORTRAN)

Refer throughout to Chapter 6 for a comprehensive description of the theory. Except for the first data card, all the data used by this program is produced by LPSTH (Appendix 1), which describes the laser plasma size and temperature as a function of time. The History chosen for LPSTH of $\sim 1\mu s$ is sufficiently long to cover the times when the plasma is beginning to cool substantially.

T(t), X(t), and N(t) are known from the data of LPSTH over closely spaced, discrete points at regular, short time-intervals. From equation (6.8) and Bekefi (1966)

$$I_\omega = \int_0^{\chi_0} S_\omega(\chi)\, e^{-\chi}\, d\chi$$

if all the emitted light is assumed to come from within the plasma. If S_ω is not a function of intensity and is the black-body source function Equation 6.3 then

$$I_\omega = \frac{\hbar\omega^3}{4\pi^3 c^2} \frac{1}{e^{\hbar\omega/kT} - 1} \left[1 - e^{-\int_0^x \alpha_\omega dx}\right]$$

for two polarisations. In units of frequency (Hz)

$$I(\nu) = \frac{R\nu^3}{e^{\varepsilon\nu/T} - 1} \left[1 - e^{-\int_0^x \kappa_\nu dx}\right] \qquad \text{(A2.1)}$$

where $R = h/c^2$ for <u>one</u> polarisation. Since all the quantities in Equation (A2.1) are known from LPSTH with K_ν given by Equation (A1.6), $I(\nu)$ is integrated by the program using Simpson's method over the whole plasma history at particular values of frequency ν. The optical depth

$$\chi = \int_0^x K_\nu\, dx$$

is calculated during the time-integration by Simpson's method,

but only a few steps (~ 6) are necessary for sufficient accuracy . This keeps the total Central Processing Time needed by the program to less than 30 seconds.

The total emission spectrum is output over a range of frequencies by the program in S.I. units, for two Polarisations. At this point in the program

$$E(\nu) = \int_0^{TFINISH} I(\nu, t)\, dt \qquad (J\, m^{-2}\, Str^{-1} \text{ per } rads^{-1})$$

is converted to the total photon emission $N(\lambda)$ of the plasma area as a function of wavelength for both polarisations.

$$N(\lambda) = \frac{\nu}{hc} E(\nu) \times 10^{-10} \qquad (\text{Photons } Str^{-1} \text{ Å}^{-1})$$

$N(\lambda)$ is then drawn by the program as a function of wavelength using high level Fortran graph-plotting routines described in the file INFO.SPEC.HIGRAPH on the Cambridge 370/165 computer.

The Data list for the Continuum Emission program

All units read into the program are S.I. All cards except the first are produced in a final data block by LPSTH.

Data Card 1:	FREQ1,	FREQ2,	AREA,	NSTEPS,	INTSTP
	(4.286D14	1.D16	2.D-7	40	6)

FREQ1 and FREQ2 are the lower and upper frequency limits of the range to be studied.
AREA is the focal area of the laser condensing lens, assumed to be the emitting area of the plasma.
NSTEPS is the no. of frequency intervals into which the range is to be divided.
INTSTP is the no. of even intervals by which the optical depth χ is calculated.

Data Card 2: NPOINTS, RANGE

(300 0.1D-5)

This and subsequent cards are supplied by 'LPSTH'. In the Output of LPSTH, this card is preceded by the statement "DATA: NO. OF STEPS AND RANGE,DIMENSION,TEMPERATURE"

All cards written after this statement make up the datalist for the Continuum Emission Program, formatted as they are by LPSTH.

```
CMF1.J(EMISSION)  23 NOV 81 14.53

      IMPLICIT REAL*8(A-H,O-Z)
      REAL FLOAT
      COMMON/ONE/SIZE(1005),TEMP(1005),FREQ,INTSTP
      COMMON/SEVEN/G,H,CF
      COMMON/NINE/DELTA,EPSILO
C THE LAST TWO COMMON BLOCKS ARE READ AT THE END OF
C THE DATAFILE AND ARE USED AS CONSTANTS BY TWO SUBPROGRAMS.
      DOUBLE PRECISION ARRAY(5)
C START DATA READ IN
      DOUBLE PRECISION X(101),Y(101)
      WRITE(6,900)
      READ(5,*) FREQ1,FREQ2,AREA,NSTEPS,INTSTP
      WRITE(6,901) FREQ1,FREQ2,AREA,NSTEPS,INTSTP
      READ(5,*) NPOINT,RANGE
C NOTE: ONLY THE FIRST DATA CARD IS UNIQUE TO THIS PROGRAM.
C THE REST HAVE BEEN GENERATED BY 'TEMPERATURE AND SPACE HISTORY'.
      NPOINT=NPOINT+1
C THE NO. OF STEPS WAS ACTUALLY READ IN, NOT POINTS!
      WRITE(6,902) NPOINT,RANGE
C INITIALISE THE DATA ARRAYS
      DO 11 I=1,1005
      SIZE(I)=-1.D0
11    TEMP(I)=-1.D0
C READ IN THE ARRAYS 'SIZE' AND 'TEMP'
      I=0
3     READ(5,*) ARRAY
      DO 1 J=1,5
1     SIZE(I+J)=ARRAY(J)
      IF(ARRAY(5).LT.0.D0) GOTO 2
      I=I+5
      GOTO 3
2     I=0
6     READ(5,*) ARRAY
      DO 4 J=1,5
4     TEMP(I+J)=ARRAY(J)
      IF(ARRAY(5).LT.0.D0) GOTO 5
      I=I+5
      GOTO 6
C READ THE COMMON BLOCKS 7 & 9
5     READ(5,*) G,H,CF
      READ(5,*) DELTA,EPSILO
      WRITE(6,903) CF,NSTEPS
C SET UP THE FREQUENCY
      DELTF=(FREQ2-FREQ1)/DBLE(FLOAT(NSTEPS))
      FREQ=FREQ1
      N=1
C SET UP THE TIME INTEGRATION
10    VAL=GRND(1)+GRND(NPOINT)
      DELTAT=RANGE/DBLE(FLOAT(NPOINT-1))
      J=NPOINT-1
      DO 7 I=2,J,2
7     VAL=VAL+4.D0*GRND(I)
      J=NPOINT-2
      DO 8 I=3,J,2
8     VAL=VAL+2.D0*GRND(I)
      EFREQ=VAL*DELTAT/3.D0
C WRITE THE ENERGY SPECTRUM AS A FUNCTION OF FREQUENCY
      WRITE(6,904) FREQ,EFREQ

C  CONVERT FREQUENCY INTO ANGSTROMS.
C  CONVERT ENERGY SPECTRUM (FOR TWO POLN) INTO TOTAL
C  PHOTON EMISSION GROM FOCAL AREA PER ANGSTROM.
C  FOR BOTH POLARISATIONS.
      X(N)=3.D18/FREQ
      Y(N)=AREA*EFREQ*FREQ*5.05D05
      IF(N.GE.(NSTEPS+1)) GOTO 9
      N=N+1
      FREQ=FREQ+DELTF
      GOTO 10
C  DRAW THE TOTAL PHOTON EMISSION AS
C  A FUNCTION OF WAVELENGTH.
C FIND OUT PHYSICAL LIMITS
9     CALL GRLM4D(PXL,PXH,PYL,PYH)
      PXHNEW=PXL+0.67D0*(PXH-PXL)
C SET NEW LIMITS
      CALL GRLM2D(PXL,PXHNEW,PYL,PYH)
      CALL GRLM7D(1)
C DRAW GRAPH WITH AUTO SCALE ON
C SET MARKS INSIDE AND NO MINOR MARKS
C SET X & Y AXIS ANNOTATION
      CALL GRFT3D(2.D0,0.D0,5,5,0.D0,1)
      CALL GRFT4D(2.D0,0.D0,5,5,0.D0,1)
      CALL GRFT2D(1,-1,1,1)
      CALL GRAN2D(5,0)
      CALL GRAN3D(0,0)
      CALL GRGR6D(X,Y,(NSTEPS+1))
C WRITE LABELS
      CALL GRAN6D('PLASMA EMISSION',15,
     &'WAVELENGTH IN ANGSTROMS',23,
     &'GEGA PHOTONS/STERADIAN/ANGSTROM',31)
      STOP
900   FORMAT(44H CONTINUUM TIME-INTEGRATED EMISSION SPECTRUM,
     &14H OF THE PLASMA)
901   FORMAT(1H0,16HFREQUENCY LIMITS,2D12.4/
     &1H ,13HEMITTING AREA,D12.4/
     &1H ,I4,20H FREQUENCY INTERVALS/
     &1H ,I4,24H SPACE-INTEGRATION STEPS)
902   FORMAT(1H0,I3,37H TIME-INTEGRATION POINTS, OVER A TIME,
     &7H RANGE ,D12.4)
903   FORMAT(1H0,37HDATA:  COLLISION CONSTANT , NUMBER OF,
     &45H INTERVALS, AND FREQUENCY-EMISSION(FREQUENCY)/
     &1H0,D12.4,I4)
904   FORMAT(1H ,2D12.4)
      END
      FUNCTION GRND(N)
      IMPLICIT REAL*8(A-H,O-Z)
      REAL FLOAT
      COMMON/ONE/SIZE(1005),TEMP(1005),FREQ,INTSTP
C FIND THE OPTICAL DEPTH
      IF(N.NE.1) GOTO 3
      GRND=0.D0
      RETURN
3     CONTINUE
      VAL=ABSORB(0.D0,N)+ABSORB(SIZE(N),N)
      DELTAX=SIZE(N)/DBLE(FLOAT(INTSTP))
      J=INTSTP-1
      DO 1 I=1,J,2
```

```
      XV=DBLE(FLOAT(I))*DELTAX
1     VAL=VAL+4.D0*ABSORB(XV,N)
      J=INTSTP-2
      DO 2 I=2,J,2
      XV=DBLE(FLOAT(I))*DELTAX
2     VAL=VAL+2.D0*ABSORB(XV,N)
      VAL=VAL*DELTAX/3.D0
C VAL IS THE OPTICAL DEPTH NOW
      IF(VAL.GE.(1.5D2)) VAL=1.5D2
      VAL=1.D0-1.D0/DEXP(VAL)
      ARG=4.801D-11*FREQ/TEMP(N)
      IF(ARG.GE.(1.5D2)) ARG=1.5D2
      VAL=VAL/(DEXP(ARG)-1.D0)
      VAL=VAL*(FREQ**3)
      IF(VAL.LT.(1.D-20)) VAL=0.D0
      VAL=1.4743D-50*VAL
      GRND=VAL
      RETURN
      END
      FUNCTION ABSORB(XV,N)
      IMPLICIT REAL*8(A-H,O-Z)
      REAL FLOAT
      COMMON/ONE/SIZE(1005),TEMP(1005),FREQ,INTSTP
      COMMON/SEVEN/G,H,CF
      COMMON/NINE/DELTA,EPSILO
      W=FREQ
      TM=TEMP(N)
      X=SIZE(N)
C FIND THE PLASMA DENSITY AT XV, DIMENSION X
      DENSIT=G*(X-XV)/X**2
      ABSORB=DELTA*(DENSIT**2)/((W**3)*DSQRT(TM))
      ARG=EPSILO*W/TM
      IF(ARG.GE.(1.5D2)) ARG=1.5D2
      ABSORB=ABSORB*(1.D0-DEXP(-1.D0*ARG))
      ABSORB=ABSORB/RINDEX(W,X,XV,TM)
      RETURN
      END
      FUNCTION RINDEX(W,X,XV,TM)
      IMPLICIT REAL*8(A-H,O-Z)
      REAL FLOAT
      COMMON/SEVEN/G,H,CF
      FQ=CF*(TM**(1.D0/6.D0))*G*(X-XV)/X**2
C  CALCULATE THE COLLISION FREQUENCY FQ.
      WP=H*DSQRT(G*(X-XV)/X**2)
C CALCULATE REFRACTIVE INDEX USING PLASMA FREQUENCY AND
C THE COLLISION FREQUENCY
      RINDEX=((1.D0-(WP/W)**2)**2+(FQ/W)**2)**0.25
      RETURN
      END
```

BIBLIOGRAPHY

Baig, A.,(1981), Private Communication

Bass, A.M.,Garvin,D. (1962), Journal of Molecular Spec. 9 114-123

Bekefi, G. (1966),'Radiation Processes in Plasmas (Wiley Series in Phys.) New York.

Berkowitz, J.,(1979), 'Photoabsorption, Photoionisation and Photoelectron Spectroscopy' New York (AP).

Breton, C., Papoular, R., (1973), Journal of Optical Soc. of America 63 1225.

Broida, H.P., Kane, W.R., (1953), Phys.Rev. 89 1053

Burgess, D.D., Fawcett, B.C., Peacock, N.J.,(1967), Proc. Phys. Soc. 92 805

Carroll, P.K., Kennedy, E.T., O'Sullivan, G. (1980), Applied Optics 19 1454

Carrington, T., Broida, H.P.,(1958), Journal Molecular Spectroscopy 2 273

Codling, K.,(1973), Rep.Prog.Phys. 36 541

Cook, A.H., (1966), Nature 211 503

Cook, A.H., (1968), Mon.Not.R.Astronom.Soc. 140 299

(1975), Mon.Not.R.Astronom.Soc. 152 383

(1977), 'Celestial Masers'. Cambridge Monographs on Physics. Cambridge University Press.

Cook, A.H. a (1977), 'Celestial Masers', CUP Section 3.3

b (1977), " " " Chapter 1

David, C. et al (1966), IEEE Journal Quantum Electronics Vol.QE2, p.493

de Reilhac, L.,Damany, N., (1977), Journal Quant.Spectrosc. Radiat. Transfer 18 121

Dieke, G.H. and Crosswhite, H.M. (1962), Journal Quant. Spectrosc. Radiat. Transfer 2 97

Douglas, A.E., (1974), Canadian Journal of Physics 52 318

Dousmanis, G.C., Sanders, T.M., Townes, C.H. (1955), Phys. Rev. 100 1735

Duncan, A.B.F., (1971), 'Rydberg Series in Atoms and Molecules', New York (AP).

Ehler, A.W., Weissler, G.L., (1966), Applied Phys.Letters 8 89

Elitzur, M., (1980), 'Physical Processes in Red Giants', Workshop at Erice, Italy. September 1980.

Fano, U., (1961), Phys.Rev. 124 1866

Fox, K., Jennings, D.E., (1978), Astrophysical Journal 226 143

Golden,D.M., Del Greco, F.P., Kaufman, F., (1963), Journal Chem. Physics, 39 3034

Griem, H.R., (1964), 'Plasma Spectroscopy', New York (AP).

Gurther, P., Saile, V., Koch, E.E. (1977), Chem. Phys. Lett. 51 386

Gwinn, W.D., Turner, B.E., Goss, W.M., Blackman, G.L., (1973) Astrophysics Journal 179 789

Herzberg, G., (1946-66),'Molecular Spectra and Molecular Structure', 3 Vols. New York (AP).

Hirschfelder, J.O. et al (1954), 'Molecular Theory of Gases and Liquids', Wiley, New York.

Johnston, I.D., (1967), Astrophs. Journal 150 33

Kaufman, F., Del Greco, F.P., (1961), Journal Chem.Phys. 35 1895

"Landolt-Bornstein Zahlenwerte und Funktionen", (1963), 6th Ed. Vol.II, Part 8, "Optische Konstanten", Springer-Verlag, Berlin, New York.

Lee, L.C., Carlson, R.W., Judge,D.L., (1975), Molec.Phys. 30 1941

Lengyl, B.A., (1962), "Lasers", Wiley.

Litvak, M.M., et al (1966), Phys.Rev.Lett. 17 821

(1969), Astrophys.Journal, 156 471

Loudon, R. (1973), "Quantum Theory of Light", Clarendon Press

Lu, K.T., Fano, U., (1970), Phys.Rev.A 2 81

Mahajan, C.G., Baker, E.A.M., Burgess, D.D., (1979), 'Optics Letters' 4 283

Maryott, A.A., Buckley, F. (1953), Natl. Bur. Stand.(US), Circ. No.537

Matsunaga, F.M., Watanabe, K., (1967), Sci. Light (Tokyo), 16 31

Metzger, P.H., Cook, G.R., (1964), Journal Chem.Phys. 41 642

Meulen, J.J. ter, Phd.Thesis.

Nakayama, T., Watanabe, K., (1964), Journal Chem.Phys. 40 558

Oka, T., (1971), "Proc. Conf. on Interstellar Molecules", Charlottesville, Virginia, U.S.A.

Oldenberg, O. (1935), Journal Chem. Phys.3 266

Panofsky, W.K.H., Phillips, M. (1955), "Classical electricity and magnetism", Addison-Wesley.

PaO, Yoh-han, (1977), "Optoacoustic Spectroscopy and detection", New York (AP).

Price, W.C., (1935), Phys.Rev. 47 444

Radford, H.E., (1961), Phys.Rev. 122 114

Ready, J.F., (1971), "Effects of High Power Laser Radiation", New York (AP).

Riley, K.F., (1974), "Mathematical Methods for the Physical Sciences", Cambridge University Press.

Rodebush, W.H., Wahl,M.H.,(1933), Journal Chem.Phys. 1 696

Samson, J.A.R., (1967), "Techniques of VUV Spectroscopy", Wiley

Sciama, D.W., (1971), "Modern Cosmology", Cambridge University Press.

Tabor, D., (1969), "Gases, Liquids and Solids",Penguin Education.

Tan, K.H., Brion, C.E., (1978), Journal Chem.Phys. 29 299

Thorne, A.P., (1979, 1974), "Spectrophysics", Chapman-Hall.

Tomboulian, D.H., Hartman, P.L., (1956), Phys.Rev. 102 1423

Viney, J.C., (1979), Phd.Thesis.

(1980), Journal Molec. Spectrosc. 83 465

Weaver, H.F., et al (1965), Nature 208 29

Weinreb, S., et al (1963), Nature 200 829

Wilkinson, P.G., (1963), Astrophys. Journal 138 778

Wynn-Williams, G. (1981), Sci. American 245 N2